Technische Universität München
Fakultät für Physik

Modeling of the Galactic Cosmic-Ray Antiproton Flux and Development of a Multi-Purpose Active-Target Particle Telescope for Cosmic Rays

Thomas Pöschl

Vollständiger Abdruck der von der Fakultät für Physik der Technischen Universität München zur Erlangung des akademischen Grades eines

Doktors der Naturwissenschaften (Dr. rer. Nat.)

genehmigten Dissertation.

Vorsitz: apl. Prof. Dr. Norbert Kaiser

Prüfer*innen der Dissertation:

1. Prof. Dr. Stephan Paul
2. Prof. Dr. Elisa Resconi

Die Dissertation wurde am 09.06.2022 bei der Technischen Universität München eingereicht und durch die Fakultät für Physik am 28.06.2022 angenommen.

Abstract

The abundances and energy spectra of cosmic-ray particles are an excellent probe to study processes in our galaxy and can hint to exotic sources of energetic particles, such as dark-matter annihilation. The precise measurement of antinuclei, such as antiprotons, antideuterons, or antihelium, is particularly informative since these particles are expected to be only rarely produced in conventional reactions. However, the interpretation of antinuclei measurements requires a good understanding of all involved processes of the creation and propagation of the antiparticles as well as a realistic estimate of the involved modeling uncertainties to distinguish potential exotic contributions from ordinary production.
In this thesis, I review the current understanding of production and propagation of charged cosmic rays in our galaxy and the thereon based modeling of galactic cosmic-ray fluxes, with a special focus on galactic antiprotons. In particular, I investigate systematic deviations that arise due to inaccuracies of the numerical solution of the propagation equation and systematic uncertainties from the production model of antiprotons in cosmic-ray collisions. For the latter, several models based on Monte-Carlo event generators and models based on analytical parameterizations are compared and their accordance with experimental data from accelerator-based experiments is evaluated. The agreement between the antiproton fluxes from the different production models and the measurement of the cosmic antiproton flux by the AMS-02 experiment is investigated. While the event-generator-based models overestimate the produced antiproton flux compared to the AMS-02 measurement, the fluxes predicted by the parameterization-based production models agree within 25 % with the data. The found model uncertainties, however, hinder a conclusive statement on whether the measured antiproton flux is consistent with a purely conventional flux from cosmic-ray interactions or exhibits contributions from additional exotic sources.
As an even more sensitive probe for exotic sources of antimatter in the galaxy, flux measurements of heavier antinuclei have been proposed as their production in ordinary cosmic-ray collisions is even rarer than that of antiprotons. However, such particles have not yet been detected in the cosmic ray spectrum due to their extremely low flux. New detector concepts are necessary to reach the sensitivity required to detect these particles. I describe the development of a novel detector concept with a large sensitivity due to its omnidirectional acceptance of particles. It is based on a segmented volume of scintillating plastic fibers and the entering particles are identified by their unique energy-deposition profile. I present two algorithms to reconstruct the particle characteristics from the detector signals and discuss limitations of the technique stemming from saturation effects of the scintillators. To showcase the ability of the detector for cosmic-ray measurements, two technology demonstration missions are currently planned: One to measure the radiation environment inside the International Space Station and one to measure geomagnetically trapped an-

tiprotons in the inner Van-Allen belt. Both missions are discussed and prospects for a future measurement of heavier antinuclei with such a detector are given.

Zusammenfassung

Die Vermessung von kosmischer Strahlung eignet sich hervorragend zur Untersuchung galaktischer Prozesse und zur Identifikation exotische Quellen von hochenergetischen Teilchen, wie zum Beispiel der Annihilationsprozess von dunkler Materie. Insbesondere die Flussrekonstruktion von Antikernen wie Antiprotonen, Antideuteronen oder Antihelium scheint besonders aufschlussreich, da wir erwarten, dass solche Teilchen nur sehr selten in konventionellen Reaktionen in unserer Galaxis entstehen. Um entscheiden zu können, ob ein gemessener Fluss an Antikernen durch rein konventionelle Reaktionen erklärbar ist, müssen die Prozesse der konventionellen Entstehung und der Ausbreitung der Teilchen in der Galaxie genau modelliert werden, inklusive einer realistischen Abschätzung der Modellunsicherheiten.
Im Rahmen dieser Arbeit wird das derzeitige Verständnis der Entstehung und der Ausbreitung geladener komischer Strahlung in unserer Galaxie betrachtet und die darauf basierende Modellierung der zu erwartenden Teilchenflüsse beschrieben, mit besonderem Fokus auf die Modellierung des galaktischen Antiprotonenflusses. Ich werde insbesondere die systematischen Abweichungen der modellierten Teilchenflüsse untersuchen, welche einerseits durch Ungenauigkeiten bei der numerischen Lösung der Gleichungen zur Beschreibung der Ausbreitung der Teilchen in der Galaxie entstehen, und andererseits durch Unsicherheiten in der Beschreibung des Produktionsmodells von Antiprotonen in Kollisionen kosmischer Strahlung mit interstellarer Materie entstehen.
Für letzteres werden verschiedene Arten von Modellen verglichen: Modelle basierend auf Mehrzweckereignisgeneratoren und Modelle basierend auf einer analytischen Parametrisierung des Produktionswirkungsquerschnitts. Die Übereinstimmung der einzelnen Modelle mit Messungen von Experimenten an Teilchenbeschleunigern wird bewertet und die modellierten kosmischen Antiprotonenflüsse der einzelnen Produktionsmodelle werden mit der Messung des kosmischen Antiprotonenflusses des AMS-02 Experiments verglichen. Während die auf Ereignisgeneratoren basierenden Modelle den zu erwartenden Antiprotonenfluss im Vergleich mit der AMS-02-Messung überschätzen, stimmen die Vorhersagen der auf analytischen Parametrisierungen basierenden Modellen innerhalb von 25 % mit den Daten überein. Die gefundenen Modellunsicherheiten erlauben jedoch keine eindeutige Aussage darüber, ob der gemessene Antiprotonfluss allein durch Interaktionen der kosmischen Strahlung erklärt werden kann oder die Existenz exotischer Quellen notwendig ist.
Als weitere Möglichkeit für die Suche von exotische Quellen von Antimaterie in der Galaxie, wurden Flussmessungen von schwereren Antikernen vorgeschlagen, da deren Produktion in konventionellen Kollisionen von kosmischer Strahlung deutlich seltener ist als die von Antiprotonen. Allerdings konnten solche Teilchen aufgrund ihres extrem geringen Flusses bisher nicht in der kosmischen Strahlung nachgewiesen werden. Neue Detektorkonzepte

sind notwendig, um die erforderliche Empfindlichkeit für den Nachweis dieser Teilchen zu erreichen. Ich werde deshalb die Entwicklung eines neuartigen Detektorkonzepts beschreiben, welches aufgrund seiner Fähigkeit zur omnidirektionalen Akzeptanz von Strahlungsteilchen eine besonders hohe Flusssensitivität aufweist. Der Detektor besteht aus einem segmentierten Volumen, welches aus szintillierenden Plastikfasern aufgebaut ist; die eintretenden Teilchen werden anhand ihres Energieverlustprofils in dem Volumen charakterisiert. Ich werde zwei Algorithmen beschreiben, welche entwickelt worden sind, um die Teilcheneigenschaften aus dem Detektorsignal zu rekonstruieren. Des Weiteren werde ich die Limitierungen dieser Rekonstruktionsmethodik durch auftretende Saturierungseffekte in den szintillierenden Fasern diskutieren.
Die Funktionsfähigkeit des Detektors in der relevanten Umgebung des Weltalls soll durch zwei Demonstrator-Missionen gezeigt werden: Eine Mission zur Messung der Strahlungsumgebung innerhalb der Internationalen Raumstation und eine Mission zur Vermessung der im Magnetfeld der Erde gefangenen Antiprotonen auf einem Kleinsatelliten. Nach einer Beschreibung beider geplanter Missionen wird eine zukünftige Verwendung des Detektorkonzepts für die Messung von schwereren Antikernen diskutiert.

Contents

Introduction

Cosmic radiation can be both, a valuable messenger of astrophysical phenomena in our universe that helps us to understand the structure and evolution of the cosmos, and a threat to human space exploration due to its biological hazard to astronauts [1, 2]. Understanding its characteristics is important to interpret existing measurements, describe the spatial and temporal dependence of its flux, and predict the exposures in future space missions. To do so, we construct physical models that describe in detail the production and transport of cosmic-ray particles—based on our current understanding of the involved processes, predict their flux at Earth, and compare this modeled flux to experimental data. By this, we can estimate the validity of our models and, if needed, refine them. Due to advances in experimental methods, the measurements become more precise and experiments unveil so-far unseen additional features in the cosmic-ray spectra. If these features are not reproduced by our models, this indicates inaccurate modeling of known processes or the existence of additional, unknown processes not yet included in our models [3]. To find the reason for the deviation and assign the corresponding process is not trivial: Since we can only probe the cosmic-ray flux at one specific point in our galaxy—namely at Earth—we cannot decide easily if a newly found feature is generated by the cosmic-ray source or if it arises due to processes during propagation of the particles to us. Especially for charged cosmic rays, the particle-species abundances and energy spectra are heavily altered during their propagation, and only accurate modeling of the transport mechanisms allows us to retrieve the spectrum of cosmic rays at their origin, which is key for the understanding of the production and acceleration processes of cosmic rays [4].

To interpret the significance and cause of a found deviation, uncertainties of measurement and model have to be quantified accurately. In the past, statistical uncertainties of measurements were often dominating, limiting the significance of a new finding. New long-term experiments, either on satellites or long-duration balloon flights, changed this picture by providing data with very high statistical precision, putting the focus on systematic uncertainties [5]. Their understanding and quantification is now the crucial point to correctly interpret novel features in new measurements: underestimating them could lead to false excess signals; overestimating them could decrease the sensitivity of an experiment unnecessarily, hindering new findings. To identify and quantify all relevant systematic uncertainties and their correlations in our models of cosmic-ray production and propagation is one of the main tasks of cosmic-ray physics today [6].

One particular process during the propagation of cosmic rays through our galaxy that modifies the spectra of cosmic rays significantly, and thus could give rise to large modeling errors, is inelastic scattering [7, 8, 9]. Cosmic-ray particles interact with the interstellar

material distributed in the galaxy, thereby altering their spectral distribution and flux. In these interactions, the cosmic-ray particles are either moderated, absorbed, or create additional energetic particles that potentially reach our detectors. These interactions can take place far away in the galaxy, altering the overall flux of cosmic-rays, or very close to Earth, giving rise to local spatial variations of the cosmic-ray flux.
Since in inelastic collisions also particles can be created that—based on our current knowledge of cosmic-ray acceleration—we do not expect to exist in the cosmic-ray spectrum, these collisions also strongly affect the search for exotic sources of cosmic rays in astrophysics. In recent years, the search for antinuclei has attracted increasing attention due to theoretical predictions of exotic production mechanisms, such as dark-matter annihilation or decay. In these searches, the contribution of antinuclei production from inelastic collisions acts as a background. To be able to decide if a measured flux of antinuclei is consistent with a pure contribution from inelastic collisions or if an additional exotic source is present, we require again an accurate model of particle creation in collisions of cosmic rays and a realistic uncertainty estimate [9].

This thesis is focused on our current models of the production and propagation of galactic nuclei and antinuclei and the ongoing development of a particle detector, based on a novel particle-identification approach, that shall be used for cosmic-ray-flux measurements in future.
After introducing galactic cosmic rays and the relevant processes of their origin and propagation in Chapter 1, I present a current state-of-the-art modeling scheme in Chapter 2 and study the influence of different numerical settings of the model on the modeled cosmic-ray fluxes.
For antiprotons and other antinuclei, the production cross section in inelastic cosmic-ray collisions is one of the largest sources of uncertainty when modeling their cosmic flux. In Chapter 3, I discuss different models for antiproton production in cosmic-ray collisions and their impact on the modeled antiproton flux. As an outlook, I discuss the impact of the antiproton-production model on the modeling of heavier antinuclei in the galaxy.
In Chapter 4, I present the development of a novel particle detector, called 'Multi-Purpose Active-Target Particle Telescope' (MAPT), that can be used to provide measurements to validate our cosmic-ray models. I present MAPT's working principle and event-reconstruction scheme and estimate the measurement capabilities of MAPT by simulations and test measurements. I give an outlook on the usage of MAPT for the search of low-energy antinuclei and upcoming technology demonstration missions in space, which shall showcase the functionality of the detector.
Chapter 5 summarizes the findings of this work.

Chapter 1

Galactic Cosmic Rays

Until the second decade of the past century, physicists believed that the main source of radiation on the surface of Earth is from radioactive decays in the soil. First measurements of the radiation environment below the soil and at altitudes of several hundred meters above ground seemed to confirm this assumption as the radiation level slightly decreased with altitude [10]. But measurements at even higher altitudes—above 1000 m—using balloons showed an increase of the radiation level to even larger values than at ground. Victor Hess, who investigated the altitude dependence of the radiation level as one of the first systematically during several balloon ascents, concluded that the radiation has its origin in outer space and has to be extraordinary energetic in order to penetrate the atmosphere [11, 12]. However, this new source of radiation was only generally accepted more than ten years after this discovery in the late 1920s after several further experiments verified his results [13, 14].

In the following decades this new form of radiation, commonly called cosmic rays, was investigated further: Of special interest was the question of its composition. Although most people originally believed cosmic rays to be photons—due to its large penetration power—it soon became clear that most cosmic rays carry electric charge. This was concluded from measurements at different geomagnetic locations that revealed a large correlation between the intensity and direction of cosmic rays and the experiment's location within Earth's magnetic field [15, 16]. With the development of advanced particle detectors, it became possible to determine the charge, its sign, and the mass of the detected cosmic-ray particles. Most of them were found to be protons and only some of them to be electrons or heavier nuclei. But additionally, particles with so far unknown combinations of charge and mass were found, including a positively charged electron-like particle, the positron—the antiparticle of the electron—which was predicted by Paul Dirac as a solution with negative energy of his relativistic wave equation [17, 18]. Not only was this the first proof of the existence of antimatter, but also the verification that it exists naturally in our universe. Later, many more fundamental but short-lived particles were found during cosmic-ray measurements, such as the muon, the pion, the kaon, and the lambda, leading to the development of human-made particle accelerators and the field of particle physics [19, 20]. But as most of these particles decay after only fractions of a second, it was directly concluded that these particles cannot be part of the initial cosmic-ray spectrum but must be created in the measurement apparatus itself or in interactions of cosmic rays with Earth's

atmosphere [21].
By using unmanned high-altitude balloons, sounding rockets, and satellites, it later became possible to conduct experiments above the disturbing influence of the atmosphere. Within a series of measurements on sounding rockets, Van Allen found another influencing factor of Earth on cosmic rays: The magnetosphere. He found that the trajectories of charged cosmic-ray particles are deflected by the magnetic field of Earth via the Lorentz force such that in some regions most cosmic rays are shielded very efficiently from reaching Earth, while in other regions they are forced to accumulate, forming belt-like structures of enhanced radiation around Earth, the so-called Van Allen radiation belts. This results in a strong location dependence of the cosmic-ray flux in the vicinity of Earth.
Additionally, a strong time dependence of the cosmic-ray flux, which had been already indirectly observed by neutron-monitor experiments at sea level in the 1950s, was also confirmed by time-displaced space-based experiments [22, 23] . The temporal change of the cosmic-ray flux was found to coincide with the sunspot-activity cycle of Sun. As the solar activity increased—more sunspots visible—the measured flux of cosmic rays decreased, and vice versa. So Sun's varying magnetic field and plasma outflow also influences the local cosmic-ray flux significantly. The variation is periodic with a 11-year cycle duration and affects especially the low-energy component of the charged cosmic rays. Later, also a 22-year cycle and several short-term variations were found [24].

In order to extract the cosmic-ray flux prior to the disturbances from the local environment of Earth and Sun, which is usually referred to as the local interstellar flux, one has to either unfold the modification of the particle fluxes from measurements using theoretical models or to measure the particle flux away from the influencing reach of Sun, outside of the so-called heliosphere [25, 26]. The latter was just recently achieved for the first time by particle detectors on the Voyager probes about 40 years after their launch [27]. Due to the long travel duration and the complexity of such a mission, further experiments are not likely to measure outside the heliosphere within the next decades and we have to focus on improving our models of the heliosphere to determine the interstellar cosmic-ray flux indirectly from the measurements within the heliosphere. However, the Voyager measurements together with measurements at very large particle energies, for which the influence of the near-Earth environment is only marginal, can be used to improve the models of the near-Earth environment and to decrease the resulting systematic uncertainties on the extracted interstellar cosmic-ray flux and its composition [28]. In Section 1.3.1, I discuss the models currently used to calculate the local interstellar fluxes from measurements inside the heliosphere.
From the interstellar flux of charged cosmic rays, we can learn about the processes in the universe that create such fast particles. Although their trajectories are heavily altered during the journey from their source to the solar system—and we cannot directly point back to their origin—we can indirectly infer information about their creation processes by investigating their abundance, composition, and energy spectra. Alone from first measurements of the spectral distribution of cosmic rays, back in the early 1940s, that had shown that the flux of cosmic rays decreases with increasing energy following a power-law [29], Enrico Fermi deduced a theory on a possible acceleration mechanism: Fast moving magnetic fields, as they might be produced in shock waves of explosions, potentially accelerate charged particles [30, 31]. Later, composition measurements of cosmic rays revealed that

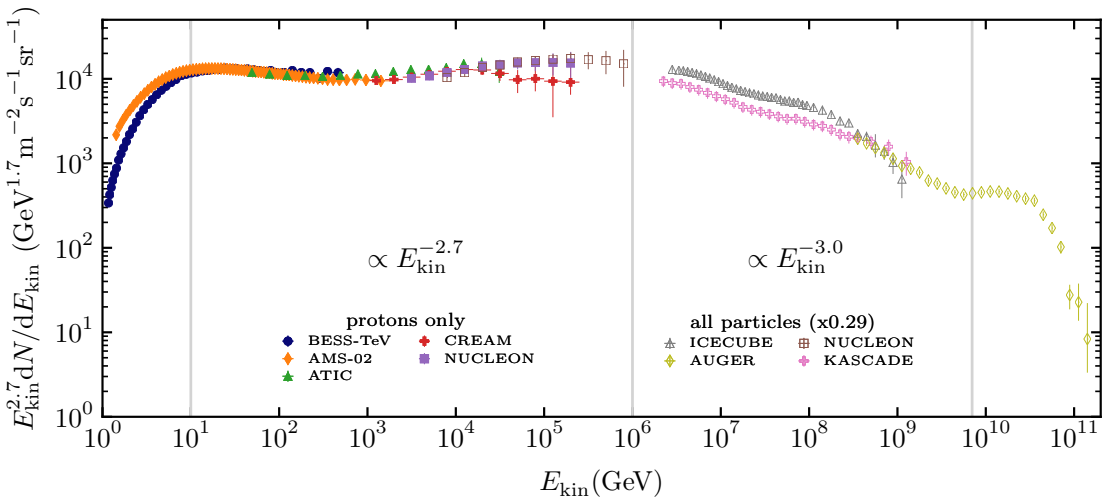

Figure 1.1: Measurements of the cosmic-ray energy-dependent proton and all-particle flux multiplied by $E^{2.7}$. The all-particle flux is scaled by 0.29. The experimental data are extracted from the cosmic-ray database [35].

the abundance of different ion species in cosmic rays is very similar to the composition of the solar system, putting large exploding stars, called supernovae, into the focus of being a good candidate for injecting and accelerating cosmic-ray particles [32, 33, 34].

More detailed investigations of the energy spectrum of cosmic rays, however, revealed deviations from the simple power-law-like energy dependence of the cosmic-ray flux, as can be seen in Figure 1.1, which shows selected measurements of the energy spectrum of cosmic-ray protons and all cosmic-ray particles. To visually highlight the deviations of the flux from a single power-law-like behavior, we multiply the measured flux by $E^{2.7}$ and scale the all-particle-flux to the proton-only measurements by using the proton-to-all-particle ratio of the NUCLEON space experiment [36]. For the most part, the cosmic-ray particle flux, $\mathrm{d}N\,/\,\mathrm{d}E_{\mathrm{kin}}$, decreases with increasing kinetic energy of the particle, E_{kin}, following a power-law,

$$\frac{\mathrm{d}N}{\mathrm{d}E_{\mathrm{kin}}} \propto E_{\mathrm{kin}}^{-\alpha}, \tag{1.1}$$

with $\alpha \approx -2.7$ for energies between 10 GeV and 1×10^6 GeV and with $\alpha \approx -3.0$ for energies between 1×10^6 GeV and 1×10^{10} GeV. At lower energies, the flux does not follow a power-law-like behavior because of the complex modulation by the near-Earth environment. At higher energies, above 1×10^{10} GeV, the flux first flattens—following a different power law with $\alpha \approx -2.6$—before becoming strongly suppressed. The suppression is believed to originate from the predicted Greisen-Zatsepin-Kuzmin limit [37, 38]. The spectral breaks at around 1×10^6 GeV and 1×10^{10} GeV are referred to as the knee and the ankle of the cosmic-ray energy spectrum. Such breaks are nowadays usually interpreted to arise at energies for which the dominant particle source changes: Above the ankle, particles are believed to be mainly of extra-galactic origin, since to date no object in our galaxy is

known that would be able to accelerate particles to such high energies [39]. Candidates to source such energetic particles are active galactic nuclei, which are galaxies with a supermassive black hole in their center [40, 41].
Below the ankle, the majority of the particles is believed to be produced within our galaxy. They are termed galactic cosmic rays.

The theories on the origin of the knee are currently still under debate: It is unclear whether the break originates from the sources or from the propagation of the particles from their sources to our detectors [42]. With advancing experimental techniques and more precise data, further breaks have been found in the spectra of galactic cosmic rays: For example at around 300 GeV [43], 1×10^4 GeV [44, 45] and, 1×10^8 GeV [46]. The existence of these breaks in the spectra of most nuclei suggests a common source type of these nuclei [47, 48]. For some particle, however, the energy spectra differ largely: mainly for nuclei that do not naturally appear in stellar nucleosynthesis, like boron, beryllium, or antinuclei [49, 50]. These particles are—by our current state of knowledge—only produced by inelastic processes of other cosmic-ray particles. They are of secondary origin and called secondary cosmic rays.
These secondary particles originate from collisions of propagating cosmic rays with the interstellar material, which is bound mainly in large gas or dust clouds. Secondary cosmic rays are of special interest when trying to model the propagation of cosmic rays in our galaxy: If one assumes a particle type to be purely secondary, its abundance can be determined from the primary cosmic-ray flux, the material traversed by the primary cosmic rays, and the microscopic production cross section. These particles can serve as a probe of our understanding of the propagation processes and can be used to constrain several unconstrained parameters of the propagation models [4]. Deviations between the modeled secondary particle flux and measurements could hint to improper modeling of the propagation or—in case of overproduction of only one specific secondary particle type—to an unknown, exotic source not included in the model. Commonly, light secondary nuclei are used to verify the propagation model, and antinuclei are then used to probe additional sources of antimatter within this propagation model (e.g. in [51]).
In the following section, I describe the current knowledge on production and propagation of galactic cosmic rays based on the supernova-remnant paradigm—an expression introduced in Blasi et al. [52].

1.1 Diffusive Shock Acceleration in Supernova Remnants

According to the supernova-remnant paradigm, it is believed that all non-secondary galactic cosmic rays are accelerated by shock-wave-induced magnetic turbulence following a supernova explosion [52].
The first reflections on supernovae being the source of high-energy cosmic particles were already carried out in 1934 by Baade and Zwicky: While investigating the rate and magnitude of abruptly occurring bright stars, which they termed Super-Novae [53], they found that the emitted energy in such events together with their occurrence quite naturally results in the measured intensity of cosmic rays at Earth [54]. This proposed mechanism also explains the lack of a visible source of high energetic particles in our galaxy, and it is

able to predict the composition of cosmic rays to follow the composition of stellar objects, which was only later confirmed by measurements [55]. Although this approach very elegantly resolved several open questions at that time, Baade and Zwicky did not provide a physical acceleration mechanism.
A first theoretical description of how energetic particles can emerge of a supernova explosion was only realized about 40 years later by various authors. They transferred the already existing Fermi acceleration principle, which had been originally developed to explain energy-gaining interactions of particles with intergalactic clouds, to supernova shocks. This solved the issue of a too-low maximum acceleration energy obtained by the originally proposed mechanism by E. Fermi [56, 57, 31, 58, 59, 60]. This new theory established under the term of first-order Fermi acceleration or diffusive shock acceleration. The theoretical progress of this new approach was heavily driven by measurements of ion speeds near Earth's bow shock, which is created by the interaction of Earth's magnetic field with the solar wind: It was found that in this region ions are accelerated to super-thermal energies by interactions with shock-induced magnetic turbulence [61, 62]. Even stronger shocks are believed to be created following a supernova explosion. The collapse and the subsequent explosion and ejection of a large amount of material into the interstellar medium at supersonic speed creates shock waves that penetrate the surrounding plasma [63]. Charged particles in the vicinity of the shock front are confined by the magnetic turbulence and magneto-hydrodynamical interactions and can cross the shock front multiple times [31]. The energy gain of a particle traversing the shock front from upstream the shock to downstream the shock and back depends on the relative velocity difference of the material upstream and downstream the shock, the relative shock velocity, $\beta_\mathrm{r} = v_\mathrm{r}/c$, with c being the speed of light. The average energy gain of the particle can be calculated as

$$\left\langle \frac{\Delta E}{E} \right\rangle = \frac{1 + \frac{4}{3}\beta_\mathrm{r} + \frac{4}{9}\beta_\mathrm{r}^2}{1 - \beta_\mathrm{r}^2} - 1 \approx \frac{4}{3}\beta_\mathrm{r} + \mathcal{O}(\beta_\mathrm{r}^2), \tag{1.2}$$

as derived for example in the review by G. Morlino [64].
The relative energy gain is independent of the initial energy, and the acceleration is more effective than what was obtained in the initial theory by E. Fermi, in which the energy gain was found to be proportional to β^2 [30]. To gain a considerable amount of energy by this mechanism, the particle has to cross the shock multiple times. If a particle crosses the shock front k-times back and forth, the energy of the particle is

$$E_k = E_0(1 + \frac{\Delta E}{E})^k. \tag{1.3}$$

However, after each crossing, there is a finite probability, P_esc, that the particle moves away from the shock front and is not accelerated further. If one assumes P_esc to be independent of the particle's energy, the probability to find a particle with an energy exceeding E_k is given as

$$P(E > E_k) \propto \frac{1}{P_\mathrm{esc}} \left(\frac{E_k}{E_0}\right)^{-\delta}, \quad \text{with} \quad \delta = \frac{\log(1 - P_\mathrm{esc})}{\log\left(1 + \frac{4}{3}\beta_\mathrm{r}\right)}, \tag{1.4}$$

and the resulting energy-differential particle spectrum follows a power law with an exponent $-\alpha = 1 + \delta$ [64]. Assuming supernova shocks to be highly supersonic and the surrounding

material to behave as an ideal gas, one obtains an exponent for the energy-differential particle spectrum of $\alpha \approx -2$ for the particle acceleration in supernova remnants. This obtained spectrum is slightly flatter than the measured spectrum of galactic cosmic rays at Earth ($\alpha \approx -2.7$) [64]. This deviation could either arise from modifications of the particle spectra during the propagation of the particles through the galaxy, which we discuss in the next section, or from oversimplifications of the acceleration mechanism that lead to an overestimation of the acceleration efficiency. Some exemplary mechanisms that could modify the particle spectra are: interactions of the accelerated particles with the plasma, which could reduce the efficiency of acceleration for increasing particle energies and successively steepen the energy-differential particle spectrum; particle-type dependent reactions during the acceleration that lead to different spectral shapes of the source spectrum for different particle types; and local density variations of the material that the shock traverses that could additionally cause spectral breaks in the source spectrum [65].
To constrain the source spectrum from supernova remnants further, is one major objective of the modeling of galactic cosmic rays. By comparing the modeled particle fluxes at Earth for different source spectra with experimental data, one can determine the unconstrained spectral indices and spectral-break positions of the source spectra. However, this procedure suffers from the limited knowledge of the propagation process. The propagation model itself involves additional unconstrained parameters which complicate the determination. In the following, I describe the current understanding of the propagation processes in our galaxy and the important processes during the propagation.

1.2 Propagation of Charged Cosmic-Rays in the Galaxy

From observational astronomy we know that Earth is located on a spiral arm within our galaxy, the Milky Way. The Milky Way is a large spiral galaxy containing a stellar mass of about $5 \times 10^{10}\,\mathrm{M}_\odot$ and just as many stars [66]. Like any spiral galaxy, the visible matter is most densely populated in a central bulk and several spiral arms that extend outwards within the galactic plane [67]. Figure 1.2 shows a schematic overview of the structure of the Milky Way.
The central bulk of the Milky Way is a spherical region of radius 3 kpc[1] and contains about 20 % of all stars in our galaxy. From there, four spiral arms emerge into the galactic plane, each extending about 20 kpc outwards with a thickness of only about 0.5 kpc [67]. The whole galaxy is surrounded by a spherical halo mainly composed of non-visible, non-baryonic material, called dark matter, which spreads up to more than 20 kpc into intergalactic space. Although this halo makes up around 90 % of the Milky Way's total mass, the particle properties of this type of matter is not yet known and its existence is solely based on its gravitation influence [68]. Many experimental efforts are ongoing to characterize the particle properties of dark matter, including measurements of galactic cosmic-rays, more specifically cosmic-ray antimatter [69]. Some models of dark matter predict reactions of dark-matter particles into standard model particles—including antiparticles—which add to the expected cosmic-ray antimatter flux from cosmic-ray interactions and manifest as an excess of the measured antiparticle flux over the modeled antiparticle flux from this conventional production mechanism [70]. To review the models of conventional antimatter

[1] $1\,\mathrm{kpc} \approx 3.0857 \times 10^{19}\,\mathrm{m}$

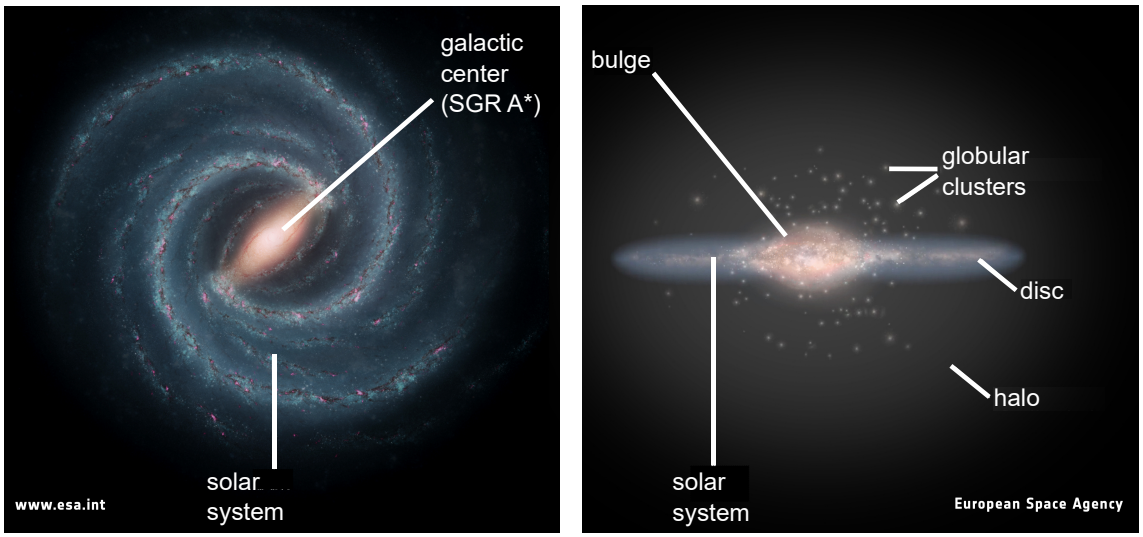

(a) Top view. (b) Side view.

Figure 1.2: Artistic view of the Milky Way. Credit: ESA (adapted by the author)

production, with a special focus on cosmic-ray antiprotons, is one of the main topics of this work.

The center of the Milky Way is populated by a massive black hole, SGR A* [71]. From astrometric and spectroscopic observations of its orbiting stars, the radial distance of Earth from the black hole, and thus from the galactic center, R_0, can be determined [72]. The most accurate determination yields $R_0 = (8.178 \pm 0.035)\,\mathrm{kpc}$ [73].

The distribution of supernova remnants—which are the sources of cosmic rays—in the Milky Way is expected to be similar to the distribution of large molecular clouds, which act as star-forming regions, as the ejected material of supernova remnants seeds star formation in this dusty environment [74]. As the amount of material in these regions is large, the resulting stars grow up to several times the mass of the Sun, potentially creating another supernova at the end of their burning phase—again injecting material for further star formation. This cycle makes it likely, that a large fraction of supernovas can be associated with such high star-forming regions [67].

Experimentally, one can survey our galaxy directly for supernova remnants or indirectly for large, heavy stars or pulsars; their distributions should be similar. It is found that most of them are located in the bulk or in the disc of the galaxy and obey similar radial distributions [75, 76, 77]. An overview of the radial distributions of supernova remnants, massive stars, and pulsars are shown in Figure 1.3. As expected, their distributions share common features: Their number densities are largest at around $0.4\,R_0$ to $0.6\,R_0$ and decrease rapidly towards the galactic center and the outer-disk region. It was found that each distribution, $f(R)$, can be parameterized well by the function

$$f(R) = \left(\frac{R}{R_0}\right)^{\alpha} \exp\left[-B\frac{R - R_0}{R_0}\right], \tag{1.5}$$

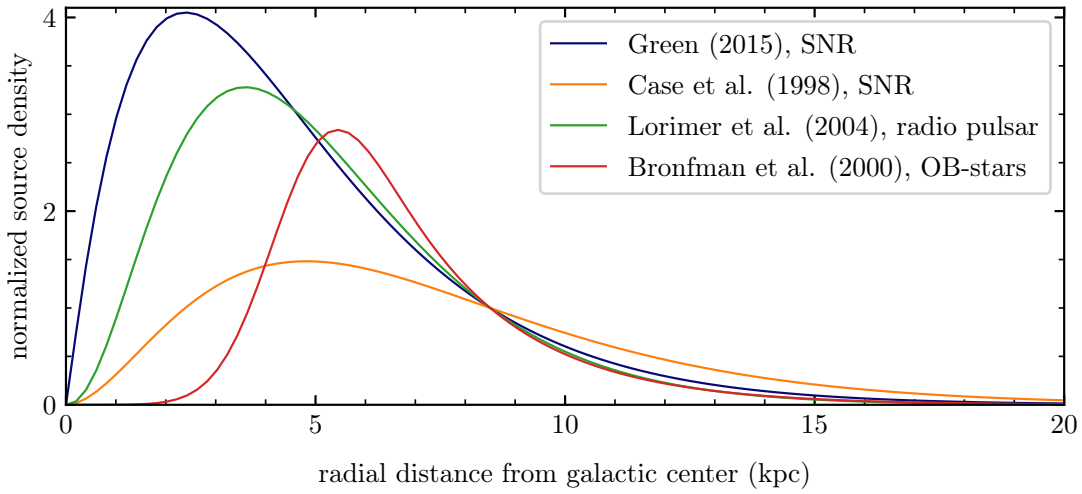

Figure 1.3: Best-fit parameterizations of the measured radial distribution of supernova remnants [75], massive stars [77], and pulsars [76] in the Milky Way using Equation 1.5. The distributions are normalized to 1.0 at 8.5 kpc.

with α and B being empirical parameters constrained by a fit to the measured distribution [78]. However, the extracted parameters differ for the distributions of the different object types and also for the same object type measured by different surveys [78]. The differences presumably arise due to systematic effects of the measurements, like systematic changes of the detection efficiency with distance, or a non-correct extraction of the distance, which cannot be directly measured but has to be derived from other measured quantities [79]. For example, the distance measurement of supernova remnants uses the relation of luminosity and angular extension of the supernova remnant—the so called Σ-D relation—to extract the distance from Earth. The applicability of this relation to extract the distance of a supernova-remnant is highly controversial and suffers from large systematic uncertainties [80, 81].
Despite some uncertainties on the distributions of the different objects remain, a consistent shape of the radial distribution of supernova-remnants as the source of cosmic rays can be extracted from these surveys.
One proposed method to validate the measured supernova-remnant distribution by directly probe the source distribution of cosmic rays is to measure the radial distribution of the diffusive gamma-ray yield. This method is based on the following consideration: If supernova remnants are truly the source of cosmic rays, the radiation density must be larger in regions near the sources, and so must the diffusive gamma-ray production created by interactions of the radiation with surrounding material [82]. Therefore, the resulting gradient of the gamma-ray emission with increasing radial distance from the galactic center should follow the supernova-remnant distribution. However, the decrease of the diffusive gamma-ray background was found in measurements to be smaller than the measured supernova-remnant distribution indicating an underestimation of supernova remnants farther outside of the Galaxy or even the existence of additional cosmic-ray sources [83]. However, the

diffusive gamma-ray emission around a source depends also on the characteristics of the surrounding matter, which has been found to vary with radial distance from the galactic center, and might also account for the deviation [84].

The experimental fact that the cosmic-ray distribution measured at Earth is isotropic to a large degree although most supernova remnants are located in direction of the galactic center already hints to a complex transport mechanism and strong randomization of the particle trajectories in the galaxy [85]. Along their way throughout the galaxy, the particles interact with galactic magnetic fields, the interstellar plasma, and scatter on baryonic matter. Depending on the strength, uniformity, and dynamic of the galactic magnetic fields, the hydro-magnetic interactions not only change the particle's direction but also lead to energy losses or gains that change the spectral shape of cosmic rays during propagation [86]. Collisional interactions, like spallation or inelastic scattering, that annihilate the initial cosmic ray particle and create other particle species, additionally change the composition of cosmic rays during propagation [4]. The amount of secondary particles that are created depends on the amount of material that the cosmic rays traverse. This is determined not solely by the material distribution in the galaxy but also by the trajectory of the particles: If the particle tracks are relatively straight and the particles leaves the galaxy within a short time, the traversed material is smaller than if the particle tracks are heavily randomized and the particles spend a longer time within the galaxy before leaving it.
The latter is expected to be the case for the Milky Way: Measurements of secondary-to-primary cosmic-ray ratios suggest that cosmic-ray particles are confined on the order of 10^8 years in our galaxy due to random magnetic fields that confine the particles [85]. In the following, I lay out the most common theory of galactic cosmic-ray transport based on a diffusive motion of cosmic rays in the galaxy.

1.2.1 Diffusion in the Galaxy

The goal of any cosmic-ray propagation model is to describe the energy-dependent cosmic-ray particle density, $\mathcal{N}_i(\vec{r}, t, E)$, of a certain particle species, i, at a given location, $\vec{r}$, and time, t, in our galaxy. We can treat the interstellar medium, in which the charged cosmic rays propagate, as a hydromagnetical fluid that interacts electromagnetically with the moving cosmic rays [87]. Due to the randomly aligned interactions, the cosmic ray particle follows a random-walk-like path, similar to particles in a fluid.
The flux of particles, j, in such systems is negatively proportional to the gradient of the particle density,

$$j_i(\vec{r}, t, E) = -D\nabla\mathcal{N}_i(\vec{r}, t, E), \tag{1.6}$$

with a tensor of proportionality, D, which is called the diffusion tensor [67]. The larger the individual coefficients of the diffusion tensor, the larger the particle's mobility. In three-dimensional space, D is a 3×3 matrix and potentially has different diagonal elements to describe different diffusion magnitudes along the different space axes. The off-diagonal elements describe induced drift movements [88].
The presence of particle sources that inject particles at certain locations with a given energy spectrum can be included in the flux equation by adding a source term, $Q_i(\vec{r}, t, E)$. The

evolution of these injected particles with time must fulfill the continuity equation,

$$\frac{\partial \mathcal{N}_i(\vec{r},t,E)}{\partial t} + \nabla \cdot j_i(\vec{r},t,E) = Q_i(\vec{r},t,E). \tag{1.7}$$

Inserting Eq. 1.6 into Eq. 1.7, one obtains an inhomogeneous differential equation, called diffusion equation [67]:

$$\frac{\partial \mathcal{N}_i(\vec{r},t,E)}{\partial t} = Q_i(\vec{r},t,E) + \nabla \cdot (D \nabla \mathcal{N}_i(\vec{r},t,E)). \tag{1.8}$$

A fundamental solution of this differential equation with a single source at the origin has the form:

$$G(\vec{r},t) = \frac{1}{8(\pi D t)^{3/2}} \exp\left[-\frac{\vec{r}^2}{4Dt}\right]. \tag{1.9}$$

$G(\vec{r},t)$ represents the probability to find a particle injected at the origin at $t = 0$ at $\vec{r}$ at t [67].
In our galaxy, the sources are spatially distributed and additional physical processes influence the particle's propagation. Both need to be included in the diffusion equation. A current state-of-the-art diffusion equation that includes the spatial distribution of the particle sources, effects induced by a potential galactic wind, momentum gains and losses by interactions of the cosmic rays with the interstellar medium, and particle losses due to spallation reactions and radioactive decays is described in Strong et al. [4]. This diffusion equation has the form:

$$\begin{aligned}\frac{\partial \mathcal{N}_i(\vec{r},t,p)}{\partial t} = & \overbrace{Q_i(\vec{r},t,p)}^{\text{source function}} + \overbrace{\nabla \cdot (D_{xx} \nabla \mathcal{N}_i - \vec{V} \mathcal{N}_i)}^{\text{spatial diffusion and convection}} \\ & + \underbrace{\frac{\partial}{\partial p} p^2 D_{pp} \frac{\partial}{\partial p} \frac{1}{p^2} \mathcal{N}_i - \frac{\partial}{\partial p}\left[\dot{p} \mathcal{N}_i - \frac{p}{3}(\nabla \cdot \vec{V}) \mathcal{N}_i\right]}_{\text{momentum changes}} \\ & - \underbrace{\frac{1}{\tau_f} \mathcal{N}_i - \frac{1}{\tau_r} \mathcal{N}_i}_{\text{particle losses}},\end{aligned} \tag{1.10}$$

with p being the particle's momentum, which relates to the total energy of the particle and the particle's rest mass, m_0, through the relativistic energy-momentum relation,

$$p = \sqrt{E^2 - m_0^2 c^4}/c. \tag{1.11}$$

The five labeled terms describe the different physical processes occurring during the propagation, which we be describe here in more detail:

The source function includes all sources of particles of type i. Beside the already discussed injection by supernova remnants, the source of primary particles, this term includes

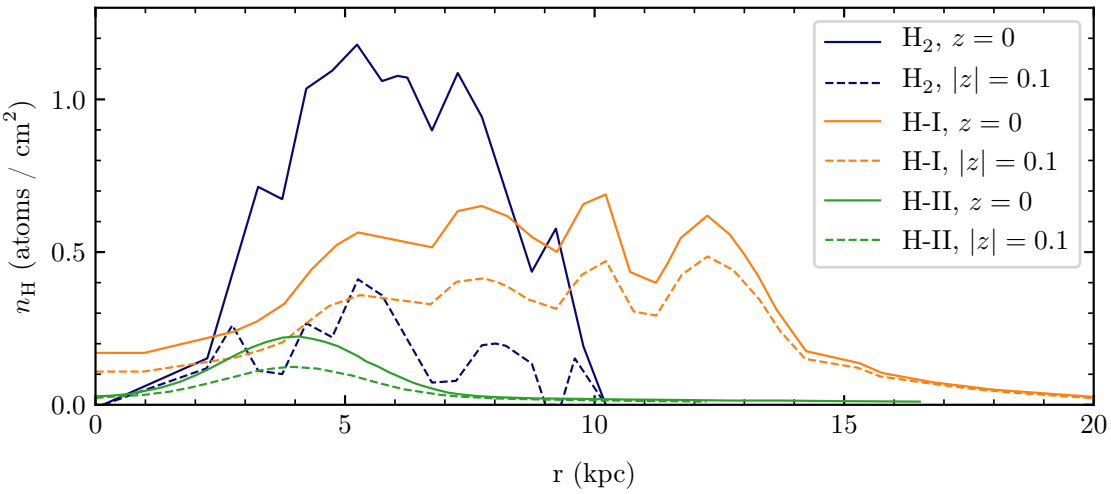

Figure 1.4: Radial distribution of the different states of hydrogen gas in the Milky Way. Figure adapted from [91].

also secondary production of i-type particles by collisions of other cosmic-ray particles with the interstellar material. The source term for the production of a secondary particle of type, i, with momentum, p_i, from an interaction between a cosmic-ray particle of type k and a gas or dust particle of interstellar matter, l, is given as

$$q_{k+l\to i}(\vec{r},t,p_i) = 4\pi \int \mathrm{d}p_k \mathcal{N}_k(\vec{r},t,p_k) n_l(\vec{r}) \frac{\mathrm{d}\sigma_{k+l\to i+X}(p_k,p_i)}{\mathrm{d}p_k}, \tag{1.12}$$

with $\sigma_{k+l\to i+X}(p_k,p_i)$ being the inclusive production cross section to create an i-type particle with momentum p_i in the interaction together with additional unspecified particles, denoted here as X. The spatial-density distribution of the l-type particles in the interstellar space is denoted as $n_l(\vec{r})$ and $\mathcal{N}_k(\vec{r},t,p_k)$ is the energy-dependent cosmic-ray particle density for k-type particles [89]. The explicit dependency of the source function of i-type particles on the particle densities of other cosmic-ray species couples the individual differential equations of all cosmic-ray particle types to form a system of differential equations that has to be solved simultaneously.
The spatial distribution of the target particles of the interstellar material can be extracted from gas and dust surveys. Most of the matter is gaseous and inhomogeneously distributed in our galaxy, a large fraction bound in giant molecular clouds. The interstellar gas is mainly composed of hydrogen, with only a small fraction of helium—approximately 10 % by number. Heavier elements are rare and their abundance varies spatially in the galaxy. Depending on temperature and the local environment, the hydrogen can either be molecular (H_2), atomic (H-I), or ionized (H-II). Their abundance and spatial distributions in the galaxy are very distinct and have to be measured with different techniques [90]. Figure 1.4 shows the current knowledge on the radial distribution of the different hydrogen states in the interstellar space of the Milky Way in the galactic plane, $z = 0$, and slightly offset at

$|z| = 0.1\,\mathrm{kpc}$.
The most abundant component in our galaxy is H-I, which makes up about 60 % of the total gas mass [90]. It can be measured by detection of its microwave emission of 21 cm wavelength from the transition between the two hyperfine states of the atom's ground state [92]. Only a small fraction of H-I is confined in the central bulk of the galaxy and most of it is distributed along the spiral arms that reach outwards to beyond 20 kpc from the galactic center. Although it is confined near the galactic plane, its spread perpendicular to the galactic plane increases with increasing distance from the galactic center due to a weaker gravitational binding [93].
Around 25 % of the gas mass consists of H_2, which must be at cold temperatures to retain its molecular binding. H_2 emits no detectable amount of radiation in the radio regime on its own and estimates of its content in a cloud must be made via the detection of a tracer molecule, CO. In interactions of CO molecules with H_2 molecules and its subsequent excitation and relaxation, the CO molecules emit radiation of 2.6 mm wavelength [94]. From the measured intensity of the emission, the number density of the H_2 molecules in the gas can be calculated. However, it was only found in the late 1990s, that the ratio of H_2 molecules and the emissivity of CO is not constant throughout the galaxy but increases with distance from the galactic center, overestimating the amount of H_2 molecules in the galactic center and underestimating it at large galactocentric distances [95]. Strong et al. pinned down the gamma-ray gradient problem—the incompatibility of the expected diffusive gamma ray emission with the measured supernova remnant distribution mentioned in Section 1.2—on this effect [84]. Most H_2 gas is distributed along the so called molecular ring, a spiral-arm-shaped region within the inner part of the galactic disk, between roughly 2 kpc and 4 kpc distance from the galactic center. For outer and more central regions the abundance of H_2 molecules diminishes [90].
The remaining 15 % of hydrogen gas in the galaxy is ionized and labeled as H-II. It can be mainly found near large O and B-type stars as only their UV radiation is powerful enough to ionize hydrogen with a higher rate than it recombines [96]. Therefore, its distribution in the galaxy follows very closely the distribution of O-B stars and it is very abundant in star-forming regions. It is often used to experimentally trace the spiral arm structure of the milky way and to define the galactic plane [97, 98].
Although dust grains in the galaxy are of special importance for star and planet formation and it strongly influences optical measurements—especially in the central region of the galaxy—its influence on cosmic rays is only minor, as it only makes up about 1 % of the interstellar material's mass [99].
This spatial distribution of interstellar matter folded with the spatial-dependent cosmic-ray flux determines the source function of secondary production. While secondary electrons, protons, and antiparticles are produced by many different collision systems and the resulting momentum distributions for a given reaction are usually very broad, heavier ions are mainly produced by fragmentation reactions or radioactive decays of even heavier ions. In these fragmentation and decay reactions, the energy per nucleon of the produced ions stays equal to the projectile's energy per nucleon, as the additionally released energy in the reaction is mostly small compared to typical cosmic-ray energies [89].

Spatial diffusion and convection is described very similar as in the simplified Equation 1.8 but with an additional term, $\vec{V}\mathcal{N}_i$. This term arises in the presence of a large-scale

collective motion of the interstellar plasma, called galactic wind, which introduces a convective motion of cosmic rays. Its existence in the Milky Way is currently matter of debate [100].
On microscopic level, the cosmic-ray particles scatter on magnetohydrodynamical irregularities generated in the galactic plasma [4]. The scattering is assumed to be of resonant character, and the cosmic-ray particles scatter mainly on the portion of the irregularities that have a wavelength, $1/k$, that is equal to the particle's gyroradius, r_g. Although locally the scattering predominantly goes into the direction parallel to the local magnetic-field lines[2], the turbulence and fluctuations are randomly aligned in the galaxy on large scale and by this create an isotropic flux [101, 102]. The resulting spatial-diffusion coefficient for the diffusion of cosmic-ray particles in the galaxy for a complete isotropic diffusion from such a magnetohydrodynamical model can be estimated to be:

$$D_{xx} \approx \left(\frac{B}{\delta B_{\mathrm{res}}(k = 1/r_g)} \right)^2 \frac{v r_g}{3}, \tag{1.13}$$

where v is the velocity of the cosmic-ray particle, r_g its gyroradius, B the interstellar magnetic-field strength, and $\delta B_{\mathrm{res}}(k = 1/r_g)$ the magnetic-field strength of the irregularities with wave number k [103]. For the spectral form of $\delta B_{\mathrm{res}}(k)^2$ several models exist, all of them assuming a power law, $\delta B_{\mathrm{res}}(k) \propto k^{-a}$, with different values of the exponent a. Most commonly $a = 5/3$ is used, implying the so-called Kolmogorov turbulence spectrum [102].
The explicit dependence of the diffusion coefficient on the gyroradius of the particle directly results in a dependence of the diffusion coefficient on the particle's momentum, p, and charge, Ze, which can be merged into one parameter, the particle's rigidity, $R \equiv pc/Ze$. Different particles with equal rigidity diffuse equally through the galaxy. Typical magnitudes of the considered magnetic-field irregularities are on the order of $\delta B_{\mathrm{res}}(k) \approx 5\,\mu\mathrm{G}$, giving an estimate of the diffusion coefficient in the Milky Way of:

$$D_{xx} \approx D_0 \beta R_{\mathrm{GV}}^{1/3}\,\mathrm{cm}^2\mathrm{s}^{-1}, \tag{1.14}$$

with $D_0 \approx 2 \times 10^{27}\,\mathrm{cm}^2\mathrm{s}^{-1}$ [3] [4]. A direct measurement of the diffusion coefficient or the turbulence spectrum is so far not yet possible, and the diffusion coefficient is a free parameter in the propagation models that has to be constrained—similar as the source spectra from supernova remnants—by fits of our modeled particle fluxes to measurements.
The diffusive motion of the particles continues only as long as they not leave the volume in which the magnetic irregularities are located. In our galaxy, the irregularities are located within the galactic disc and extend several kpc into the galactic halo perpendicularly [86]. The exact extend is also unknown, and the extent, often labeled as the galactic halo size, z_{h}, is also a free parameter in the propagation models. For particles with rigidities large enough so their gyroradius exceeds this distance, the probability for scattering multiple times on the irregularities is too low to contain a diffusive-like movement, and the particle

[2] the perpendicular component is suppressed by more than an order of magnitude in the most commonly used quasi-linear theory [101].

[3] estimates found in literature mostly vary between $1 \times 10^{27}\,\mathrm{cm}^2\mathrm{s}^{-1}$ and $5 \times 10^{28}\,\mathrm{cm}^2\mathrm{s}$.

directly leaves the galaxy. This gives an upper rigidity limit for the diffusive propagation in the Milky Way of about $R \approx 1 \times 10^9$ GV [101]. Particles with higher rigidity spend only a very short time in the galaxy and their flux within the galaxy is consequently smaller than for particles that are confined over a longer period. Particles with lower rigidities spend a longer time within the Galaxy due to their diffusive motion. With the estimated diffusion coefficient, the escape time of a 1 GV ion from the galaxy is on the order of 1×10^9 yr, approximately a factor 10^5 longer than if the particle would leave the galaxy in a straight path. Experimentally, the average confinement time can be estimated by measurements of the flux of secondary cosmic-rays and unstable isotopes and their respective decay products [104, 105].
As already stated, the existence of a galactic wind in our galaxy is debatable [106]. Many other spiral galaxies show large outflows of material away from the galactic plane with increasing material's velocity with distance from the plane. Large outflows are mostly powered by active galactic nuclei or supermassive black holes, which are absent in our galaxy. Smaller velocities, however, can also be reached by solar winds from large O-B stars or even induced by cosmic rays [107]. In the first case, velocities up to several thousand km/s are reachable, in the latter several tens [108, 109]. The magnetic irregularities which scatter the cosmic-rays are spatially bound to the surrounding interstellar material and move along with it. Due to their collective, convectional movement into the direction of the galactic wind, the cosmic-ray particles scatter predominately into this direction and the resulting flux of cosmic rays becomes anisotropic. However, an measured anisotropy of cosmic rays is not a unique signal of a galactic wind as it can also be created by anisotropic diffusion in the galaxy due to a large-scale magnetic field in the galaxy or spatial changes of the diffusion tensor [110]. To proof the existence of an galactic wind in the Milky Way, a direct evidence in the halo is required.

Momentum changes are induced by interactions of the cosmic ray particles with different constituents of the interstellar medium. The first term describes the diffusion in momentum space of the particles, which is induced by the same scattering process on the magnetic irregularities that also causes spatial diffusion. If the irregularities have a non-vanishing relative velocity compared to the galactic bulk, a momentum transfer between them and the cosmic ray particles can occur, similar to the crossing of a shock described by Fermi acceleration [4].
The magnitude of the momentum change can be quantified by a momentum-diffusion coefficient, D_{pp}, which relates to the spatial-diffusion coefficient by

$$D_{pp} = \zeta(\delta B_{\mathrm{res}}(k)^2) p^2 v_{\mathrm{A}}^2 \frac{1}{D_{xx}}, \tag{1.15}$$

with v_{A} being the velocity of the magnetic irregularities in the interstellar medium, and ζ a factor depending on the wave-spectrum of the magnetic irregularities [4]. Assuming the same Kolmogorov-like wave-spectrum as for spatial diffusion results in $\zeta \approx 0.2$ [111]. The propagation speed of the magnetohydrodynamical irregularities is equal to the Alfven velocity, v_{A}, of the surrounding interstellar medium. Its value varies within the galaxy with the local magnetic-field strength and particle density and is on the order of 20 km/s to 150 km/s [112]. Calculations show that the relative energy gain of cosmic rays that

are confined in the galaxy for around 1×10^7 yr by momentum diffusion can be as large as 50 %, and is energetically in a similar order of magnitude as the initial acceleration of the particles by supernova remnants. This large energy transfer from the interstellar medium to the cosmic rays can have significant influence on the magnetic turbulence of the interstellar medium and potentially influence the efficiency of cosmic-ray scattering on them [111].
The second part of the momentum-loss term in the diffusion equation describes momentum losses due to inelastic scattering, ionization, synchrotron emission, and a potential galactic wind. For light charged particles like electrons and positrons, radiative losses are the dominant source of momentum loss, especially at high energies [113]. In the interstellar magnetic fields these particles are deflected and by this emit soft electromagnetic radiation with energies corresponding to microwave to x-ray photons [114]. For heavier particles like nuclei, the energy emission by this process is suppressed by the much larger mass of the particle and plays only a minor role [115]. For these particles, the momentum loss by interactions with interstellar material is dominant. Charged particles that traverse matter continuously lose part of their kinetic energy by electromagnetic interactions with the Coulomb fields of the surrounding atoms, molecules, or ions, often referred to as ionization energy loss. Although the average density in the disk of the galaxy is very low, about $1.6 \times 10^{-24}\,\mathrm{g/cm^3}$, the total amount of traversed material of the particles due to the long confinement is on the order of $5\,\mathrm{g/cm^2}$ [104]. Protons with 1 GeV kinetic energy lose about 2 % of their kinetic energy when traversing this amount of material. Iron ions (Fe-56) with an equal energy per nucleon lose already about 25 % of their kinetic energy [116, 21]. A more detailed description of the energy loss by ionization will be given in Section 4.1.1, when discussing the interactions of nuclei with a particle detector.
In addition, particles can loose a large fraction of their kinetic energy in a single, inelastic collision in which the projectile particle stays intact but transfers much of its kinetic energy to newly produced secondary particles. Although the probability for such events to happen is small, they have to be considered in our propagation model, as such reactions modify the spectral form of the energy distribution of cosmic rays.

Particle losses also occur in interactions of cosmic rays with interstellar material and due to radioactive decay. In contrast to the previously considered processes that changed the particle's momentum, the particle vanishes completely by these interactions. Newly created secondary particles that emerge during the process are described by their respective source function. As an approximation in most propagation models, the statistical nature of these processes are neglected and the particle loss is described solely by its mean rate, $R = 1/\tau_{\mathrm{loss}}$, with τ_{loss} being the mean time after which the process occurs and the particle vanishes. For unstable particles that undergo radioactive decay, the mean rate is directly related to the at-rest lifetime, τ_0, of the particle by

$$R_{\mathrm{decay}} = \frac{1}{\gamma \tau_0}, \tag{1.16}$$

with the Lorentz factor, γ, which accounts for the relativistic time dilation [117].
For collisional losses, the mean rate, R_{coll} depends on the amount of traversed material per

time of the cosmic-ray particle and the corresponding reaction cross section as

$$R_{\mathrm{coll}} = \beta c n_{\mathrm{ISM}} \sigma_{\mathrm{loss}}, \tag{1.17}$$

with β being the velocity of the cosmic ray particle, n_{ISM} the particle density of the interstellar material, and σ_{loss} the reaction cross section encompassing all interactions that destroy the cosmic-ray particle [89]. Due to several conservation laws that apply in these reactions, the reactions also produce other particle types which has to be included in their respective source terms in the diffusion equation. Interacting ions fragment into lighter ions, protons, and neutrons; antiparticles annihilate mainly into protons, neutrons, and several short-lived mesons, which subsequently decay into leptons and gammas [118, 119]. Protons, however, are mostly not lost due to baryon-number conservation, and often only lose a large fraction of their energy in inelastic collisions [89].

The energy-differential particle flux—the observable we measure by our detectors—can be calculated from the differential particle density of the diffusion equation by

$$\frac{\mathrm{d}\psi_i}{\mathrm{d}E_{\mathrm{kin}}} = \frac{\beta c}{4\pi} \frac{\mathrm{d}\mathcal{N}_i}{\mathrm{d}p} \frac{\mathrm{d}p}{\mathrm{d}E_{\mathrm{kin}}} = \frac{c}{4\pi} \mathcal{N}_i(p) A_i, \tag{1.18}$$

with A_i being the mass number of the i-type ion.

In contrast to Equation 1.8, the full diffusion equation in Equation 1.10 cannot be solved analytically, except if some terms are neglected or further approximations are used [4]. The most common approximation is the so-called leaky-box approximation, or more advanced, the nested leaky-box approximation. These models assume that particles are confined within the volume of the galaxy and possess a certain probability to leave the volume each time they hit the surface of the volume. By this, a homogeneous particle flux throughout the galaxy is created and the resulting flux depends only on the probability of the particles to leave the galaxy [120].
In the more advanced case, the nested leaky-box model, a second box is 'nested' into the galaxy which encompasses the source region of cosmic rays which in turn confines the particles before entering the outer volume of the galaxy. By this, several features of measured cosmic-ray spectra and secondary-to-primary ratios can be explained, which could not be reproduced by the simple leaky-box model [121]. However, both models are empirical and return only an effective flux of the cosmic-ray particles inside the volume but they do not incorporate the physical processes that lead to the observed fluxes. A detailed interpretation of the resulting fluxes is therefore not easily possible, and the influence of different processes or additional exotic sources is limited and does not replace investigations of the full diffusion equation [4]. A commonly used method to solve the full diffusion equation is to use numerical methods, as we will present in more detail in Section 2.1.

In addition, the propagation model contains several unconstrained parameters that can only be constrained by fitting the modeled cosmic-ray flux for different particle species to

measurements near Earth. As our propagation model of the galaxy obtains the local interstellar flux outside of the solar system only, we need an additional model to describe the modification of the cosmic-ray fluxes due to the influence of Sun, called solar modulation. The generation of the magnetic field of Sun and current models of solar modulation of cosmic-ray fluxes in the heliosphere are discussed in the next section.

1.3 Heliospheric Transport

The transport processes of galactic cosmic rays in the heliosphere is described in general similarly to the transport of the cosmic rays in the galaxy but with some changing aspects: The much smaller size of the heliosphere in comparison to the galaxy and the consequently much shorter confinement period of the cosmic-ray particles within the heliosphere alters the relevance of certain processes: While the influence of residual material of interplanetary space and the hereby induced processes of absorption and secondary-particle production can be neglected, the description of diffusive and convective motions of the cosmic-ray particles in the magnetic field of Sun is more complex [24]. Temporal variations and spatial inhomogeneities play an important role. In the models of galactic transport, temporal variations are mostly neglected due to the long confinement time of the cosmic-ray particles compared to typical variation times of galactic fields and the epoch of cosmic-ray measurements on Earth [4]. Thus, the cosmic-ray flux is assumed to be steady in our models, and the aim of the numerical solution of the diffusion equation is to find this steady-state cosmic-ray flux within the Galaxy. In the heliosphere, however, the typical timescales of particle confinement, field variations, and measurement times of cosmic-ray experiments are comparable [24]: The confinement duration of galactic cosmic-ray particles is on the order of hundreds of days; typical variation times of the solar magnetic field are on the order of years to days; and measurement times of current cosmic-ray experiments range from days to decades, experiencing most of the temporal variations of the heliosphere and the measurements are thus affected by the temporal configuration of the heliosphere at the time of the experiment.
Most spatial variations of the cosmic-ray flux in the heliosphere are also coupled to the temporal variations and both must be considered in models of the heliosphere.
In the following I describe the mechanism of the creation of Sun's magnetic field and the structure of the heliosphere. Thereafter, I describe the interaction of the heliosphere with galactic cosmic rays and the consequent solar modulation of cosmic rays and present two models of solar modulation that are commonly used to model the effect of solar modulation: The simple force-field approximation; and the more complex HELMOD model.

1.3.1 The Heliosphere

Sun generates a local magnetic field by intrinsic, large-scale plasma flows [122]. Its long-term existence implies a dynamo process that counteracts the natural diffusive decay of directed, inductive plasma flows to sustain the magnetic field [123]. Such a process is called solar dynamo and must contain a non-axisymmetric component to overcome Cowling's theorem, which states that an axis-symmetric field cannot be self-maintained [124]. In case of Sun, it is believed that the combination of its surface rotation and gravity provides such

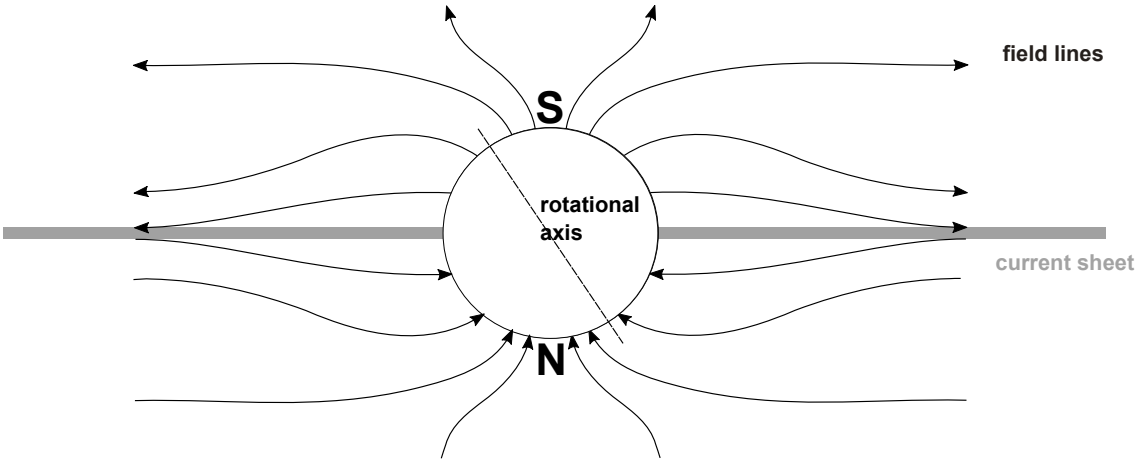

Figure 1.5: Effect of the interaction of the solar wind with Sun's dipole-like magnetic field.

a mechanism. The forces acting on the flowing plasma and the magnetic fields generated by the flow of the plasma form together a highly dynamical system, which results in a temporal sequence of recurring poloidal and toroidal-dominated field configurations on a 22-years basis, the so-called solar cycle [125].
Periods in which the toroidal-field component dominates were recognized to coincide with a frequent emergence of sunspots and dynamic changes of local magnetic-field structures and are thus termed as periods of high solar activity [126, 127]. Phases in which the poloidal field dominates are termed as periods of low solar activity. During low solar activity, the general feature of the solar magnetic field in the inner heliosphere is a dipole-like poloidal field, which starts to become increasingly toroidal over time with increasing solar activity [125]. Shortly after the maximum of solar activity, about 5.5 years after the minimum of the solar activity, the poloidal-field component starts again to regenerate from the toroidal field by the decay of the active regions on the Sun [128]. This process results in a dipole-like field with a reversed polarity with respect to the previous poloidal-field 11 years earlier [123]. After another repetition of this cycle, the initial poloidal field is again obtained and the full 22-year solar cycle is completed [128]. From this point on, the process repeats.

In addition to the creation of the magnetic field, Sun permanently emits ionized gas which is accelerated by the static expansion of the isothermal corona to supersonic velocities, called solar wind [129]. The density and the velocity of the solar wind is strongly latitude dependent and varies with the solar cycle. During solar minimum, the solar wind velocity is maximal near the poles, with a small particle density, and a high-density but slow wind near the equator. During phases of high solar activity, the particle and velocity gradients diminish and the solar-wind outflow becomes more homogeneous [130].
The particles of the solar wind interact with the solar magnetic field, distort the magnetic field lines, and pull them open. By this, open field lines emerge from Sun into interplanetary space, as sketched in Figure 1.5. The open field lines are transported through the interplanetary space by the solar wind particles with a finite velocity. Together with the rotation of the Sun, this causes the initial radial orientation to be twisted into a spiral in

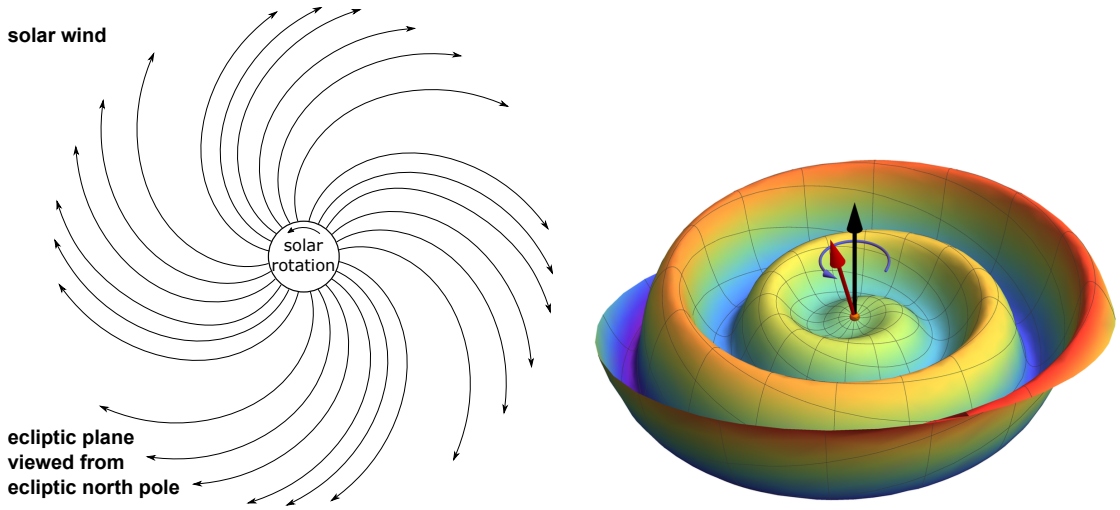

(a) Shape of the heliospheric magnetic-field lines in the ecliptic plane.

(b) Shape of the heliospheric current sheet. Credit: Orcinha et al. [134]

Figure 1.6: Large-scale heliospheric magnetic field.

the ecliptic plane, as depicted in Figure 1.6a [131]. The polarity of the open field lines is opposite on the two hemispheres of Sun. At the magnetic equatorial plane, this leads to an abrupt change of the polarity and a magnetically neutral plane with a thickness of about 1×10^4 km, in which a large flowing current is required to exist. This plane is called heliospheric current sheet (HCS) [132]. Due to the offset of the magnetic axis from the ecliptic plane and Sun's rotation axis, the orientation of the HCS is constantly changing in a fixed celestial coordinate frame. The resulting shape of the HCS is shown in Figure 1.6b and is often referred to as the ballerina's skirt or the Parker spiral [132, 133]. At solar minimum, the tilt angle of the HCS with respect to the ecliptic plane is only about 10° to 20°, while during solar maximum the plane of the heliospheric current sheet can be nearly perpendicular to the ecliptic plane [135]. Even during coronal mass ejections, which happen mostly near solar maximum, this ordered structure of the heliosphere is vastly maintained and disruptions are only local and short-lived [132].
Resulting from the solar-wind driven transport of the magnetic field in the heliosphere, the dominant radial component of the magnetic field decreases with distance from the Sun due to magnetic-flux conservation. Due to the spiral-shaped movement of the solar wind, the initially pure radial field becomes more and more azimuthal with increasing distance [133]. An opposing pressure from the interstellar medium reduces the velocity of the solar wind with distance from Sun. As the Sun moves through the galaxy, the relative velocities between the interstellar medium and the solar wind is not constant along a spherical shell around Sun but is maximal in direction of Sun's movement and minimal in opposite direction. By this, a nose-tail asymmetry of the heliosphere builds up, which's magnitude depends on the relative velocity of Sun in the local interstellar space and the magnetic field strength and relative alignment of the interstellar magnetic field with respect to the direction of motion [136]. At around 75 AU to 100 AU in nose direction and approximately 150 AU in tail direction, the solar wind velocity falls below the local sound velocity, leading to a shock front and an associated region with increased particle temperature and

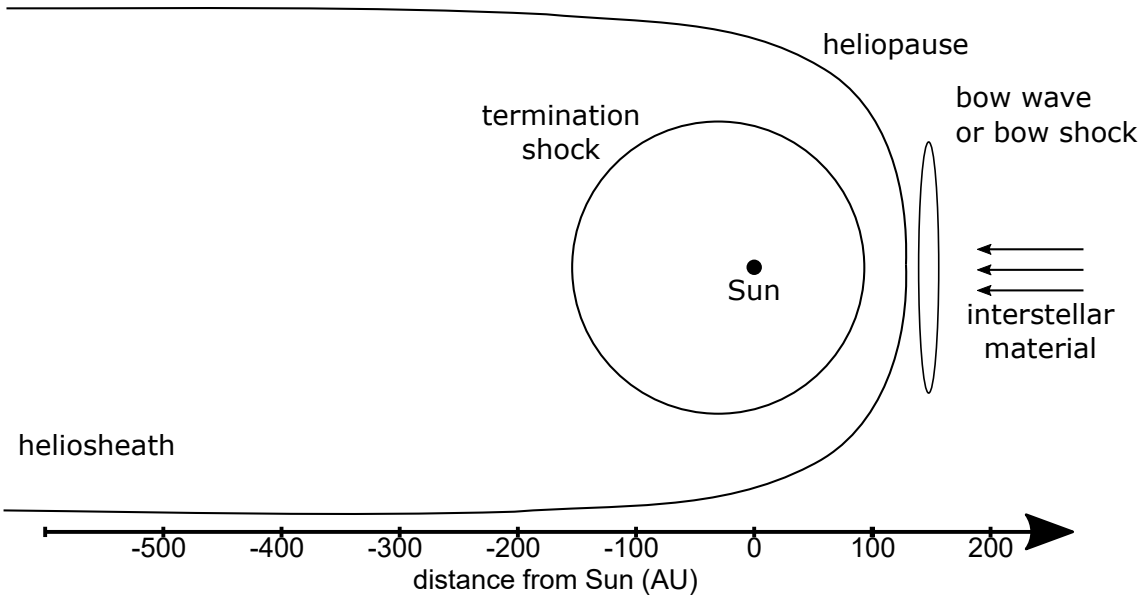

Figure 1.7: Schematic view of the features of the heliosphere and their distance to Sun.

magnetic field, the so called termination shock [137]. As the velocity of the solar wind changes during the solar cycle, it is expected that the location of the termination shock does as well [24]. Beyond the termination shock, the solar wind loses its radial direction and becomes more turbulent, mixing with the plasma of the interstellar medium [138]. The ambient magnetic field beyond the termination shock changes direction accordingly and its magnitude increases. The region beyond the termination shock is referred to as the outer heliosphere and is called heliosheath. Its extension in radial direction is about 25 AU in nose direction. It ends at the heliopause, where the pressure of the interstellar medium balances the solar-wind pressure and confines the solar particles. The structure of the heliosheath in tail direction—often referred to as the heliotail—and the shape of the heliopause is not yet agreed upon. Although it is generally accepted that the heliosphere has a coma-like shape, it is not clear how pronounced the expansion of the tail is and how turbulent the boundary between the solar wind and the interstellar medium is in this region [139]. Since both Voyager probes have left the heliosphere in head direction, there is not yet any in-situ measurement of the properties of the tail region of the outer heliosphere. But from measurements of energetic neutral atoms by the IBEX experiment it was already found that the heliotail has several complex multi-lobe structures [140]. As the heliopause decelerates the interstellar plasma particles rapidly—especially in nose direction—the heliosphere potentially is enclosed by a region of compressed hydrogen that can form a bow shock or a bow wave. The pronounceness of this region and whether it can form a shock front, depends on the relative velocity between the local interstellar medium and the heliosphere and is not yet experimentally fully solved but a no-bow-shock scenario is preferred by IBEX data [141, 136]. Figure 1.7 gives an overview of the different heliospheric regions and interfaces mentioned above and their distance from Sun.

1.3.2 Solar Modulation

Charged cosmic rays that enter the heliosphere interact electromagnetically with the presented features and must cross them to reach Earth. They interact with the shock-like structures like the termination shock, the heliopause, or the bow-wave; are scattered off magnetic irregularities of the interplanetary magnetic field that is transported by the solar wind particles; and drift along large-scale gradients and curvatures of the interplanetary field [24].
The shock-like structures reflect and re-accelerate cosmic rays back into the interstellar space at their shock fronts. This results in a reduction of the cosmic-ray flux in the inner heliosphere with respect to the local interstellar flux [142]. The measured energy gains of cosmic rays in these reactions are, however, small, as measurements by the Voyager probes and the IBEX experiment affirm, which indicates that the shocks are relatively weak [143, 137].
Most magnetic irregularities of the interplanetary magnetic field are on the order of 1×10^5 km to 1×10^7 km, as measured for example by the EXPLORER XVII probe [144]. As these irregularities scatter most-effectively ions with a gyroradius is of similar size, cosmic-ray particles with energies of hundreds of MeV/n to several GeV/n are most affected. The scattering leads to a random-walk like motion of these particles through the heliosphere, which can be described mathematically in a similar way as the diffusion of cosmic rays through the galaxy (c.f. Section 1.2). Due to the much smaller strength of the magnetic field in the heliosphere compared to the galactic magnetic field, the diffusion coefficient in the heliosphere is around six orders of magnitude smaller than the galactic diffusion coefficient, namely on the order of $1 \times 10^{21}\,\mathrm{cm^2 s^{-1}}$ [144]. This results in a typical confinement time of particles in the heliosphere of several days to weeks [24].
As the solar-wind strength and orientation varies spatially and temporally, the diffusion tensor is not constant throughout the heliosphere and cannot be approximated as such; the directed outflow of the solar wind leads to a highly anisotropic diffusion tensor and induces a strong convective motion directed radially outwards. As the particles have to overcome this directed motion, they adiabatically lose energy when propagating to the inner region of the heliosphere [144].
Especially at times near the maximum of solar activity, the interaction of the dynamically changing solar wind and the interplanetary magnetic field leads to regions in the heliosphere with intense magnetic irregularities. These regions act as barriers to the cosmic rays that try to penetrate them, resulting in a significant short-term decreases of the particle flux in the inner heliosphere. As these irregularities drift radially outwards, they increase in size and might merge with other such interaction regions, forming a so-called merged interaction region (MIR). During solar maximum, often several of such MIRs are drifting through the heliosphere and reduce the cosmic-ray flux in the inner regions [145]. Together with the overall enhancement of magnetic irregularities caused by the faster and more intense solar wind during high solar activity and the more inclined HCS, cosmic rays are shielded from the inner heliosphere most efficiently during this time of the solar cycle. When approaching the period of solar minimum, the MIRs dissipate and the solar wind becomes more homogeneous and calm. The cosmic-ray flux in the inner regions of the heliosphere then reaches its maximum. Time-resolved measurements of the cosmic-ray intensity over several solar cycles confirm this anti-cyclic behavior of the modulation of

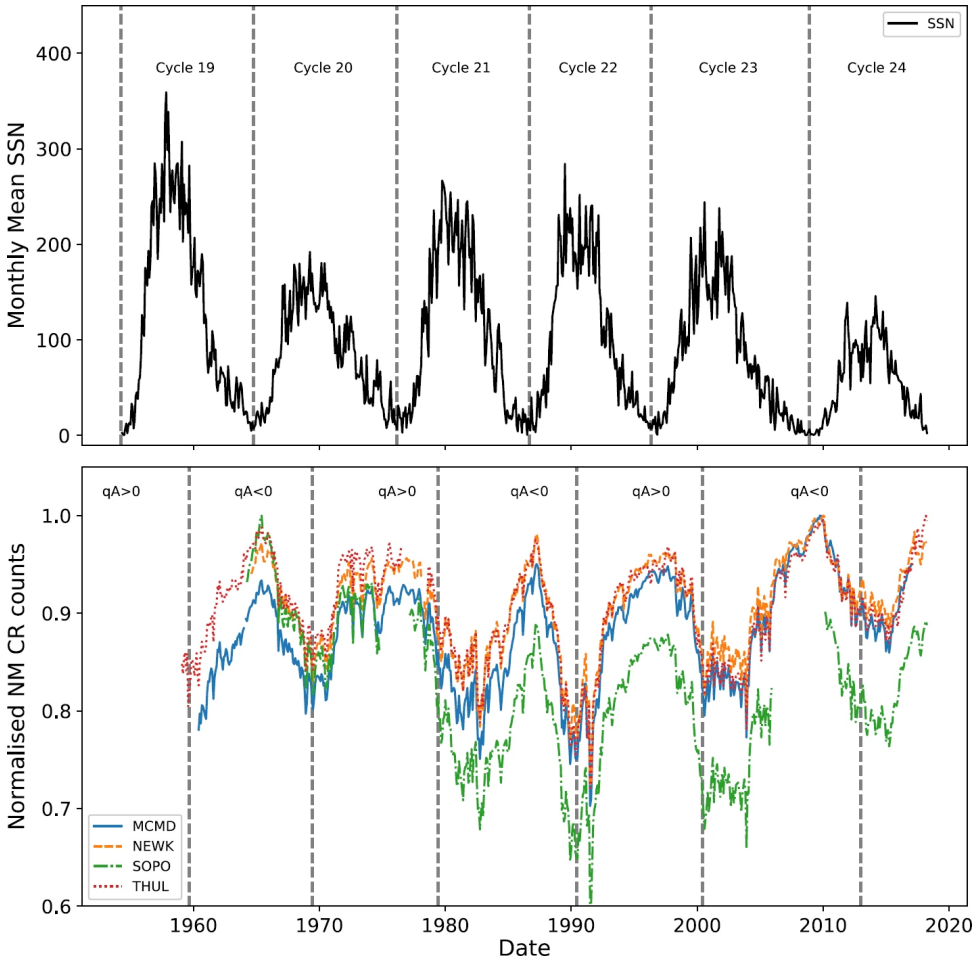

Figure 1.8: Cosmic-ray modulation along the solar cycle. Upper figure: sunspot number measured for the last six solar cycles. The cosmic-ray modulation anti-correlates with the sunspot number, which is a measure for Sun's activity. Lower figure: normalized count rates for various neutron monitors on Earth's surface. The neutron-monitor count rates correlate with the total cosmic-ray flux on top of the atmosphere. Credit: Ross et al. [146]

cosmic rays with solar activity, as exemplary shown in Figure 1.8. The visible short-term fluctuations of the flux are mainly due to the forming and dissipation of MIRs [24].
Between solar minimum and solar maximum the particle flux up to a few GeV varies by more than an order of magnitude. During several balloon flights at different times within a solar cycle, the BESS experiment measured the energy-differential cosmic-ray proton flux to study the energy-dependence of solar modulation [25]. As can be seen in Figure 1.9b, the measured fluxes measured at different times in the solar cycle start to deviate from each other below approximately 10 GeV, reaching deviations of more than an order of magnitude at the lowest measured energies around 100 MeV.
Additional charge-dependent particle drifts along the large-scale gradients and structures of the interplanetary magnetic field have long been considered to be only of minor relevance for cosmic-ray modulation. Only in the last decades their importance became clear after

measurements of cosmic rays with opposing charge, such as electrons and protons, electrons and positrons, or protons and antiprotons, revealed a different modulation of particles with equal absolute charge but different sign over time [147]. The difference was most notable in times of low solar activity, when the influence of the magnetic irregularities on the cosmic rays is minimal and the influence of the large-scale heliospheric fields on the particles is therefore relatively large. Especially for particles whose drift velocity is on the same order of magnitude as the solar-wind velocity, this effect was found to be most distinct [148]. In the heliosphere, this corresponds to particles with a rigidity of around 0.3 GV. These particles drift along the curvature of the heliospheric field and are guided in their entirety from the polar regions of the heliosphere to regions near the heliospheric current sheet or vice versa. The drift direction solely depends on the sign of the particle's charge and the polarity of the solar magnetic field [24].
The polarity of the interplanetary magnetic field changes every 11 years due to the solar-dynamo process. Epochs where the solar magnetic field emerges the solar north pole and returns on the solar south pole are commonly labeled as $A > 0$ epochs, and epochs where the solar magnetic field emerges the south pole and returns on the north pole are commonly labeled as $A < 0$ epochs [149].
The charge-dependent drift causes the oppositely charged particles to pass different regions of the heliosphere, and thus experience different densities and velocities of the embedded magnetic irregularities of the solar wind. This leads to different effective modulation of positively and negatively charged particles for a given time [150].
The charge-dependent modulation is of special importance for experiments that aim to measure the proportion of antimatter to matter in our galaxy. As so far no experiment measured cosmic-ray antiparticles outside the heliosphere, all current measurements of the electron-to-positron or proton-to-antiproton ratio are affected by solar modulation, and the local-interstellar-flux ratio has to be extracted from these measurements by applying advanced models of solar modulation that include the charge-sign dependent particle drifts [24]. The magnitude of the solar modulation on the antiproton-to-proton ratio is exemplarily shown in Figure 1.9. Especially for energies below 200 MeV, the effect of solar modulation can modify the flux ratio by more than one order of magnitude, and the measured ratio changes with time in the solar cycle.

To calculate the modifications of the cosmic-ray spectra due to the interaction with the heliosphere, a similar approach as for the cosmic-ray propagation in the galaxy is applied. The diffusive motion of the cosmic-ray particles is described by a Fokker-Planck diffusion equation, with the boundary condition that the cosmic-ray-particle density at the heliopause has to coincide with the local interstellar particle density.
In the most basic form, the diffusion equation for a particle with rigidity, R, propagating in the heliosphere can be written as

$$\frac{\partial \mathcal{N}_i(\vec{r},t,R)}{\partial t} = \overbrace{-\left(\vec{V}+\vec{v_{\mathrm{d}}}\right)\cdot\nabla\mathcal{N}_i}^{\text{convection and drift}} + \overbrace{\nabla\cdot\left(\vec{D}\cdot\nabla\mathcal{N}_i\right)}^{\text{diffusion}} + \overbrace{\frac{1}{3}(\nabla\cdot\vec{V})\frac{\partial\mathcal{N}_i}{\partial\log(R)}}^{\text{energy change}}, \tag{1.19}$$

with $\vec{V}$ being the solar wind velocity, $\vec{v_{\mathrm{d}}}$ being the drift velocity of the particle due to gradients and curvatures of the magnetic field and the heliospheric current sheet, and $\vec{D}$

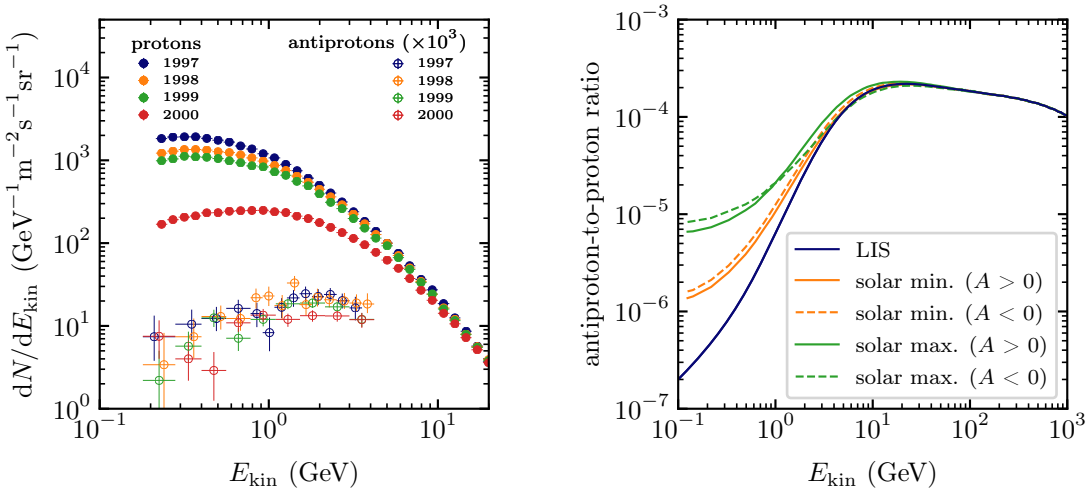

(a) Measurement of the energy-differential cosmic-ray proton and antiproton flux with the BESS experiment at different times during the solar cycle. The experimental data is extracted from the cosmic-ray database [35].

(b) Modification of the antiproton-proton ratio in the heliosphere at different times in the solar cycle, modeled with the HELMOD simulation tool [28].

Figure 1.9: Modulation of the cosmic-ray flux during the solar cycle.

being the (3×3)-dimensional diffusion tensor that describes the anisotropic diffusion along all three spatial dimensions [24]. All of the parameters have a spatial and temporal dependence. As the heliospheric magnetic field and solar-wind structure change significantly during the solar cycle, the equation has different stationary solutions depending on the current heliospheric configuration. In order to solve the equation for a given time in the solar cycle and to determine the cosmic-ray particle density at a certain location within the heliosphere for a given local interstellar particle flux, further simplifications are required, as the magnetic-field configuration is too complex to allow an analytical solution.
In a series of publications, Gleeson and Axford, as well as Parker and others, found an approximate analytical solution of the heliospheric diffusion equation for particle rigidities larger than a few hundred MV. The solution is often called force-field approximation and accounts only for the radial directed solar wind but neglects all other features of the heliosphere [151, 144, 152]. They found that the modulated particle flux inside the heliosphere, $\psi_i(E_{\mathrm{kin}}, r, t)$, at a given time, t, and a heliocentric distance, r, can be related to the local interstellar particle flux, ψ_i^{LIS}, by

$$\psi_i(E_{\mathrm{kin}}, r, t) = \psi_i^{\mathrm{LIS}}\left(E_{\mathrm{kin}} + \frac{Ze}{A}\phi(r,t), r, t\right) \frac{E_{\mathrm{kin}}\left(E_{\mathrm{kin}} + 2E_0\right)}{\left(E_{\mathrm{kin}} + \frac{Ze}{A}\phi(r,t)\right) + \left(E_{\mathrm{kin}} + \frac{Ze}{A}\phi(r,t) + 2E_0\right)}, \tag{1.20}$$

with E_0 being the rest energy of the particle and $\phi(r,t)$ being the time and spatial-dependent solar-modulation potential.
The formula shows that in average particles are slowed down when propagating into the

heliosphere due to the convective, outwards-directed motion of the solar wind. To reach a certain position within the heliosphere, the average rigidity loss a particle is equal to $\phi(r,t)$ [151]. A determination or prediction of ϕ from the heliospheric configuration is unfortunately not possible, and the modulation potential for a given time and location has to be constrained experimentally. To do so, a measurement of the solar-modulated particle flux and a model for the corresponding local interstellar flux is required. This results in an unpleasant model dependence of the modulation parameter on the assumed local interstellar particle flux, as currently no suitable data outside of the heliosphere is available[4].

Further downsides of the force-field model is that the accuracy of the approximation worsens with decreasing energy [151]. When the model was developed in the 1960s and 1970s, the experimental data was not yet as precise as it is nowadays, and deviations of the model were only found below 400 MV. Today, more precise data from long-duration experiments on satellites are available, which allow more detailed studies on the validity of the force-field approximation. By comparison of the model's ability to describe monthly-averaged particle fluxes from the PAMELA experiment and the AMS-02 experiment, Corti et al. found that deviations of the force-field approximation on the measured fluxes are significantly larger than the measurement uncertainties of the considered experiments up to several GV [153]. Therefore, the usage of the force-field approximation for studies that employ such precise data would generate a significant systematic uncertainty, which to quantify is not simple. In addition, effects which stem from the detailed structure of the heliosphere, like charge-sign dependent particle drifts, are not included in this model, generating further uncertainties. Especially when studying antiparticles or particle-to-antiparticle-flux ratios, the negligence of the charge-sign dependence of the modulation can lead to large model uncertainties and more sophisticated models should be used.

More accurate models are often based on solving the heliospheric diffusion equation (Equation 1.19) numerically. Depending on the level of detail of the employed magnetic-field model of the heliosphere, the various effects of the different structures in the heliosphere can be included in the calculation of the solar-modulated particle fluxes. One of the most commonly used models today is the HELMOD model [154].

The HELMOD computer code solves the diffusion equation in the heliosphere numerically using a Monte-Carlo-integration method [155]. The heliosphere is modeled in two dimensions—in helio-colatitude and radial distance from the Sun—and includes global structures such as the heliospheric current sheet, the termination shock, and the heliopause [154]. The time dependence of the tilt angle of the heliospheric current sheet and the locations of the shocks are included in the model. To evaluate the solar-modulation particle flux at a given time and location in the heliosphere, global observables such as sunspot numbers, tilt-angle of the heliospheric current sheet, and magnetic-field strength measurements from satellites, are used as an input for the heliospheric configuration for the desired time period [156].

The effect of the configured model on the penetrating cosmic rays is then evaluated by a backward-propagation algorithm, which simulates particles starting from the desired location inside the heliosphere to the heliopause and by this extracts numerically the

[4] Although the Voyager probes provide measurements outside of the heliosphere, the energy range covered by them is too low to fully constrain the local interstellar particle flux for the whole relevant energy range.

energy-dependent mapping function that transforms the particle flux from outside of the heliosphere to the modulated flux at the desired location for a given configuration. This mapping function can be used to transform any local interstellar flux to a solar-modulated flux and is thus independent of the local interstellar flux. The accuracy of the HELMOD model is claimed to be on the order of the experimental uncertainties of current cosmic-ray experiments, such as AMS-02, and the prediction accuracy for solar-modulation studies in future time periods is on the level of 5 % to 15 % [156].
As the model includes charge-dependent drift motions, HELMOD is better suited to modulate fluxes of cosmic antiparticles than the force-field model. I employ the HELMOD model later in this thesis to model the solar-modulation of our obtained local interstellar particle fluxes to compare them to experimental data from the AMS-02 experiment. I use the stand-alone module of HELMOD, version 4.1, which can be downloaded from http://www.helmod.org/. The stand-alone module has pre-calculated parameterizations of the mapping function for several time periods, experiments, and particle types, which spares repetitive execution of the Monte-Carlo integration and allows a fast modulation of modeled local interstellar cosmic-ray fluxes.

Chapter 2

Modeling of the Galactic Propagation of Cosmic Rays

To test different hypotheses of the origin of galactic cosmic rays and to probe exotic sources indirectly by measuring the cosmic-ray flux at Earth, one needs to model the propagation through the galaxy and—depending on the location of the regarded experiment—the propagation through the heliosphere. As discussed in the previous chapter, all propagation models have several unconstrained physical parameters, for example, the size of the galactic halo, the diffusion coefficient in the galaxy, or the time-dependent diffusion tensor in the heliosphere. In order to constrain them, one needs to fit the particle flux predicted by the model at Earth to cosmic-ray measurements, with the unconstrained physical parameters as free fit parameters [4]. Depending on which processes are included in the model, which parameterizations of the different processes are assumed, and which cosmic-ray measurements are used for the fit, the number of free parameters that need to be constrained by the fit varies, and the obtained best-fit values of the parameters can differ for different models [157, 158].

For most propagation-model fits, data from several different cosmic-ray particle species are required, as some parameters are only constrained by the primary component of cosmic rays, some are only constrained by the secondary component, and a few are even only constrained by radioactive secondary particles [4].

From the primary-particle spectra measured at Earth, one can learn about the spectral parameters of cosmic-ray acceleration in supernova remnants.

From secondary-to-primary flux ratios, one can extract the amount of material cosmic rays traversed during their propagation and processes that change the spectral shape of the cosmic-ray spectrum during propagation. Such processes influence the spectra of secondary particles more pronounced than the spectra of primary particles. The secondary-to-primary flux ratios thus constrain many propagation parameters, for example parameters describing the magnitude of diffusive reacceleration or convection [4]. Due to the relatively well-measured fragmentation cross section of carbon and heavier ions into boron and the relatively large cosmic fluxes of both particles, the boron-to-carbon flux ratio has been used in many studies for this purpose [91]. Unfortunately, the flux of stable secondary particles constrains only the total amount of material that the cosmic-ray particles traverse during

their propagation, and thus they can only help to constrain the ratio of the galactic-halo size and the diffusion coefficient, $z_\mathrm{h}/D_\mathrm{xx}$ [86].
To constrain both values independently, a flux measurement of an radioactive isotope with an lifetime of around the confinement time in the galaxy is needed. This lifts the so-called $z_\mathrm{h}/D_\mathrm{xx}$ ambiguity by restricting the absolute diffusion time of the particles in the galaxy, which allows to determine both parameters individually [4]. Commonly used for this purpose is the flux ratio of the radioactive beryllium isotope, beryllium-9, and the stable isotope, beryllium-10 [159].
If a model can simultaneously describe these different components of the cosmic-ray particle spectrum, the model poses a good candidate for a valid source and propagation model, and one can either validate the model's generalization ability on particle types not used in the parameter fit or use the obtained self-consistent propagation scheme to search for additional exotic contributions in specific particle spectra, like in the spectra of antiprotons or heavier antinuclei.

Since I want to investigate different production models of antiprotons and the influence of the production-model selection on the modeled cosmic antiproton flux at Earth in Chapter 3, I require to set up a valid, self-consistent propagation model that reproduces the measured fluxes of nuclei at Earth and can be used to propagate the produced antiprotons accordingly. Therefore, I need to select a suitable propagation scheme which is fitted to experimental cosmic-ray data and use it as a propagation model in our antiproton-production study.
Different propagation frameworks have been developed that solve the galactic diffusion equation numerically and allow for different parameterizations of the particle injection spectra and the processes during propagation. The most common frameworks for this purpose are the DRAGON-II [110, 89] and the GALPROP [91] computer codes.
Based on them, various studies have been published that constrain propagation parameters and injection spectra by fitting the modeled particle fluxes at Earth to cosmic-ray measurements. These studies often used different combinations of experimental data to fit to, distinct parameterizations of the involved propagation processes, and different settings for the numerical scheme to solve the diffusion equation shown in Equation 1.10. Due to these differences, no concurrent values for the injection and propagation parameters have been reached yet, even when using the same propagation framework. The selection of a suitable propagation setup thus requires a more detailed investigation of the propagation schemes used by the different studies. As I aim to use the GALPROP framework in our study, as it is the most commonly used propagation framework to date, I restrict this investigation to studies that employed GALPROP.
The most comprehensive studies using GALPROP and the new experimental data from AMS-02 and Voyager are from Boschini et al. [157, 160, 161, 162, 163] and Korsmeier et al. [164, 158, 165]. Both employed a similar model of galactic propagation, with some distinctions: While Boschini et al. used the HELMOD solar-modulation model [166], Korsmeier et al. applied the force-field method for solar modulation (c.f. Section 1.3.1); Boschini et al. used a gradually increasing velocity of the galactic wind with distance from the galactic plane, while Korsmeier used a constant velocity, which results in an unphysical divergence of the galactic-wind velocity at the galactic plane, $z = 0$; the most distinct differences, however, are the differing parameterizations of the injection spectra: While Boschini et

al. used an individual injection spectrum for each nuclei, violating the assumption of a universal particle injection in supernova remnants, Korsmeier et al. used a single spectrum for all nuclei except for protons, as it is established by experimental data that the proton spectrum has a significant different slope compared to helium [165]. However, Korsmeier et al. concluded in their study that in order to match the data of AMS-02 for different nuclei, a single, universal injection spectrum requires a nuclei-dependent diffusion coefficient [165]. Therefore, both studies point to an inaccuracy of the understanding of the involved physical processes, as both obtained results contradict the assumption of a universal cosmic-ray injection and propagation for different nuclei [165], but solve the discrepancy in a different manner. Since both studies obtained good agreement for the fitted cosmic-ray fluxes with the experimental data, a data-driven judgment of which implementation of the propagation processes and injection spectra is more valid is not possible.
Beside the different parameterizations of the physical processes, the studies also differ in terms of their settings of the numerical scheme that is used to obtain the approximated solution of the diffusion equation. The differences that arise from the different settings and the deviations of the modeled cosmic-ray fluxes from the accurate solution of the diffusion equation have not yet been studied. Before selecting a suitable propagation model for the study of different antiproton-production models, I first investigate the settings of the numerical-solution method in GALPROP and investigate the reached accuracies of the modeled cosmic-ray fluxes in different published studies.

2.1 Numerical Solution of the Diffusion Equation with GALPROP

For modeling the transport process of charged cosmic rays in our galaxy, we use the most commonly used computer code on this problem, GALPROP. First results of GALPROP were already published in 1998 [100]. Since then, the code has been maintained and upgraded on regular basis and is publicly available. In this thesis, we use version 56 of the code, which can be downloaded from https://galprop.stanford.edu/. In GALPROP, the full diffusion equation, as shown in Equation 1.10, is solved numerically including all previously discussed processes: The distributed primary particle sources, secondary production, spatial diffusion and convection, momentum changes, and energy losses and particle decays.
In GALPROP, the galaxy is modeled as a cylinder with a given radius, which corresponds to the radius of the Milky Way, and a height, which relates to the height of the galactic halo as $2z_h$. The source distribution is parameterized following Equation 1.5 with adjustable parameters. For the diffusion and convection processes, different parameterizations are available and can be selected by the user. A full overview on the available parameterizations of the different processes can be found in GALPROPs explanatory supplement [167].

As we assume the process of particle creation and transport to already happen continuously for a time span much longer than the typical confinement time of the cosmic rays—which is on the order of 10^8 years (c.f. Section 1.2.1)—and the state of our galaxy to be unaltered within this time, in terms of the distribution of cosmic-ray sources, magnetic fields, galactic winds, and interstellar material, we expect the cosmic-ray density to have reached a steady-state distribution within the galactic volume, meaning that $\partial \mathcal{N}_i(\vec{r}, p, t)/\partial t \ll \mathcal{N}_i(\vec{r}, p, t)$

everywhere in the galaxy. In the diffusion equation this state is reached for $t \to \infty$. Our goal is to retrieve an accurate approximation of this steady-state location and momentum-dependent particle density from the diffusion equation by evolving the diffusion equation numerically from an initial state over a long time period until the particle-density distribution does not significantly change anymore. In the initial state, the particle-density distribution is equal to the primary-source distribution—the distribution of supernova remnants—and the momentum distribution is equal to the injection spectrum of the primary sources. To evolve the distribution from this initial state with time, GALPROP uses the finite-difference method, which is in detail described in the GALPROP explanatory supplement [167] and that I summarize here.
In the finite-difference method, the derivative of the particle density with respect to time is approximated by a finite difference,

$$\frac{\partial \mathcal{N}_i(\vec{r}, p, t)}{\partial t} \approx \frac{\mathcal{N}_i(\vec{r}, p, t + \Delta t) - \mathcal{N}_i(\vec{r}, p, t)}{\Delta t}, \tag{2.1}$$

with discrete, finite timesteps, Δt. The spatial and momentum dimensions are also discretized to apply the same finite-difference method to approximate spatial and momentum derivatives that also occur in the diffusion equation. GALPROP uses a two-dimensional description of the intra-galactic space, with variables R and z describing the radial distance from the galactic center and the offset from the galactic plane, respectively. Thereby, one implies—as an approximation—the galaxy and the corresponding particle-density distribution to be circular symmetric around the galactic center, $R = 0$. From the discretization of the variable space, one obtains a multidimensional grid for which $\mathcal{N}_i(\vec{r}, p, t)$ has to be evaluated for each grid point. To get an accurate approximation of the time derivative by this finite difference, Δt must be smaller than the smallest timescale of the processes included in the diffusion equation [167]. For charged cosmic rays, the processes with smallest timescales are energy losses by ionization or radiative emission, which have timescales of approximately 10^3 to 10^4 years for nuclei. On the contrary, the time required to reach the steady-state solution depends on the processes with the largest timescale. For nuclei, these are the diffusive motion through the galaxy and the secondary production, which both have timescales on the order of 10^7 years. Thus, one needs to evolve the particle-density distribution on each grid point for at least a few-billion years in steps of a few-thousand years, which requires many iterations and thus a large number of computations. However, this approach is most accurate in terms of approximating the steady-state solution of the diffusion equation. Starting from the initial state, one successively calculates the particle densities of all grid points for each consecutive timestep by the help of a set of boundary conditions. At all times the boundary conditions,

$$\mathcal{N}_i(R, z_{\max}, p) = \mathcal{N}_i(R, -z_{\max}, p) = \mathcal{N}_i(R_{\max}, z, p) = 0, \tag{2.2}$$

with $R_{\max}$ and $z_{\max}$ being the radial size of the galaxy and the height of the galactic halo from the galactic plane, apply[167]. The particle density of a grid point, j, at $t + \Delta t$ can then be approximated from its previous value at t and the particle-density values of the neighboring points using different updating schemes. The simplest is the so-called explicit

method and can be written as:

$$\mathcal{N}_i(j, t+\Delta t) = \mathcal{N}_i(j,t) + \left(\frac{\alpha_{j,1}\mathcal{N}_i(j-1,t) - \alpha_{j,2}\mathcal{N}_i(j,t) + \alpha_{j,3}\mathcal{N}_i(j+1,t)}{\Delta t} + q_i \right) \Delta t, \quad (2.3)$$

with $\alpha_{j,1,2,3}$ being coefficients which stem from the finite differentiation of the various terms of the diffusion equation at j. An explicit calculation of the finite difference of the terms of the diffusion equation and a table of the coefficients for the different terms can be found in the GALPROP explanatory supplement [167].
To reach the steady-state result, this updating procedure has to be repeated until the particle-density values at all grid points become stable and do only marginally change with each successive timestep. A typical criterion to quantify the stability and accuracy of the obtained result is to compute the timescale, $\mathcal{N}_i(\vec{r},p,t)/\partial\mathcal{N}_i(\vec{r},p,t)/\partial t$, and require it to be much larger than the typical timescales of the included processes and the evolution time of the updating procedure. If the result is stable, the calculated timescale can be orders of magnitude larger than the evolved timespan or even reach machine infinity. Although this method is computationally simple and gives an accurate approximation of the solution of the diffusion equation, an enlargement of Δt to speed up the evolution and to reduce the required number of iterations until the steady-state is reached is not possible as the result becomes unstable if the timesteps are larger than the smallest timescale of included processes. Thus, the method must remain very slow, which makes the method for most applications that require many evaluations of the steady-state particle density not applicable, like it is, for example, in fitting procedures. To overcome this drawback, a method is required that can be sped up by allowing larger Δt—of course at the cost of accuracy—without losing the stability of the numerical result. This can be achieved by the so-called implicit method: The particle-density values on the grid points are updated in each new timestep using the neighboring values evaluated also at $t + \Delta t$, which is in contrast to the explicit method where the values of the neighboring points at t are used. The corresponding calculation scheme for the particle densities at $t + \Delta t$ is then given as

$$\begin{aligned}\mathcal{N}_i(j, t+\Delta t) &= \mathcal{N}_i(j,t) + \\ &\left(\frac{\alpha_{j,1}\mathcal{N}_i(j-1,t+\Delta t) - \alpha_{j,2}\mathcal{N}_i(j,t+\Delta t) + \alpha_{j,3}\mathcal{N}_i(j+1,t+\Delta t)}{\Delta t} + q_i \right) \Delta t. \quad (2.4)\end{aligned}$$

Unlike as for the explicit method, the terms of the neighboring points are all unknown and cannot straightforwardly be calculated sequentially. Instead, this leads to a $(N_j - 1) \times (N_j - 1)$-dimensional coupled system of linear equations, with N_j being the number of grid points per dimension, $j \in [R, z, p]$, which has to be solved for each timestep [168]. The solution of the system of linear equations can be obtained by using standard matrix-formalism-based methods [169, 170]. Although the implicit method is computationally more complex than the explicit method, it is stable also for larger timesteps and in turn reduces the number of iterations required until the steady state is reached. Overall, it reduces the total computing time. Unfortunately, larger timesteps reduce the accuracy of the obtained solution and the accuracy of the implicit method depends on first order on Δt [167].
To increase the accuracy with respect to the implicit method, GALPROP uses the so-called

Crank-Nicolson method [171], which uses an averaged value calculated from the explicit and implicit method. The calculation of the particle densities for each timestep can be written as:

$$\begin{aligned}\mathcal{N}_i(j, t+\Delta t) = \mathcal{N}_i(j,t) + \\ \Bigg(\frac{\alpha_{j,1}\mathcal{N}_i(j-1, t+\Delta t) - \alpha_{j,2}\mathcal{N}_i(j, t+\Delta t) + \alpha_{j,3}\mathcal{N}_i(j+1, t+\Delta t)}{2\Delta t} + \\ \frac{\alpha_{j,1}\mathcal{N}_i(j-1, t) - \alpha_{j,2}\mathcal{N}_i(j,t) + \alpha_{j,3}\mathcal{N}_i(j+1, t)}{2\Delta t} + q_i \Bigg) \Delta t. \end{aligned} \quad (2.5)$$

Similar to the implicit method, the Crank-Nicolson method is numerically stable for all Δt, but the accuracy of the result is of second order in Δt, allowing for larger timesteps or a more accurate result for a fixed timestep compared to the implicit method [167]. The Crank-Nicolson method, however, is generally only applicable in one-dimensional problems, while our application requires three dimensions (two spatial and one momentum dimension). To adapt it to the multi-dimensional case, the calculation scheme is in turn applied on the different dimensions sequentially for each timestep. In each call, only the corresponding partial derivatives of the operators on the current turn's dimension are used. Although this dimensional splitting is mathematically not unconditionally stable and neglects some of the higher-order correlations between the dimensions, it was found that it returns an accurate solution for small-enough grid spacing [100]. However, the stability and accuracy for a given grid and Δt has to be tested and validated beforehand by comparing the results between different settings.
As an additional feature to speed up the finding of the steady-state solution, the Crank-Nicolson method implemented in GALPROP does not use a single, fixed value of Δt but starts with a large Δt for several steps before reducing Δt to a smaller value. This is repeated several times during the calculation. The successive shrinking of Δt adapts the results gradually to include the short-term variations by the processes with small timescales in an accelerated way. The reduction factor of Δt and the number of repetitions per Δt have to be tuned to reach an accurate and stable solution.

To model the cosmic-ray flux for all particle species, the described adapted-Crank-Nicolson method is applied to all ion species sequentially from heavy to light ions to incorporate the fragmentation of heavier ions as a source term in the diffusion equation for the lighter ions. The local interstellar particle density at the position of the solar system in the galaxy can then be retrieved from the found steady-state solution at the grid point corresponding to $R = R_0$ and $z = 0\,\mathrm{kpc}$.
As discussed, the characteristics of the grids in space and momentum together with the setting of Δt used in the Crank-Nicolson method are important settings that need to be correctly set to obtain an accurate particle-flux for a given propagation model. Although the usage of the explicit method or the usage of very narrow grid spacing and small timesteps would in general give the best accuracy, the calculation speed would hinder to use GALPROP in fitting procedures, as such fits require a great number of evaluations of the steady-state particle flux during the tuning of the parameters. Typical numbers of evaluations of the diffusion equation found in literature for such use cases are on the order

of 2×10^5 to 3×10^6[158]. The computing time for a single evaluation of the steady-state particle density depends strongly on the used settings of the grid parameters and the settings of the Crank-Nicolson algorithm and can vary between a few seconds to a few hours on a single CPU. For the longest evaluation times, the total required computational time of a full fit would thereby often exceed the available capacities and an trade-off between numerical accuracy and runtime has to be found. Especially in the light of recent cosmic-ray measurements from long-term experiments, which reach statistical precision on the order of 1 % or less, the settings have to be validated so that the accuracy of the numerical solution is compatible or better than the experimental uncertainties because otherwise no meaningful constraints on the fit parameters can be obtained.
In the following section I describe the investigation of the influence of some of the most important settings of the numerical-solution method of GALPROP on the accuracy of the produced particle fluxes. The aim is to find an optimal setting that allows for an accurate prediction of the particle flux at Earth on the level of the experimental uncertainties with a computational time that still allows for using GALPROP in parameter-fitting procedures and to estimate the systematic effect of different settings used in existing studies on the extracted propagation parameters.

2.2 Studies of Solution and Grid Parameters

We aim to assess the influence of the different parameters on the accuracy of the obtained particle fluxes and whether deviations might influence the resulting values of propagation parameters when fitting propagation models to data. To do so, we compare the resulting particle fluxes from GALPROP with different solution-and grid-parameter settings with the results from a benchmark model, which we believe to be most accurate but computationally most costly. We focus on comparing the particle fluxes with the different settings at Sun's location ($R = R_0, z = 0\,\mathrm{kpc}$) and in an energy range that is relevant for studies that compare to AMS-02 and Voyager data, namely between around $1 \times 10^{-1}\,\mathrm{GeV/n}$ and $1 \times 10^{3}\,\mathrm{GeV/n}$. We start with investigating the solution parameters of the explicit method and the accelerated Crank-Nicolson method. After this, we analyze the influence of different settings for the grids of the spatial and momentum dimensions.
For the study we need to fix the parameters of propagation and injection such that we can test the different configurations of the solution and grid parameters on a realistic setup of the galaxy and the propagation. Therefore, we use the propagation parameters and injection spectra obtained by the fitting procedure from Boschini et al. [163]. Compared to other studies, Boschini et al. used relatively elaborate settings, which we believe to result in an accurate representation of the solution of the diffusion equation. The yielded cosmic-ray fluxes in their model agree well with experimental data. In Figure 2.1, exemplarily the modeled proton flux using the settings from Boschini et al. is shown and the relative deviation to the measurement of AMS-02 [172]. As can be seen, the model agrees well with the measurements, and it deviates from the data points less than 5 % over the whole measurement range. Another reason for us to use the propagation and injection parameters from Boschini et al., is that they found a non-zero Alfven velocity and a non-zero galactic wind velocity, giving non-zero terms for reacceleration and convection. This is important as some deviations may arise only from specific processes during propagation and we want

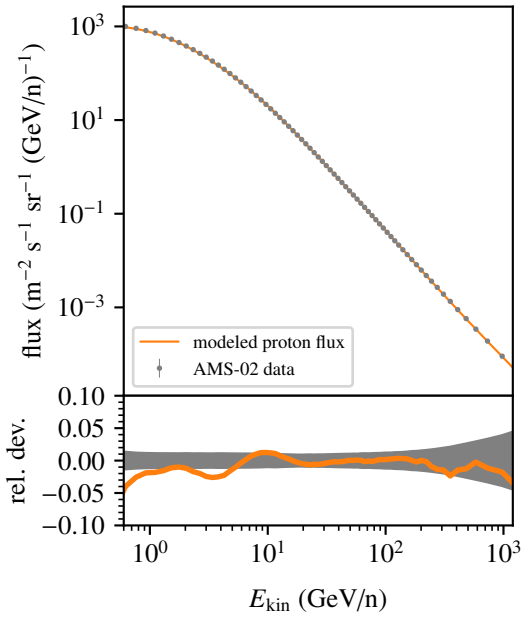

Figure 2.1: Comparison of the modeled proton flux at Earth and the experimental data from AMS-02 [172]. The propagation model GALPROP is used together with the parameter settings of Boschini et al. [163]. Solar modulation is modeled using HELMOD [154].

to include all relevant processes in our study.
As the computations for the finest grid settings and the execution of the explicit method require large computational effort, we restrict our analysis of the different settings to protons. We investigate the primary and secondary component of the proton flux independently to learn whether found deviations are more pronounced for primary or secondary cosmic rays. At the end of the study, we also analyze the influence of different settings on other nuclei which are of particular interest for propagation studies, such as helium, boron, and carbon. To assess the importance of the found deviations, we also compare their magnitude to the relative uncertainties of the AMS-02 experimental data and perform an exemplary fit of the injection parameters for protons to the AMS-02 data with different settings to estimate the impact of the solution and grid parameters on obtained fit results.

2.2.1 Solution Method and Parameters

2.2.1.1 Explicit Method

We start with an examination of the explicit method and its settings, the total evolution time, t_{evol}, until the steady-state result is reached, and the minimal required timestep to be used to cover all small-timescale processes accurately. In initial tests of GALPROP, an evolution time of about 1×10^8 years and a timestep of 1×10^3 years gave stable and accurate results for most applications at that time [167].
We run GALPROP with different evolution times between $t_{\mathrm{evol}} = 5 \times 10^7$ years and $t_{\mathrm{evol}} =$

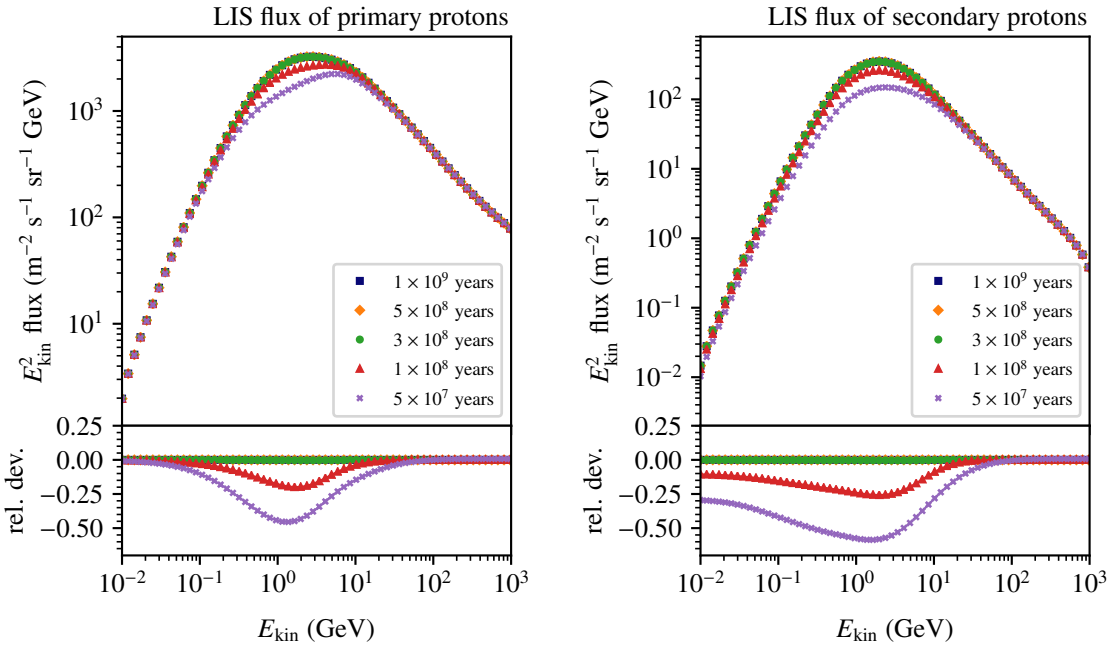

(a) Flux of primary protons.

(b) Flux of secondary protons.

Figure 2.2: Resulting local interstellar flux of protons from GALPROP using the explicit method with different evolution times and $\Delta t = 1 \times 10^3$ years. The fluxes are multiplied by E^2_{kin} to increase the visibility of the deviations.

1×10^9 years with a fixed $\Delta t = 1 \times 10^3$ years. We compare the obtained fluxes of primary and secondary protons from the different runs at Sun's location in the Milky Way, at $R = 8.5\,\mathrm{kpc}$[1] and $z = 0\,\mathrm{kpc}$. The corresponding settings file used for this and the following studies can be found in Appendix A. Figure 2.2 shows the obtained particle fluxes for the different evolution times and the corresponding relative deviations from the run with $t_{\mathrm{evol}} = 1 \times 10^9$ years. If not otherwise stated, we define the energy-dependent relative deviation between the obtained flux from a run with settings, s, and the run with the benchmark settings, b, which is given as the first entry in the corresponding figure legend, as

$$\text{rel. dev} \equiv \frac{f_s(E) - f_b(E)}{f_b(E)}. \tag{2.6}$$

For both, primary and secondary protons, the flux changes visibly for $t \leq 1 \times 10^8$ years with respect to the runs with longer evolution times. The relative deviations of the fluxes

[1] Recent measurements suggest Sun's location at $R = 8.2\,\mathrm{kpc}$ but all of the considered studies used $R = 8.5\,\mathrm{kpc}$. To ease comparison of our results with the older studies, we also use 8.5 kpc for Sun's location. By comparing fluxes at different radial locations, we have found that this choice does not influence the found results. Although a differing radial location yields a different absolute magnitude for all cosmic-ray fluxes—without any energy dependence—the normalization procedure of GALPROP compensates the effect. In GALPROP, all obtained particle fluxes are normalized such that the proton flux at 100 GeV at Sun's location coincides with experimental measurements. A radial shift of Sun's location in the galaxy would therefore only affect this normalization constant.

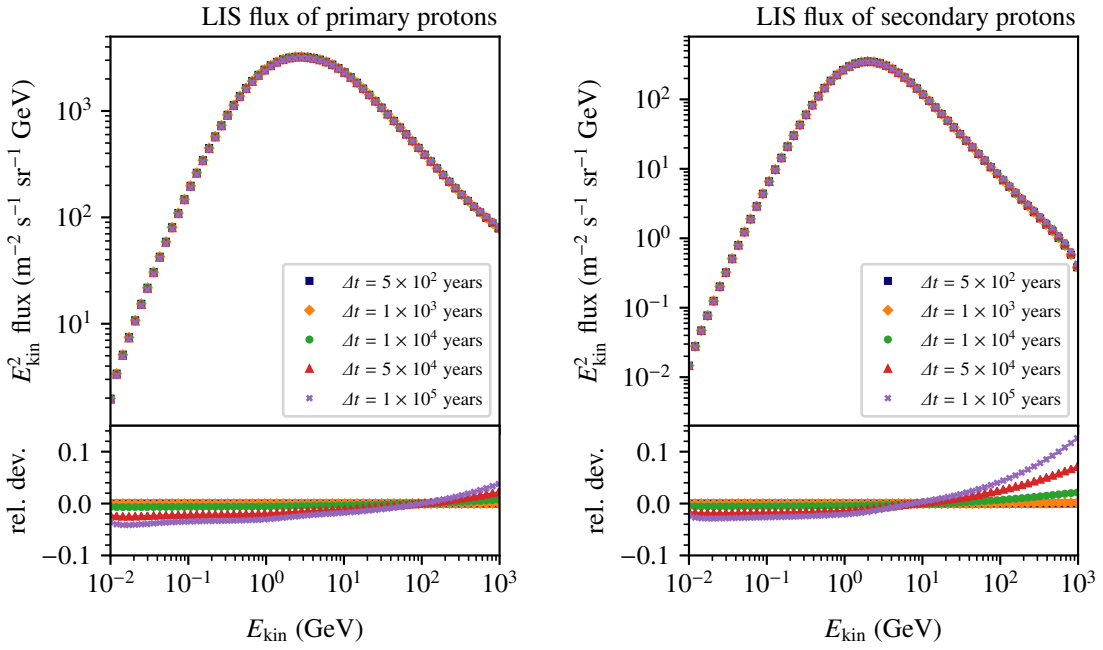

(a) Flux of primary protons.

(b) Flux of secondary protons.

Figure 2.3: Resulting local interstellar flux of protons from GALPROP using the explicit method with an evolution time of $t_{\mathrm{evol}} = 1 \times 10^9$ years and different timesteps. The fluxes are multiplied by E_{kin}^2 to increase the visibility of the deviations.

are larger for secondary protons than for primary protons. This is expected as the secondary production depends on the primary cosmic-ray flux, and the secondary flux thus can only reach the steady-state after the primary flux. For evolution times longer or equal 3×10^8 years, no deviations are visible and the steady-state flux seems to be reached. As the required evolution time is expected to be dependent on the halo size of the galaxy, we conducted the same analysis with different halo sizes. Most studies so far found the halo size of our galaxy to be in the range of 3 kpc to 12 kpc [4].[2]. Within this range, the required evolution time to reach the steady-state does, however, not change.
To study the dependency of the proton flux on Δt, we evolve the particle density for 1×10^9 years with different Δt in the range from 1×10^3 years to 5×10^4 years. Figure 2.3 shows the different fluxes and relative deviations with respect to the run with the shortest timesteps, $\Delta t = 5 \times 10^2$ years. Again, the deviations are more pronounced for secondary protons. The deviations are relatively small for most energies, even for the largest tested timesteps. As the processes with smallest timescale are energy losses, we expect the deviations to arise from these processes. The relative increase of the particle flux at high energies with increasing Δt, and the decrease at low energies could hint to an under-representation of energy losses for such large timesteps. Since energy losses of charged cosmic rays scale with their charge, we expect these deviations to be larger for particles with higher charge.

[2] We use the term 'halo size' as a synonym for z_{h} The total size of the galactic halo is twice the halo size, z_{h}.

To obtain the minimal required Δt also for higher-charged ions, we conduct the same study with a medium and a highly charged ion, silicon-28 ($Z = 14$) and iron-56 ($Z = 26$). The found relative deviations are similar to the deviations of the protons, and no smaller timesteps are required to describe higher charged particles accurately as well.
In summary, we confirm the findings from Strong et al. [167], and yield an accurate representation of the steady-state solution of the diffusion equation with the explicit method already for $t_{\mathrm{evol}} \geq 3 \times 10^8$ years and $\Delta t \leq 1 \times 10^3$ years.
The runtime of the explicit method with such settings, however, is around 7×10^3 s for each ion type on a modern Intel i9-10900K processor with 3.7 GHz and parallelization on up to 12 threads. This long execution time makes the explicit method not usable for most applications in which the whole ion network—with up to 20 or more ion types—has to be solved successively. Therefore, in most applications the accelerated Crank-Nicolson solution method is used instead.

2.2.1.2 Accelerated Crank-Nicolson Method

We compare the accuracy of the accelerated Crank-Nicolson to the accurate solution found by the explicit method for different settings of the time-reduction factor, $f_{\Delta t}$, and the number of repetitions per timestep, $n_{\Delta t}$. For each time-step reduction, the previous Δt is multiplied by $f_{\Delta t}$ and the new Δt is applied $n_{\Delta t}$ times before the next reduction step.
We test different combinations of $f_{\Delta t}$ and $n_{\Delta t}$, which result in different execution times, and compare their results to the accurate result found by the explicit method. Figure 2.4 shows selected results of the tested combinations with respect to the result of the explicit method with $t_{\mathrm{evol}} = 1 \times 10^9$ years and $\Delta t = 1 \times 10^3$ years. For small timestep-reduction factors and large number of iterations per timestep, the accelerated Crank-Nicolson method gives very accurate results. For $f_{\Delta t} = 0.95$ and $n_{\Delta t} = 100$ the maximum deviation from the result obtained by the explicit method is smaller than 4×10^{-3} although the execution time is about 160 times shorter. Smaller values for $f_{\Delta t}$ and $n_{\Delta t}$ decrease the execution time further but at the cost of larger deviations from the numerically accurate solution. Settings which have been employed in published studies are $0.25 \leq f_{\Delta t} \leq 0.75$ and $20 \leq n_{\Delta t} \leq 30$, which result in deviations from the accurate solution of up to 5 % for the total proton flux within the energy range covered by the AMS-02 experiment. As this deviation is already larger than the experimental uncertainties from AMS-02, this systematic uncertainty is non-negligible when comparing the predictions from GALPROP with experimental results.

2.2.2 Space and Momentum Grids

In most studies, the particle density is evaluated for each timestep on a three-dimensional grid in GALPROP, two spatial dimensions, R and z, and one momentum dimension. Commonly the range and grid-point density of the momentum dimension is set via an energy-per-nucleon grid, and the values are transformed within GALPROP. We investigate the influence of the grid sizes of the different dimensions independently. For the spatial dimensions, the parameters of interest are the spatial density of the grid points. For the energy-per-nucleon grid the density of the grid points and additionally the minimum and maximum energy of the grid.
The grid size perpendicular to the galactic plane depends on the galactic halo size and

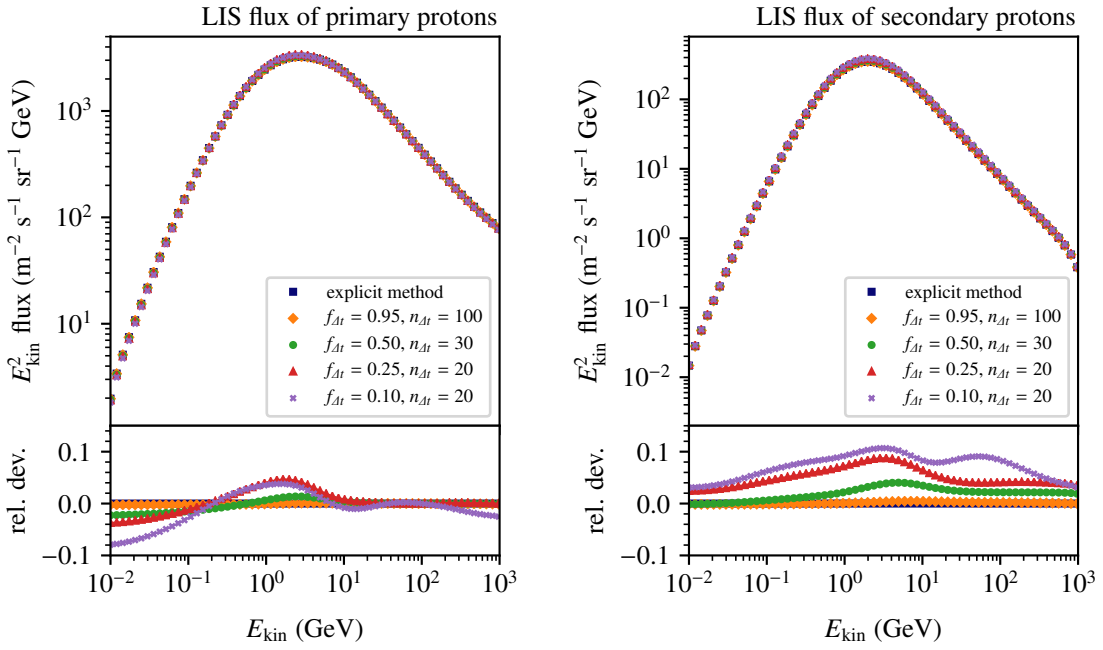

(a) Flux of primary protons.

(b) Flux of secondary protons.

Figure 2.4: Resulting local interstellar flux of protons from GALPROP using different settings of the accelerated Crank-Nicolson method in comparison to the result of the explicit method. The fluxes are multiplied by E_{kin}^2 to increase the visibility of the deviations.

the distance between two neighboring grid points. To investigate the influence of different grid-point densities, which are defined by the distance of two grid points, Δz (in kpc), we compare the resulting proton flux from runs with different Δz and a fixed total halo size of 4 kpc with each other. Figure 2.5 shows the corresponding results. The deviations are mainly visible at small energies for primary protons except for values of $\Delta z \geq 1$, where large deviations occur also in the secondary component. However, this setting belongs to only eight grid points along the z-direction in total, which is clearly to coarse. For grid-point distances of $\Delta z = 0.1$, the found deviations are below 0.6 %.

The radial extend of the galaxy is more constrained than its halo size and is in most cosmic-ray studies fixed to 20 kpc [28, 158]. We again compare the results for different grid-point distances in terms of ΔR evaluated at Sun's location at $R = 8.5$ kpc. For grids in which Sun's location does not coincide with a grid point, a linear interpolation of the fluxes of the two closest neighboring points is used. This approach is the common procedure in many published studies in which $\Delta R = 1$ kpc are used [28, 158]. Figure 2.6 compares the resulting proton fluxes for different ΔR settings. For all settings in which the Sun's location coincides with a grid point—$\Delta R \leq 0.5$ kpc—no significant differences are found. However, for settings that require interpolation, the differences are much larger, hinting to an inaccuracy of the linear interpolation procedure. Although the difference is mostly constant with energy—and the deviations would be absorbed by the normalization proce-

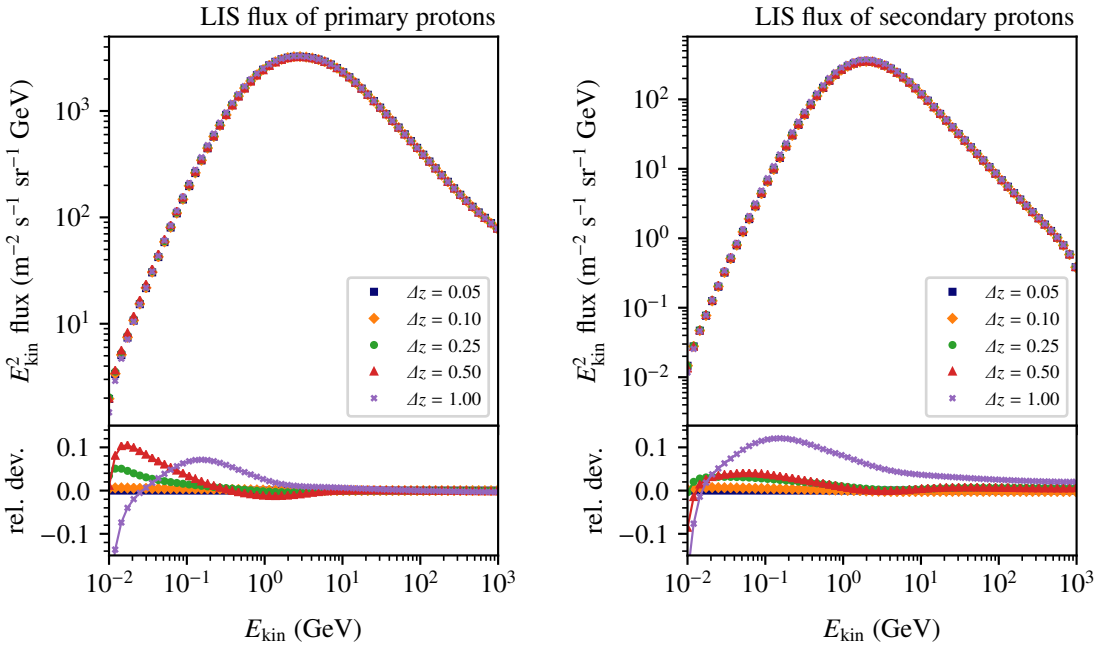

(a) Flux of primary protons.

(b) Flux of secondary protons.

Figure 2.5: Resulting local interstellar flux of protons from GALPROP with different grid-point spacing perpendicular to the galactic plane. The size of the galactic halo is set to 4 kpc. The fluxes are multiplied by E^2_{kin} to increase the visibility of the deviations.

dure of the obtained particle fluxes in GALPROP—some energy-dependent deviations are visible. For $\Delta R = 1.0\,\mathrm{kpc}$, which is used most commonly in studies employing GALPROP, these energy-dependent deviations are found to be significant only below $1 \times 10^{-1}\,\mathrm{GeV/n}$, not influencing most studies that compare the predicted particle fluxes to AMS-02 data.

The energy grid has three parameters that need to be set: The maximum energy per nucleon, E_{max}, the minimum energy per nucleon, E_{min}, and a factor, $f_{\Delta E}$, that defines the point density within the grid. The neighboring grid points of the energy grid are related to each other by $E_i = E_{i-1} \cdot f_{\Delta E}$, starting from $E_{i=0} = E_{\mathrm{min}}$. In most applications, the energy range between $1 \times 10^{-2}\,\mathrm{GeV/n}$ and $1 \times 10^{3}\,\mathrm{GeV/n}$ are of interest—the energy range covered by the particle detectors on the Voyager probes and the AMS-02 experiment, requiring the energy grid to be at least to cover this range. However, setting the energy boundaries just outside the range of energies one is interested in is not enough due to the kinematics of secondary production and diffusive reacceleration, as we will see in the following.
Choosing E_{max} just above the maximum energy that one is interested in, influences the spectra of secondary particles at lower energies, as the produced secondary particles from fragmentation or inelastic processes are often less energetic as the initial particle. The missing source term from the higher-energetic collisions can reduce the secondary particle flux over a large range of energies. To quantify this effect, we varied E_{max} be-

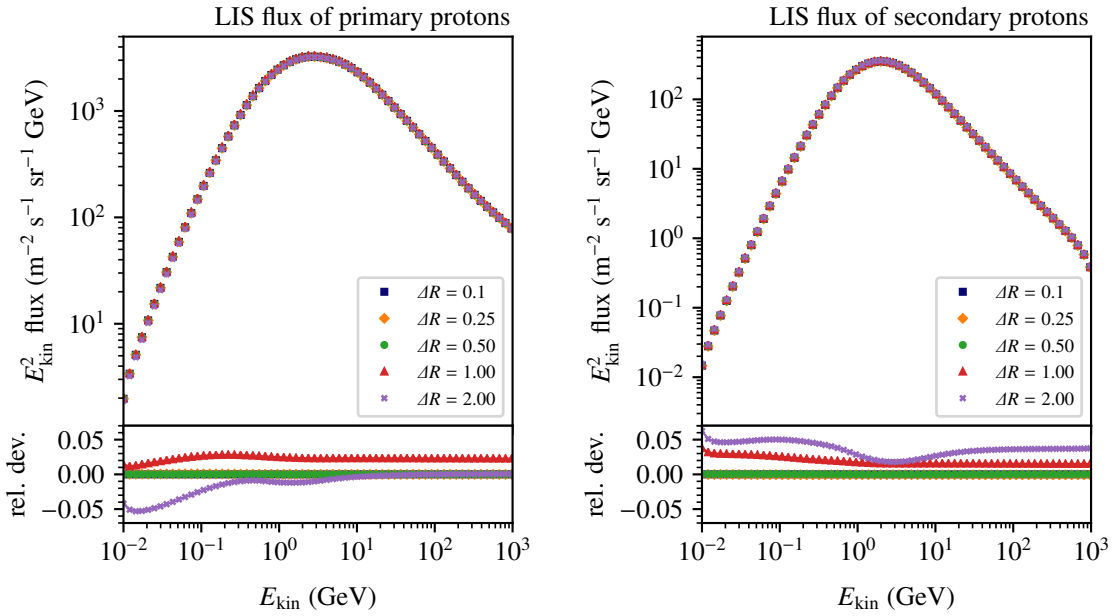

(a) Flux of primary protons.

(b) Flux of secondary protons.

Figure 2.6: Resulting local interstellar flux of protons from GALPROP with different grid-point spacing in radial direction. The radial size of the galaxy is set to 20 kpc. The fluxes are multiplied by E_{kin}^2 to increase the visibility of the deviations.

tween 1×10^3 GeV/n and 1×10^6 GeV/n and investigated the relative changes of the secondary proton and additionally the antiproton flux. Figure 2.7 shows the secondary proton and antiproton fluxes and their relative deviations with respect to the run with $E_{\mathrm{max}} = 1 \times 10^6$ GeV/n within our energy range of interest. Although the primary proton flux is not altered within this shown range, the secondary particle fluxes are. This effect is especially large for antiprotons as they are created in high-energetic collisions, and the creation of very fast antiprotons requires even faster projectiles. In order to not alter the secondary particle fluxes significantly within the energy range up to 1×10^3 GeV/n, we find that $E_{\mathrm{max}} \geq 1 \times 10^8$ GeV/n is required.
For E_{min} we perform a similar study. We vary the lowest energy-grid point between 1×10^{-1} MeV/n and 100 MeV/n[3] and investigate the changes of the primary and secondary proton flux. The results are shown in Figure 2.8. Although nearly no deviations are visible for the runs with $E_{\mathrm{min}} \leq 10$ MeV, large deviations, even above 1 GeV, occur for larger E_{min}. The corresponding fluxes are reduced with respect to the runs with smaller E_{min}. This effect can be attributed to the process of reacceleration. For small E_{min}, more low-energy particles are propagated and can be re-accelerated during the diffusion through the galaxy, while for large values of E_{min}, these particles are not injected and propagated at all. When changing E_{min} between 10 MeV/n and 0.1 MeV/n, no further changes are

[3] Althought 50 MeV/n and 100 MeV/n are already within the measurement range of Voyager, we show these values to emphasize the modification of the particle fluxes for such large values of E_{min} at even larger energies.

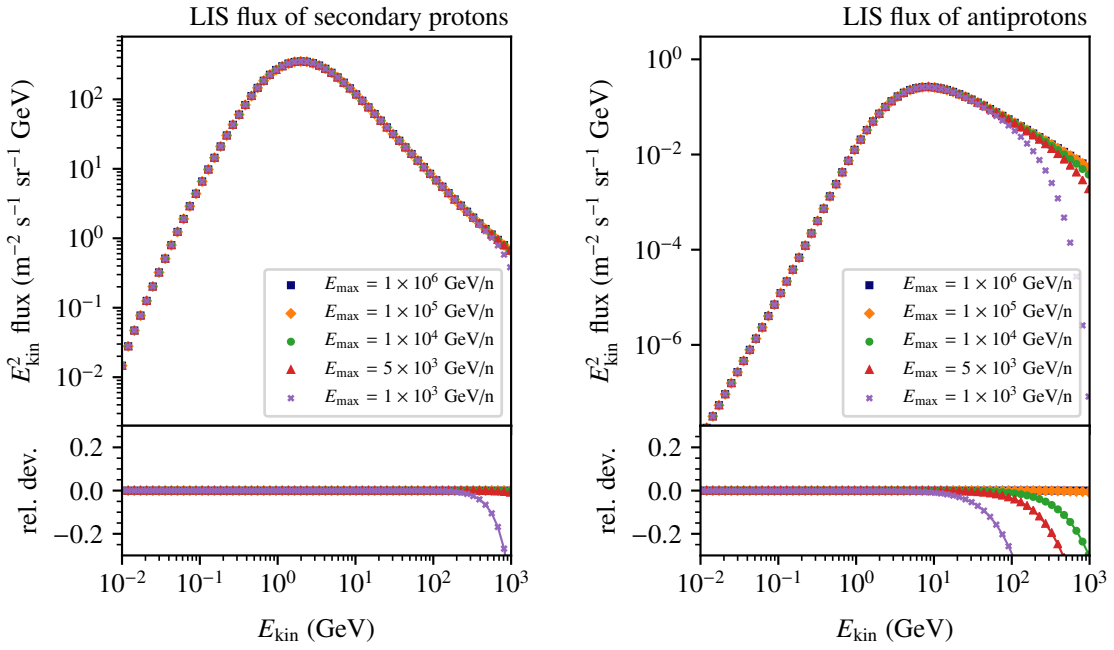

(a) Flux of secondary protons.

(b) Flux of secondary antiprotons.

Figure 2.7: Resulting local interstellar flux of protons and antiprotons stemming from proton interactions on interstellar material from GALPROP with different settings of E_{max} and their relative deviations within the energy range covered by Voyager and AMS-02. For the antiproton production cross section, the parameterization by Tan et al. [173] is used (see Chapter 3 for more details on cosmic antiproton production). The fluxes are multiplied by E_{kin}^2 to increase the visibility of the deviations.

visible, indicating that particles below around 10 MeV/n are not re-accelerated efficiently anymore due to their high relative energy losses from ionization and Coulomb scattering. Therefore, E_{min} should be chosen smaller than approximately 10 MeV/n, even in applications that are focused only on an energy range above 1 GeV/n. For models without diffusive reacceleration, we find no dependence of the resulting particle fluxes on E_{min}.
The third parameter to set for the energy grid is $f_{\Delta E}$. From its definition, it follows that $f_{\Delta E} > 1$. It must be chosen appropriately to the experimental dataset that one wants to compare the GALPROP output to: depending on the binning of the measured energy-differential particle flux of the experiment, the result from GALPROP requires an additional interpolation to be compared to the experimental data. The larger the grid-point spacing used in the GALPROP run, the larger potential systematic errors due to the interpolation become. In Figure 2.9, we show the proton fluxes for different values of $f_{\Delta E}$ and compare them to a grid with smallest grid-point spacing, $f_{\Delta E} = 1.01$, which has in total 230 grid points per decade of energy. For the calculation of the relative deviations, all other fluxes are interpolated to the grid point values from the grid with $f_{\Delta E} = 1.01$ using a so-called lin-log interpolation, meaning a linear interpolation of the flux values on logarithmic energies. This is a standard approach for exponential-like functions and employed in many

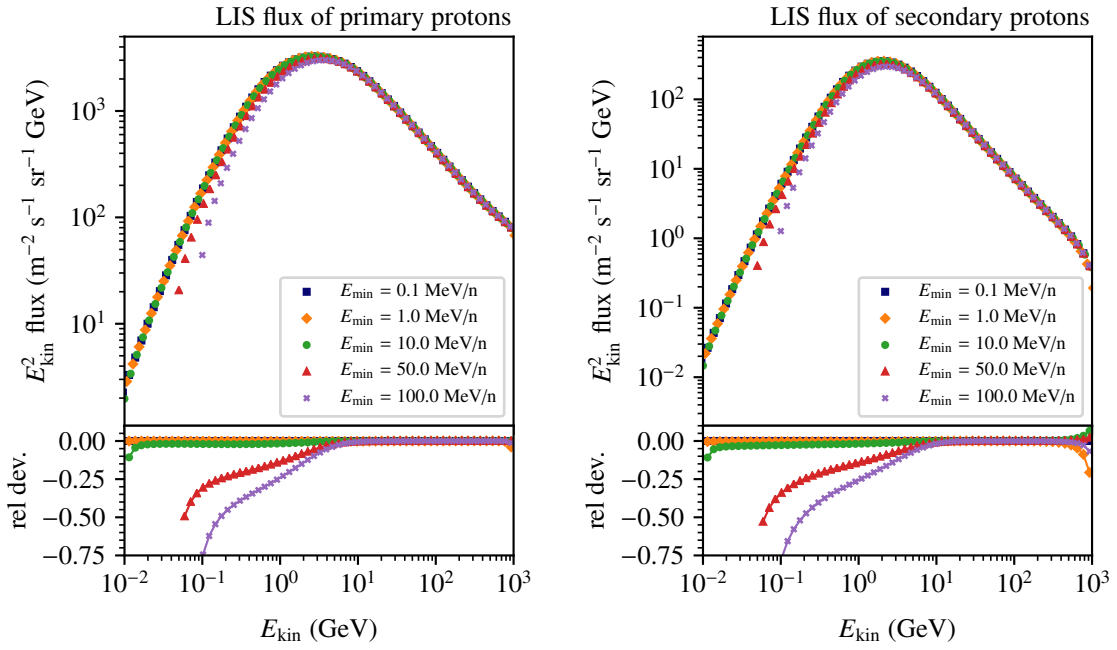

(a) Flux of primary protons.

(b) Flux of secondary protons.

Figure 2.8: Resulting local interstellar flux of protons from GALPROP with different E_{min}. The fluxes are multiplied by E_{kin}^2 to increase the visibility of the deviations.

cosmic-ray related computer programs including GALPROP and HELMOD [166]. For large values of $f_{\Delta E}$, the effect of this interpolation is clearly visible in forms of small, peaking structures in the figure of the relative deviation. Such artifacts arise due to the mismatch of the interpolation function, which is based on an exponential, and the true, underlying function of the particle flux, which is more power-law like. In order to get rid of these artifacts, one could use a more suited interpolation function or reduce the distance between neighboring grid points. Additionally, large deviations are visible at the boarders of the energy grid due to boundary effects, which can be migrated by extending the grid. For secondary protons however, an additional large deviation that peaks at an energy of about 10 GeV/n is noticeable. This deviation is found to be independent of E_{max}.
We notice that the deviations stemming from a too large energy-grid density are comparably large with respect to the other found deviations from other grid parameters, and that even for small values of $f_{\Delta E} \approx 1.2$ significant. An appropriate choice of this parameter is thus inevitable.

2.2.3 Systematic Errors from the Solution Settings

As we have seen, several of the grid and solution parameters strongly influence the accuracy of the obtained solution and alter the resulting cosmic-ray flux for primary and secondary particles. Since it is not possible in most applications to simply use the finest and most accurate settings due to the large computational effort, we need to quantify the deviations

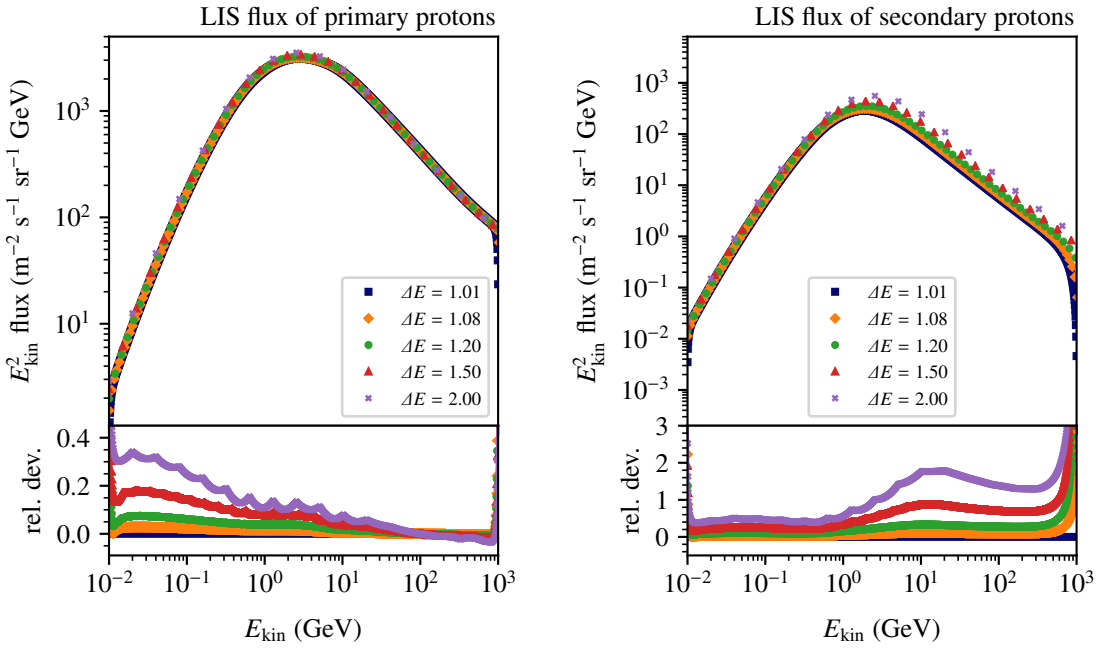

(a) Flux of primary protons.

(b) Flux of secondary protons.

Figure 2.9: Resulting local interstellar flux of protons from GALPROP with different energy-grid densities. The fluxes are multiplied by E^2_{kin} to increase the visibility of the deviations.

made for a given set of settings and assign them as systematic uncertainties that have to be taken into account when drawing conclusions from studies using GALPROP. To assess the systematic uncertainties from the selected grid and solution settings in published studies, we compare the modeled fluxes from the settings used in the studies with the solution of one of our investigated benchmark settings that obtains an accurate solution of the diffusion equation. Additionally, we aim to quantify how these deviations influence obtained physical parameters of cosmic-ray production and propagation in fitting procedures. Therefore, we perform a simplified fit of the injection parameters for protons using the AMS-02 proton-flux measurement with different solution and grid-parameter settings and compare the obtained parameters.

In Table 2.1 we list the employed settings of selected studies that we aim to compare. Beside the two recent studies in which the propagation and injection parameters were extracted using GALPROP from Boschini et al. [163] and Korsmeier et al. [158, 165], we also compare the settings used in a recent study of the cosmic-ray antideuteron flux by D. Coral [174], and the default values of the GALPROP webrun, which allows to run GALPROP over the internet [175]. We calculate the deviations of the particle fluxes obtained with the different settings with respect to the solution from a run with specifically fine grids and solution parameters, which we tested to obtain an accurate steady-state solution. We label the run with those settings as the benchmark model and list the corresponding settings also in Table 2.1. Figure 2.10 shows the obtained proton fluxes for identical propagation and injection parameters—as given in Appendix A—and the relative deviations from the fluxes

Reference	solution settings	spatial-grid settings	energy-grid settings
Boschini et al. [157, 163]	$\Delta t_{\mathrm{max}} = 1 \times 10^{8}$ years $\Delta t_{\mathrm{min}} = 1 \times 10^{2}$ years $f_{\Delta t} = 0.75$ $n_{\Delta t} = 100$	$\Delta z = 0.1\,\mathrm{kpc}$ $\Delta R = 1.0\,\mathrm{kpc}$	$E_{\mathrm{min}} = 1 \times 10^{-3}\,\mathrm{GeV/n}$ $E_{\mathrm{max}} = 1 \times 10^{5}\,\mathrm{GeV/n}$ $f_{\Delta E} = 1.07$
Korsmeier et al. [164, 165]	$\Delta t_{\mathrm{max}} = 1 \times 10^{9}$ years $\Delta t_{\mathrm{min}} = 1 \times 10^{2}$ years $f_{\Delta t} = 0.50$ $n_{\Delta t} = 20$	$\Delta z = 0.1\,\mathrm{kpc}$ $\Delta R = 1.0\,\mathrm{kpc}$	$E_{\mathrm{min}} = 1 \times 10^{-3}\,\mathrm{GeV/n}$ $E_{\mathrm{max}} = 1 \times 10^{4}\,\mathrm{GeV/n}$ $f_{\Delta E} = 1.30$
Coral [174]	$\Delta t_{\mathrm{max}} = 1 \times 10^{9}$ years $\Delta t_{\mathrm{min}} = 1 \times 10^{2}$ years $f_{\Delta t} = 0.25$ $n_{\Delta t} = 20$	$\Delta z = 0.1\,\mathrm{kpc}$ $\Delta R = 1.0\,\mathrm{kpc}$	$E_{\mathrm{min}} = 1 \times 10^{-1}\,\mathrm{GeV/n}$ $E_{\mathrm{max}} = 1 \times 10^{6}\,\mathrm{GeV/n}$ $f_{\Delta E} = 1.36$
GALPROP Webrun [175]	$\Delta t_{\mathrm{max}} = 1 \times 10^{9}$ years $\Delta t_{\mathrm{min}} = 1 \times 10^{2}$ years $f_{\Delta t} = 0.25$ $n_{\Delta t} = 20$	$\Delta z = 0.1\,\mathrm{kpc}$ $\Delta R = 1.0\,\mathrm{kpc}$	$E_{\mathrm{min}} = 1 \times 10^{-2}\,\mathrm{GeV/n}$ $E_{\mathrm{max}} = 1 \times 10^{4}\,\mathrm{GeV/n}$ $f_{\Delta E} = 1.30$
benchmark	$\Delta t_{\mathrm{max}} = 1 \times 10^{9}$ years $\Delta t_{\mathrm{min}} = 1 \times 10^{2}$ years $f_{\Delta t} = 0.95$ $n_{\Delta t} = 100$	$\Delta z = 0.1\,\mathrm{kpc}$ $\Delta R = 1.0\,\mathrm{kpc}^{\dagger}$	$E_{\mathrm{min}} = 1 \times 10^{-3}\,\mathrm{GeV/n}$ $E_{\mathrm{max}} = 1 \times 10^{5}\,\mathrm{GeV/n}$ $f_{\Delta E} = 1.01$

Table 2.1: Different settings used in various studies employing GALPROP. Settings that are not published in the specified reference have been obtained by private communication with the corresponding author. † Although this setting of ΔR requires interpolation to extract the local interstellar flux at Sun's location at $R_0 = 8.5\,\mathrm{kpc}$, which is used in all other models, we use this value for consistency of GALPROP's internal normalization throughout the comparison of the models.

obtained by the benchmark model. In order to compare the magnitude of the found relative deviations with the relative experimental uncertainties from AMS-02, Figure 2.12 shows the resulting particle fluxes after solar modulation using the HELMOD solar-modulation model together with the relative uncertainties of the AMS-02 experiment for the corresponding flux measurement as a grey band. In addition to protons, we show also the cosmic-ray helium flux, the antiproton flux, and the boron-to-carbon flux ratio, which is an important observable used to constrain several propagation parameters. Especially for protons and helium, for which the relative measurement uncertainties are small, the deviations from numerical inaccuracies due to the employed settings in most studies exceed the experimental

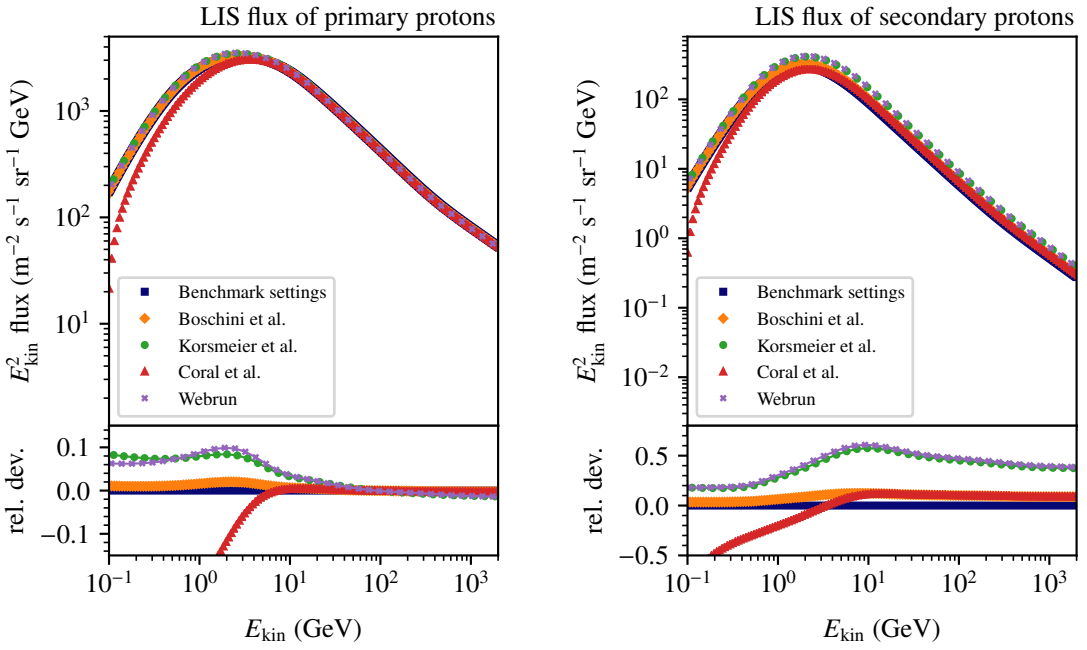

(a) Flux of primary protons.

(b) Flux of secondary protons.

Figure 2.10: Resulting local interstellar flux of protons from GALPROP with different settings of the solution and grid parameters used in literature, listed in Table 2.1. The fluxes are multiplied by E^2_{kin} to increase the visibility of the deviations.

uncertainties by far, meaning that obtained propagation and injection parameter based for the modeled proton and helium fluxes might suffer from a large systematic error. Due to the larger measurement uncertainties, the relative effect on the modeled boron-to-carbon ratio and the antiproton flux is not as severe. For antiprotons, all models obtain a flux that coincides within 10 % with the accurate solution of the diffusion equation, which is comparable to the current experimental uncertainties from AMS-02.

In order to illustrate a possible effect of the numerical settings on obtained parameters from a fit of the propagation model to cosmic-ray data, we perform a simplified fit to the AMS-02 experimental data with a unique propagation model but different grid and solution settings and compare the obtained parameters by the fit. Instead of fitting all propagation and injection parameter, we use only selected injection parameters as free parameters and fix all propagation parameters beforehand to the values obtained by Boschini et al. [163]. The parameters used for this study are again the ones listed in Appendix A.
In Boschini et al. [163], the proton-injection spectrum is modeled as a broken power law with four breaks, as

$$Q_{\mathrm{p}}(R) = \left(\frac{R}{R_0}\right)^{-\gamma_0} \prod_{i=0}^{3} \left[1 + \left(\frac{R}{R_i}\right)^{\frac{\gamma_i - \gamma_{i+1}}{s_i}}\right]^{s_i}, \tag{2.7}$$

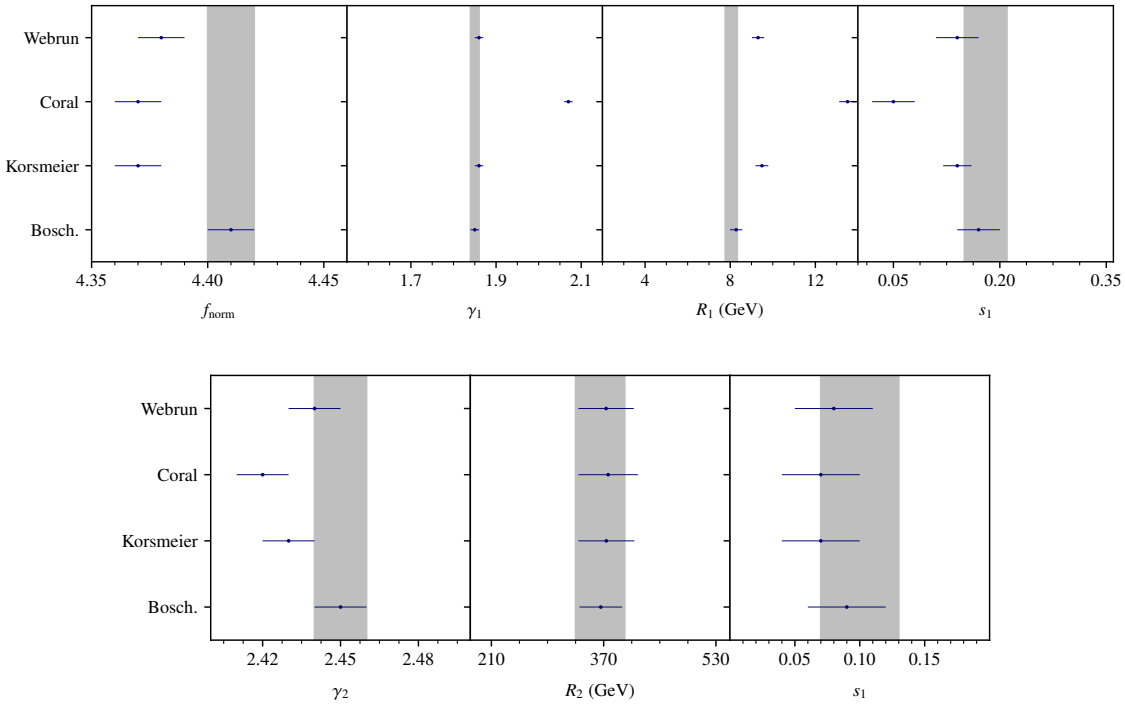

Figure 2.11: Fit results for the proton-injection parameters for different solution and grid parameters obtained from a fit to the AMS-02 proton-flux data [172]. The result of the numerically accurate benchmark model is shown as a grey band.

with $\gamma_{i=0-4}$ being the spectral indices, $R_{i=0-3}$ the rigidities of the spectral breaks, and $s_{i=0-3}$ smoothing parameters for each break. As we expect the positions of the breaks to be similar to the best-fit values in [163], we expect the lowest and highest break position outside of the AMS-02 measurement range and we therefore fix the following parameters additionally beforehand to the best-fit values of [163]: $\gamma_0 = 2.24$, $R_0 = 0.95\,\mathrm{GV}$, $s_0 = 0.29$, $\gamma_3 = 2.19$, $R_3 = 16.0 \times 10^3\,\mathrm{GV}$, $s_3 = 0.09$, and $\gamma_4 = 2.37$. Additionally to the remaining injection parameters, also the flux normalization parameter, f_{norm}, which gives the flux of protons at $E_{\mathrm{kin}} = 1 \times 10^2\,\mathrm{GeV}$ at Sun's location in the galaxy, is treated as a free parameter.

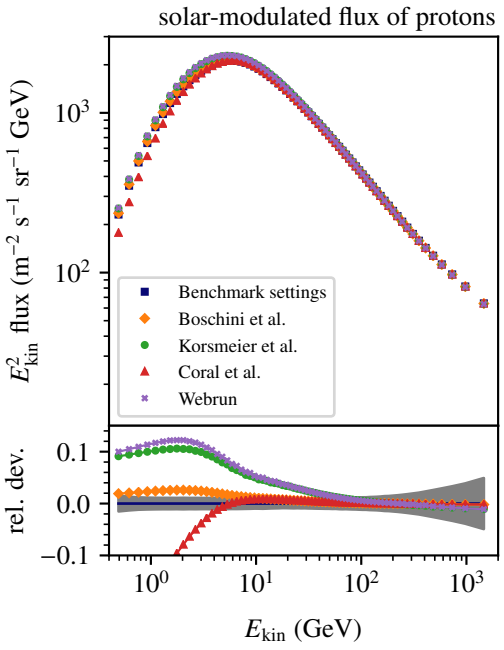

(a) Flux of protons.

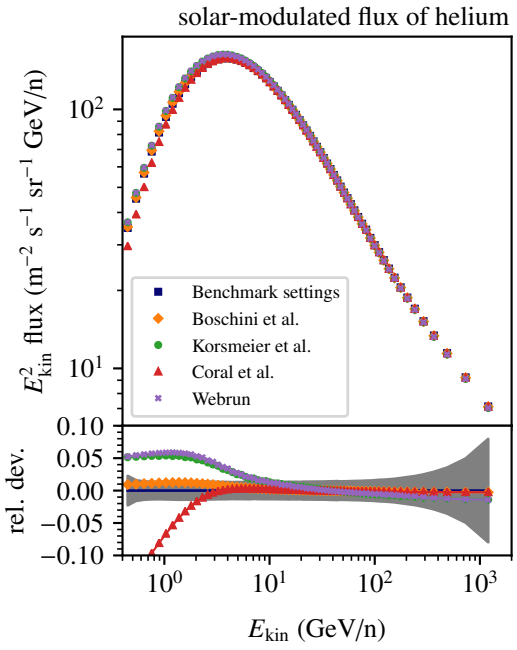

(b) Flux of helium.

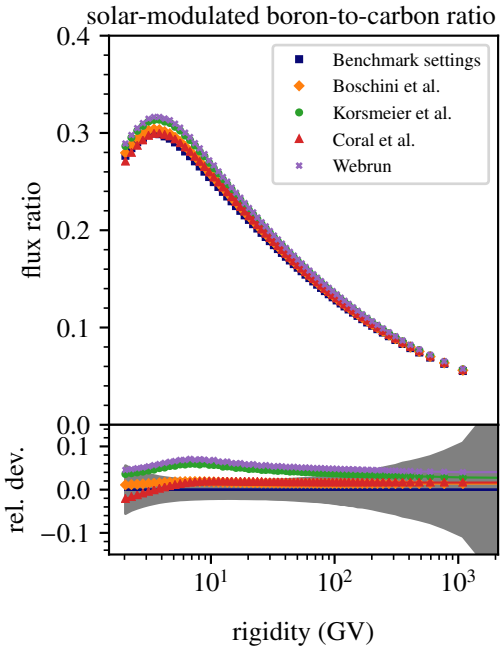

(c) Boron-to-carbon flux ratio. Note that the B/C ratio is shown as a function of rigidity.

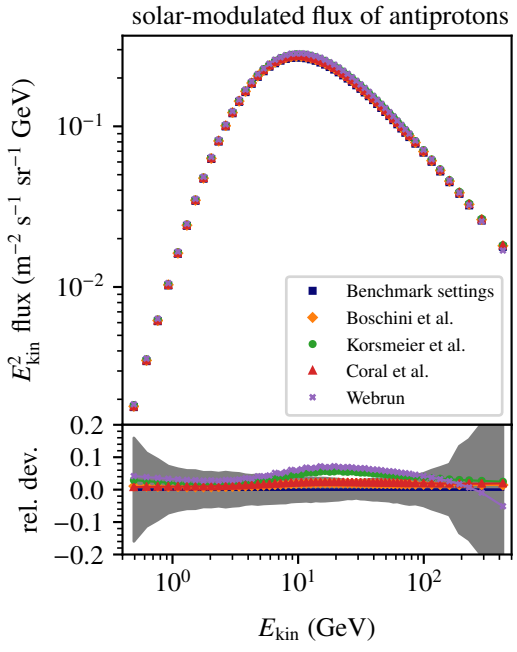

(d) Flux of antiprotons.

Figure 2.12: Resulting local interstellar flux of protons from GALPROP with different settings of the solution and grid parameters used in literature, listed in Table 2.1. For comparison, the relative uncertainties of the AMS-02 measurements are shown [172]. The fluxes are multiplied by E_{kin}^2 to increase the visibility of the deviations.

parameter	prior range	best-fit value				
		Benchmark model	Boschini et al. [157, 163]	Korsmeier et al. [164, 165]	Coral [174]	GALPROP Webrun [175]
$f_{\rm norm}(\times 10^{-9})$	$[4-5]$	4.41 ± 0.01	4.41 ± 0.01	4.37 ± 0.01	4.37 ± 0.01	4.38 ± 0.01
γ_1	$[1.3-2.3]$	1.85 ± 0.01	1.85 ± 0.01	1.86 ± 0.01	2.07 ± 0.01	1.86 ± 0.01
$R_1(\times 10^3)$ MV	$[4-20]$	8.05 ± 0.28	8.28 ± 0.29	9.49 ± 0.30	13.51 ± 0.39	9.31 ± 0.29
s_1	$[0.01-0.3]$	0.18 ± 0.03	0.17 ± 0.03	0.14 ± 0.02	0.05 ± 0.03	0.14 ± 0.03
γ_2	$[2.0-3.0]$	2.45 ± 0.01	2.45 ± 0.01	2.43 ± 0.01	2.42 ± 0.01	2.44 ± 0.01
$R_2(\times 10^3)$ MV	$[200-600]$	365 ± 35	366 ± 31	374 ± 40	376 ± 42	373 ± 39
s_2	$[0.01-0.2]$	0.10 ± 0.03	0.09 ± 0.03	0.07 ± 0.02	0.07 ± 0.03	0.08 ± 0.03

Table 2.2: Prior ranges and obtained best-fit values for the different injection-spectrum parameters for the different grid and solution-method settings in GALPROP.

The free parameters and their prior ranges are summarized in Table 2.2 together with the fit results for the different numerical settings.
We perform the fit using the Bayesian-inference framework ULTRANEST [176]. Given the likelihood, ULTRANEST explores the multidimensional parameter space using the nested-sampling Monte-Carlo algorithm, MLFriends [177, 178], and returns the marginalized posterior-probability distributions for each parameter, the covariance matrix and samples distributed according to the posterior-probability distribution. Additionally it calculates the maximum likelihood found during the fit procedure and the Bayesian evidence that can be used for model comparison [176]. For each call of the likelihood, a numerical evaluation of the proton flux at Sun's location using GALPROP is performed and the resulting flux is solar modulated using the HELMOD model. The corresponding logarithmic likelihood is defined as the sum of the logarithmic likelihood for each data point of the AMS-02 measurement of the proton flux [172], i, and is given as

$$\ln \mathcal{L} = -\frac{1}{2} \sum_i \left(\frac{f_i - \mu_i}{\sigma_i} \right)^2 , \tag{2.8}$$

with f_i being the predicted particle flux from GALPROP for data point, i, and μ_i and σ_i the mean and uncertainty of the measured flux for i. Figure 2.11 shows the marginalized mean values and central-68 % intervals obtained for the parameters for the different fits.
As expected, the injection parameters at low energy are most affected by changes of the solution and grid settings. We find that the systematic deviations of the obtained parameters between the different settings are up to 20-times larger than the fit uncertainties of the parameters stemming from the experimental uncertainties, posing a large systematic bias on the resulting values of the parameters. From our previous investigations of the different effects from the different settings, we can assign most of the deviations to originate from the different energy-grid settings.
The found deviations due to the settings of the grid and solution parameters therefore contribute to the differing parameter values obtained by different studies. The settings used by Boschini et al [163] obtain the most accurate results from the analyzed studies, and in our simplified fitting procedure these settings do not show significant deviations with respect to the numerically accurate solution. However, the computational effort of these settings is already around 10 to 20-times larger compared to the settings employed in the other studies and already requires a large computational effort for the fitting procedure.
For the usage of the propagation model to predict the created secondary antiproton flux for different production models, the numerical accuracy of the settings of Boschini et al. [163] is found to be sufficient, as the deviation of the antiproton flux is found to be smaller than the relative uncertainties of the current antiproton flux measurements. However, with increasing precision of upcoming experiments or longer measurement times of existing experiments, the systematic deviation of the numerical solution might also become a significant source of uncertainty for other particle species as well. Therefore, it is essential for upcoming studies to adapt the solution and grid settings such, that the numerical accuracy is not biasing the intended results.

2.3 A Propagation Model for Galactic Antiprotons

As we have seen, recent propagation models employ not only different parameterizations of the various processes involved in the propagation of cosmic rays, but use also different settings for the numerical solution of the diffusion equation of cosmic-ray transport to obtain the expected particle fluxes at Sun's location in the Milky Way. Although these studies obtain well-matching solar-modulated particle fluxes for the particle types they are fitted to, the modeled local interstellar fluxes and the fluxes of particles not included in the fit might differ.
However, we need to select a propagation scheme to study the influence of the production model of antiprotons on the cosmic-ray antiproton flux in the next chapter. As already discussed in the beginning of this chapter, the scheme by Boschini et al. [163] and Korsmeier et al. [164, 158] are promising models for this task. Although both are in similar good agreement with the experimental data of AMS-02, the models have some distinct features: They use different methods to model the effect of solar-modulation, which leads to different local interstellar particle fluxes at low rigidities to obtain the same modulated flux and to be consistent with AMS-02 measurements. In addition, the injection spectra and some other propagation processes are also parameterized differently. These differences might also lead to a different local interstellar antiproton yield even for an equal production of antiprotons in the galaxy.
The factors that determine the modeled secondary antiproton flux at Earth are the galactic flux of protons and helium at energies above approximately 10 GeV/n, as they are the most abundant projectile particles that create antiprotons in interactions with the interstellar material; the propagation parameters, which determine the amount of material the protons and helium nuclei traverse during their confinement in the galaxy and influence the spectrum of the produced antiprotons during the propagation to Earth; and the antiproton-production cross section. While the latter has to be determined from measurements of antiproton production at accelerator-based experiment, the first two factors are determined by the selection of the propagation model.
The deviation of the local interstellar fluxes of the projectile particles, protons and helium, for the propagation model from Boschini et al. [163] and Korsmeier et al. [164, 158] are shown in Figure 2.13 and represent the spectra of the projectile particles in the galaxy. Although the modeled fluxes coincide for most of the energy range that is covered by the AMS-02 experiment—which we expect as both models are tuned to reproduce the AMS-02 experimental data and coincide equally well—some deviations arise for energies below 10 GeV/n and above 1×10^3 GeV/n. The difference at low energies stems from the different models of solar modulation. As both obtain a coinciding solar-modulated particle flux in agreement with AMS-02 data, the local interstellar particle flux has to compensate differences of the modulation model. The increasing difference for energies above 1×10^3 GeV/n, which is above the energy range covered by AMS-02, stems from the extrapolation of the fitted spectra. As experimental data above the energy range of AMS-02 is less precise, both models are still consistent with data from experiments at higher energies [163, 164]. The model from Boschini et al. yields a higher proton and helium flux for energies above the AMS-02 measurement range than the model by Korsmeier et al..
The differences of the energy spectra of the projectile particles are expected to be visible also in the modeled antiproton spectra. To quantitatively compare the influence of the

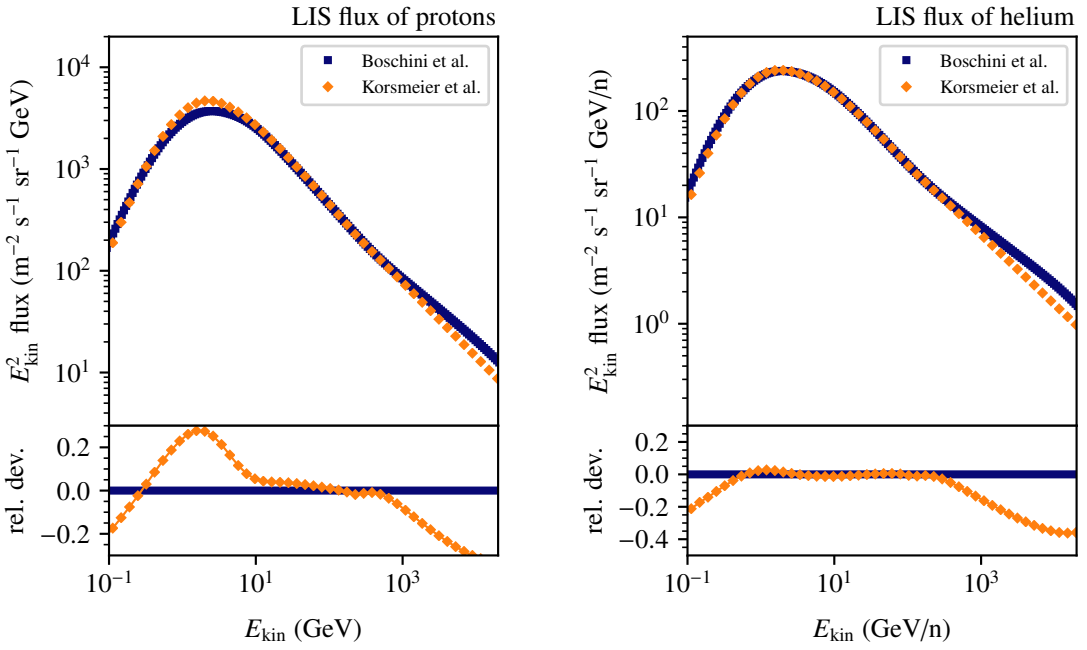

(a) Flux of protons.

(b) Flux of helium.

Figure 2.13: Comparison of the local interstellar flux of protons and helium from the propagation model of Boschini et al. [163] and the model of Korsmeier et al. [164, 158]. The fluxes are multiplied by E^2_{kin} to increase the visibility of the deviations.

different projectile spectra and the different propagation of the created antiprotons, we show the propagated local interstellar antiproton flux for an identical production model of antiprotons by Tan et al. [173] in Figure 2.14. Due to the identical antiproton production cross section used, the obtained difference of the antiproton flux must stem solely from the difference of the projectile spectra and the propagation of the antiprotons. As expected due to the lower proton and helium yield at large energies, the antiproton yield for the propagation model from Korsmeier et al. [164, 158] is lower than the obtained antiproton flux from the model by Boschini et al. [164, 158] at antiproton energies above approximately 1×10^2 GeV/n. At lower energies, the yield obtained by the Korsmeier model, however, exceeds the antiproton flux obtained by the Boschini model by up to 50 %, which stems from a different propagation of the antiprotons in the galaxy.
The extracted difference of the obtained local interstellar antiproton flux for these two state-of-the-art propagation models can be used as a rough estimate of the current model uncertainties of propagation in the galaxy on the flux of cosmic antiprotons. Above around 10 GeV, the model uncertainty is on the order of 25 %; below, even up to 50 %. The much larger deviation at low energy arises from the large uncertainty of the solar-modulation process and hinders a better constrain of the propagation processes in the galaxy for low-energy particles. In order to reduce the model uncertainties in the region of a few GeV, the effect of solar modulation has to be modeled as precisely as possible to resolve any ambiguities.

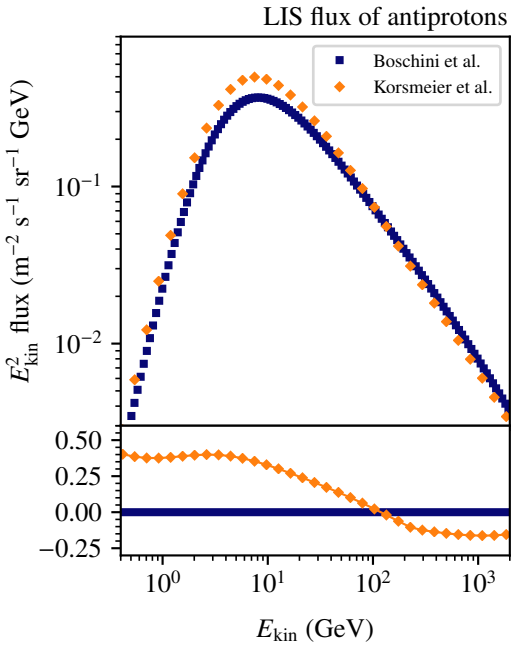

Figure 2.14: Comparison of the local interstellar antiproton flux obtained by the propagation model of Boschini et al. [163] and the the propagation model of Korsmeier et al. [164, 158] with an identical antiproton-production model. Here, exemplarily the model from Tan et al. [173] is used. The fluxes are multiplied by E^2_{kin} to increase the visibility of the deviations.

So far, we have investigated the uncertainty of the propagation model on the modeling of the flux of cosmic antiprotons. In the following chapter, I present the model uncertainty stemming from the antiproton-production model. I discuss the agreement of current antiproton-production models with data from accelerator-based experiments, and I compare the modeled antiproton flux for different production models using an identical propagation scheme. For this task, the introduced propagation scheme from Boschini et al. is used [163], which is not tuned to a specific antiproton-production model. Therefore, the antiproton flux at Earth for this particular propagation model for different choices of the antiproton-production cross section can be predicted and the obtained antiproton flux at Earth can be compared to the measurement of AMS-02.

Chapter 3

Antiprotons from Cosmic-Ray Interactions

In the current standard model of the production of cosmic-rays, antiprotons are believed to be produced solely by interactions of nuclei with interstellar matter. Antiprotons are the antiparticles of protons and hence the lightest antinuclei. They consist of two up antiquarks and one down antiquark as valence quarks and have an electric net charge of $Z = -e$ [21]. Antiprotons undergo the same physical processes as protons and their propagation is very similar. However, due to their conjugate charge they behave differently than protons within the heliosphere (c.f. Section 1.3.1). During the propagation in the galaxy, antiprotons can additionally also annihilate with nuclei of the interstellar matter. In this process, the antiproton is absorbed. The probability for an annihilation process to happen increases inversely with decreasing antiproton velocity and becomes significant for kinetic energies of the antiproton below 300 GeV [21, 179].[1] Experimentally, this inelastic process is well constrained and is included in GALPROP [91].

In the following sections, I describe the production mechanisms for antiprotons in collisions of cosmic-ray particles with the interstellar matter in more detail: first, the underlying inelastic-scattering processes that are driven by the strong interaction and that lead to the emergence of antiprotons. I discuss different models that describe the production rate and spectral distribution of antiprotons in collisions relevant for galactic production of antiprotons. I compare the antiproton production modeled by phenomenological parameterizations and Monte-Carlo event generators and study their agreement with experimental data. The predicted antiproton fluxes by the different models are compared and the uncertainties of the prediction stemming from the limited knowledge of the production cross section are investigated. Based on these results, I estimate the cosmic antiproton flux at Earth and discuss its agreement with the antiproton-flux measurement from AMS-02. I close the chapter by briefly discussing the implications of the found results on the prediction of the flux of heavier cosmic antinuclei, such as antideuterons.

[1] For more details on the annihilation process, I refer the reader to the Master's thesis of the author [180].

3.1 Inclusive Antiproton Production

Because of the composition of cosmic rays and the interstellar matter, the most abundant collisions in our galaxy are proton-proton (p-p), proton-helium (p-He), helium-proton (He-p), and helium-helium (He-He) collisions. In this notation, the first particle name indicates the fast cosmic-ray particle, i.e. the projectile particle, the second particle indicates the particle of the interstellar material, i.e. the target particle, which in the galactic frame is approximately at rest. The above described collision systems contribute to more than 90 % of the antiproton production in the galaxy, as we discuss later in Section 3.4 [181].
Due to baryon-number conservation, antiprotons can be created only if the collision energy is large enough to either directly produce a proton-antiproton pair or to produce some other baryon-antibaryon pair, where the latter then decays into an antiproton [182]. At the collision energies relevant for antiproton production, a nucleus-nucleus collision is dominated by single nucleon-nucleon interactions. In these interactions, the center-of-momentum energy, $\sqrt{s_{NN}}$, hence has to larger than $4m_{\mathrm{p}}$, with m_{p} being the rest mass of the (anti)proton. As the target particle is approximately at rest, the collision has a fixed-target kinematics in the galactic frame, and the minimal kinetic energy per nucleon of the projectile particle has to surpass $E_{\mathrm{kin}} \approx 5.7\,\mathrm{GeV/n}$ to reach the required collision energy.
The inclusive production rate of antiprotons in reactions of the form $\mathrm{A} + \mathrm{B} \rightarrow \overline{\mathrm{p}} + \mathrm{X}$, where A is one of the projectile nuclei, B is one of the target nuclei, and X represents the other produced particles, is given by the inclusive, differential antiproton-production cross section. This cross section quantifies the probability with which antiprotons with a certain three-momentum are produced in an interaction. The differential cross section is independent of the interaction rate and can be related to the antiproton-production rate as

$$\frac{\mathrm{d}\sigma_{\mathrm{A+B}\rightarrow\overline{\mathrm{p}}+\mathrm{X}}}{\mathrm{d}^3 p_{\overline{\mathrm{p}}}} = \frac{1}{\Phi_A} \frac{\mathrm{d}N_{\overline{\mathrm{p}}}}{\mathrm{d}^3 p_{\overline{\mathrm{p}}}\,\mathrm{d}t}, \tag{3.1}$$

with Φ_A being the flux of the incoming projectile particles, $\mathrm{d}N_{\overline{\mathrm{p}}}\,/\,\mathrm{d}t$ the production rate of antiprotons, and $\mathrm{d}^3 p_{\overline{\mathrm{p}}}$ the infinitesimal phase-space-volume element of the produced antiprotons [182]. The inclusive cross section is determined by the underlying physical processes of the collision and is obtained by summing all contributing sub-processes in which the final state of the reaction contains an antiproton.
Independently of whether the antiproton is produced directly in the collision or shortly after, as a decay product of a heavier antibaryon which was produced in the collision, the nucleon-nucleon interaction and the particle production therein is dominated by the strong force and can be described theoretically by quantum chromodynamics (QCD).

QCD is a quantum field theory, in which hadrons consists of quarks that are bound by gluons, which are the force carriers. The fact that the gluons also carry the charges of the strong interaction (color charges), leads to the effect of confinement of particles carrying color charge into hadrons [183]. Neither free quarks nor free gluons are observed in nature. In a simplified picture, the dependence of the potential energy between two opposite color charges and their distance, r, or equivalently on the inverse of the squared 4-momentum

transfer between them, $1/Q^2$, has the form

$$V(r) \propto -\frac{1}{3\pi} g_s^2(r) \frac{1}{r} + kr, \tag{3.2}$$

where the first term is a Coulomb-like term that decreases with distance and corresponds to a one-gluon exchange; the factor g_s is the strong interaction coupling constant, which itself depends on r (resp. on Q^2) and becomes large at large distances (low Q^2) and small for small distances (large Q^2); and the second second term is the confinement term, which increases linearly with distance, with k being the constant of proportionality [67]. This linearly increasing term leads to the confinement of quarks and gluons into hadrons. In the simplest model, the constituent-quark model, hadrons are bound states either of a quark and an antiquark, which are called mesons, or of three quarks which are called baryons.[2] The binding of the quarks is realized by the exchange of soft gluons, meaning gluons with small Q^2 in order to not tear apart the hadron. As in this low-Q^2 regime, which is often referred to as the soft-interaction regime, the strong-coupling constant is large, i.e. $g_s(Q^2) \gg 1$, and the method of perturbation theory cannot be applied to calculate these processes and the resulting binding, called hadronization. So far, no analytical approach has been found to solve the QCD equations in this regime. Therefore, one has to revert to empirical models or numerical simulations to calculate the binding process.
In contrast, hard processes, which are characterized by a large Q^2 between the contributing quarks and gluons can be calculated well by perturbation theory. Such hard scattering processes of quarks and/or gluons—in this regard often referred to as partons—appear often in high-energy hadron-hadron collisions and are followed by soft processes that confine the scattered partons again in color-charge-neutral hadrons.
In the parton model, a nucleon-nucleon interaction is described as a superposition of all possible parton-parton interactions. In this model, hadrons consist of several partons, each carrying a fraction of the hadron's total momentum, $x_{\mathrm{part}} = p_{\mathrm{part}}/p_{\mathrm{had}}$. The cross section of a nucleon-nucleon interaction is then given by factorizing the initial hard interactions and the succeeding soft interactions of hadronization of the outgoing partons into new hadrons, and by summing over all possible hard parton-parton interactions of the participating nucleons. Therefore, the inclusive, differential antiproton-production cross section can be written as

$$\frac{\mathrm{d}\sigma_{\mathrm{A+B}\to\overline{\mathrm{p}}+\mathrm{X}}}{\mathrm{d}^3 p_{\overline{\mathrm{p}}}} = \sum_{a,b,c,d} \int_0^1 \mathrm{d}x_a \int_0^1 \mathrm{d}x_b \, f_A^a(x_a) f_B^b(x_b) \frac{1}{\pi x_c} \frac{\mathrm{d}\sigma_{a+b\to c+d}}{\mathrm{d}\bar{Q}^2} D_{\overline{\mathrm{p}}}^c(x_c), \tag{3.3}$$

with a being the parton from the projectile nucleon and b being the parton of the target nucleon that participate in the hard-scattering process [185]. The produced partons c and d hadronize together with the non-scattered spectator partons into an antiproton and other hadrons. The parton-distribution functions, $f_A^a(x_a)$ and $f_B^b(x_b)$, describe the probability to find a parton with a certain momentum fraction within the hadron. The fragmentation function $D_{\overline{\mathrm{p}}}^c(x_c)$ describes the probability that parton c hadronizes into a

[2] In principle, also states with more quarks that yield a total net color charge of zero, such as pentaquarks, hexaquarks, or heptaquarks, or even pure gluonic states, so called glueballs are allowed by QCD. They are expected to appear only rarely in nature and are not yet all experimentally confirmed [184].

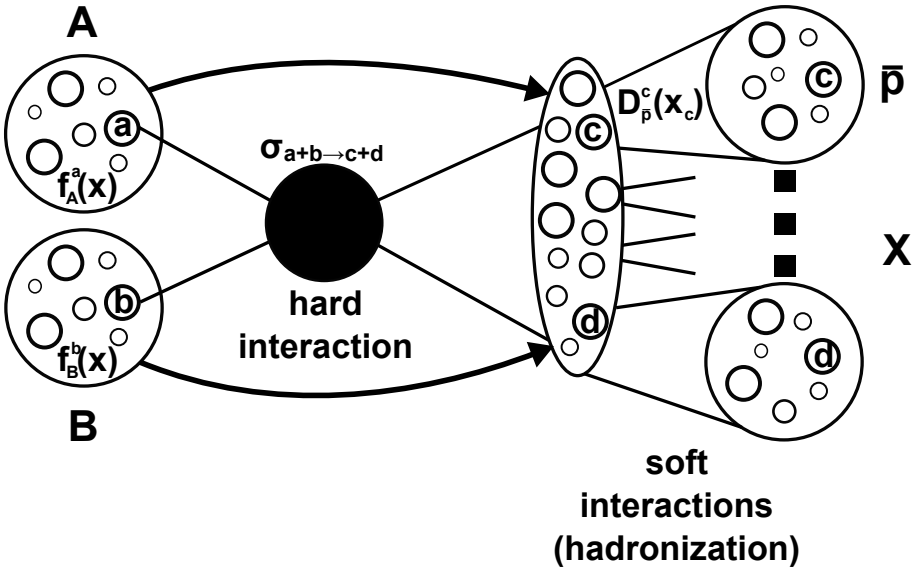

Figure 3.1: Illustrative sketch of the nucleon-nucleon interaction to form an antiproton within the parton model. Time evolves from left to right.

certain hadron, in our case an antiproton. The hard parton-parton interaction to crate the partons c and d from the initial partons a and b is described by the parton-parton cross section $\mathrm{d}\sigma_{a+b\to c+d}\,/\,\mathrm{d}\bar{Q}^2$. Figure 3.1 illustrates the corresponding different parts of the interaction.

The parton-distribution functions are experimentally well constrained by deep inelastic lepton-hadron scattering and can also be extracted from lattice QCD calculations [186, 187]. They also depend on Q^2 of the reaction. This dependence is described by the so-called DGLAP evolution[188].

The fragmentation functions can only be calculated analytically for heavy quarks and are not well constrained for light quarks. Experimentally they can be accessed in single-annihilation processes or semi-inclusive deep inelastic scattering [185]. Fragmentation functions are often calculated based on phenomenological string-fragmentation models, which are tuned to experimental hadron yields [189].

The parton-parton cross sections of the underlying hard process are related to the quantum-mechanical transition amplitudes, A, according to

$$\frac{\mathrm{d}\sigma_{a+b\to c+d}}{\mathrm{d}\bar{Q}^2} = \frac{|A_{a+b\to c+d}|^2}{\hat{s}^2}, \tag{3.4}$$

with $\hat{s}^2$ being the center-of-momentum energy of the parton-parton subsystem [190]. The transition amplitude for such a scattering reaction can be calculated by standard QCD perturbation theory to any given order. The lowest-order processes that contribute to this kind of interaction and the corresponding transition amplitudes can be found in [191, 190]. Although the hard parton-parton collision can be calculated, the complexity of the soft interactions happening during the hadronization of the produced partons prevents us to write down a full analytical expression for the inclusive, differential antiproton-production

cross section, and numerical models or further approximations are required to obtain the cross section.
The most advanced models to calculate production yields of particles from hadron-hadron collisions are Monte Carlo event generators based on the aforementioned string-fragmentation models. The event generators simulate the complete reaction and calculate the different parts of Equation 3.3 numerically, including the underlying hard process, initial and final-state radiative effects, and the hadronization process, on an event-by-event basis.
The most commonly used multi-purpose event generators in high-energy physics today that are based on a string-fragmentation model are the PYTHIA and the EPOS event generators. These models are available already since 1980 and 2006, respectively, and have been upgraded ever since. Today, many different tunes and subversions are available as the event generators are constantly improved and tuned to match newly available data better.
A second, computationally simpler, approach to describe the antiproton-production cross section is to find an empirical parameterization that approximates the antiproton-production cross section well. The functional form of such parameterizations is often based on kinematic characteristics of the underlying hard process and some additional degrees of freedom that shall account for the soft processes. The parameterizations contain several free parameters that are constrained by fitting the antiproton-production model to available experimental measurements of the antiproton production. The parameterization with the obtained best-fit parameters can then be used to inter and extrapolate the antiproton-production cross section to collision energies and phase-space regions where no experimental data is yet available.
In the following, I describe both approaches for modeling the antiproton-production cross section, Monte Carlo event generators and empirical analytical parameterizations: I compare them with current experimental data and use them to estimate the secondary cosmic-ray antiproton flux at Earth. The focus is to compare the results obtained with the different approaches and investigate the production-model dependence of the cosmic-ray antiproton flux.

3.2 Measurements of Antiproton Production

Since the development of particle accelerators that are energetic enough to produce antiprotons in collisions, antiproton-production measurements have been performed at various different collision energies and with different types of colliding particles. The first observation of antiprotons was accomplished in 1955 at the Bevatron in Berkeley in collisions of protons with energies of around 6 GeV and a copper target [192]. Since then, the accelerators, as well as the particle-detector systems, advanced and allow measurements for center-of-momentum energies ranging from the production threshold of antiprotons up to several TeV and for different colliding systems, from proton-proton collisions up to lead-lead collisions. Due to the complexity of the experimental setups, individual experiments often only measure at one collision energy or within a small range of collision energies. Several different experimental setups are required to cover different collision energies.
Commonly, fixed target experiments are used for collision energies up to $\sqrt{s} \approx 20\,\text{GeV}$. In a fixed-target experiment, an accelerated projectile particle hits an at-rest target particle. Due to the Lorentz boost of the produced antiprotons into the flight direction of the

projectile particle, a particle detector placed behind the target covers nearly the complete phase space of the produced antiprotons and allows to study the phase-space distribution of the antiprotons comprehensively. However, to reach higher collision energies, collider experiments are commonly used, in which the projectile and the target particle are accelerated in beams of opposing directions that intersect each other in a certain point to collide the beam particles. The particle detectors that measure the produced particles have to surround the beam pipe. Due to the complex experimental geometry, these detectors are often not sensitive to particles that emerge from the collision in a direction close to the initial directions of the beams. Therefore, experiments at colliders typically cover a smaller fraction of the phase space of the produced antiprotons compared to fixed-target experiments. To nevertheless measure particles that move close to the beamline in collider experiments, often dedicated experiments have to be built that are sensitive to very forward-or backward-produced particles, as for example the BRAHMS experiment at RHIC or the LHCb experiment at the LHC[193, 194].
In addition to different phase-space coverage, different experimental setups also have different efficiencies for antiprotons stemming from different production reactions. As discussed, antiprotons can be either produced directly in the hadronization phase of the collision, or produced later by the decay of heavier antibaryons. Depending on the lifetime of the heavier antibaryons, the decays might be displaced so far from the collision that the antiprotons might not be detectable.
Experimentally the production of antiprotons is therefore discerned into two different classes: Prompt production and production from weakly decaying particles. Antiprotons are termed promptly produced if they are created during the hadronization phase of the collision or are produced by the decay of heavy baryons via the strong force. Typical lifetimes of particles that predominantly decay by the strong force are only on the order of 1×10^{-24} s and in current particle detectors the displacement of the decay from the collision vertex cannot be resolved. The two production processes are indistinguishable.
Antibaryons that decay via the weak force have much longer lifetimes compared to particles that decay via the strong force. Lifetimes of particles that decay by the weak force into antiprotons are on the order of 1×10^{-10} s, except the lifetime of the antineutron, which is much longer, approximately 880 s, and is discussed separately [21]. Depending on the experimental setup, antiprotons from weak decays can be distinguished from prompt antiprotons by their displaced production vertex. While most of the current experiments can use this technique to distinguish the origin of the antiproton, the spatial resolution of older experiments was not sufficient to separate them, and only the cumulative antiproton production could be measured. Antineutrons from the collisions leave all detectors before they decay into antiprotons. Since the antineutron also does not carry electric charge, it is not easily reconstructable. Therefore, measurements of antineutrons are rare, and their contribution to the total antiproton production is experimentally not well accessed and has to be estimated from theoretical models.
As most experiments nowadays can distinguish between prompt antiprotons and antiprotons from weak decays (except for antineutrons), the production models are often also discussed separately and the total antiproton production in the galaxy is given as the sum of both contributions. About 40 % of the antiprotons are created promptly; about 40 % are created from the decay of (promptly produced) antineutrons; and about 20 % are created from other weakly decaying particles, that either decay directly into antiprotons or first

into antineutrons and then into antiprotons [195].
In the following, I describe the investigation of the agreement of current antiproton-production models with experimental data for antiproton production.

3.3 Comparison of Different Antiproton-Production Models

For our study we compare two different event generators based on the PYTHIA model and two different event generators based on the EPOS model with experimental data of antiproton production: PYTHIA-8 (v.8.2.44) with the Monash 2013 tune, which is the most up-to-date version of the PYTHIA model and the most commonly used tune [196]; GiBUU (v.2019), which is based on PYTHIA-6 with an additional transport-model code to describe final-state interactions more precisely, especially for center-of-momentum energies of a few GeV [197]; EPOS-3 (v.3.117), which is a retuned version of EPOS-2 to early LHC data and includes particle flow effects and collective motions mainly relevant for heavy ion collisions [198]; and EPOS-LHC (implemented in CRMC v.1.6.0), which's development was dedicated to describe early LHC data and collisions relevant for high-energy cosmic-ray collisions with the atmosphere and the description of the successive particle shower creation [199, 200].
The analytical parameterizations we compare are from M. Winkler [195] and from Di Mauro et al. [201]. They are two of the most recent parameterizations developed that including the new insights from the LHC for large collision energies. Most parameterizations focus on the prompt production of antiprotons in proton-proton collisions and use scaling relations to include the contribution of weakly decaying particles and from heavier collisions systems [181].
Therefore, we compare the prompt production of antiprotons in proton-proton collisions to selected experimental data within the energy range of available antiproton-production data between $\sqrt{s} = 6.1\,\mathrm{GeV}$ up to $\sqrt{s} = 900\,\mathrm{GeV}$ first.[3] In a second step, we investigate the production of antihyperons—as the most abundant particles that decay via weak decay into antiprotons and antineutrons—and antineutrons to validate the non-prompt antiproton component. In a third step, we investigate the modeling of antiproton production in heavier collision systems, which is important to describe the full antiproton production in the galaxy.

3.3.1 Prompt Production of Antiprotons

Commonly, the momentum-differential antiproton-production cross section for prompt antiprotons is given in a Lorentz-invariant form, depicted as $f_{\bar{\mathrm{p}}}$, to ease comparison between data from collider and fixed-target experiments.[4] The phase-space distribution of the created antiprotons is described by different kinematic variables by most experiments and the

[3] Experimental data above 1 TeV is not relevant for the production of antiprotons that have kinetic energies within the measurement range of AMS-02 and are thus excluded in this study.

[4] To ease readability, I interchange the expression 'Lorentz-invariant momentum-differential production cross section' with 'cross section'.

cross section for the most common kinematic variables can be written as:

$$f_{\overline{\mathrm{p}}} = E\frac{\mathrm{d}^3\sigma}{\mathrm{d}p^3} = \frac{E}{2\pi p^2}\frac{\mathrm{d}^2\sigma}{\mathrm{d}p\,\mathrm{d}\cos\theta} = \frac{E}{2\pi p}\frac{\mathrm{d}^2\sigma}{\mathrm{d}p_\mathrm{l}\,\mathrm{d}p_\mathrm{t}} = \frac{1}{\pi}\frac{\mathrm{d}^2\sigma}{\mathrm{d}y\,\mathrm{d}p_\mathrm{t}} = \frac{E}{\pi\sqrt{s}}\frac{\mathrm{d}^2\sigma}{\mathrm{d}x_\mathrm{F}\,\mathrm{d}p_\mathrm{t}}, \tag{3.5}$$

with E being the energy, p the momentum, θ the angle measured with respect to the beam direction, p_l the longitudinal component of the momentum, p_t the transverse component of the momentum, y the rapidity, and x_F the Feynman scaling variable, $x_\mathrm{F} = 2p_\mathrm{l}/\sqrt{s}$, of the produced antiproton [201]. $\sqrt{s}$ is the center-of-momentum energy of the proton-proton collision. Another parameterization of the phase space of the produced antiprotons, which is often used for phenomenological descriptions of the production mechanism—including the ones we discuss in Section 3.3.1.2—uses p_t together with the radial-scaling variable, x_r, which is defined as

$$x_\mathrm{r} \equiv E/E_\mathrm{max} = \frac{2\sqrt{p_\mathrm{t}^2 + m_\mathrm{p}^2}}{\sqrt{s}}\cosh y, \tag{3.6}$$

with

$$E_\mathrm{max} = \frac{s - 8m_\mathrm{p}^2}{2\sqrt{s}} \tag{3.7}$$

being the kinematically maximum-possible energy of the antiproton in the inclusive reaction and E being the antiproton energy, both measured in the center-of-momentum frame [201].
We compare the antiproton-production cross section obtained by the different production models to experimental data from five different experiments taken at nine different collision energies for proton-proton collisions. The considered datasets are listed in Table 3.1 together with their center-of-momentum energy, whether the datasets include antiprotons from weak decays—so-called feed-down events—or reject them during analysis, and the approximate phase-space coverage of the experimental setups. The phase-space coverage is extracted by the help of one of the event generators that we compare the measurements to in the next section, the EPOS-LHC event generator. We use the event generator to mimic the antiproton production in the corresponding experiment and filter the produced antiprotons according to whether they fall within the stated acceptance region of the experiment. The ratio of the accepted antiprotons to all produced antiprotons gives the phase-space coverage. Auxiliary information on the used datasets is given in Appendix B.1.

3.3.1.1 Prompt Antiprotons from Event Generators

For each event generator we simulate 1×10^7 proton-proton collisions for each collision energy listed in Table 3.1 and select the promptly produced antiprotons to compare with the experimental data. To compare to the experiments that did not distinguish prompt and non-prompt antiprotons, we additionally select all antiprotons from weak decays except from antineutrons, since antineutrons do not decay in the sensitive volume of any of the regarded experiments. The antiproton-production cross section in then calculated in kinematic bins that are equal to the the bins of the experimental data. The cross section is

experiment	$\sqrt{s}$ (GeV)	contribution from antihyperons	phase-space coverage (%)
Dekkers et al. [202]	6.1	included	9.0
	6.7		6.3
NA61 [203]	7.7	excluded	99.6
	8.8		99.3
	12.3		98.8
	17.3		98.0
NA49 [204]	17.3	excluded	98.7
PHENIX [205]	62.4	included[†]	12.3
	200.0		13.5
BRAHMS [206]	200.0	included	0.2
ALICE [207]	900.0	excluded	11.3

Table 3.1: Overview of experimental data for prompt-antiproton production that we use for comparing different antiproton-production models with. [†] Although PHENIX has additionally published feed-down-corrected values, we use the non-corrected data, as the magnitude of the correction is found to be unexpectedly large and is not consistent with any model of the antiproton production from antihyperon decays [195].

calculated from the multiplicity of the antiprotons in the bin and the inelastic cross section given by the event generator for the corresponding collision energy.
In the following, I summarize the findings of the comparison of the prompt-antiproton production modeled by the event generators with the different datasets. A full, and more detailed overview of the obtained cross sections of the event generators and the bin-by-bin deviations to the experimental data are given in Appendix B.2.
Overall, the considered event generators overproduce antiprotons for most collision energies but in particular at low collision energies ($\sqrt{s} \lesssim 20\,\text{GeV}$). The overproduction is more pronounced in the PYTHIA-based generators compared to the EPOS models. Due to the large phase-space coverage at low collision energies by the NA49 and NA61 experiments, it is also visible that the overproduction is not uniform in phase space but increases for most tested generators with transverse and longitudinal momentum of the produced antiproton. A similar trend is found at $\sqrt{s} = 200\,\text{GeV}$ by the comparison of the event generator results with the experimental data from PHENIX and BRAHMS. Especially the EPOS models tend to overproduce antiprotons at forward rapidity stronger than for central rapidity. At $\sqrt{s} = 900\,\text{GeV}$, the overall overproduction of antiprotons with respect to the experimental data seems to vanish.
In order to qualitatively compare the disagreement of the different tested event generators with the different datasets, we define a metric, χ^2, as a measure of the deviation of the

experiment	$\sqrt{s}$ (GeV)	data points	χ^2			
			EPOS-LHC	EPOS3	PYTHIA8	GiBUU
Dekkers et al.	6.3	5	2.5	3.4	174.8	70.6
	6.7	5	0.4	6.9	48.8	18.4
NA61	7.7	41	1.3	4.2	349.2	30.6
	8.8	33	15.3	2.4	510.5	164.0
	12.3	119	11.06	19.1	98.6	92.6
	17.3	126	7.6	53.5	111.9	146.9
NA49	17.3	148	38.7	100.1	1070.3	5727.2
PHENIX	62.4	27	2.6	25.1	9.3	74.65
	200.0	34	2.2	10.9	3.1	24.4
BRAHMS	200.0	33	3.0	5.3	0.9	14.7
ALICE	900.0	24	9.5	32.9	15.7	$-^{\dagger}$

Table 3.2: Results of the event generator comparison to prompt-antiproton-production data.[†] Due to an internal error of GiBUU for collision energies above 200 GeV, no results could be obtained for the dataset at $\sqrt{s} = 900\,\text{GeV}$.

antiproton production by an event generator from the experimental data. For a dataset consisting of n data points,i, the χ^2 for a given event generator, labeled 'gen', is defined as

$$\chi^2_{\text{gen}} \equiv \frac{1}{n} \sum_{\text{i}} \left(\frac{f^{(i)}_{\text{gen}} - f^{(i)}_{\text{data}}}{\sigma^{(i)}_{\text{data}}} \right)^2 , \tag{3.8}$$

with $f^{(i)}_{\text{gen}}$ being the modeled antiproton flux of the kinematic bin, i, by the event generator and $f^{(i)}_{\text{data}}$ and $\sigma^{(i)}_{\text{data}}$ the experimental antiproton cross section and its uncertainty. The so-obtained χ^2 values for the various data sets and the different event generators are listed in Table 3.2. EPOS-LHC shows overall the smallest deviations to experimental data over the whole range of tested collision energies. This is a similar result than what has been obtained by D. Coral, who compared a different set of event generators to experimental antiproton production data but also has found EPOS-LHC to match best [174]. However, the large values of χ^2, even for EPOS-LHC, shows that none of the models can accurately describe the available experimental data of antiproton production. The found overproduction of antiprotons by all tested event generators would lead to an overestimation of the antiproton flux in the galaxy from cosmic-ray collisions, which I discuss in more detail in Section 3.4, when comparing the antiproton source term and the obtained antiproton flux at Earth from EPOS-LHC and PYTHIA-8 with the corresponding values from the tested analytical parameterizations and the experimental data from AMS-02. The model-

ing of prompt-antiproton production using analytical parameterizations is discussed in the following section. In Section 3.3.1.3 I compare the deviations of the prompt production from the event generators to the obtained deviations for the analytical parameterizations to investigate which approach gives a more accurate representation of prompt antiproton production.

3.3.1.2 Fit of Empirical Parameterizations to Prompt-Antiproton Data

The use of analytical parameterizations to approximate the antiproton-production cross section is the most common approach to include antiproton production in propagation codes such as GALPROP.
An analytical parameterization of the prompt-antiproton production requires an mathematically expression of the invariant production cross section of prompt antiprotons, f_0, as a function of the collision energy and two phase-space variables in order to fully describe the antiproton production. Most often f_0 is parametrized as a function of $\sqrt{s}$, p_t, and one of the scaling variables, x_F or x_r, as it was experimentally found in the 1970s that for $\sqrt{s} \gtrsim 10\,\mathrm{GeV}$, the invariant cross section for inclusive hadron production becomes constant with increasing $\sqrt{s}$ [208], meaning that

$$f(x_\mathrm{F}, p_\mathrm{t}, \sqrt{s}) \xrightarrow[\sqrt{s}\gtrsim 10\,\mathrm{GeV}]{} f(x_\mathrm{F}, p_\mathrm{t}), \text{ or equivalently} \tag{3.9a}$$

$$f(x_\mathrm{r}, p_\mathrm{t}, \sqrt{s}) \xrightarrow[\sqrt{s}\gtrsim 10\,\mathrm{GeV}]{} f(x_\mathrm{r}, p_\mathrm{t}). \tag{3.9b}$$

The usage of x_r—implying so-called radial scaling—was found to be advantageous compared to x_F—which implies so-called Feynman scaling—as the scaling limit is reached for lower collision energies and is valid up to larger values of p_t [208]. Within the radial-scaling regime, Kinoshita and Noda have found that the invariant cross section for inclusive production of a certain hadron type has the form

$$f(x_\mathrm{r}, p_\mathrm{t}) \propto (1 - x_\mathrm{r})^\beta F(p_\mathrm{t}), \tag{3.10}$$

with β being a constant and $F(p_\mathrm{t})$ a p_t-dependent function that both have to be determined by experimental data [209]. Based on this approach, Tan and Ng developed an empirical functional form of the antiproton-production cross section by studying antiproton-production data from CERN's Intersecting Storage Rings. They obtained

$$f(x_\mathrm{r}, p_\mathrm{t}) \propto \left[a \exp\left(-b x_\mathrm{r}\right) \Theta\left(0.5 - x_\mathrm{r}\right) + c\left(1 - x_\mathrm{r}\right)^d\right] \exp\left[-\left(e p_\mathrm{t} + f p_\mathrm{t}^2\right)\right], \tag{3.11}$$

with

$$\Theta(U) = \begin{cases} 0, & \text{if } U < 0 \\ 1, & \text{if } U \geq 0 \end{cases} \tag{3.12}$$

and the parameters a to f being free parameters that they constrained by fitting the parameterization to experimentally obtained cross sections [210].
Below $\sqrt{s} = 10\,\mathrm{GeV}$, the scaling limit is not yet reached and the production cross section exceeds the expectation from the radial scaling. This enhancement was also parametrized

by Tan and Ng as a function of $\sqrt{s}$ and x_r in a later study [173].
One consequence of the independence of the inclusive cross section from the collision energy within the radial-scaling limit is that the total inelastic cross section should flatten with increasing collision energy. However, recent experiments, reaching up to $\sqrt{s} = 13\,\mathrm{TeV}$, found that the inelastic cross section further increases with collision energy and such a flattening is not existing [195]. This implies a violation of the radial scaling at large collision energies, starting at around $\sqrt{s} \approx 50\,\mathrm{GeV}$. In addition, found particle multiplicities increase and the p_t spectra change, giving further modifications to the produced particle spectra as expected from radial scaling [195].
Based on the concept of radial scaling and the violation of it at collision energies below $\sqrt{s} \approx 10\,\mathrm{GeV}$ and above $\sqrt{s} \approx 50\,\mathrm{GeV}$, several further empirical parameterizations of the antiproton production cross section have been developed, some of them based on the parametrization from Tan and Ng.
Two of the most recent and commonly used parameterizations are from Di Mauro et al. and Winkler et al. [201, 195]. The parameterization by Di Mauro et al. is an adaption of the parameterization by Tan and Ng and additionally includes an explicit $\sqrt{s}$ dependence of the invariant cross section to account for radial-scaling violation at high collision energies [201]. Di Mauro et al. parameterize the prompt-antiproton production in proton-proton collision as

$$f(\sqrt{s}, x_\mathrm{r}, p_\mathrm{t}) = \sigma_\mathrm{inel}(1 - x_\mathrm{r})^{C_1} \exp\left(-C_2 x_\mathrm{r}\right) \times \left[C_3(\sqrt{s})^{C_4} \exp(-C_5 p_\mathrm{t}) + C_6(\sqrt{s})_7^C \exp\left(-C_8 p_\mathrm{t}^2\right)\right], \quad (3.13)$$

with the free parameters C_1 to C_8 that have to be constrained by a fit to experimental data. The inelastic proton-proton cross section is given as the difference of the total and the elastic cross section, $\sigma_\mathrm{inel} = \sigma_\mathrm{tot} - \sigma_\mathrm{el}$, which are parameterized and fitted to experimental data provided by the PDG, yielding

$$\sigma_\mathrm{tot} = 33.44 + \frac{\pi(\hbar c)^2}{2.06^2} \log^2\left(\frac{s}{(2m_\mathrm{p} + 2.06)^2}\right) + 13.53\left(\frac{(2m_\mathrm{p} + 2.06)^2}{s}\right)^{0.324} - 6.38\left(\frac{(2m_\mathrm{p} + 2.06)^2}{s}\right)^{0.324} \quad (3.14)$$

and

$$\sigma_\mathrm{el} = 144.98 + \frac{\pi(\hbar c)^2}{2.06^2} \log^2\left(\frac{s}{(2m_\mathrm{p} + 2.06)^2}\right) + 2.64\left(\frac{(2m_\mathrm{p} + 2.06)^2}{s}\right)^{1.57} - 137.27\left(\frac{(2m_\mathrm{p} + 2.06)^2}{s}\right)^{-4.65\times10^{-3}}, \quad (3.15)$$

with s being the squared center-of-momentum energy and m_p the mass of the proton [201]. In their most recent work, they fitted the free parameters of their invariant-cross-section

parametrization to experimental data from Dekkers et al., NA49, NA61, and BRAHMS [181].[5] In our study, we refit the parameters of the parameterization by additionally using the experimental data from PHENIX and ALICE to complement the BRAHMS data at high energy, as BRAHMS data is taken at large forward rapidity and accounts only for a very small fraction of the produced antiprotons at $\sqrt{s} = 200\,\mathrm{GeV}$. By adding further experimental data at the same collision energy but covering the central-rapidity region, we add additional information on the rapidity distribution of produced antiprotons at a relative large value of $\sqrt{s}$. This is complementary to the experimental data below $\sqrt{s} = 20\,\mathrm{GeV}$, where the full phase-space is experimental probed by the fixed target experiments NA49 and NA61.
The second parameterization we aim to fit to the described experimental data is from Winkler et al.[195], and it is given as

$$f(\sqrt{s}, x_\mathrm{r}, p_\mathrm{t}) = \sigma_\mathrm{inel} R C_1 (1 - x_\mathrm{r})^{C_2} \left[1 + X \left(\sqrt{p_\mathrm{t}^2 + m_\mathrm{p}^2} - m_\mathrm{p}\right)\right]^{-\frac{1}{XC_7}}, \tag{3.16}$$

with

$$X = C_8 \log^2 \left[\frac{\sqrt{s}}{4 m_\mathrm{p}}\right], \tag{3.17}$$

$$R = \begin{cases} 1, & \text{if } \sqrt{s} \geq 10\,\mathrm{GeV} \\ \left[1 + C_5 \left(10 - \frac{\sqrt{s}}{\mathrm{GeV}}\right)^5\right] \exp\left[C_6 \left(10 - \frac{\sqrt{s}}{\mathrm{GeV}}\right) \left(x_\mathrm{r} - \frac{m_\mathrm{p}}{E_\mathrm{max}}\right)^2\right], & \text{if } \sqrt{s} < 10\,\mathrm{GeV} \end{cases}, \tag{3.18}$$

and

$$\sigma_\mathrm{inel} = 30.9 + -1.74 \log \sqrt{s} + 0.71 \log^2 \sqrt{s}. \tag{3.19}$$

The parameterization has in total six free parameters, C_1 to C_6, and describes the radial-scaling violation at low collision energies by an enhancement factor, R, similar as in the extended parameterization from Tan and Ng in 1983 [173]. At high energies, the exponential p_t distribution passes over to a so-called Tsallis distribution, as it is expected from statistical models of particle production [211].
In addition to the original parameterization by Winkler et al., we aim to test in addition an modified version of this parameterization, which we term 'adapted Winkler parameterization' in the following. The parameterization remains the same as in the original parameterization by Winkler et al. beside of the substitution of

$$(1 - x_\mathrm{r})^{C_2} \rightarrow (1 - x_\mathrm{r})^{C_2 \left(1 + C_7 \log^2 \frac{\sqrt{s}}{4 m_\mathrm{p}}\right)} \tag{3.20}$$

in Equation 3.16. By this we add a $\sqrt{s}$-dependent degree-of-freedom to the x_r distribution of the produced antiprotons. This is motivated by the effect described by Ostapchenko et al., who argued that for large collision energies multiple-scattering of the final-state

[5] The used dataset for NA61 included only positive rapidity and the BRAHMS dataset included only the data points for $2.9 < y < 3.1$ (M. Korsmeier, priv. comm.).

partons suppresses the production of particles at large x_r [212]. The chosen functional form, however, is so-far purely artificial and not physically motivated. Nevertheless, such an additional degree-of-freedom increases the agreement of the parameterization with the experimental data from PHENIX, BRAHMS, and ALICE, as we will see when comparing the fit results of the different models to the experimental data.

For our fits of the parameterizations to the experimental data of Dekkers et al., NA61, NA49, PHENIX, BRAHMS, and ALICE, we use a likelihood-based fitting method. We define the total logarithmic likelihood, $\log\mathcal{L}$, as the sum of the logarithmic likelihoods of each data point, i, of each dataset, j, as

$$\log\mathcal{L}\left(\vec{D}|\vec{\lambda},M\right) \equiv \sum_j \sum_i \log\mathcal{L}_{j,i}\left(D_{j,i}|\lambda,M\right), \tag{3.21}$$

with $D_{j,i}$ being the i-th datapoint of dataset j, and $\vec{\lambda}$ the fit parameters of the investigated parameterization, M. The likelihood for each individual datapoint is defined as

$$\log\mathcal{L}_{j,i}\left(D_{j,i}|\lambda,M\right) \equiv -\frac{1}{2}\left(\frac{f^M_{j,i}(\vec{\lambda}) - f^D_{j,i}}{\sigma^D_{j,i}}\right)^2, \tag{3.22}$$

with $f^M_{j,i}$ being the predicted invariant cross section for datapoint i in dataset j by parameterization M with parameters $\vec{\lambda}$; $f^D_{j,i}$ the measured invariant cross section for i in j; and $\sigma^D_{j,i}$ the corresponding experimental uncertainty. For the datasets of NA61 and ALICE, in which only the invariant multiplicity—instead of the invariant cross section—was measured, $f^M_{j,i}(\vec{\lambda})$ is divided by the inelastic cross section predicted by M. For the Dekkers, PHENIX, and BRAHMS datasets, we removed the feed-down contribution from antihyperon decays by using the approach from Winkler et al.[195], which I describe in Section 3.3.2.

As the parameterizations describe the invariant cross section as a function of x_r and p_t, we transform the experimental data for the likelihood calculation also into the x_r-p_t space. The center value of each bin of the experimental data is transformed and the measured invariant cross section is assigned to the transformed center value. This implies that we approximate the experimental data as a point estimate instead of explicitly averaging the parameterizations over the complete experimental bin. To verify that this procedure does not induce unwanted systematic errors, we have performed the fit for one parameterization with both approaches: One with the point estimate, and one where we explicitly integrate the antiproton production over the whole experimental bin. As we have found no statistically significant deviation between both, we have concluded to use the computationally much faster approach of the point estimate.

In addition to the experimental uncertainties that are assigned to each individual data point, each experiment suffers from an systematic uncertainty that systematically scales each datapoint of the experiment equally. This uncertainty is often referred to as the normalization uncertainty and stems from uncertainties of the luminosity measurement, the overall trigger efficiency, or other experimental effects that change the relative yield at

each datapoint equally [88]. The assumed magnitude of this uncertainty for the different datasets are 10 % for the dataset from Dekkers et al., 5 % for NA61, 6.5 % for NA49, 10 % for PHENIX, 10 % for BRAHMS, and 3.6 % for ALICE [202, 203, 204, 205, 206, 207, 88]. We also assume this uncertainty to be identical for datasets measured by the same experiment but at different collision energies.
To account for this uncertainty in the fit, we use one nuisance parameter for each experiment that scales the measured antiproton-production cross section for all datapoints of the datasets of the corresponding experiment by this parameter. The prior-probability distributions of the nuisance parameters are normal distributions centered at one with standard deviations equal to the normalization uncertainty of the corresponding experiment. The posterior-probability distribution of these parameters additionally serves as a qualitative measure of whether a certain dataset can be well described by the parameterization or if the model systematically over or underproduces antiprotons with respect to the data. The larger the shift of the posterior-probability distribution from the prior-probability distribution, the larger the systematic deviations. Shifts to larger values indicate an overproduction of antiprotons and a shift to smaller values an underproduction of antiprotons by the parameterization with respect to the experimental dataset.
To explore the parameter space for each model and to find the most-probable parameter configuration, we employ a Bayesian formulation of probability and use a Markov-Chain-Monte-Carlo-based method (MCMC-based method) implemented by the Bayesian Analysis Toolkit [213, 214, 215]. By this, we explore the posterior-probability distribution, $\log P\left(\vec{\lambda}|\vec{D};M\right)$, which is related to the logarithmic likelihood, $\log\mathcal{L}$, and the logarithmic prior probability, $\log P_0$, as

$$\log P\left(\vec{\lambda}|\vec{D};M\right) \propto \log\mathcal{L}\left(\vec{D}|\vec{\lambda};M\right) + \log P_0\left(\vec{\lambda}|M\right). \tag{3.23}$$

The prior probability is determined by the values of the normalization parameters alone, as the free parameters of the parameterization have a constant probability over their complete range of values since we imply no prior information on them. The set of parameters which belongs to the maximum $\log P$ value of the posterior-probability distribution is termed as the best-fit point and gives the most-probable parameter configuration for the parameterization and the data it is fitted to. Beside the best-fit point, the MCMC method allows to extract the correlation matrix of the parameters as well as the marginalized posterior-probability distributions for all parameters.

The found maximum probability and the corresponding best-fit parameters for the three different models obtained by the MCMC fit method are listed in Table 3.3. We additionally give the obtained correlation matrices for the fit parameters and a detailed comparison of the fit results with the individual datasets—which is also summarized in the following—in Appendix B.3.
To investigate the agreement of the fitted parameterizations with the experimental data and to compare them to the results obtained by the event generators, we calculate a χ^2 for the best-fit configurations similar as in Section 3.3.1.1 for each model to qualitatively compare the disagreement of the different models with the experimental datasets in Table 3.3. In addition to the χ^2 values of the best-fit parameters of the parameterizations, we also show the χ^2 values obtained for the parameters of the parameterizations from the origi-

	Korsmeier param.	Winkler param.	adapted Winkler param.
C_1	1.837 ± 0.548	$(4.230 \pm 0.132) \times 10^{-2}$	$(4.783 \pm 0.134) \times 10^{-2}$
C_2	7.808 ± 0.718	8.081 ± 0.071	7.498 ± 0.080
C_3	$(3.657 \pm 0.650) \times 10^{-3}$	$(1.578 \pm 0.010) \times 10^{-1}$	$(1.590 \pm 0.010) \times 10^{-1}$
C_4	$(4.171 \pm 0.290) \times 10^{-1}$	$(4.170 \pm 0.085) \times 10^{-2}$	$(4.341 \pm 0.086) \times 10^{-2}$
C_5	2.74 ± 0.026	$(1.405 \pm 0.380) \times 10^{-3}$	$(3.020 \pm 2.347) \times 10^{-4}$
C_6	$(2.793 \pm 0.136) \times 10^{-2}$	5.681 ± 0.641	3.790 ± 0.756
C_7	0.000 ± 0.001	–	$(3.188 \pm 0.290) \times 10^{-2}$
C_8	2.635 ± 0.024	–	–
n_{Dekkers}	0.663 ± 0.060	1.113 ± 0.094	1.070 ± 0.089
n_{NA61}	0.662 ± 0.029	0.877 ± 0.027	1.035 ± 0.030
n_{NA49}	0.645 ± 0.028	0.852 ± 0.025	0.976 ± 0.027
n_{PHENIX}	1.097 ± 0.041	1.082 ± 0.036	1.222 ± 0.038
n_{BRAHMS}	1.828 ± 0.064	1.915 ± 0.061	1.190 ± 0.072
n_{ALICE}	1.005 ± 0.03	0.800 ± 0.02	0.905 ± 0.025
$\max \log P$	-602.9	-506.2	-412.5

Table 3.3: Best-fit points for the fit of the parameterizations to the experimental data. The uncertainties give the 68 % confidence interval for the parameters of the best-fit point.

nal studies by Winkler et al. and Di Mauro et al., which were constrained by different fit methods and a different set of experimental data [181, 195]. When comparing the χ^2 values obtained by our refit and the original parameters, deviations for some datasets increase while the deviations for other datasets decrease. These large changes hint to systematic deviations of the underlying production cross-section and its dependence on the kinematic variables and the experimental data. Especially the simultaneous description of the two datasets at $\sqrt{s} = 200\,\text{GeV}$ with different covered rapidities from PHENIX and BRAHMS seem to be described inaccurately.

As discussed we can also use the shifts of the normalization parameters to identify potential inaccuracies of the antiproton production of our parameterizations. In order to describe the measured data, most of the normalization parameters obtain values that are unnaturally far away from one. This can be seen in the comparison of the prior-probability distribution and the posterior-probability distributions of the normalization parameters in Figure 3.2. While for the datasets with $\sqrt{s} \leq 17.3\,\text{GeV}$ the parameterizations tend to underproduce antiprotons, they tend to overproduce antiprotons for larger collision energies. Especially the dataset from BRAHMS, which exclusively covers a non-central-rapidity region at such large $\sqrt{s}$, overproduces antiprotons significantly. This issue could be related to the fact that both parameterizations imply a x_r dependence that is identical for all collision energies. Due to the full phase space coverage of the fixed-target experiments for $\sqrt{s} \leq 17.3\,\text{GeV}$, the parameters are mainly tuned to describe the x_r dependence for

experiment	$\sqrt{s}$ (GeV)	χ^2				
		Di Mauro et al. (orig. param.)	Winkler (orig. param.)	Di Mauro et al. (refitted)	Winkler (refitted)	adapted Winkler
Dekkers et al.	6.3	3.3	3.5	5.9	2.3	2.6
	6.7	10.4	11.8	18.8	9.4	9.0
NA61	7.7	1.82	1.83	7.0	3.3	1.5
	8.8	2.9	2.4	6.5	1.6	2.8
	12.3	2.3	2.6	10.1	3.4	2.0
	17.3	3.1	3.0	22.2	6.2	2.5
NA49	17.3	7.6	3.4	106.9	24.2	2.2
PHENIX	62.4	14.3	23.6	2.2	4.5	7.4
	200.0	37.8	28.0	4.4	1.4	6.1
BRAHMS	200.0	1.6	141.0	26.7	33.8	2.2
ALICE	900.0	38.2	2.7	4.8	10.5	3.8

Table 3.4: Disagreement of the antiproton-production of the parameterizations with their best-fit parameters for the different fitted datasets. In addition, the obtained χ^2 values for the original parameters of the parameterization of Di Mauro et al. and Winkler are given.

low collision energies. At larger $\sqrt{s}$, each experiment covers only a very narrow rapidity region and the probed x_r region is limited. However, when using PHENIX and BRAHMS data, we cover three different rapidity regions at a constant $\sqrt{s}$, covering a larger x_r region requiring a good description of the x_r-dependence of the antiproton production at this collision energy. The disagreement of the models with the data, however, seems to indicate that the x_r-dependence at this large collision energy is in tension with the x_r-dependence at lower collision energies. To probe this assumption, we adapt the Winkler parameterization as given in Equation 3.20 and fit it also to the experimental data. As can be seen by the obtained results, this additional degree of freedom for the x_r-dependence of the antiproton production decreases the overall deviation of the antiproton production by the parameterization to the experimental data significantly. This supports our assumption of a collision-energy dependent x_r—or equivalently x_F—distribution.

3.3.1.3 Comparison of the Prompt-Production Models

In comparison to the event-generator models, however, the deviations of the parameterizations from the experimental data are generally smaller. To visually compare the magnitudes of the deviations of the different production models and the dependency on the collision energy, Figure 3.3 shows the χ^2 values for all tested models for each collision energy.

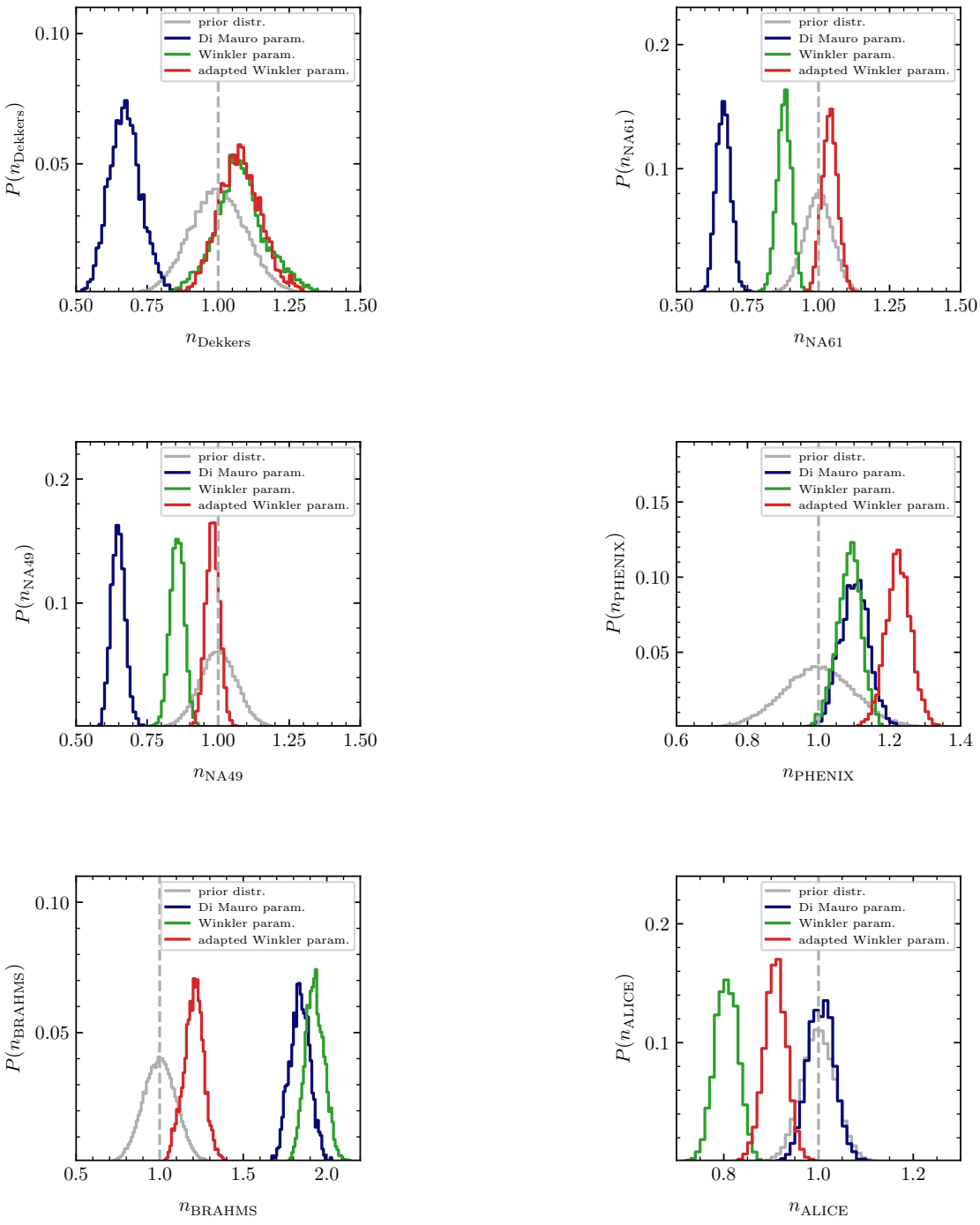

Figure 3.2: Posterior-probability distributions of the normalization parameters for the different experiments for the different parameterizations. In gray the corresponding prior-probability distributions are shown.

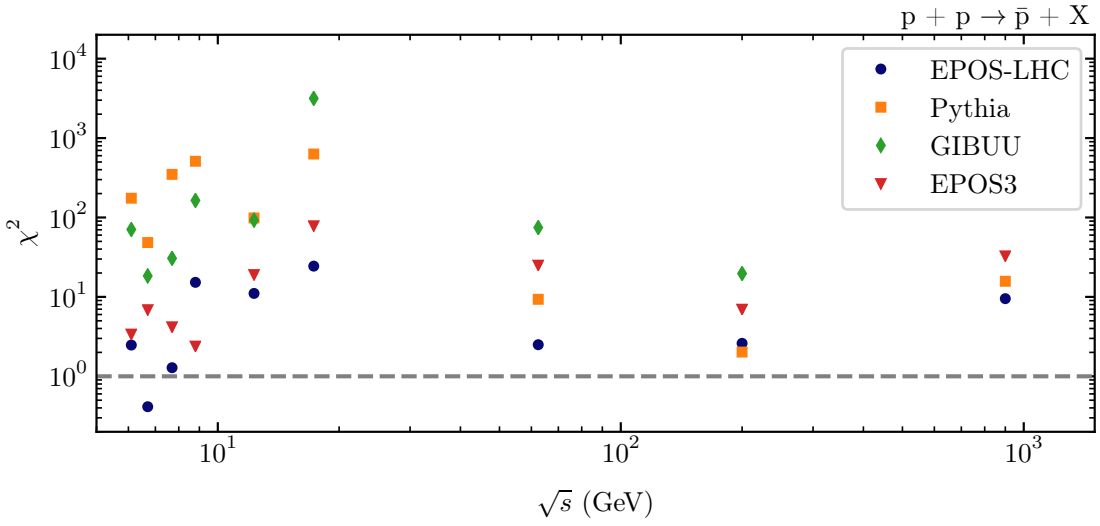

(a) χ^2 values for the event-generator-based models.

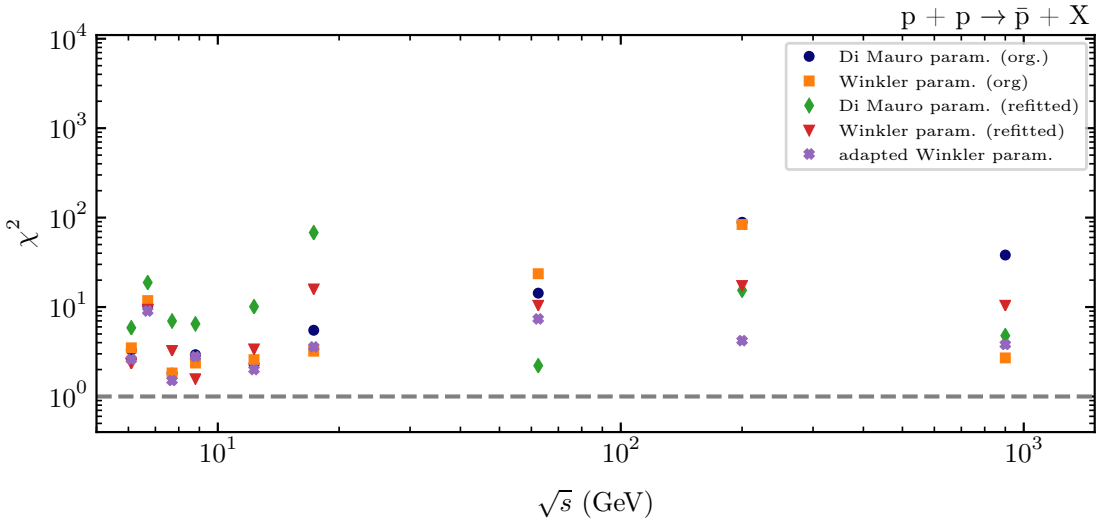

(b) χ^2 values for the analytical parameterizations.

Figure 3.3: Obtained χ^2 values of the comparison of the different production models as a function of the collision energy.

It is visible that the event generators have particular issues to describe the data for low collision energies. This is mainly due to the tuning of most of the current models to collisions at higher energies, mainly LHC data. Although the analytical parameterizations have in total a smaller deviation, the spread of the χ^2 values and the shifts of the normalization parameters indicate that they also cannot describe all datasets simultaneously well. Even for the best tested model, the adapted Winkler parameterization, the found deviations are still on the order of 20 % in some regions of phase space at some collision energies and the

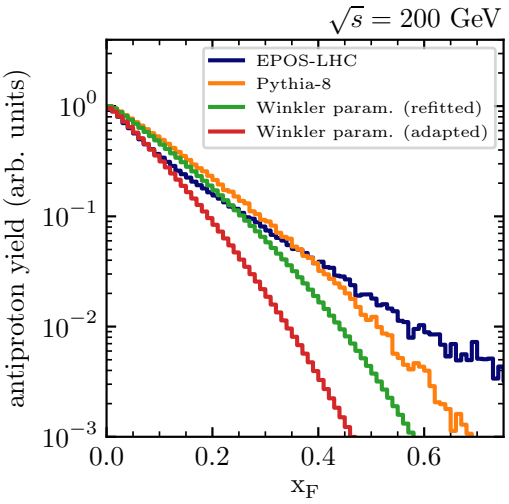

Figure 3.4: Comparison of the shape of the x_F distribution of produced antiprotons at $\sqrt{s} = 200\,\text{GeV}$ for different models of the antiproton production.

found χ^2 values show statistical significant deviations from the data.
A direct interpretation of the impact of the found deviations on the produced antiproton flux is however complicated. Most datasets measure the antiproton production in many bins of p_t. However, due to the strong decrease of the production cross section with increasing p_t, the importance of the datapoints for larger p_t for the produced antiproton momentum spectrum in the galaxy is small. More important is the rapidity distribution—or equivalently the x_r or x_F distribution—as it determines the momentum spectrum of the produced antiprotons. Unfortunately, at large collision energies only sparse data for different rapidity regions is available and the distributions have to be extrapolated by models from measurements at lower collision energies, mostly below $\sqrt{s} \approx 17.4\,\text{GeV}$. This leads to very different particle spectra at high energies for the different production models. To visualize this differences, we exemplarily show the normalized x_F distribution of antiprotons at $\sqrt{s} = 200\,\text{GeV}$, for some of the tested models. The steeper the distribution decreases with x_F, the less antiprotons with large total momentum are produced, and the the flux of cosmic ray antiprotons at large energies is reduced. More explicit studies and more experimental data is required to constrain the total-momentum distributions of antiprotons in collisions, especially for $\sqrt{s} \geq 20\,\text{GeV}$.
Beside the prompt production of antiprotons, also weakly decaying particles, namely antihyperons and antineutrons, significantly contribute to the galactic antiproton flux. In the following, I discuss their production and their decay into antiprotons and how well the different available models describe these processes.

3.3.2 Antiprotons from Antihyperon Decays

The contribution of antiprotons from weak decays is dominated by decaying antihyperons and antineutrons. The contribution from decaying antihyperons depends on the production

rate of the antihyperons in the collisions and the branching fraction into antiprotons in their decay. The most abundant antihyperons produced in collisions contain only a single strange antiquark [21]. The contribution from antihyperons that contain two or more strange antiquarks or other baryons containing heavier antiquarks that decay directly into antiprotons are small, as most of these heavier states first decay back into an antihyperon with a single strange antiquark before decaying into an antiproton. The two lightest antihyperons which contribute most to the antiproton production are the charge-neutral antilambda hyperon, $\bar{\Lambda}$, and the negatively charged antisigma hyperon, $\bar{\Sigma}^-$, with masses of $m_{\bar{\Lambda}^0} = 1.116\,\mathrm{GeV}$ and $m_{\bar{\Sigma}^-} = 1.189\,\mathrm{GeV}$, respectively [21, 195]. The branching ratios of lambda hyperons and sigma hyperons have been measured precisely, and assuming their antiparticles to decay similarly as expected from CP invariance[6], the dominant decays and branching fractions of $\bar{\Lambda}$ and $\bar{\Sigma}^-$ into antiprotons, as given by the PDG [21], are

$$\bar{\Lambda} \to \bar{\mathrm{p}} + \pi^+ \qquad (63.9 \pm 0.5)\% \text{and} \tag{3.24a}$$

$$\bar{\Sigma}^- \to \bar{\mathrm{p}} + \pi^0 \qquad (51.57 \pm 0.30)\%. \tag{3.24b}$$

As both antihyperons almost exclusively decay into antiprotons via a two-body decay, the momentum distribution of the produced antiprotons is determined by the momentum distributions of the respective mother particles.
While for $\bar{\Lambda}$ measurements at many different collision energies and for different colliding systems exist, no data is available for $\bar{\Sigma}^-$ production in (for us relevant) collisions. Therefore, in many models the momentum distribution of produced $\bar{\Sigma}^-$ particles is assumed to be identical to the momentum distribution of produced $\bar{\Lambda}$ particles and their yield, $f_{\bar{\Sigma}^-}$, can be estimated from the $\bar{\Lambda}$-to-Λ ratio following symmetry arguments as

$$f_{\bar{\Sigma}^-} = 0.8 \frac{f_{\bar{\Lambda}}}{f_{\Lambda}} f_{\Sigma^+}, \tag{3.25}$$

with f_{Σ^+} being the production cross section of Σ^+, for which experimental data are available, for example from NA49 [217, 218]. A summary of measurements of the yield of $\bar{\Lambda}$ particles relative to prompt antiprotons has been given by M. Winkler together with an empirical function to describe the collision-energy dependence of the yield ratio [195]. The ratio was found to be fairly constant for collisions with center-of-momentum energies between the antihyperon production threshold and $\sqrt{s} \approx 50\,\mathrm{GeV}$ and above $\sqrt{s} \approx 400\,\mathrm{GeV}$. In between, the ratio of $\bar{\Lambda}$ to prompt antiprotons rises from approximately 0.3 to 0.6. Winkler parametrized the dependency of the yield on the collision energy as

$$\frac{f_{\bar{\Lambda}}}{f_{\bar{\mathrm{p}}}}(\sqrt{s}) = c_1 + \frac{c_2}{1 + \left(c_3/\sqrt{s}^2\right)^{c_4}}, \tag{3.26}$$

[6] Although the weak force does ab-initio not provide CP symmetry, CP-violation is assumed to be very small for light baryons and is not yet experimentally detected. Experimentally, a possible CP asymmetry between the decay of the Λ and $\bar{\Lambda}$ has been investigated e.g. by Ireland et al. [216], and the symmetry is confirmed within a percent precision [21].

with his obtained best-fit parameters $c_1 = 0.31$, $c_2 = 0.30$, $c_3 = (146\,\mathrm{GeV})^2$, and $c_4 = 0.9$ [195]. This parameterization of the contribution to the antiproton production from the decay of $\bar{\Lambda}$ is also used in the recent study by Korsmeier et al. [181].
Driven by experimental data from the NA49 collaboration, the momentum distribution of antiprotons from decayed $\bar{\Lambda}$ particles in proton-proton collisions is often assumed to be identical to the momentum distribution of prompt antiprotons [217]. At larger collision energies, however, this assumption is still unproven. Naïvely, in hadron collisions at large energies it is expected that the phase-space distributions of produced hadrons follow the Tsallis thermodynamics, and their momentum spectra depend solely on the characteristics of the hot fireball created during the initial phase of the collision and do not depend on the quark content of the produced hadrons [211].[7] The resulting hadron spectra are very similar to each other and only differ slightly due to the different masses of the particles. As the mass difference between the two antihyperons and the antiproton is small, their spectra are expected to be very similar. Experimentally this can be tested, for example at $\sqrt{s} = 200\,\mathrm{GeV}$, by comparing the p_t spectrum of prompt antiprotons at central rapidity from the PHENIX experiment with the corresponding spectrum for $\bar{\Lambda}$ measured by STAR [205, 219]. Both spectra normalized to one for $p_\mathrm{t} = 0.36\,\mathrm{GeV}$ are shown in Figure 3.5a, together with a prediction of the antiproton spectrum after the $\bar{\Lambda}$ decay. For the calculation of the antiproton spectrum from the $\bar{\Lambda}$ spectrum we employ two different techniques: The spectrum labeled '(calc)', uses a simple mass-scaling of the production cross section following the approach from Winkler et al. for the NA49 data [217]. The calculation of the transverse momentum and the invariant production cross section for the antiprotons from the $\bar{\Lambda}$ decay is performed bin-by-bin and is given as

$$f_{\bar{\mathrm{p}}}(p_{\mathrm{t},\bar{\mathrm{p}}}, y = 0) = f_{\bar{\Lambda}}(p_{\mathrm{t},\bar{\Lambda}}, y = 0) \left(\frac{m_{\bar{\Lambda}}}{m_{\bar{\mathrm{p}}}}\right)^2, \tag{3.27}$$

with

$$p_{\mathrm{t},\bar{\mathrm{p}}} = p_{\mathrm{t},\bar{\Lambda}} \frac{m_{\bar{\mathrm{p}}}}{m_{\bar{\Lambda}}}. \tag{3.28}$$

As a second method, labeled '(gen)', we use a Monte-Carlo simulation of the decay kinematics. The decay of the $\bar{\Lambda}$ particle is modeled in its center-of-momentum frame using a dedicated computer code that models the phase-space distribution of the outgoing particles in the decay, which is integrated in the so-called TGenPhaseSpace class of the high-energy physics analysis toolkit ROOT [220, 221]. The momentum of the produced antiproton is subsequently Lorentz-transformed into the initial proton-proton center-of-momentum frame and is counted if the particle falls into the acceptance region of the experiment. In comparison to the first method, this approach incorporates the relativistic effects from the boost of the $\bar{\Lambda}$. However, as can be seen in Figure 3.5a, the difference between the obtained spectra from both methods is small.
The p_t spectrum of antiprotons from $\bar{\Lambda}$ decay is found to be slightly harder than the spectrum of prompt antiprotons. However, we have to note that the experimental data of prompt antiprotons and $\bar{\Lambda}$ stem from different experiments and the result could be affected by systematic uncertainties.

[7] When assuming the collision energy much larger than the individual hadron and quark masses.

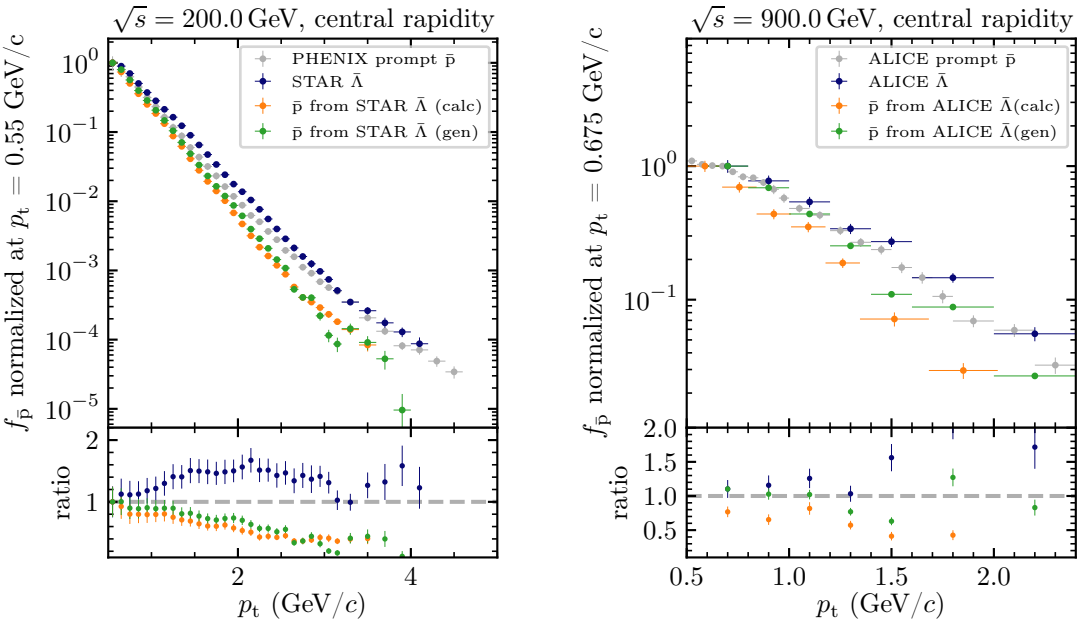

(a) Spectrum of prompt antiprotons measured by PHENIX [205]. Spectrum of $\bar{\Lambda}$ by STAR [219].

(b) Spectrum of prompt antiprotons and $\bar{\Lambda}$ measured by ALICE [207, 222].

Figure 3.5: Experimental data of prompt antiproton production and $\bar{\Lambda}$ production, together with modeled antiprotons from the decayed $\bar{\Lambda}$ for $\sqrt{s} = 200\,\text{GeV}$ and $\sqrt{s} = 900\,\text{GeV}$. The antiproton spectra from the decaying $\bar{\Lambda}$ particles are obtained by using a simple mass-scaling relation, labeled (calc), and a Monte-Carlo based approach, labeled (gen).

We perform the same analysis at an even higher collision energy of $\sqrt{s} = 900\,\text{GeV}$ using experimental data from proton-proton collisions by the ALICE experiment. ALICE measured the transverse-momentum spectrum of prompt antiprotons as well as of $\bar{\Lambda}$ [207, 222]. Both, together with the prediction from the decay models, are shown in Figure 3.5b. Unfortunately, due to the limited precision of the $\bar{\Lambda}$ measurement, no conclusive statement on a possible spectral difference between prompt antiprotons and antiprotons from weak antihyperon decays can be made and more precise data is desirable.

To test the agreement of the antihyperon production by the event generators with experimental data, we compare the production of antilambda particles. We investigate the production rate relative to prompt antiprotons, the spectral distribution, and the branching ratio into antiprotons implemented in the event generators. We restrict the comparison to the EPOS-LHC model, as it exhibits the smallest deviations of the prompt-antiproton production over the whole range of collision energies, and PYTHIA-8, as it is the most recent PYTHIA-model based generator.
The branching ratios of the $\bar{\Lambda}$ decaying into an antiproton are extracted from the source code of the generators and yield 64.2 % in EPOS-LHC and 63.9 % in PYTHIA-8, both in

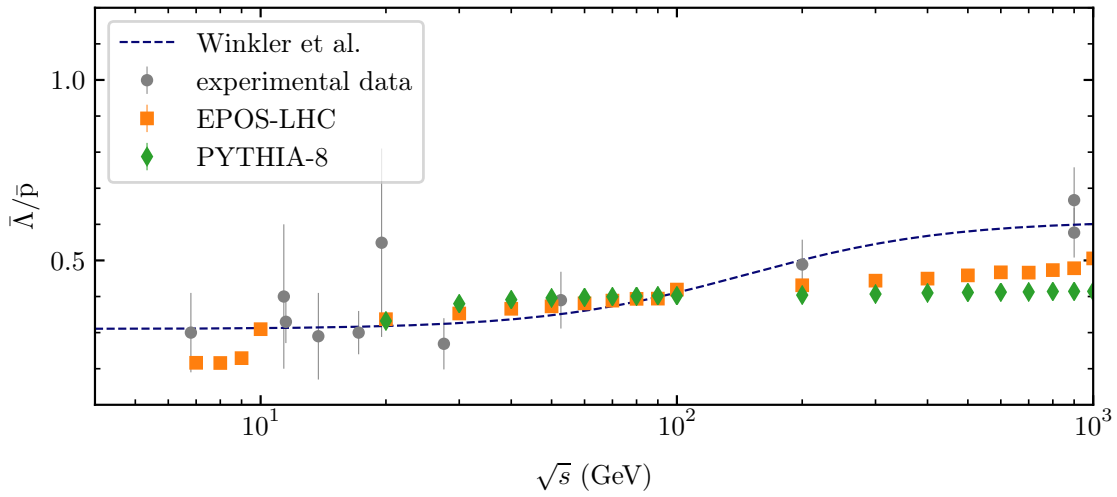

Figure 3.6: Comparison of the relative antilambda-particle production with experimental data and the parametrization from M. Winkler [195].

agreement with the experimentally obtained value quoted by the Particle Data Group [21]. The production yield of $\bar{\Lambda}$ relative to prompt antiprotons, $\bar{\Lambda}/\mathrm{p}$, is evaluated at 30 different collision energies between $\sqrt{s} = 7\,\mathrm{GeV}$ and $\sqrt{s} = 7\,\mathrm{TeV}$. Figure 3.9 compares the obtained results by the event generators with the experimental data summarized by M. Winkler and his parametrization, as discussed in Section 3.3.2 [195]. Both tested event generators produce a slightly smaller $\bar{\Lambda}/\mathrm{p}$ than experimentally measurement for collision energies above $\sqrt{s} = 100\,\mathrm{GeV}$. At lower energies, the result from EPOS-LHC is in agreement with the experimental data, while for PYTHIA-8, the $\bar{\Lambda}$ production sharply falls off at $\sqrt{s} = 11\,\mathrm{GeV}$. To further study the absolute yield and the spectral shape of the produced $\bar{\Lambda}$ particles, we additionally compare the production by the event generators to the measured p_t distributions of $\bar{\Lambda}$ measured by the STAR collaboration at $\sqrt{s} = 200\,\mathrm{GeV}$ and the ALICE collaboration at $\sqrt{s} = 900\,\mathrm{GeV}$ [219, 222]. Both experimental data and the results from both event generators are shown in Figure 3.7. The deviations of EPOS-LHC are within 20 % for both datasets while PYTHIA-8 overproduces antilambda particles at small p_t. The underproduction of the relative antilambda-to-antiproton ratio, which we investigated in Figure 3.9, therefore is expected to stem from the large overproduction of antiprotons rather than from an underproduction of antilambda particles. Compared to the found deviations of the prompt production, the deviations of the antihyperon production seem to be less significant.

3.3.3 Antiprotons from Antineutron Decays

Experimentally, the direct production of antineutrons in hadron collisions has not yet measured due to the complexity of detecting high-energy antineutrons. As they are charge neutral, they are not measured by tracking detectors and their characteristic annihilation pattern, which is commonly used to distinguish antineutrons from neutrons at low energies,

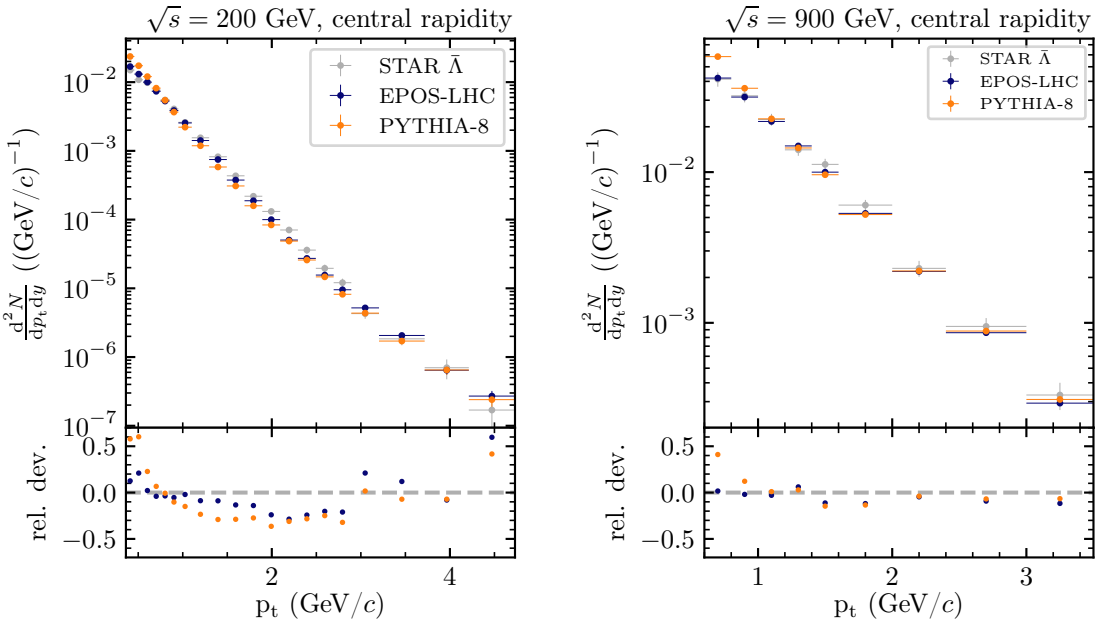

(a) $\bar{\Lambda}$ spectrum from p-p collisions measured by STAR at $\sqrt{s} = 200\,\text{GeV}$ [219].

(b) $\bar{\Lambda}$ spectrum from p-p collisions measured by ALICE at $\sqrt{s} = 900\,\text{GeV}$ [222].

Figure 3.7: Comparison of the spectral distributions of $\bar{\Lambda}$ from event-generator-based production and experimental data.

yields no significant signal at such high-energy collisions in the calorimeter, as the energy release of the annihilation compared to the energy released by the hadronic shower is too small. Therefore, most often the antineutron yield from proton-proton reactions is modeled from underlying physical principles. The concept used to model the antineutron yield in such reactions is the concept of isospin symmetry within the strong interaction. For high-energy reactions these particles can be treated as a doublet state and so can the antineutron and the antiproton [223].[8] In collisions, the production rate of $\overline{\text{p}}$-p and $\overline{\text{n}}$-n pairs is then expected to be equally abundant. Additionally, the antinucleons can also be created in pairs of $\overline{\text{p}}$-n or $\overline{\text{n}}$-p which are, at large collision energies, also expected to be equal. At lower energies, however, measurements of NA49 at $\sqrt{s} = 17.3\,\text{GeV}$ showed that the production of the mixed antinucleon-nucleon pairs depends on the value of I_3, the third component of the isospin, of the initial state—or equally the charge value of the initial state [224]. For p-p collisions, NA49 measured an enhancement of created $\overline{\text{n}}$-p pairs and a depletion of $\overline{\text{p}}$-n pairs relative to the respective yields in n-p collisions. In cosmic-ray interactions in the galaxy, the underlying nucleon-nucleon interactions feature more often p-p collisions than n-p or n-n collisions, posing an enhanced production of antineutrons over antiprotons based on the result from NA49. The strength of this asymmetry, its dependence on the collision energy, and the distribution of the asymmetry within the phase space of the produced antinucleons in a collision are not yet well known. The experimental

[8] The same statement is also valid for the ordinary particles, neutrons and protons.

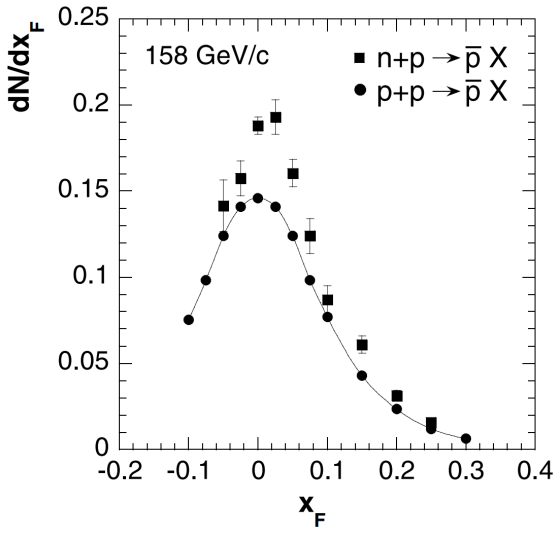

Figure 3.8: Experimental data of antiproton production in p-p and n-p collisions from NA49. Figure taken from [224].

data of NA49 shows that the asymmetry of the production reaches factors of 1.5 to 1.6 and seems to be maximal at $x_F = 0$. A more detailed study of the phase-space distribution of this effect and at different collision energies, however, is pending.

At higher collision energies, like at the LHC, the effect can also be investigated by the $\overline{\mathrm{p}}$-to-p ratio in p-p collisions. A possible enhancement of $\overline{\mathrm{n}}$p pairs with respect to $\overline{\mathrm{p}}$n pairs would also decrease the $\overline{\mathrm{p}}$-to-p ratio. As at these high energies the ratio is expected to be one, deviations from this value could be associated with this effect. However, data confirms that the $\overline{\mathrm{p}}$-to-p ratio is consistent with a symmetric production of $\overline{\mathrm{n}}$-p and $\overline{\mathrm{p}}$-n pairs [225]. Therefore, the effect seems to depend strongly on the collision energy and the dependence has to be parameterized appropriately to correctly model the enhancement of $\overline{\mathrm{n}}$ production in cosmic-ray collisions. M. Winkler performed a first estimate of the collision-energy dependence of the effect by interpolating the available data [195]. He extracted the energy-dependent isospin enhancement factor, $\Delta_{\mathrm{is}} = f^0_{\overline{\mathrm{n}}}/f^0_{\overline{\mathrm{p}}} - 1$, by fitting the parametrization

$$\Delta_{\mathrm{is}}(\sqrt{s}) = \frac{c_{14}}{1 + \left(\sqrt{s}^2/c_{15}\right)^{c_{16}}} \tag{3.29}$$

to the available data. The best-fit values of the free parameters he extracted as $c_{14} = 0.28$, $c_{15} = 12.12$, and $c_{16} = 1.04$.[9] The parameterization with the best-fit parameters and the upper boarder of the 68 % central interval of the posterior probability distribution of the isospin asymmetry are shown in Figure 3.9. As can be seen in the figure, the isospin asymmetry affects mainly the production of antiparticles at lower energies and is with the current experimental status not yet confirmed. The isospin asymmetry poses a large systematic uncertainty of the antiproton production from antineutrons of up to approxi-

[9] As unfortunately the parameter values are not given in the publication, we repeat the fit to obtain the quoted values.

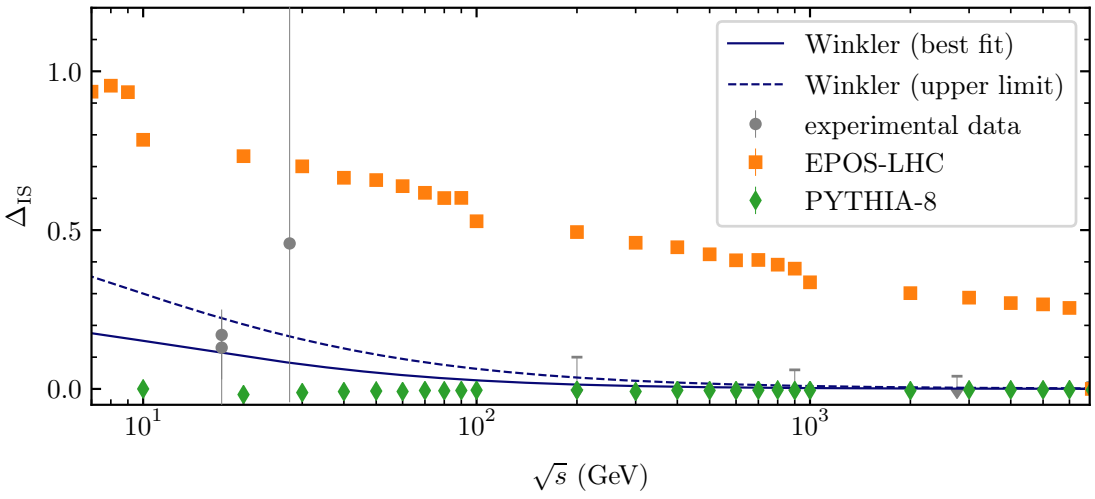

Figure 3.9: Comparison of the isospin-asymmetric production of antineutrons and antiprotons in EPOS-LHC and PYTHIA-8 compared with experimental data and a fitted parametrization from Winkler [195].

mately 40 % that has to be taken into account when interpreting the obtained cosmic-ray antiproton flux.

For the event generators we probe the antineutron production by calculating Δ_{is} for 30 different collision energies between $\sqrt{s} = 7\,\text{GeV}$ and $\sqrt{s} = 7\,\text{TeV}$ for EPOS-LHC and PYTHIA-8. The obtained results are also shown in Figure 3.9. While in PYTHIA-8 antineutrons are produced exactly symmetric to antiprotons, EPOS-LHC produces more antineutrons than antiprotons for all collision energies. At $\sqrt{s} = 10\,\text{GeV}$, EPOS-LHC produces two times more often an antineutron than an antiproton and even at LHC energies of $\sqrt{s} = 7\,\text{TeV}$, the asymmetry is still on the order of 20 %. EPOS-LHC thus overproduces antineutrons over the whole range of tested energies. The found overproduction is also not directly related to an explicit isospin asymmetry depending on the initial isospin configuration of the collision, as can be probed by comparing the yields of antineutrons and antiprotons for proton-proton, proton-neutron, and neutron-neutron collisions. All initial states yield the same antineutron-to-antiproton ratio and we conclude that EPOS-LHC overproduces antineutrons over the whole range of collision energies independently of the isospin configuration of the initial state.

Summarizing our study of the production of antiprotons by commonly used event generators and analytical parameterizations in proton-proton collisions, we have found large discrepancies between the production yields of the models and the available experimental data. For the event generators, EPOS-LHC has been found to have the least deviations from measurements for prompt-antiproton production but it overproduces antineutrons strongly. The production of antihyperons is well described by both, the EPOS and

PYTHIA models. Due to the large deviations we expect no reliable prediction of the cosmic-ray antiproton flux using event generators.
The analytical parameterizations describe the experimental data better. However, statistically significant deviations of the prompt antiproton production from experimental data are still present and the impact on the modeled antiproton flux is not yet quantifiable. The yields of antihyperons and antineutrons with respect to prompt antiprotons are well described by additional parameterizations that scale the prompt-production cross section. For the antineutron production, however, the lack of precise data on the isospin asymmetry at low collision energies poses a large uncertainty.
Beside of proton-proton collisions, collisions including heavier nuclei contribute also to the galactic antiproton production. In the following I discuss how this contribution is modeled by the event generators and by scaling relations from the antiproton production cross section from proton-proton collisions.

3.3.4 Antiproton Production in Heavier Collision Systems

Most experimental measurements of antiproton production are conducted in proton-proton collisions or heavy ion collisions, with heavy nuclei like gold or lead. In such collisions strong in-medium effects and collective-flow motions have been measured that modify the production and phase-space distribution of secondary particles [226]. However, in the galaxy such collisions are very rare and most cosmic-rays and interstellar atoms are—beside of protons—light nuclei such as helium, carbon, nitrogen, or oxygen. The collision system of these nuclei is much smaller than for heavy ions and the in-medium effects are less pronounced, and therefore results from heavy ion collisions cannot be easily scaled-down to describe light-ion collisions. Often the results obtained in proton-proton collision are scaled to describe the expectation from collisions of protons with light nuclei or light nuclei with light nuclei. To find a suitable parameterization of the scaling for antiproton production, the NA49 collaboration measured the antiproton production in proton-proton collisions (see Figure B.3) as well as in proton-carbon collisions, as shown in Figure 3.10. As the experiment covers nearly the complete phase-space of the produced antiprotons they were able to not only compare the yield but also the difference in phase-space distribution of the antiprotons in the two collision systems. Their data reveals that in forward direction in the center-of-momentum system—$x_\mathrm{F} > 0$—the phase-space distribution of antiprotons is very similar for both colliding systems, while for $x_\mathrm{F} < 0$ larger differences occur. This was explained by the assumption that in forward direction most particles stem from the fragmentation of the projectile nucleus, which in both cases was a proton, while in backward direction in the center-of-momentum frame the particles mainly stem from the fragmentation of the target nucleus which are different in proton-proton and proton-carbon collisions. From the comparison of both datasets the NA49 collaboration developed a phenomenological scaling of the antiproton production cross-section from proton-proton collisions to collisions of arbitrary nuclei A_1 and A_2 as

$$\left(\frac{\mathrm{d}n}{\mathrm{d}x_\mathrm{F}}\right)_{\mathrm{A_1+A_2\to\bar{p}+}X} = \left(\langle v_{\mathrm{A}_1}\rangle F_\mathrm{pro}(x_\mathrm{F}) + \langle v_{\mathrm{A}_2}\rangle F_\mathrm{tar}(x_\mathrm{F})\right)\left(\frac{\mathrm{d}n}{\mathrm{d}x_\mathrm{F}}\right)_{\mathrm{p+p\to\bar{p}+}X}, \tag{3.30}$$

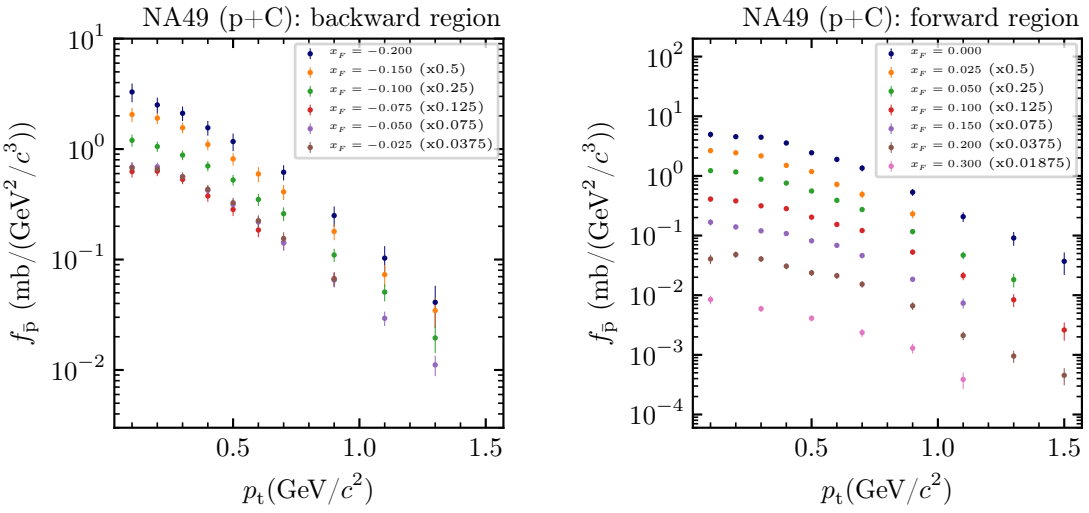

(a) $x_F < 0$. (b) $x_F \geq 0$.

Figure 3.10: Experimental data of antiproton production in p+ C collisions from NA49 [227].

with $\langle \nu_{A_1} \rangle$ and $\langle \nu_{A_2} \rangle$ being the average number of projectile and target nucleon-nucleon scatterings and F_{pro} and F_{tar} the projectile and target fragmentation functions [227]. The average number of nucleon-nucleon scatterings of a nucleus A with a proton is calculated as

$$\langle \nu_A \rangle = A \frac{\sigma_{pp,inel}}{\sigma_{pA,inel}}, \tag{3.31}$$

with A being the mass number of the corresponding nucleus and $\sigma_{pp,inel}$ and $\sigma_{pA,inel}$ the proton-proton and proton-nucleus inelastic cross sections. The fragmentation functions $F_{pro}(x_F)$ and $F_{tar}(x_F)$ give the probability of a particle emitted with a given x_F to stem from the fragmentation of the projectile or the target particle. A tabulation of the projectile fragmentation function into antiprotons, as extracted by NA49 [227], is given in Table 3.5 and the target fragmentation function is related to projectile fragmentation function by

$$F_{tar}(x_F) = F_{pro}(1 - x_F). \tag{3.32}$$

At larger collision energy, LHCb measured the antiproton production in proton-helium collisions at $\sqrt{s} = 110.5\,\text{GeV}$ [228]. As unfortunately at this collision energy no data from proton-proton collisions are available, a direct comparison between the production of both colliding systems is not possible and the aforementioned scaling cannot be tested for such large collision energies.
Event generators are often used to describe different colliding systems, even heavy ion collisions. However, not all event generators are capable to simulate such collisions but only single nucleon-nucleon reactions. In these cases, the results from the simulated proton-proton collisions have to be scaled by Equation 3.30. PYTHIA-8 only recently added the feature of simulating nuclei collisions other than proton-proton. But unfortunately, in our

x_F	$F_{\bar{\mathrm{p}}}$	x_F	$F_{\bar{\mathrm{p}}}$
−0.250	0.0	0.250	1.0000
−0.225	0.0003	0.225	0.9997
−0.200	0.0008	0.200	0.9992
−0.175	0.0027	0.175	0.9973
−0.150	0.010	0.150	0.990
−0.125	0.035	0.125	0.965
−0.100	0.110	0.100	0.890
−0.075	0.197	0.075	0.803
−0.050	0.295	0.050	0.705
−0.025	0.4	0.025	0.6
		0.000	0.5

Table 3.5: Fragmentation function into antiprotons as given by NA49. Table reproduced from [227].

used version a failure of the computing code hinders us to use of this novel feature, and we use the analytical scaling to emulate the production of antiprotons in cosmic proton-helium, helium-proton, and helium-helium collisions for PYTIHA-8 [229].
For EPOS-LHC, the simulation of ion collisions is possible, and we qualitatively compare the antiproton production from EPOS-LHC with the two mentioned experimental datasets. Figure 3.11 shows the relative deviation of the double-differential antiproton-production cross section from EPOS-LHC to the measured values of the proton-carbon collisions by NA49 [227]. The deviation as a function of the phase-space variables is similar to the deviations found for the antiproton production in proton-proton collisions from the same experiment (c.f. Figure B.9b), which indicates that the deviations stem mainly from the underlying antiproton production model rather than from the description of the larger collision system for this collision energy.
The results for the proton-helium collisions at $\sqrt{s_\mathrm{NN}} = 110\,\mathrm{GeV}$ to compare with the LHCb data are shown in Figure 3.12. As no experimental data for proton-proton collisions at this collision energy is available, we additionally show the obtained result for simulated proton-proton collisions by EPOS-LHC scaled to proton-helium collisions by Equation 3.30. The antiproton yield of EPOS-LHC is for both approaches—directly simulating the proton-helium collision and scaling the result from the proton-proton collision—smaller than the experimental data. The difference between both approaches is small compared to the overall deviation but increases with increasing p_t. In addition to EPOS-LHC, also the result from EPOS-3 is shown, which is explicitly tuned to describe physical effects that appear in heavy-ion collisions at the LHC, such as in-matter effects of the produced particles and collective motions. However, the antiproton production of EPOS-3 exceeds the measured antiproton yield by LHCb significantly. As unfortunately no antiproton-production data from proton-proton collisions at $\sqrt{s} = 110\,\mathrm{GeV}$ is available, it stays unclear whether the

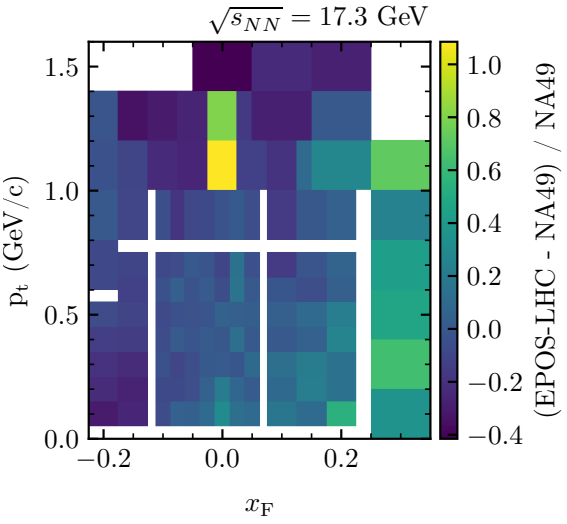

Figure 3.11: Comparison of the antiproton-production yield of EPOS-LHC in proton-carbon collisions at $\sqrt{s_{\mathrm{NN}}} = 17.3\,\mathrm{GeV}$ with the experimental data from NA49.

deviations stem from a deviation of the underlying antiproton production in the nucleon-nucleon interaction or due to the scaling to the larger collision system. The experimental dataset from proton-proton collisions that has the closest collision energy to the LHCb data is the data from PHENIX at $\sqrt{s} = 62.4\,\mathrm{GeV}$, in which both generators, EPOS-LHC and EPOS-3, tend to overestimate the antiproton production (c.f. Figure B.10). However, we have to note that the experimental data from PHENIX is taken at central rapidity, while the data from LHCb is at non-central rapidity, probing a different region of the phase-space of the produced antiprotons. Nevertheless, the found result might hint to an underestimation of the scaling of the antiproton production from proton-proton to proton-helium in EPOS-LHC for this specific collision energy, but more data for different colliding systems are required to verify this assumption.
Similar to the modeling of antiproton production in proton-proton collisions, the modeling of the production in larger colliding systems is not completely accurate. Due to the lack of experimental data, it is not possible to attribute the deviations to the description of the larger colliding system or due to the antiproton production in the underlying nucleon-nucleon reactions.

The described models and approaches to approximate the antiproton-production in collisions relevant for the creation of cosmic-ray antiprotons in our galaxy obtain different antiproton-production cross sections. Although they all deviate for certain collision energies from the experimental data, especially the analytical parameterizations currently approximate best the antiproton production. In the following, I compare the resulting antiproton fluxes at Earth stemming from these different production models and I present the study of the agreement of the measured cosmic-ray flux from AMS-02 with the parameterizations and the event generators.

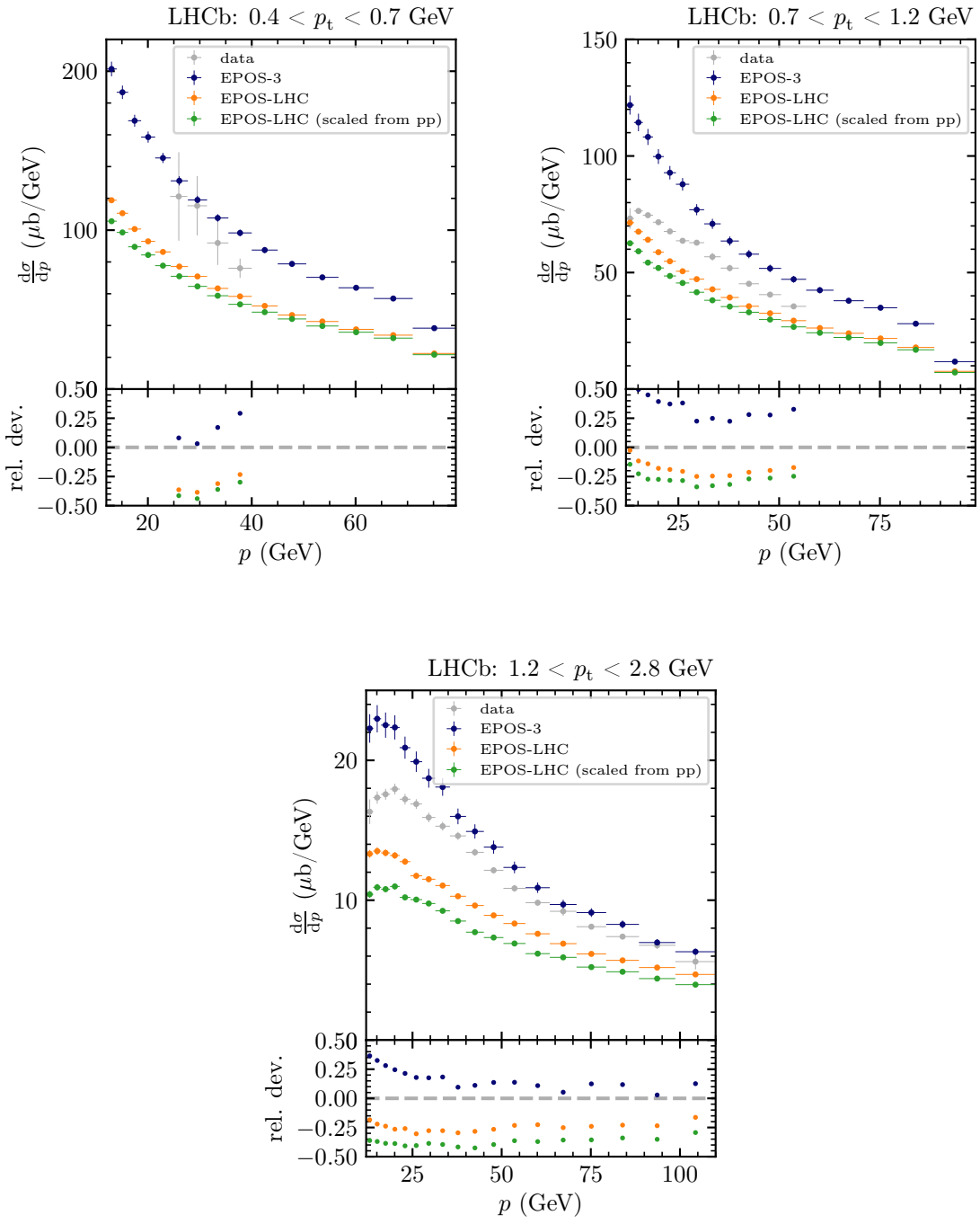

Figure 3.12: Comparison of antiproton production of EPOS-LHC and EPOS-3 in proton-helium collisions at $\sqrt{s_{\mathrm{NN}}} = 110\,\mathrm{GeV}$ with experimental data from LHCb [228]. In addition, the result of the scaled proton-proton result from EPOS-LHC, using the parametrization from Section 3.3.4 is shown.

3.4 Prediction of the Antiproton Flux for Different Production Models

The different models of antiproton production—either based on an analytical parameterization or on event generators—produce different antiproton yields and phase-space distributions. Although we have compared them at several collision energies to experimental data, most collision energies and regions of the phase space of the produced antiprotons stay untested due to the limited data on antiproton production. Therefore, one cannot easily predict how different the resulting antiproton flux in the galaxy is for the different production models. Therefore, we investigate the differences in two ways: We first calculate the so-called source function of antiprotons, which gives the yield of antiprotons from cosmic-ray interactions at their origin—excluding effects of the propagation—and afterwards we investigate the differences of the propagated antiproton flux at Earth, which includes the modification of the antiproton spectrum due to the processes during propagation. However, only the propagated fluxes can be experimentally probed.
The source function, as introduced in Section 1.2.1 for the general case, can be written for antiprotons as

$$q_{i+j\to\bar{\mathrm{p}}}(\vec{r},t,E_{\bar{\mathrm{p}}}) = 4\pi \sum_i \sum_j n_j(\vec{r}) \int\limits_{E_i^{\min}}^{\infty} \mathrm{d}E_{\bar{\mathrm{p}}} \frac{\mathrm{d}\sigma_{i+j\to\bar{\mathrm{p}}+X}(E_i,E_{\bar{\mathrm{p}}})}{\mathrm{d}E_{\bar{\mathrm{p}}}} \Phi_i(\vec{r},t,E_i), \tag{3.33}$$

with i representing the different cosmic-ray nuclei that act as projectiles with kinetic energies, E_i, and their corresponding particle flux, $\Phi_i(\vec{r},t,E_i)$; j represents the nuclei of the interstellar medium that act as target particles with corresponding densities, n_j; and $\mathrm{d}\sigma_{i,j}/\mathrm{d}E_{\bar{\mathrm{p}}}$ is the energy-differential inclusive antiproton production cross section for the collision of nuclei i and j. $E_{i,\mathrm{min}}$ represents the kinetic threshold of nuclei i to be able to produce antiprotons in the collision. The source function of antiprotons comprises the contributions from prompt production as well as from the decays of antineutrons and antihyperons from all collisional systems that occur in the galaxy. As discussed in Section 3.2, the non-prompt contributions and the contributions from colliding systems heavier than proton-proton, can be all expressed in terms of the prompt-antiproton production in proton-proton collisions. Therefore, we investigate the source function of prompt antiprotons from proton-proton collisions first to quantify the model dependence of the source function for the different models of production we have analyzed.
It is notable in Equation 3.33, that the source function inhibits a location and time dependence due to the time and location-dependent flux of the projectile particles, and we have to choose a corresponding projectile flux to evaluate the source function. We use the steady-state local interstellar flux of protons obtained by Boschini et al. using GALPROP [163], as described in Section 2.3, for this study.
To calculate the source function from the analytical parameterizations with the proton flux from GALPROP, which is discretized on an energy grid as described in Section 2.1, we need to integrate the invariant cross section corresponding to each energy. As the energy of the created antiprotons is also discretized on the same grid, we have to calculate the source

function for antiprotons at each energy-grid point as

$$q_{\bar{\mathrm{p}}}\left(E_{\bar{\mathrm{p}}}^{(l)}\right) = 4\pi < n_{\mathrm{H}} > \sum_{E_{\mathrm{p}}^{(k)}=E_{\mathrm{p}}^{\mathrm{min}}}^{E_{\mathrm{p}}^{\mathrm{max}}} \left(E_{\mathrm{p}}^{(k)} - E_{\mathrm{p}}^{(k-1)}\right) \frac{\mathrm{d}\sigma}{\mathrm{d}E_{\bar{\mathrm{p}}}}\left(E_{\mathrm{p}}^{(k)}, E_{\bar{\mathrm{p}}}^{(l)}\right) \Phi_{\mathrm{LIS}}\left(E_{\mathrm{p}}^{(k)}\right), \quad (3.34)$$

with $E_{\bar{\mathrm{p}}}^{(l)}$ being the antiproton energy, $< n_{\mathrm{H}} > \approx 1\,\mathrm{cm}^{-3}$ the average density of the interstellar hydrogen, $E_{\mathrm{p}}^{\mathrm{min}}$ the minimum kinetic energy of the projectile protons to create an antiproton in the collision, $E_{\mathrm{p}}^{\mathrm{max}}$ the maximum energy-grid point for which particles are propagated in GALPROP, $\Phi_{\mathrm{LIS}}(E_{\mathrm{p}}^{(k)})$ being the local interstellar flux of protons, and $\mathrm{d}\sigma/\mathrm{d}E_{\mathrm{p}}$ being the energy-differential antiproton production cross section, which can be calculated from the invariant cross section as

$$\frac{\mathrm{d}\sigma}{\mathrm{d}E_{\bar{\mathrm{p}}}}\left(E_{\mathrm{p}}^{(k)}, E_{\bar{\mathrm{p}}}^{(l)}\right) = 2\pi p_{\bar{\mathrm{p}}} \int \mathrm{d}\cos(\theta) f_{\bar{\mathrm{p}}}\left(E_{\mathrm{p}}^{(k)}, E_{\bar{\mathrm{p}}}^{(l)}, \theta\right), \quad (3.35)$$

with θ being the angle between the incoming proton and the produced antiproton and $f_{\bar{\mathrm{p}}}$ being the invariant cross section for prompt antiproton production.
To obtain the source function for the event-generator-based production, we simulate proton-proton collisions for each $E_{\mathrm{p}}^{(k)}$ and calculate from this the production cross section as

$$\frac{\mathrm{d}\sigma}{\mathrm{d}E_{\bar{\mathrm{p}}}}\left(E_{\mathrm{p}}^{(k)}, E_{\bar{\mathrm{p}}}^{(l)}\right) = \sigma_{\mathrm{inel}}\left(E_{\mathrm{p}}^{(k)}\right) \frac{N_{\bar{\mathrm{p}}}}{N_{\mathrm{coll}}\left(E_{\bar{\mathrm{p}}}^{(l)} - E_{\bar{\mathrm{p}}}^{(l-1)}\right)}, \quad (3.36)$$

with N_{coll} being the number of simulated collisions, $\sigma_{\mathrm{inel}}(E_{\mathrm{p}}^{(k)})$ being the inelastic cross section, and $N_{\bar{\mathrm{p}}}$ being the number of created antiprotons in the energy interval $E_{\bar{\mathrm{p}}}^{(l-1)}$–$E_{\bar{\mathrm{p}}}^{(l)}$.
In Figure 3.13a, we show the obtained source function for prompt antiprotons from proton-proton collisions multiplied by $E_{\bar{\mathrm{p}}}^{2.7}$ for several of our tested production models: For the event generators EPOS-LHC and PYTHIA-8; for the adapted Winkler model with its best-fit parameters, which has given the best agreement to the experimental data of antiproton production of all investigated models and thus is expected to give the most accurate estimation of the source function; and the original parameterizations by Winkler and Di Mauro et al. with their originally obtained parameters from their publications [195, 164].

As expected from the comparison of the different models with the antiproton-production data from accelerator-based experiments, the source functions of the event generators PYTHIA-8 and EPOS-LHC are exceeding the obtained source functions of the analytical parameterizations over the whole energy range. The source terms of the parameterizations differ only on the order of 10 % from each other. For the adapted Winkler model, for which we performed the parameter fit, we additionally show the central-68 % interval of the source term which visualizes the propagated uncertainty from the antiproton production model. This interval is obtained by using the posterior-probability-distributed samples of the parameters from the MCMC sampling. We calculate the source function for each obtained sample, and mark for each $E_{\bar{\mathrm{p}}}$ the interval around the value from the best-fit parameters

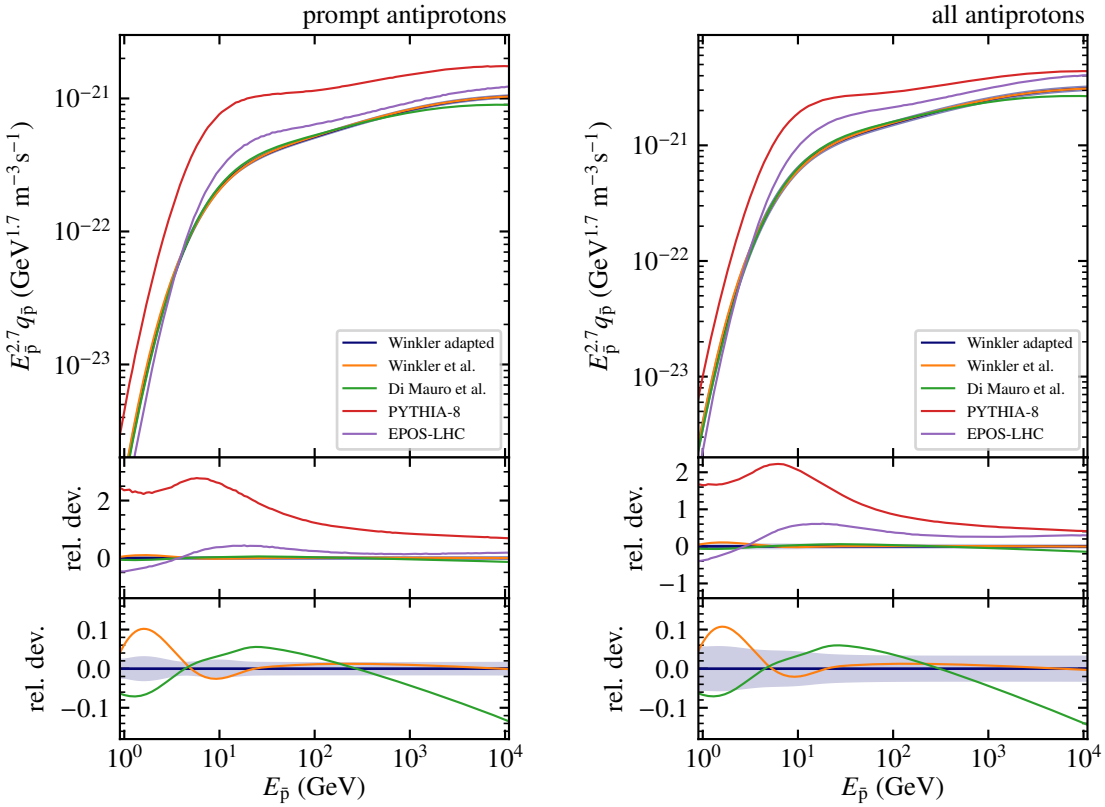

(a) Source function of prompt antiprotons.

(b) Source function including antiprotons stemming from weak decays.

Figure 3.13: Comparison of the local antiproton source functions for proton-proton collisions of different production models. The relative deviations are calculated with respect to the best-fit result of the adapted Winkler model.

in which 68 % of all samples fall. Although in the studies of Winkler and Di Mauro et al. different experimental datasets and fit procedures have been used, their given relative uncertainties are similar to what we obtained for our adapted Winkler model [195, 164]. When including the uncertainties from the fitting procedure, the predicted source functions for all three analytical models coincide up to energies of around 1×10^3 GeV. Above this energy, the model by Di Mauro et al. predicts a smaller source function.
In addition to prompt antiprotons, antiprotons from decayed antineutrons and antihyperons also contributes to the source function of antiprotons in the galaxy. To include these contributions in the analytical parameterizations, we scale the invariant prompt-antiproton production cross section following the approach from M. Winkler as

$$f_{\bar{p}}^{\text{all}} = f_{\bar{p}} \left(2 + \Delta_{\text{is}} + 2\Delta_{\text{hyp}}\right), \tag{3.37}$$

with Δ_{is} from Equation 3.29, to account for asymmetric antineutron-to-antiproton production, and $\Delta_{\text{hyp}} = (0.81 \pm 0.04) f_{\bar{\Lambda}}/f_{\bar{p}}$, with the ratio of the antilambda-to-antiproton production cross section, which is parametrized as a function of collision energy using

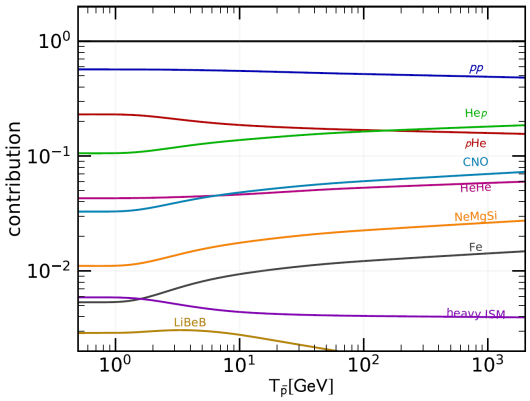

Figure 3.14: Relative contribution of the various contribution channels to the source spectrum. Figure taken from Korsmeier et al. [164].

Equation 3.27 [195].
To include the contributions from antihyperons and antineutrons in the event-generator-based models, we include the corresponding weak decays in the simulations and let all antineutrons and antihyperons decay.
The obtained full source functions for galactic proton-proton collisions are shown in Figure 3.13b. While the relative deviations between the analytical parameterizations do not change—since we scale them all equally—the relative deviation of EPOS-LHC with respect to them increases due to the overproduction of antineutrons. As both, the production of antineutrons and antihyperons, suffer from additional uncertainties which are independent from the prompt-antiproton cross section, we include them as well in our central-68 %-interval band of the result from the adapted Winkler model. To do so, we additionally sample Δ_{is} and Δ_{hyp} according to their posterior-probability distributions that we obtain by reproducing the fits to experimental data from Winkler et al. [217, 195]. The combined central-68 % interval that includes the uncertainties from the prompt-antiproton-production fit, from the isospin asymmetry, and from the antihyperon contribution has a relative magnitude on the order of 5 % of the source function and increases with decreasing antiproton energy due to the increasing uncertainty from the antineutron production.

In order to obtain the full antiproton source term and to model the full antiproton flux at Earth, the contributions from colliding systems other than proton-proton have to be added as well. As found by Korsmeier et al., the proton-proton channel accounts for around 50 % to 60 % of the total source function [164]. The remaining fraction distributes mainly to helium-proton, proton-helium, and helium-helium collisions. But even heavier ions contribute measurably to the total production. Figure 3.14 shows the relative contributions to the source function as obtained by Di Mauro et al. for their production model from the different collisional systems. The contributions from the heavier collision systems can be calculated for a given production model by scaling the antiproton production from proton-proton collisions as discussed in Section 3.3.4 using Equation 3.30. Although the relative deviations of the source functions for the different production models do not significantly change, the inclusion of the contribution from the heavier collision systems is important to

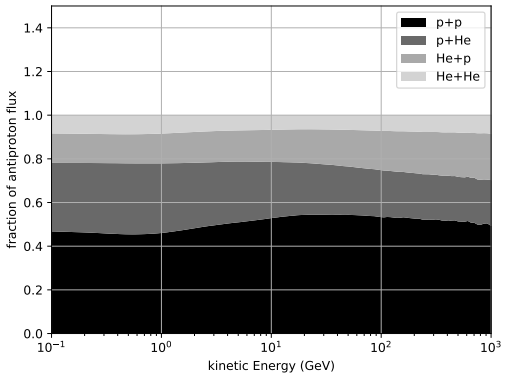

Figure 3.15: Relative contribution to the LIS flux of antiprotons extracted from EPOS-LHC.

be able to compare the resulting antiproton flux to cosmic-ray measurements. To obtain a good approximation of the total antiproton flux for our models, we use Equation 3.30 to add the contribution from proton-helium, helium-proton, and helium-helium collisions to our flux prediction. These collisional systems together with proton-proton collisions account for more than 90 % of the total antiproton production. In order to account for the missing fraction from even heavier systems, we scale the calculated contribution from helium-proton collisions by a factor 1.4, as the next leading contributions from carbon, nitrogen, oxygen, neon, magnesium, and silicon follow a very similar energy dependence in their contribution as can be seen in Figure 3.14. By this scaling, we expect the models to account for more than 97 % of the total antiproton production in the galaxy. For EPOS-LHC, we perform the simulations of the proton-helium, helium-proton, and helium-helium collisions and extract the corresponding antiproton-production cross sections similar as for the proton-proton case. To again compensate the missing contribution from heavier systems, we scale the result from the helium-proton collsion by a factor of 1.4. The contribution of the different collision systems for the final antiproton flux at Earth for EPOS-LHC is depicted in Figure 3.15 excluding the scaling of the helium-proton contribution. For PYTHIA-8, as mentioned, we apply the same scaling as for the analytical parameterizations.

To obtain the propagated antiproton fluxes for the different production models we again use the propagation setup of Boschini et al. as discussed in detail in Section 2.3 [163]. The obtained local interstellar antiproton fluxes for the different production models are shown in Figure 3.16a together with the relative deviations to the obtained flux by the adapted Winkler model. Again, the blue uncertainty band shows the central-68 % interval of the prediction, which is accounting for the uncertainties from the prompt production, the isospin asymmetry, and the antihyperon contribution. The interval is obtained by using the samples from the Markov-Chain Monte-Carlo procedure, similar as for the uncertainty calculation of the source function, and executing the GALPROP simulation for each sample to obtain the propagated antiproton flux. The uncertainties for the models by Winkler and Di Mauro et al. are expected again to be of similar magnitude.

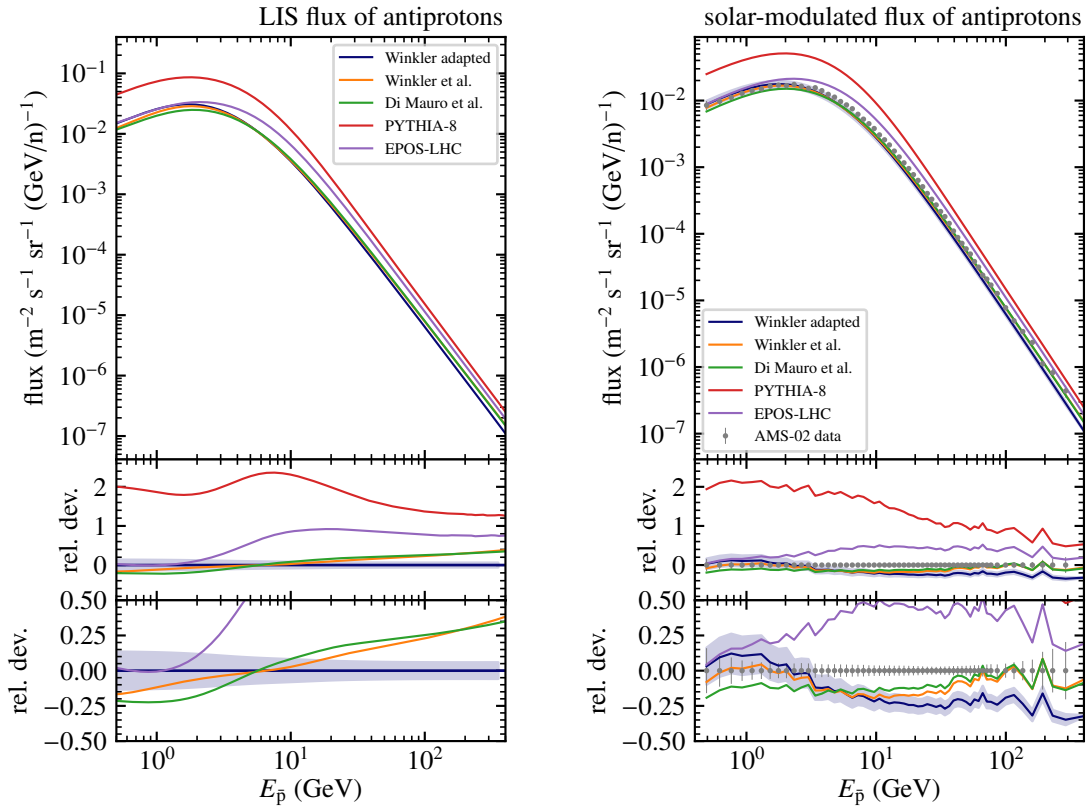

(a) LIS flux of antiprotons.

(b) Solar-modulated flux of antiprotons compared to AMS-02 data.

Figure 3.16: Prediction of the antiproton flux for the different antiproton-production models obtained with GALPROP and the parameters of the Boschini propagation model. The solar modulation is performed using HELMOD.

The obtained antiproton fluxes for the original models by Winkler and Di Mauro et al. have a slightly flatter spectrum as the flux from the adapted Winkler model and result in a larger antiproton flux at energies above a few tens of GeV. This is as expected from the comparison of the production models with the experimental antiproton-production data, in which both, the Winkler and Di Mauro model, overestimated the total antiproton production at $\sqrt{s} = 62.4\,\text{GeV}$ and $\sqrt{s} = 200\,\text{GeV}$ by the PHENIX and BRAHMS experiment. Collisions with $\sqrt{s} \approx 50\,\text{GeV}$ contribute most to the antiproton flux on the order of 200 GeV kinetic energy of the antiprotons.
The modeled fluxes from the event generators yield way larger antiproton fluxes. Only at the lowest energies, below a few GeV, the flux from EPOS-LHC decreases to the flux predicted by the analytical parameterizations. This is found to be due to an instant drop of the antiproton production in EPOS-LHC to zero below $\sqrt{s} = 6\,\text{GeV}$, as the generator does not produce any secondary particles below this collision energy. Since the energy threshold for antiprotons is smaller, at approximately $\sqrt{s} = 4\,\text{GeV}$, the contribution of antiprotons produced within this range of collisions is missing, reducing the flux of very low-energy antiprotons.

To compare the modeled antiproton fluxes to AMS-02 data near Earth, we include solar modulation on the obtained local interstellar antiproton fluxes using the HELMOD code described in Section 1.3.2 [28]. The modulated fluxes and their relative deviations from the AMS-02 data are shown in Figure 3.16b. Except for the result of PYTHIA-8, all models produce an antiproton flux that is not deviating more than 50 % from the AMS-02 data over the whole measurement range. The analytical parameterizations, which are much more in agreement with the antiproton production measurements at accelerator-based experiments are only deviating at maximum 25 % from the AMS-02 measurement. While the model by Winkler and Di Mauro et al. only deviates in the energy range of 10 GeV to 30 GeV, our adapted Winkler model deviates also at larger energies.
Similar as for the source term, the lower flux at high energies is a consequence of simultaneous use of PHENIX and BRAHMS data in our fitting procedure of the antiproton production cross section, which suggests a different x_r distribution of antiprotons as measured at lower collision energies by NA49 or NA61. The data suggests an increased suppression of antiproton production at large x_r and thus at large kinetic energy of the antiproton. Due to the lack of further measurements at non-central rapidities at such large collision energies, we cannot further probe the evolution of this suppression and whether our ad-hoc parameterization of the collision-energy dependence of the suppression is justified. With the so-far available data, however, the adapted Winkler model yields the best agreement with the antiproton-production measurements and might give a more realistic estimate of the antiproton flux. To further pin-down the correct antiproton-production model, more experimental data, covering a larger fraction of the phase space—especially for large collision energies are required.
When interpreting the deviations of the modeled antiproton flux from the AMS-02 data, the uncertainties of the propagation model must be also taken into account. As we have seen in Section 2.3, the variations of the propagated antiproton flux for a given production model but a different propagation model—which is still in agreement with cosmic-ray measurements of other particle species—is on the order of 20 % below around 30 GeV as can be seen in Figure 2.14. Combining the uncertainties from the propagation and production of antiprotons, our current models cannot provide a convincing statement on whether the assumption of a purely secondary antiproton flux explains the measured antiproton yield or if an additional exotic contribution is required to explain the measured flux. Further efforts to reduce the uncertainties on the flux modeling are required to improve the exclusion limits of exotic sources or to identify an exotic contributions of antimatter in the galaxy using antiprotons.

Due to this complication, in the last decade the search for heavier antinuclei has been proposed, as the collisional production of such particles is expected to be suppressed compared to the single antinucleon production and the detection of such particles might be a hint to an exotic source of antimatter in our galaxy. In the following section we want to shortly review this idea as an outlook and discuss possible implications of the here presented study of the antiproton and antineutron production on the models of antinuclei production in the galaxy.

3.5 Outlook on Heavier Antinuclei in Cosmic Rays

The comparison of the measured cosmic-ray antiproton flux with flux models have served as a good constraint on exotic sources in the past, often limited only by the statistical precision of the cosmic-ray antiproton measurement. As we have seen, however, this has changed and the uncertainties of the propagation model and the production model of antiprotons currently hinder further improvements of the constraints of exotic sources or to confirm them. Because of these drawbacks, in the last decade the measurement of heavier antinuclei has been proposed as a more sensitive probe for exotic sources with respect to antiprotons [230].
Similarly to ordinary nuclei, antiprotons and antineutrons can form a bound state, an antinucleus, if they are close enough in space and momentum. Hence, processes which are energetic enough to produce at least two antinucleons potentially also produce them in a bound state. In cosmic-ray collisions, the minimum collision energy required is around $\sqrt{s} \approx 6m_{\mathrm{p}}$. For exotic processes such as dark-matter decay or annihilation the mass of the involved dark-matter particles has to be above $\sqrt{s} \approx 4m_{\mathrm{p}}$ [231].
Although the expected fluxes of such antinuclei are much smaller than the flux of antiprotons due to the much lower probability to produce two antinucleons close in phase space in any reaction, kinematic considerations suggest that the produced antinuclei flux from cosmic-ray collisions at low energies is even lower than a potential flux from many proposed exotic sources, such as dark-matter annihilation or decay, that are still in agreement with the current limits set by the flux of antiprotons in the galaxy [232]. Antinuclei that emerge a cosmic-ray collision are largely boosted due to the fixed-target kinematics of the reaction and inherit a large kinetic energy. The production of low-energy antinuclei is thus very unlikely. On the other hand, most models of dark matter annihilation and decay for dark matter particles in the GeV to TeV range, or exotic sources like primordial black holes, predict antinuclei fluxes that peak at these low kinetic energies. Figure 3.17 shows exemplarily some current estimates of the antideuteron flux for different exotic source hypotheses together with estimates of the antideuteron flux from cosmic ray collisions. Especially at energies below 1 GeV/n the flux from exotic sources can exceed the flux from cosmic ray collisions significantly. However, at energies around several GeV both fluxes are expected to be on the same order of magnitude and a good estimate of the antideuteron flux from cosmic-ray interactions is required to interpret possible future measurements of antideuterons. The differences between the obtained antideuteron fluxes from cosmic-ray interactions stem mainly from different modeling of the antideuteron formation from the two initially independently created antinucleons. The most commonly used model to describe this process is the so-called coalescence model. In this model, only the distance of the two antinucleons in momentum space determines whether a bound state is formed. The maximum allowed distance to be able to form an antideuteron is called the coalescence momentum, p_0, which cannot be constrained from first-principles but has to be extracted from antideuteron-production measurements [232].
In the most simple form, the so-called factorized coalescence model, the invariant production cross section of antideuterons, $f_{\bar{\mathrm{d}}}$, is calculated from the invariant production cross

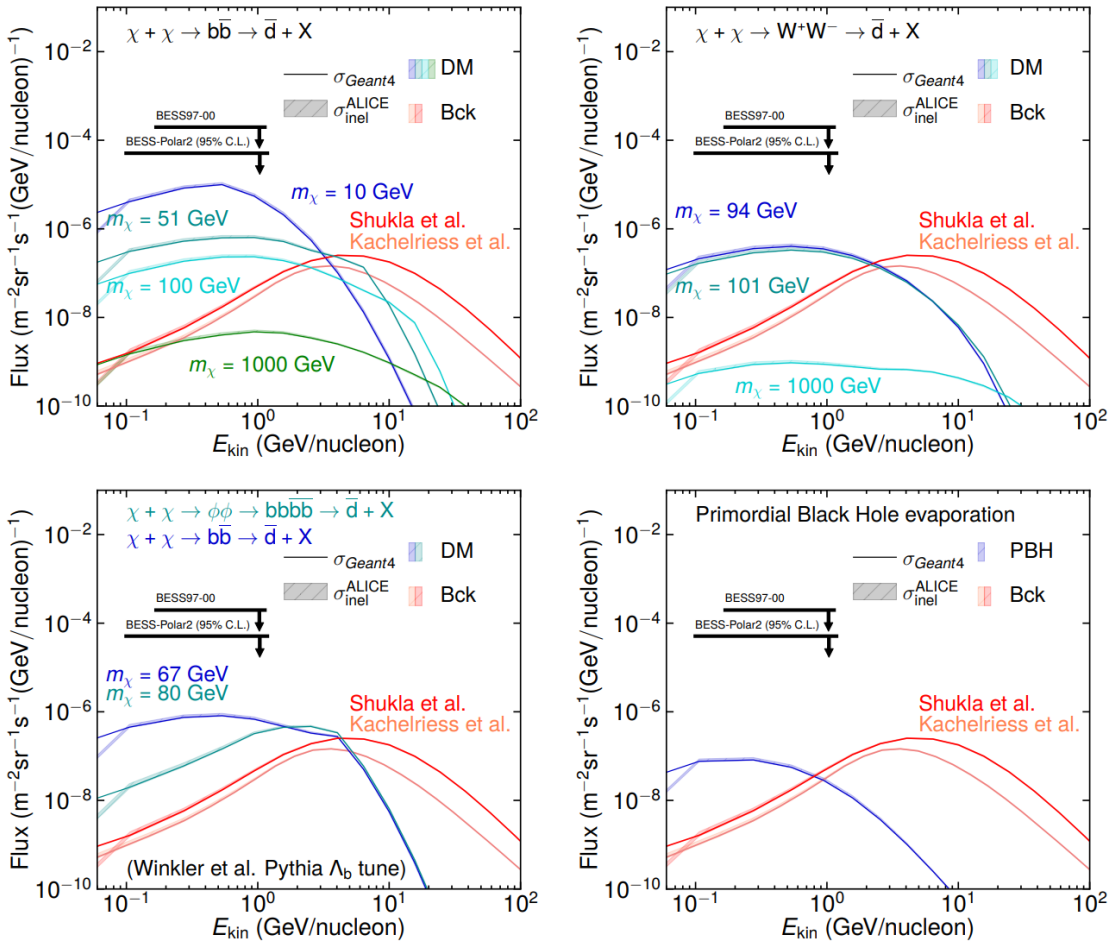

Figure 3.17: Estimates of antideuteron fluxes obtained for different exotic source hypothesis and from cosmic-ray interactions from Serksnyte et al [232]. The green and blue lines show the prediction for dark-matter annihilation with different characteristics of the annihilation process and from primordial black hole evaporation (lower-right figure). The red lines show the prediction of the background of antideuterons created by cosmic-ray interactions for two different models of the antideuteron-production cross section based on the studies by Shukla et al. and Kachelriess et al. [233, 234]. The difference between the lines and the shaded bands stems from different antideuteron annihilation cross sections assumed for propagation. Figure taken from Serksnyte et al. [232].

section of antiprotons, $f_{\bar{p}}$ and antineutrons, $f_{\bar{n}}$, and the coalescence momentum as

$$f_{\bar{d}} \approx \frac{\pi p_0^3}{6} \frac{m_{\bar{d}}}{m_{\bar{p}} m_{\bar{p}}} f_{\bar{p}} f_{\bar{n}}. \tag{3.38}$$

This model, however, assumes a completely uncorrelated production of the individual antinucleons, which is questionable especially for low collision energies in which the available

phase-space for the production of the second antinucleon shrinks significantly in comparison to the production of the first one due to the reduced available energy to create further baryon-antibaryon pairs [231]. To take this and further particle-particle correlations during the production of the antinucleons into account, an event-by-event coalescence has been proposed, in which the coalescence requirement, $p_{\bar{\mathrm{p}}} - p_{\bar{\mathrm{n}}} \leq p_0$, is evaluated for each produced antiproton-antineutron pair in each event individually [231]. To model such individual events, event generators are used, often the already discussed EPOS-LHC or PYTHIA-8 generator.
Recent studies have used different event generators and obtained different coalescence momenta when fitting to similar experimental data of antideuteron production [233, 234]. These obtained deviations can be either assigned to different particle-particle correlations employed by the event generators or—as discussed in Section 3.3.1.1—to a differing production of individual antinucleons.
To disentangle the influence of the two effects and estimate their magnitude, we exemplarily compare the antideuteron production of EPOS-LHC and PYTHIA-8 at $\sqrt{s} = 17.3\,\mathrm{GeV}$ using the event-by-event coalescence model and compare the obtained antideuteron spectra to spectra obtained by the two generators with identical antiproton and antineutron production. To obtain an identical production of the single antinucleons, a weighting procedure is employed, which is described in the following.
As we have seen, both generators overproduce antiprotons and antineutrons significantly at $\sqrt{s} = 17.3\,\mathrm{GeV}$. While PYTHIA-8 produces antiprotons and antineutrons symmetrically and overestimates the antiproton yield by roughly a factor of two, the deviation of EPOS-LHC to the measured antiproton yields are smaller but the antineutron yield is around 1.75 times larger than the antiproton yield, which is exceeding expectations—even when including models of isospin asymmetry—significantly. The full antiproton and antineutron spectra for this collision energy are shown in Figure 3.19a and Figure 3.19b, respectively. To compare the differences in antideuteron yields stemming from only the different particle-particle correlations employed by the two event generators and to obtain the antideuteron yield for single-antinuclei spectra that are consistent with experimental data, we correct the invariant yield of the single antinucleons to the yield obtained by our adapted Winkler model, which accurately described the NA49 data. In addition, we assume isospin symmetric production of antiprotons and antineutrons. To correct the yields of the antinucleons produced by the event generators, we assign a weight, w, to each produced antinucleon of the generators as

$$w(y, p_\mathrm{t}) = \frac{f^{\mathrm{gen}}(y, p_\mathrm{t})}{f^{\mathrm{param}}(y, p_\mathrm{t})}, \tag{3.39}$$

with $f^{\mathrm{gen}}(y, p_\mathrm{t})$ being the invariant production cross section obtained by the event generator and $f^{\mathrm{param}}(y, p_\mathrm{t})$ being the invariant production cross section of the adapted Winkler parameterization. The invariant production cross section of the event generators and the calculated weights are obtained in bins of $\Delta y = 5.9 \times 10^{-2}$ and and $\Delta p_\mathrm{t} = 4.0 \times 10^{-2}\,\mathrm{GeV/c}$ using 1×10^8 collisions. In Figure 3.18, we show exemplarily the obtained weights for the EPOS-LHC event generator.
The weighted particle production yields identical spectra of antiprotons and antineutrons for both event generators. The created antinucleons follow the phase-space distributions

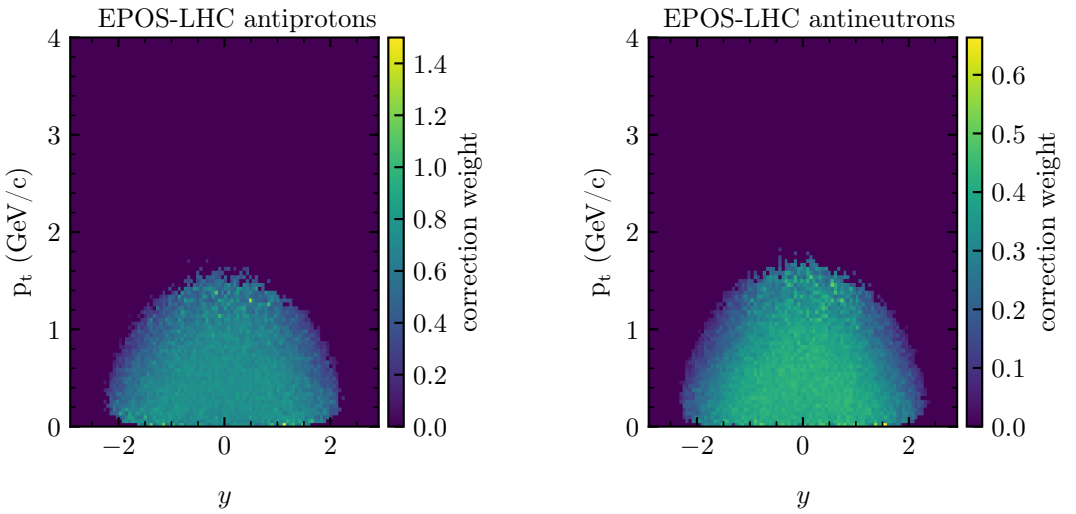

(a) Correction weights for antiprotons.

(b) Correction weights for antineutrons.

Figure 3.18: Binned correction weights for EPOS-LHC antinucleon production.

and yields of our adapted Winkler model, as can be seen in Figure 3.19a and Figure 3.19b. In order to obtain antideuterons event-by-event with the corrected antinucleon yields, we assign to each antiproton-antineutron pair that is produced in an event the weight

$$w_{\bar{\mathrm{d}}} = w_{\bar{\mathrm{p}}} w_{\bar{\mathrm{n}}}, \tag{3.40}$$

with the corresponding weights of the antiproton,$w_{\bar{\mathrm{p}}}$, and antineutron, $w_{\bar{\mathrm{n}}}$. The weights are interpreted as a probability to produce the event given the experimental constraints of the single-particle spectra. The antideuteron spectra for an exemplary value of $p_0 = 150\,\mathrm{MeV}$ without and with the described correction of the single-antinucleon yields are shown in Figure 3.19c and Figure 3.19d, respectively. For each generator we simulate 5×10^8 collisions and the coalescence criterion is checked for each produced antiproton-antineutron pair in each event. If the pair fulfills the criterion, the pair is assigned to form an antideuteron with kinetic energy per nucleon of $E_{\bar{\mathrm{d}}} = (E_{\bar{\mathrm{p}}} + E_{\bar{\mathrm{n}}})/2$.
Comparing the obtained antideuteron spectra with and without the correction, we see that the obtained antideuteron yields are reduced by more than a factor three. For the corrected case, in which EPOS-LHC and PYTHIA-8 inhibit the same single-antinucleon production from the weighting, the yield of antideuterons obtained by PYTHIA-8 is only roughly half of the obtained yield by EPOS-LHC. As the initial antideuteron spectra from EPOS-LHC and PYTHIA-8 by accident coincide, this difference can now be assigned to stem solely from the different particle-particle correlations of the two event generators.
In this small exemplary analysis, we have shown that the differences of antideuteron yields in different event generators stem from both, the different single-antinucleon production and the different modeling of particle-particle correlations. To extract an accurate value of p_0 and an accurate prediction of the cosmic-ray antideuteron flux from collisional production, both processes have to be modeled accurately. Nevertheless, even with the current

uncertainties, the search for antideuterons as a promising approach to improve our limits on exotic antimatter sources or prove their existence.

However, the measurement of the cosmic-ray antideuteron flux—or even the detection of a single cosmic antideuteron—is experimentally very challenging due to the very low flux of antideuterons. This requires experiments with ultra-long measurement time and large geometrical acceptance and also demands new particle-detector concepts, especially for measurements of low-energy antinuclei. Beside AMS-02, which might improve our current limits on the antideuteron flux, several experiments are planned to specifically measure cosmic-ray antinuclei, like exemplarily the upcoming GAPS experiment, or proposed experiments like ADHD, or GRAMS [9].
In the next chapter I describe a novel detector approach which identifies particles solely using the characteristic interactions of them with the detector material and is omnidirectionally sensitive, which results in a large geometrical acceptance for a given system size. Considering the scalablity of the concept, the detector system might be a potential experimental approach for future measurements of antinuclei.

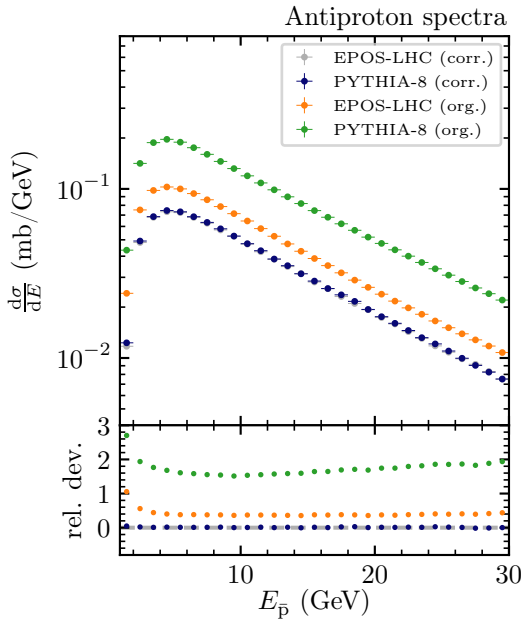

(a) Antiproton spectra

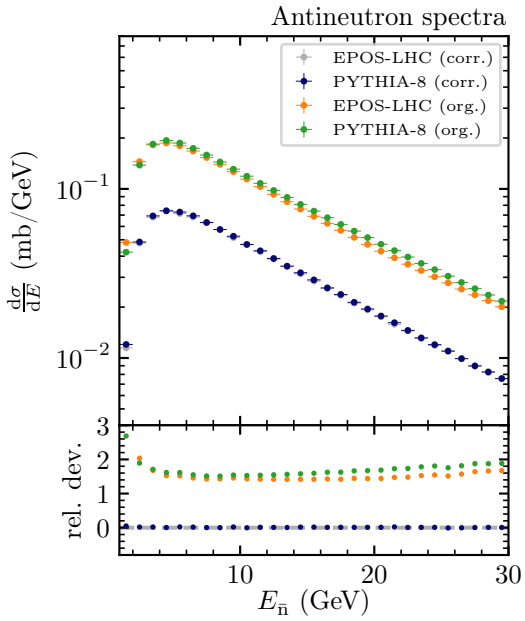

(b) Antineutron spectra

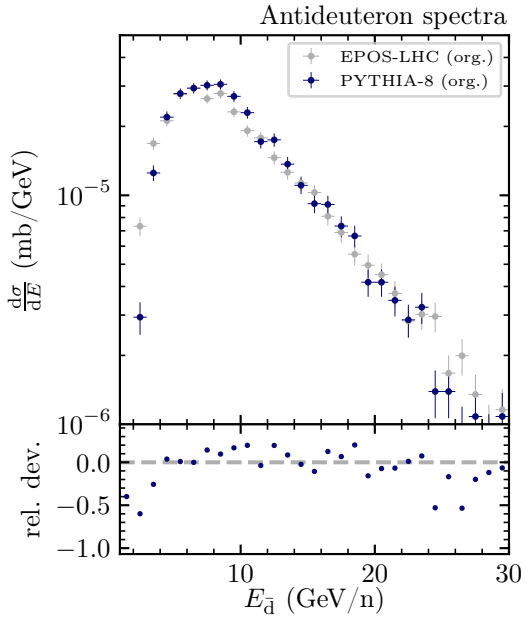

(c) Antideuteron spectra without correction

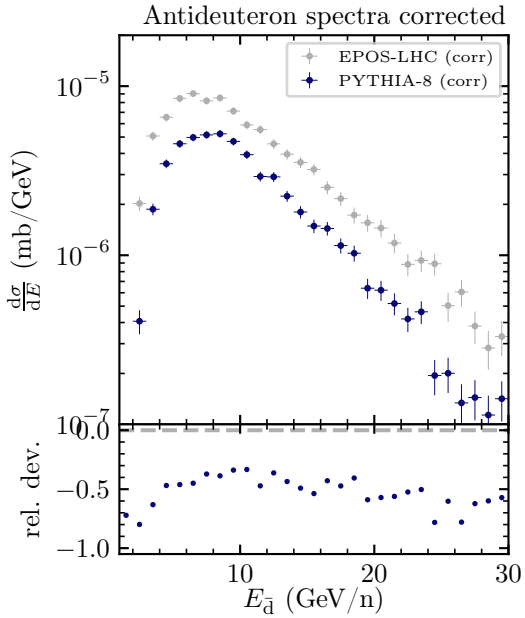

(d) Antideuteron spectra from corrected single-nucleon spectra

Figure 3.19: Obtained antiproton, antineutron, and antideuteron spectra at $\sqrt{s} = 17.3\,\text{GeV}$ from EPOS-LHC and PYTHIA-8 obtained with and without correction of the single-antinuclei spectra.

Chapter 4

A Multi-Purpose Active-Target Particle Telescope for Cosmic Rays

The Multi-purpose Active-Target Particle Telescope (MAPT) is a particle detector that is currently under development at the Technical University of Munich. The detector shall allow omnidirectional measurements of cosmic-ray nuclei and antinuclei in space, while being compact, lightweight, and low-power demanding to be deployable on a variety of spacecrafts—even CubeSats with sizes of only a few tens of centimeters in each dimension. The detector consists of a stack of scintillating-plastic fibers coupled to silicon photomultipliers. The identification of charged particles is based on their energy-loss characteristics in the detector's material. MAPT's concept is easily scalable and larger versions of the detector can be realized to increase the sensitivity of the detector to probe rare cosmic-ray particles such as antinuclei.
The development of the detector also serves educational purposes and many subtasks of the development have been performed by students in the scope of their Bachelors' and Masters' theses. A list of MAPT-related theses that have been co-supervised by the author is given in Appendix D. In this work, I focus on the developed concepts of the particle-reconstruction scheme and the designed algorithms to analyze the detector signals in MAPT.
In Section 4.1, I describe the layout of the detector and the basics of the particle-identification principle, which is based on the ionizing interactions of the charged cosmic-ray particle with the detector material. In Section 4.2, I discuss the signal-generation processes of the scintillating plastic fibers and the silicon photomultipliers and highlight the physical effects that affect the particle-reconstruction capabilities of MAPT. Most important are saturation effects of the scintillator, so-called ionization quenching. After assessing the magnitude of the effect experimentally in Section 4.3, I estimate the impact on the particle-identification capability of MAPT. In Section 4.4, I describe the planned reconstruction algorithms to identify the particle species, the direction, and the energy of a particle that hits MAPT. I present two algorithms for the reconstruction: one based on a Bayesian particle filter, which is intended to be used for a detailed analysis of the recorded detector data after transmission to ground; and one based on neural networks to analyze the measured particle events in near real-time directly on the on-board computer of MAPT, which is required for applications with a limited data-transmission contingency. I evaluate the performance

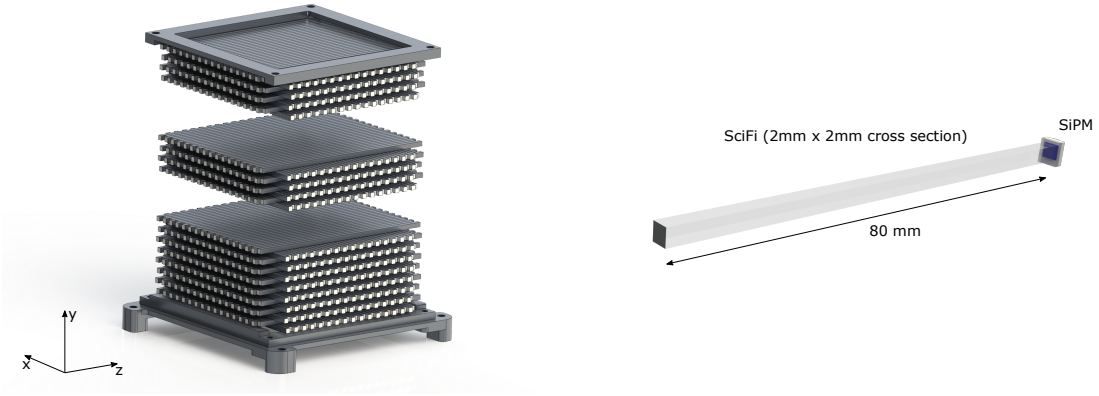

(a) Exploded view of MAPT's fiber stack. (b) Schematic view of a fiber coupled to a SiPM.

Figure 4.1: The active tracking volume of MAPT, consisting of 1024 scintillating-plastic fibers coupled to SiPMs.

of both algorithms for light nuclei using simulated detector data. In Section 4.5, I present two planned technology demonstration missions in which the functionality of the MAPT concept shall be demonstrated: The measurement of the radiation environment inside of the International Space Station, and the measurement of geomagnetically trapped antiprotons on a CubeSat. Concluding, I give an outlook on the possibility of cosmic-ray antinuclei measurements using a particle detector based on the concept of MAPT in Section 4.6.

4.1 Detector Layout and Detection Principle

MAPT consists of a stack of 1024 scintillating plastic fibers, each 80 mm long with a $(2 \times 2)\,\mathrm{mm}^2$ cross section coupled at one end to a silicon photomultiplier (SiPM). A charged particle that traverses a scintillating fiber transfers part of its kinetic energy into scintillation light due to electromagnetic interactions [235]. The so-created scintillation light travels along the fiber and is detected by the silicon photomultiplier, a state-of-the-art photon detector which creates an electrical signal that we can digitize and record using a suitable data-acquisition system [236].
Figure 4.1b depicts one of the 1024 individual fiber-SiPM channels of MAPT. The fibers are arranged in 32 layers of 32 fibers each, spanning a segmented, cube-shape volume that is sensitive to charged particles traversing it from all directions. The fiber layers are rotated by 90° with respect to their neighboring layers to allow a three-dimensional reconstruction of the particle's track within the volume. I refer to the two different oriented arrays of fibers as different projections. Each second layer per projection is additionally shifted by half a fiber width (1 mm) with respect to the former layer of the projection to increase the effective spatial resolution within the tracking volume.
Figure 4.1a shows an exploded view of the fiber stack. A typical representation of the resulting hit pattern in the detector from a traversing particle is shown in Figure 4.2. The displayed event shows the simulated signals created by a 3 GeV proton. The simulation is performed using Geant4, a toolkit for the simulation of the passage of particles through

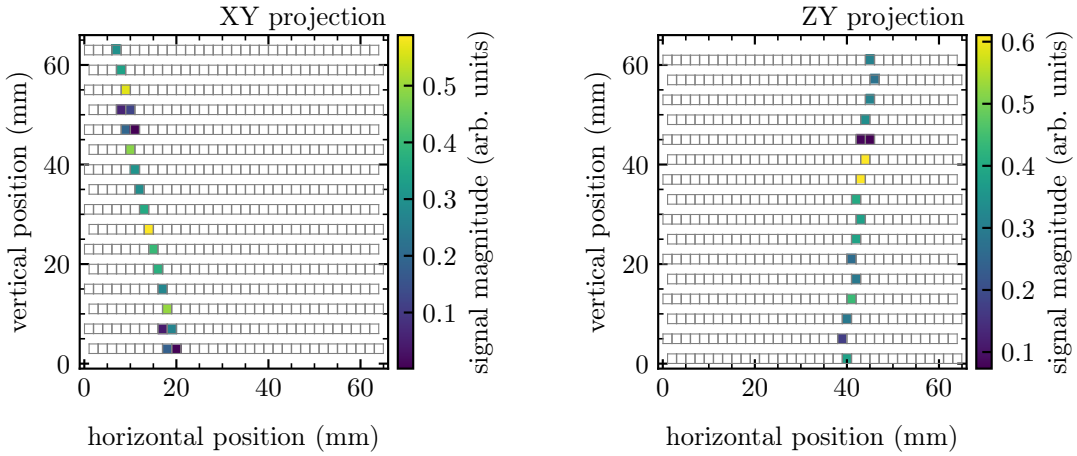

Figure 4.2: Representation of a simulated particle event in MAPT. The two projections show the signals obtained for the two perpendicular fiber orientations. The gray squares depict all fiber positions for the corresponding projection.

matter [237]. The two projections, labeled as XY and ZY, show the obtained signals in all fibers of MAPT separated into the two projections. Following the definition of the coordinate system shown in Figure 4.1a, the XY and ZY projections correspond to the projections in which the fibers' end surfaces are aligned within the XY and ZY plane, respectively. From the hit pattern in both projections we can reconstruct the full three-dimensional particle track through the detector.
In addition to the geometrical information of the particle's track, we aim to use the signal strength in the individual fibers and the change of the signal strength along the particle's track to reconstruct the characteristics of the nuclei, such as its charge number, mass number, and kinetic energy. To achieve this, we must extract the stopping power of the particle along its track within the detector from the signals in the individual fibers. The stopping power is an informative observable to infer characteristics of the traversed particle, especially if the particle stops in the detector [235].
In the following, I briefly review the physical process of electronic energy loss of heavy charged particles in matter, and I introduce the concept of Bragg-curve spectroscopy, which can be used to identify the charged particle using the energy-loss profile along its track.

4.1.1 Energy Loss of Nuclei in Matter

Charged particles that traverse matter interact electromagnetically with the atoms of the material. More specifically, heavy charged particles—those with masses on the order of the proton mass and thus much larger than the mass of the electron—most probably scatter elastically on the material's nuclei or inelastically on the material's electrons [235]. While the former mainly leads to a change of the particle's direction, the latter leads to an

energy transfer from the particle to the electron. Although the energy transferred in a single collision is often small compared to the kinetic energy of a fast particle, only on the order of a few hundred eV, the large density of electrons in the material results in many interactions during the passage of the particle and thus in a non-negligible total energy loss [21]. This transferred energy is often called 'electronic energy loss'. The electronic energy loss divided by the path length through the material is called 'stopping power'. The electronic energy loss is the dominant energy-loss mechanism for nuclei in matter at the for us relevant energies of a few MeV/n and above.
Although the energy loss is of statistical nature and can for a single particle only be predicted with a limited certainty, the Bethe formula can be used to calculate the mean stopping power, $\langle -\mathrm{d}E/\mathrm{d}x \rangle$, for a nucleus with kinetic energy, E, velocity, β, and charge, z, as

$$\left\langle -\frac{\mathrm{d}E}{\mathrm{d}x} \right\rangle = \frac{4\pi e^4 z^2}{m_0 c^2 \beta^2} AZ \left[\ln \frac{2m_0 c^2 \beta^2}{I} \ln\left(1-\beta^2\right) - \beta^2 \right], \tag{4.1}$$

with A and Z being the average mass and charge number of the stopping material and I its average ionization and excitation potential, which has to be extracted experimentally for each material [235]. A list of values of I for different materials was for example collected by Seltzer et al. [238]. For non-relativistic particle velocities, $\beta \ll 1$, the stopping power increases in good approximation quadratically with decreasing velocity. At large velocities, the stopping power increases logarithmically with increasing velocity. In between, at around $\beta\gamma \approx 3$, the stopping power reaches a minimum. Particles with such a minimal stopping power are often referred to as minimum-ionizing particles (MIPs) [21]. The Bethe formula is valid for kinetic energies of nuclei between approximately 0.1 MeV/n and a few TeV/n
The stopping power of several different nuclei in polystyrene—the base material of our detector—as a function of kinetic energy per nucleon is shown in Figure 4.3a exemplarily for protons ($z = 1$), helium-4 ($z = 2$), and lithium-7 ($z = 3$). The values are extracted from Geant4 [237]. Clearly visible is the z^2-dependence of the stopping power on the particle's charge. Visualizing the stopping power of different ions as a function of the kinetic energy per nucleon, which results in identical particle velocities for a given energy per nucleon, reveals the identical trend of the stopping power for the different particles. At around 3 GeV/n, all nuclei reach their minimum-ionizing regime.
One consequence of the steep increase of the stopping power for nuclei below 1 GeV is that these particles deposit most of their kinetic energy shortly before stopping in the material due to the electric energy loss [239]. The mean range of a particle in a material can be obtained by integrating the reciprocal of the stopping power from the particle's initial energy down to approximately zero. [1] The method to obtain the mean particle range like this is called continuous-slowing down approximation (CSDA). Within the CSDA, the obtained range is slightly overestimated with respect to measurements as the CSDA does not take into account the effective prolongation of the particle's path length due to multiple scattering [240]. However, this effect is relevant only for particles below approximately 1 MeV/n

[1] Below a few hundred keV per nucleon the Bethe formula fails to describe the stopping power accurately and other models have to be used to describe the stopping power for even lower energies. However, for our application the residual energy and range of particles below this energy can be neglected, introducing only uncertainties on the order of a few-hundred keV per nucleon or several micrometer for the range.

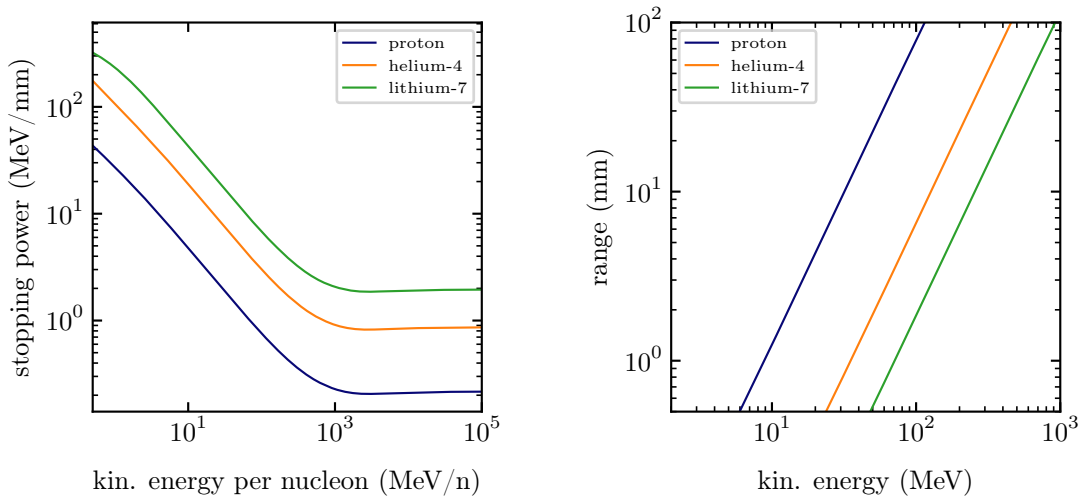

(a) Stopping power in polystyrene.

(b) CSDA range in polystyrene.

Figure 4.3: Mean stopping power and range of different ions in polystyrene. The range is calculated by the continuous-slowing-down approximation (CSDA). Both values are extracted from GEANT-4 [237].

in polystyrene [241]. The CSDA ranges for protons, helium-4, and lithium-7 in polystyrene as a function of the their kinetic energies are shown in Figure 4.3b. For kinetic energies below 100 MeV for protons, 400 MeV for helium-4, and 700 MeV for lithium-7, the ranges of the nuclei are comparable with the size of MAPT, allowing us to stop them within the detector.

The change of the energy deposition along the track of a nucleus as a function of the depth in the material before it is completely stopped follows the so-called Bragg curve [235]. The shape of the Bragg curve is unique for a certain particle type with a given energy. From a recorded Bragg curve from an energetic nucleus, the charge number, mass number, and the initial kinetic energy—the energy before entering the detector volume—can be reconstructed. Figure 4.4a exemplary shows Bragg curves of 250 MeV/n protons and alpha particles which slowed down in high-density polyethylene, measured by the Brookhaven Science Associates [242]. The stopping power is normalized to one at depth zero, and the Bragg curve of helium-4 is additionally scaled by the ratio of the stopping power of protons and helium-4 particles at 250 MeV/n to visualize the absolute difference of the Bragg curves stemming from the different charges of the two nuclei. The typical shape of the Bragg curve is clearly visible for both nuclei: Both have a rather constant energy deposition in the beginning and a steep increase shortly before stopping. For a completely stopped nucleus, the integral of the Bragg curve corresponds to the initial kinetic energy of the nucleus; the depth at which the nucleus stops, the range, is related to the charge, mass, and initial velocity of the nucleus; and the maximum value of the Bragg curve, the so-called Bragg peak, depends only on the charge of the nucleus. Using these observables, one can reconstruct the characteristics of the nucleus that stopped in the detector. This method is called Bragg-curve spectroscopy and was developed by C. R. Gruhn et al. in

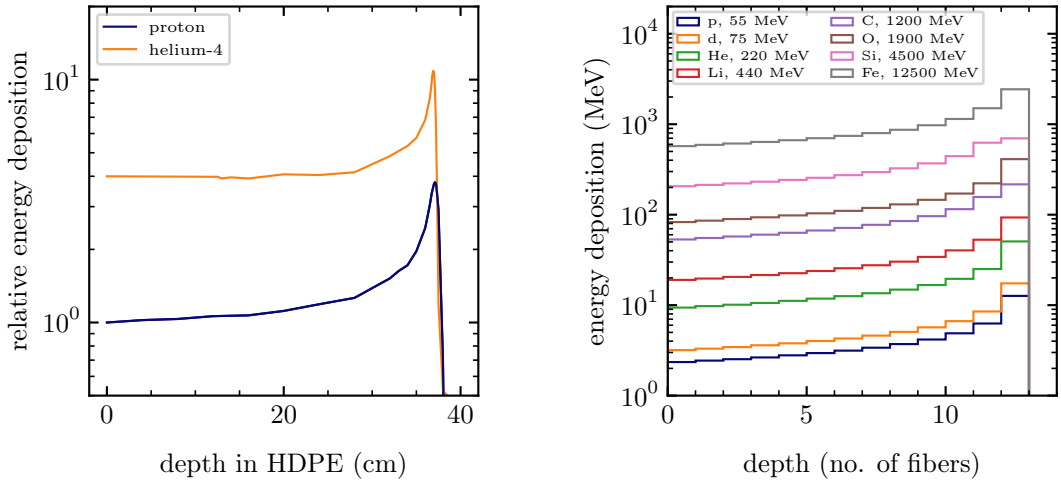

(a) Normalized stopping power in high-density polyethylene, as measured by the Brookhaven Science Associates [242].

(b) Bragg curves in a segmented detector like MAPT.

Figure 4.4: Bragg curves for different particles.

1982 [243].
In a segmented detector like MAPT, however, we cannot directly measure the stopping power itself but only the integrated stopping power per traversed fiber, the deposited energy, ΔE. It depends not solely on the stopping power but also on the path length of the particle in the fiber. The deposited energy is given as the integral over the stopping power along the particle's track through the fiber as

$$\Delta E = \int_{x_{\text{in}}}^{x_{\text{out}}} \left\langle \frac{\mathrm{d}E}{\mathrm{d}x} \right\rangle \mathrm{d}x, \tag{4.2}$$

with x_{in} and x_{out} the entrance and exit point of the track in fiber. For tracks that penetrate MAPT perpendicular to the fiber layers, the track length per fiber is constant and the obtained Bragg curves are very similar to the previously shown unsegmented case. Figure 4.4b exemplarily shows the segmented Bragg curves in MAPT for different particle species with similar range and constant track length per fiber. For tracks that penetrate the detector not perpendicular to the fiber layers, the track length in the different fibers can vary, and the shape of the Bragg curve is distorted. In order to still reconstruct the particle characteristics from the underlying Bragg curve for such events, the direction and location of the track in the detector must be reconstructed simultaneously to constrain the track length per fiber.
For particles that are too energetic to be stopped completely in the detector, the Bragg curve is not completely recorded and extrapolation techniques must be applied to be still able to characterize the particle, as exemplarily done by Terasa et al. [244]. The reduced

information of these events, however, increase the uncertainty of the energy reconstruction and particle identification.
In Section 4.4 we show two algorithms based on Bragg-curve spectroscopy to determine the energy and identify the species of a traversing nucleus from the MAPT data: one based on a Bayesian particle filter and one using neural networks.

4.1.2 Annihilation of Antinuclei

From Bragg curve spectroscopy alone we cannot distinguish particles from their antiparticles as the stopping powers of nuclei and antinuclei with equal energy are mostly identical and the energy deposition along the track in MAPT for both are equal.[2] However, during slowing down, antinuclei are likely to annihilate with the nuclei of the detector material [246]. In such annihilation events, the incoming antinuclei disintegrate and several neutral and charged secondary particles emerge from the annihilation vertex [119]. As the annihilation probability increases with decreasing velocity, low-energy antinuclei that enter MAPT will to a certain proportion first slow down—depositing energy according to their Bragg curve—before annihilating and creating secondary particles [179]. This gives a unique distribution of fiber hits, which I call 'hit pattern' in the following, in the detector that can be used to distinguish a particle from its antiparticle.
To visualize this concept, Figure 4.5 compares the different hit pattern of a stopped proton (Figure 4.5a) to that of an annihilated antiproton (Figure 4.5b) with identical initial kinetic energies of 50 MeV. While slowing down, both particles deposit their energy similarly in the detector, following the same Bragg curve. For the antiproton, an additional star-like pattern created by emerging secondary charged particles from the annihilation process is visible. These tracks are created by several charged pions and nuclei that emerge from the annihilation together with several neutral particles that leave the detector unnoticed. A detailed investigation of the annihilation process of antiprotons on polystyrene has been conducted in the Master's thesis of the author, obtaining that in average around four additional charged particle tracks are visible in the detector [180]. For heavier antinuclei, such as antideuterons or antihelium, even more charged secondary particles are expected to be created and the multiplicity of the secondary particles can potentially be used as a second observable to distinguish different types of antinuclei beside by their Bragg curve [247].

The identification of the species of both antinuclei and nuclei in MAPT, using Bragg-curve spectroscopy, requires an accurate reconstruction of the deposited energy of the particle in the fibers from the measured signals. However, the signal generation of a scintillating fiber coupled to a silicon photomultiplier is complex. In order to find the accurate relation between the measured signal and the deposited energy, we require an accurate description of the involved physical processes. The relation between the deposited energy and the signal magnitude measured in a channel of MAPT is also required to generate accurately simulated data to test and verify the developed particle-reconstruction algorithms due to the unavailability of appropriate experimental data for the detector currently in development. For this purpose, the simulated data must be as realistic as possible to allow an accurate performance measurement of the algorithms and to exclude potential systematic

[2] Neglecting the Barkas effect, which is only significant for kinetic energies below 1 MeV [245].

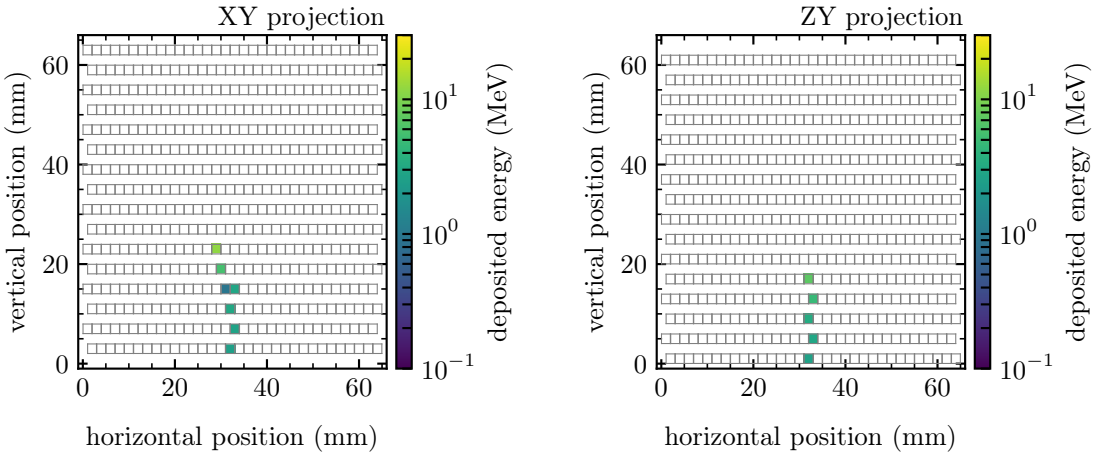

(a) Stopping proton.

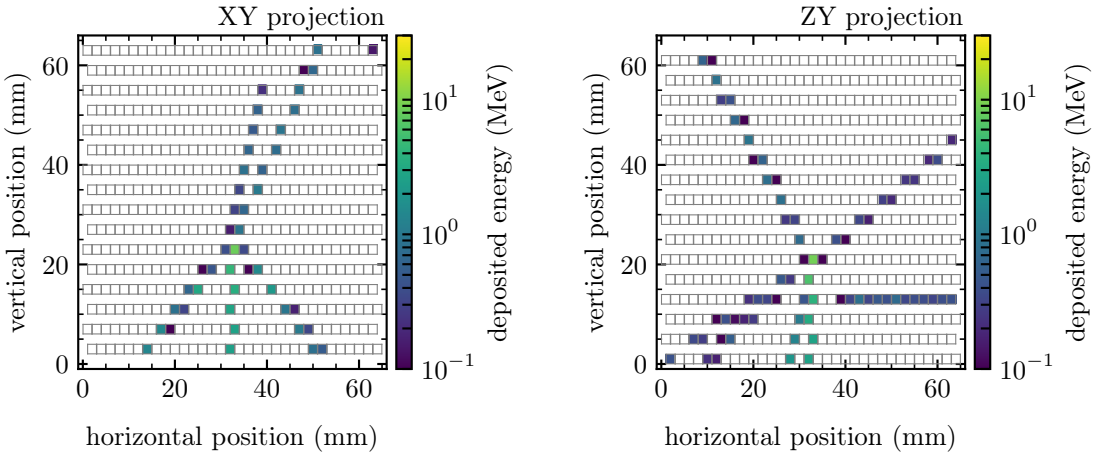

(b) Annihilating antiproton.

Figure 4.5: Comparison of the hit pattern in MAPT for a stopping proton and an annihilating antiproton with 50 MeV initial kinetic energy each. The initial particles enter from below at approximately central position (30 mm).

errors stemming from the event-reconstruction scheme. This is of particular importance for our neural-network-based reconstruction algorithm that employs a supervised-learning approach using simulated data (see Section 4.4.3.2).
In the following, I discuss the most important effects that must be taken into account to reconstruct the deposited energy in a fiber from the recorded signals.

4.2 Signal Generation

The signal generation in a single fiber-SiPM channel of MAPT involves several processes: First, a fraction of the electronic energy loss of the traversing charged particle is converted into scintillation light; the produced light subsequently spreads within the fiber and some of the photons are transported to the SiPM, which is glued to one end of the fiber; the photons that hit the SiPM eventually create an electrical pulse that is converted by an analog-to-digital converter into a digital signal and recorded by the data acquisition system. To relate the magnitude of the obtained recorded signal to the magnitude of the energy deposition in the fiber, the relations of all the sub-processes have to be known for each of the 1024 fiber-SiPM systems of MAPT. Although most relations are linear and require only a calibration with a known signal magnitude, some effects might introduce non-linear relations that can affect the reconstruction capability of MAPT. Especially saturation effects worsen the achievable separation power of nuclei and antinuclei and the energy resolution.

4.2.1 Relevant Detector Components

In the following, I shortly introduce the relevant parts of MAPT for the signal generation: the scintillating fibers, the silicon photomultipliers, and the data-acquisition system. I focus on effects that influence our event reconstruction, and I discuss their impact.

4.2.1.1 Scintillating Plastic Fibers

The active tracking volume of MAPT consists of scintillating-plastic fibers of type SCSF-78, produced by Kuraray [248]. The scintillator is made from polystyrene and several proprietary admixtures, so-called dopants, which are added to the plastic to increase the scintillation-light yield of the fiber. In addition, the fiber has a cladding of polymethylmethacrylate (PMMA) to increase the efficiency of the light transport to the SiPMs by improving the internal-reflection probability of the created photons along the fiber. The thickness of the cladding is 4 % of the total fiber thickness [248]. Within the cladding, no scintillation light is created by the traversing charged particle. Additionally, all surfaces but the end surface that is glued by optical glue to the SiPM are coated by a thin layer of aluminum (a few hundred nm) to prevent scintillation light from leaving the fiber and generating a signal in a SiPM of another fiber.
The average number of scintillation photons created by unit of distance of a traveling charged particle in the scintillator is in general linearly dependent on the mean electric energy loss of the particle. The mean light yield per unit distance can be written as

$$\left\langle \frac{\mathrm{d}L}{\mathrm{d}x} \right\rangle = S \left\langle \frac{\mathrm{d}E}{\mathrm{d}x} \right\rangle , \tag{4.3}$$

with S being the specific light yield of the scintillator [249]. Although the exact value of S is heavily dependent on the dopant molecules added, and has to be experimentally determined for each scintillator type individually, typical values for polystyrene-based scintillators are on the order of 1×10^4 photons/MeV [235].
For large values of $\langle \mathrm{d}E/\mathrm{d}x \rangle$, which occur during the stopping of nuclei and antinuclei,

several authors found that the dependence of the light yield on the energy loss becomes non-linear due to saturation effects of the scintillation mechanism. This effect is called ionization quenching [249]. As large stopping powers occur especially during the slowing-down process of nuclei near their Bragg peak, a detailed quantification of this effect is crucial for our application. I therefore discuss the effect explicitly in more detail and investigate it experimentally in Section 4.3.
The scintillation photons are created isotropically at the location of the traversing charged particle and only a small fraction of the produced light reaches the SiPM. The rest of the produced photons is absorbed in the aluminum cladding of the fibers. The fraction of photons that in total reaches the SiPM, however, is independent of the initial light yield. In principle, one would expect the fraction of the produced light that reaches the SiPM to depend on the location of its production along the fiber due to an increased re-absorption probability and decreased transport efficiency with increasing distance to the SiPM. However, due to the short length of our fibers, no such a dependency was found experimentally and measured signal magnitudes are constant within 10 %.
In summary, the scintillation process and the subsequent light transport to the SiPM retains the linear relation between the deposited energy and the scintillation light that reaches the SiPM. Only for highly ionizing radiation the ionization-quenching effect disrupts this relation and requires further investigation.

4.2.1.2 Silicon Photomultipliers

To ease the assembly, the $(2\times2)\,\mathrm{mm}^2$ fibers are read out by $(3\times3)\,\mathrm{mm}^2$ SiPMs. The SiPMs are attached on alternating ends of the fibers in a layer to assure a complete overlap of each fiber end with the active area of the corresponding SiPM. A SiPM is an array of micro avalanche photodiodes, called cells, that are interconnected in parallel [236]. For MAPT we use PM3325 SiPMs manufactured by KETEK, which consist of 14400 cells each, with each cell having a size of $(25 \times 25)\,\mu\mathrm{m}^2$ [250].
The cells are reversed biased above their breakdown voltage, so that a photon entering them and being absorbed by the silicon triggers a charge avalanche that leads to a complete discharge of the cell. The charge signal from the breakdown is independent of the number of photons that have hit the single cell and constant for a given bias voltage. Only when photons hit different cells of the SiPM simultaneously—each photon triggering a breakdown of one cell—the total created signal is proportional to the number of absorbed photons. Due to the large number of cells of a SiPM, the probability for multiple photons hitting the same cell is small, and the produced signal is proportional to the amount of photons. When a large amount of photons hits the SiPM simultaneously, a non-linear response of the signal to the number of photons hitting the SiPM can occur since the probability for several photons to hit the same cell cannot be neglected anymore. From a probabilistic approach of the spatial photon distribution over the surface of the SiPM, one can deduce the average number of cell breakdowns, N_{av}, as a function of the number of photons hitting the SiPM, N_γ, as

$$N_{\mathrm{av}} = N_{\mathrm{pixel}} \left(1 - e^{-\frac{\epsilon_{\mathrm{PDE}} N_\gamma}{N_{\mathrm{cells}}}}\right), \tag{4.4}$$

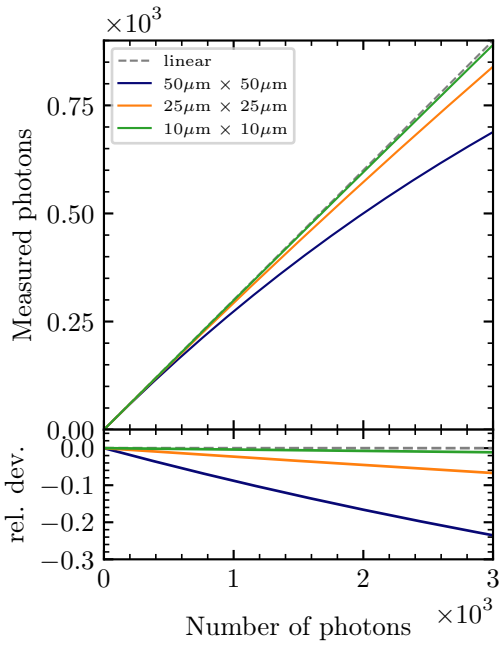

Figure 4.6: Effect of SiPM saturation for different cell sizes of the SiPM for large light yields using $\epsilon_{\mathrm{PDE}} = 0.3$, a typical value of the photon-detection efficiency. The shown range depicts roughly the range of signals expected in MAPT.

with N_{cells} being the number of cells of the SiPM and ϵ_{PDE} the probability of a photon to create a cell breakdown [236]. ϵ_{PDE} is the product of the probability of the photon to hit a cell of the SiPM, which is not unity as the surface of the SiPM has non-active structures in between the cells covering around 30 % of the surface, and the probability that a photon hit on a cell creates an breakdown, which is around 45 % and depends on the applied bias voltage [250].
Figure 4.6 shows the relation of Equation 4.4 for different cell sizes of $(50 \times 50)\,\mu\mathrm{m}^2$, $(25 \times 25)\,\mu\mathrm{m}^2$, and $(10 \times 10)\,\mu\mathrm{m}^2$ and an active area of $(2 \times 2)\,\mathrm{mm}^2$ and the relative deviation of the measured signal to the actual number of photons hitting the SiPM given a constant photon detection efficiency for all SiPMs. The range of the number of photons shown corresponds to the range of expected signals in MAPT assuming 200 photons per MeV energy deposition as it was measured during a prototype test in 2014, and a maximum effective energy deposition of around 15 MeV per fiber after accounting for ionization quenching [180]. Using a SiPM with a larger number of cells is advantageous to minimize the influence of the saturation of the SiPM. However, a larger cell number also decreases the overall photon detection efficiency as the amount of the non-active surface on the SiPM increases, reducing the sensitivity of the SiPM for low light yields. In a first prototype measurement in 2014, the effect of SiPM saturation using $(50 \times 50)\,\mu\mathrm{m}^2$ has been encountered [180], and we decided for MAPT to use SiPMs with $(25 \times 25)\,\mu\mathrm{m}^2$ cells to reduce the non-linearity of this effect to an acceptable level (less than 10 %).

4.2.1.3 Data Acquisition System

The electrical signals from the SiPMs need to be digitized and recorded to be analyzed by event-reconstruction algorithms. The data acquisition system of MAPT is currently under development and is planned to be based on the IDE3380 integrated circuit for the readout of photosensors by Integrated Detector Electroncis AS [251]. The magnitude of the SiPM signal is digitized by a 12-bit analog-to-digital converter. Such systems generally obtain a very good linearity between the incoming signal magnitude and the digitized value that represents the signal magnitude. The main challenge for the DAQ system is to provide a large enough dynamic range to be able to record small SiPM signals, as they are created by minimum ionizing particles traversing our fiber, up to very large signals as they are produced by stopping nuclei. The concept, development, and an estimate of the performance of the data-acquisition system for MAPT will be given in the upcoming PhD thesis by M. Losekamm [252].
As the final data-acquisition system is not yet fully characterized, its influence on the reconstruction capability of the deposited energy in a channel is not yet known and is not considered in the performance tests of the reconstruction in this work. However, we expect that any non-linearity of the DAQ system is small compared to the non-linear effects induced by SiPM saturation and ionization quenching. The latter is expected to be the most limiting effect for MAPT. In the following I investigate this effect in more detail.

4.3 Measurement of Ionization Quenching

The magnitude of ionization quenching is dependent on the scintillator type and has not yet been investigated for SCSF-78 plastic fibers. I proceed with a description of our measurement of the ionization-quenching effect for this scintillator type using a beam of stopping protons. We compare different ionization-quenching models to our data to find the most suitable analytical dependence of the quenching magnitude on the stopping power of the traversed particle. To verify our method, we also probe the quenching magnitude for a second plastic scintillator for which measurements of the ionization-quenching effect exist. In addition, we also use a model-independent approach to describe the quenching effect that allows us to probe the agreement of the different ionization-quenching models with our data.

The following description of the different quenching models, the experimental method, and the results of our experiment—Section 4.3.1 through Section 4.3.4—have been published in *Nuclear Instruments and Methods in Physics Research A*, Volume 988, as part of our article *Measurement of ionization quenching in plastic scintillators* in 2021 [253] and is reprinted here.

4.3.1 Quenching Models[3]

The response of a scintillating material to a charged particle is characterized by its light yield per unit of distance traveled by the particle, $\mathrm{d}L/\mathrm{d}x$. However, the light yield per unit

[3] Section reprinted from [253]

of energy deposited by the particle over that distance, $\mathrm{d}L/\mathrm{d}E$, is more useful in modeling and simulation. The two are related to each other by

$$\frac{\mathrm{d}L}{\mathrm{d}x} = \frac{\mathrm{d}L}{\mathrm{d}E} \cdot \frac{\mathrm{d}E}{\mathrm{d}x}, \tag{4.5}$$

where $\mathrm{d}E/\mathrm{d}x$ is the energy lost by the particle per unit of distance, which depends on the energy of the particle (as well as its species and the scintillator material). To simplify our equations, we denote $\mathrm{d}E/\mathrm{d}x$, a function of the particle's kinetic energy, T, as $\epsilon(T)$. The light yield per unit of energy deposited is a function of ϵ, and therefore indirectly of T:

$$\left.\frac{\mathrm{d}L}{\mathrm{d}E}\right|_T \equiv S \cdot Q(\epsilon(T)), \tag{4.6}$$

where $Q(\epsilon)$ is the unitless quenching function, defined such that at small ϵ (that is, at high kinetic energy), it goes to unity; S is the linear proportionality of light yield to energy deposition at high energy and has units of photons per energy. So the light yield per unit of distance is

$$\left.\frac{\mathrm{d}L}{\mathrm{d}x}\right|_T = \epsilon(T) \cdot S \cdot Q(\epsilon(T)). \tag{4.7}$$

Scintillation light is produced via several steps [249]: a passing particle ionizes molecules of the scintillator's base plastic material, which then emit light. In a pure plastic, this light is quickly reabsorbed by other molecules. To allow the light to propagate further, the plastic is doped with a molecule that absorbs this light and emits light of a shifted wavelength. Since neither the base molecule nor the dopant efficiently absorbs the wave-length-shifted light, it propagates long distances. However, dopant molecules can absorb photons without re-emitting them or can re-emit them at wavelengths unsuitable for detection. This occurs when they have been excited by interaction with the ionizing particle.

J. B. Birks developed the first model of ionization quenching in the early 1950s, which is still widely used [249]. He parametrized quenching in terms of the density of excited dopant molecules, B, and the probability for non-radiative relaxation, k:

$$Q_{\mathrm{Birks}}(\epsilon) = 1/(1 + kB\,\epsilon). \tag{4.8}$$

Since k and B appear only as a product, they act as one parameter, kB, called Birks' coefficient, which has units of distance per energy. Its value depends on the scintillating material.

Many authors have extended Birks' model: Chou *et al.* accounted for secondary effects by adding a term to the denominator that is second order in ϵ:

$$Q_{\mathrm{Chou}}(\epsilon) = 1/(1 + kB\,\epsilon + C\epsilon^2), \tag{4.9}$$

where $\sqrt{C}$ has the same units as kB [254, 255]. Wright *et al.* defined the phenomenological quenching function

$$Q_{\mathrm{Wright}}(\epsilon) \equiv \frac{1}{W\epsilon}\log(1 + W\epsilon), \tag{4.10}$$

where W has the same units as kB [256]. Voltz *et al.* developed the first model to distinguish between primary and secondary ionization: The primary particle can produce high-energy electrons as it ionizes the scintillator molecules. They travel away from the path of the primary particle, losing energy via ionization of the scintillator and spreading out the energy deposition, which weakens quenching. The Voltz model assumes that a fraction of deposited energy, f, is unquenched and parametrizes the quenching of the remaining fraction with an exponential function:

$$Q_{\text{Voltz}}(\epsilon) \equiv f + (1-f)e^{-V(1-f)\epsilon}, \tag{4.11}$$

where V has the same units as kB [257].
Like Birks' coefficient, C, W, and V all depend on the scintillator material. All four must be positive and are independent of the species of the particle interacting with the scintillator. The Voltz model's f depends on both the scintillator material and primary particle species [258]. None of the parameters can be predicted from first principles—all must be measured experimentally.
These quenching functions have some common features: As we require of a quenching function, they are all bounded by 1 above, which is approached as $\epsilon \to 0$; and by 0 below, which may be approached as $\epsilon \to \infty$. All have negative first derivatives ($\mathrm{d}Q/\mathrm{d}\epsilon$) everywhere regardless of their parameters and therefore always monotonically decrease. Birks', Wright's, and Voltz' functions all have positive second derivatives everywhere regardless of their parameter values; only Chou's function allows for a negative second derivative and a potential inflection point. These properties will be important when we compare model-dependent and model-independent results.

4.3.2 Quenching Measurement[4]

To determine each model's parameters and which model most accurately describes quenching, we measure $\mathrm{d}L/\mathrm{d}E$ at several kinetic energies and fit the parameterizations of $Q(\epsilon)$ to this data using equation (4.6).
Many issues complicate this task: We cannot directly measure $\mathrm{d}L/\mathrm{d}E$; instead we measure the amount of light, L, produced by a particle that has lost energy in the scintillator. So we must integrate equation (4.6):

$$L(T^{\text{in}}, T^{\text{out}}) = S\int_{T^{\text{out}}}^{T^{\text{in}}} Q(\epsilon(T))\ \mathrm{d}T\,, \tag{4.12}$$

where T^{in} and T^{out} are the incoming and outgoing kinetic energies of the particle. Q is not directly a function of T, but instead of $\epsilon(T)$, which is a stochastic function: At a particular kinetic energy, we know the mean energy loss per unit distance for particles with that energy from both the Bethe formula and experiment [186, 240]. But an individual particle's energy loss stochastically deviates from the mean according to distributions whose shapes are also T dependent [240, 259, 260]. This stochastic behavior is difficult and computationally

[4] Section reprinted from [253]

expensive to model. So instead of studying the behavior of individual particles, we study the behavior of an ensemble of particles. We measure the distribution of $L(T^{\text{in}}, T^{\text{out}})$ and fit the quenching model parameters to the mean amount of light, $\bar{L}$, produced by an ensemble of particles given a mean energy loss, $\bar{\epsilon}$:

$$\bar{L}(\bar{T}^{\text{in}}, \bar{T}^{\text{out}}) = S \int_{\bar{T}^{\text{out}}}^{\bar{T}^{\text{in}}} \bar{Q}(\bar{\epsilon}(T))\, \mathrm{d}T\,, \tag{4.13}$$

where $\bar{T}^{\text{in}}$ and $\bar{T}^{\text{out}}$ are the mean incoming and outgoing kinetic energies of the ensemble and $\bar{Q}$ is the quenching function of the mean energy of an ensemble. We assume quenching of the mean energy loss is described identically to quenching of the stochastic energy loss: $\bar{Q} = Q$.

The above equations are further complicated by how the scintillation light is measured: it propagates through the scintillator to a light detector. Both propagation and detection cause losses of light. In our experimental setup, these losses linearly scale the light yield and can be canceled out by measuring with respect to a reference light yield. To simplify our calculations, we measure with respect to the signal produced by a particle with $\epsilon x \ll T$ for distances, x, even much larger than our setup. To very good approximation, the light yield of such a particle is

$$\bar{L}_{\text{ref}} = S \int_{\bar{T}-\bar{\epsilon}_{\text{ref}}\bar{x}}^{\bar{T}} \bar{Q}(\bar{\epsilon}(T))\, \mathrm{d}T \approx \bar{\epsilon}_{\text{ref}}\, \bar{x}\, S\, \bar{Q}(\bar{\epsilon}_{\text{ref}}), \tag{4.14}$$

where $\bar{\epsilon}_{\text{ref}}$ is the mean energy loss per unit distance of the reference particle and $\bar{x}$ is the mean length of scintillator passed through. We define the relative mean light yield as

$$\bar{\Lambda}(\bar{T}^{\text{in}}, \bar{T}^{\text{out}}) \equiv \frac{\bar{L}(\bar{T}^{\text{in}}, \bar{T}^{\text{out}})}{\bar{L}_{\text{ref}}} = \frac{1}{\bar{\epsilon}_{\text{ref}}\, \bar{x}\, \bar{Q}(\bar{\epsilon}_{\text{ref}})} \int_{\bar{T}^{\text{out}}}^{\bar{T}^{\text{in}}} \bar{Q}(\bar{\epsilon}(T))\, \mathrm{d}T. \tag{4.15}$$

To gather granular data for a range of $\bar{\epsilon}$, we use a segmented detector consisting of an array of scintillating fibers laid in a row. We shoot a beam of protons and pions into the detector such that pions could traverse all fibers successively and protons could stop within the array. We vary the energies of the beams and the angle of incidence on the fibers, θ, which changes $\bar{x}$. The protons serve as test particles for measuring quenching, and the pions serve as the low-ϵ reference particles for the relative light yield measurement. From initial kinetic energies in the range of tens to hundreds of MeV to stopping, the range of $\bar{\epsilon}$ for the protons varies by two orders of magnitude, while the through-going pions are always in their minimum-ionizing energy range, regardless of incoming beam energy. Though changes of the angle only translate into small changes of the protons' path lengths in the fibers, they strongly affect their energy-loss profiles because of the high stopping power of protons shortly before stopping. Where the energy loss is largest, quenching effects are most pronounced; so small variations of the angle lead to large variations in quenching and

significantly improve our measurement sensitivity. We label each different setting of beam energy and incidence angle as a run.
In each run, we measure $\bar{\Lambda}_i$ for each fiber, with i labeling the fiber; this is the data set for each run. Unfortunately we do not know $\bar{T}_i^{\text{in}}$ and $\bar{T}_i^{\text{out}}$ for individual fibers. In our fits to the $\bar{\Lambda}_i$, the mean energy of the proton beam prior to it entering the fiber array, $\bar{T}_0$ is a free parameter. We calculate all the incoming and outgoing energies, $\bar{T}_i^{\text{in}}$ and $\bar{T}_i^{\text{out}}$ $(i \geq 1)$, with the continuous-slowing-down approximation (CSDA) using data from the National Institute of Standards and Technology (NIST) for $\bar{\epsilon}(T)$ [240, 116]. We account for inactive coatings on the fibers, so $\bar{T}_0 \neq \bar{T}_1^{\text{in}}$ and $\bar{T}_i^{\text{out}} \neq \bar{T}_{i+1}^{\text{in}}$. This calculation depends on $\bar{x}$, and therefore on the incidence angle, which is also a free parameter in our fits.

4.3.2.1 Fit Likelihood

To fit a quenching model, M, to our data, we must quantify how well it describes the data given particular values of its parameters, $\vec{\lambda}$. This is the likelihood of the data given the model and its parameters. Since the likelihood for the data of an individual run has a common form for all runs, we factorize the likelihood to describe our total data set, $\vec{D}$, into the product of likelihoods to describe the data of individual runs, $\vec{D}_r$:

$$\mathcal{L}(\vec{D} \,|\, \vec{\lambda}, \vec{\nu}; M) \equiv \prod_r \mathcal{L}_r(\vec{D}_r \,|\, \vec{\lambda}, \vec{\nu}_r; M), \tag{4.16}$$

where $\vec{\nu}$ is the vector of beam parameters vectors, $\vec{\nu}_r = \{\bar{T}_{r0}, \theta_r\}$, for all runs; and the data for a particular run, $\vec{D}_r$, are the observed $\bar{\Lambda}_{ri}^{\text{obs}}$ and their uncertainties, σ_{ri}. The likelihood for an individual run is

$$\mathcal{L}_r(\vec{D}_r \,|\, \vec{\lambda}, \vec{\nu}_r; M) \equiv \prod_i \mathcal{N}\Big(\bar{\Lambda}_i^{\text{exp}}(\vec{\lambda}, \vec{\nu}_r; M) \,|\, \bar{\Lambda}_{ri}^{\text{obs}}, \sigma_{ri}\Big), \tag{4.17}$$

where $\mathcal{N}$ is the normal distribution and $\bar{\Lambda}_i^{\text{exp}}$ is the expectation for the quenched mean relative light yield calculated according to equation (4.15) using quenching model M.
To calculate $\bar{\Lambda}_i^{\text{exp}}$, we first simulate the trajectory of a particle with an initial energy $\bar{T}_{r0}$ and incidence angle θ_r through the fiber array, calculating its energy losses in both the active and inactive layers of the array with NIST's CSDA data. From the simulation we know the integration limits of equation (4.15). To account for the variation in the pion momentum from run to run, we replace $\bar{\epsilon}_{\text{ref}}$ in equation (4.15), with a run-dependent mean pion energy-loss density, $\bar{\epsilon}_r^{\pi}$. The mean distance traversed by a pion in a fiber is calculated from the incidence angle for the run: $\bar{x} = w/\cos\theta_r$, where w is the width of the active layer of a fiber. To emphasize the parameter dependence, we rewrite equation (4.15) explicitly for this context:

$$\bar{\Lambda}_i^{\text{exp}}(\vec{\lambda}, \vec{\nu}_r; M) = \frac{\cos\theta_r}{\bar{\epsilon}_r^{\pi}\, w\, \bar{Q}_M(\bar{\epsilon}_r^{\pi}; \vec{\lambda})} \int_{\bar{T}_i^{\text{out}}(T_{r0},\theta_r)}^{\bar{T}_i^{\text{in}}(T_{r0},\theta_r)} \bar{Q}_M\Big(\bar{\epsilon}(T); \vec{\lambda}\Big)\, \mathrm{d}T\,, \tag{4.18}$$

where now $\vec{\nu}_r = \{\bar{T}_{r0}, \theta_r, \bar{\epsilon}_r^{\pi}\}$.

Runs with different angles were taken at common beam momenta; and runs with different beam momenta were taken at common angles. Runs with a common beam momentum share a single T_{r0} and a single $\bar{\epsilon}_r^{\pi}$; and runs with a common angle share a single θ_r.

We explore the parameter space of each model using a Bayesian formulation of probability and a Markov-Chain Monte-Carlo (MCMC) algorithm implemented by the Bayesian Analysis Toolkit [213, 214, 215]. This defines the posterior probability—the probability for parameters given our knowledge after the experiment—as the product of the above likelihood and a prior probability:

$$P(\vec{\lambda}, \vec{\nu} \,|\, \vec{D}; M) \propto \mathcal{L}(\vec{D} \,|\, \vec{\lambda}, \vec{\nu}; M) \times P_0(\vec{\lambda}, \vec{\nu} \,|\, M), \tag{4.19}$$

where proportionality is used since the right-hand side must be normalized for the product to be a probability. The prior probability, P_0, of parameters reflects our knowledge before the experiment. For each model and for each scintillator type, we fit the parameters to all data sets simultaneously. The free parameters in each fit are all T_{r0}, θ_r, and $\bar{\epsilon}_r^{\pi}$ and the parameters of the quenching model studied.

This approach necessitates that we choose a prior probability distribution for all parameters. Although we have precise knowledge of the proton and pion energies in the beam, we use informative uniform prior probability distributions for the T_{r0} and $\bar{\epsilon}_r^{\pi}$. We do this since the beam passes through two windows and a short gap of air before entering the detector array. Interaction with the windows and air smears out the energy distribution. The prior for each θ_r is a normal distribution with mean and standard deviation learned from an independent fit to pion data that calibrates the experiment's rotatory table. The priors for the model parameters are discussed below alongside the fit results.

The NIST data used to calculate the $\bar{\Lambda}^{\mathrm{exp}}$ has an uncertainty that scales the entire stopping-power data set up or down together, not affecting the T dependence of $\bar{\epsilon}$. We account for this uncertainty with a parameter that scales the CSDA data. It has a normal prior probability distribution centered at unity with a standard deviation of 4 %—the known uncertainty from NIST. This parameter is also free in the fit, but its posterior probability is identical to its prior probability. Though this uncertainty affects all analyses that rely on NIST data, it has been neglected in most existing measurements.

4.3.2.2 Model Comparison

We compare models to each other by calculating Bayes factors, which quantify the relative abilities of two models to describe the data regardless of the best-fit values found for their parameters [261]. This approach accounts for model complexities, full posterior probability distributions, and overfitting (acting as an Occam's razor).

The Bayes factor, K_{AB}, comparing model A to model B, is the ratio of the model evidences, z_{A} and z_{B},

$$K_{\mathrm{AB}} \equiv \frac{z_{\mathrm{A}}}{z_{\mathrm{B}}}. \tag{4.20}$$

The evidence of a model is a measure of its ability to describe the data regardless of the

values of its parameters. It is the integral over the right-hand side of equation 4.19

$$z_M = \int \mathcal{L}(\vec{D} \,|\, \vec{\lambda}, \vec{\nu}; M)\, P_0(\vec{\lambda}, \vec{\nu} \,|\, M)\, \mathrm{d}\vec{\lambda}\, \mathrm{d}\vec{\nu}, \tag{4.21}$$

—the integrand is the product of the likelihood and the prior probability density and the integration is over all parameters and over the entirety of each parameter's allowed range. The posterior belief in preferring model A over model B is

$$\frac{P(\mathrm{A})}{P(\mathrm{B})} = K_{\mathrm{AB}} \cdot \frac{P_0(\mathrm{A})}{P_0(\mathrm{B})}, \tag{4.22}$$

where $P_0(M)$ and $P(M)$ are the prior and posterior probabilities for a particular model—that is, one's belief in the model before and after the experiment. The prior probabilities, $P_0(A)$ and $P_0(B)$, are subjectively chosen by each scientist. The Bayes factor thus quantifies the objective part of our learning process and separates it from the subjective priors. If K_{AB} is greater than one, model A is preferred over model B by the data; if K_{AB} is less than one, model B is preferred over model A by the data.
The integral in equation (4.21) is not generally easy to calculate. We used a harmonic-mean estimator (HME) algorithm to calculate evidences from the MCMC samples [262]. We calculate the evidence from the samples by

$$z_{\mathrm{M}} \approx \left(\frac{1}{N} \sum_{i=1}^{N} \frac{1}{\mathcal{L}(\vec{D} \,|\, \vec{\lambda}_i, \vec{\nu}_i; M)\, P_0(\vec{\lambda}_i, \vec{\nu}_i \,|\, M)} \right)^{-1}, \tag{4.23}$$

where the sum is over the N sampled parameter points in the Markov chain. Since this method suffers from numerical instabilities in regions of small posterior probability density, we restricted our evaluation of the HME to a volume in which the calculation is well behaved and accounted for this restriction in calculating the evidence using an algorithm developed in [263].

4.3.3 Experimental Setup[5]

Our detector consists of 16 scintillating fibers, each 71 mm long with a square 2 mm × 2 mm cross section. We arrange them such that their long sides were perpendicular to the beam and place them in a row such that the beam passed through them sequentially. Figure 4.7 shows a schematic view of the experimental setup. We measured with two different scintillating materials: SCSF-78 from Kuraray, with a polystyrene base; and BC-408 from Saint-Gobain, with a polyvinyltoluene base [248, 264].
The light produced in each fiber is detected by a square 3 mm×3 mm Hamamatsu Photonics S13360-4935 silicon photomultiplier (SiPM) glued to one end of the fiber [265]. Each SiPM has a pitch size of 25 µm with 14 400 pixels in total, of which 6400 overlap with the fiber end. The large SiPM eases the gluing process and minimizes variations due to positioning errors. The measurements were performed with constant overvoltages on the SiPMs and constant temperatures to ensure consistent gains throughout measuring. From

[5] Section reprinted from [253]

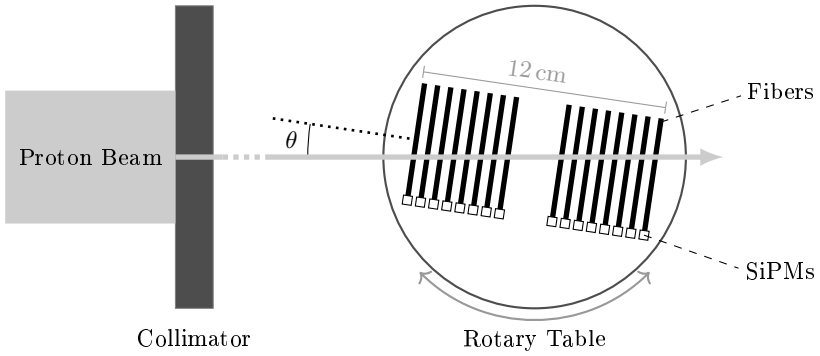

Figure 4.7: Schematic of the experimental setup. Figure taken from [253].

simulation, we estimate an average SiPM signal of 10 to 15 photoelectrons for a pion and around 200 photoelectrons for the maximum signal from a proton. So saturation effects are negligible and we have constant light detection efficiency for both the pions and the protons [236]. From test measurements in which we varied the vertical position of the detector relative to the beam, we observed no dependence of our measurements on this alignment. To digitize the SiPM signals, we use multichannel mezzanine-sampling analog-to-digital converters (ADCs) [266].

We measured in the πM1 beamline of the high-intensity proton accelerator at the Paul Scherrer Institute [267]. The πM1 beam consists of protons and pions with momenta adjustable between 220 MeV/c and 450 MeV/c with a resolution of about 1 % [268]. The beam spot size was 10 mm × 10 mm (at fwhm) and centered on the middle of our fibers. To reduce the beam divergence, we placed a copper collimator with a 2 mm-diameter bore before the fiber array, with 20 cm between the exit of the collimator and the first fiber (at perpendicular incidence). The collimator produced a strongly collimated beam of protons that hit the center of the fiber array (at perpendicular incidence), but did not significantly alter the pion beam. The fiber array was mounted on a rotary table that allowed us to vary the angle of incidence of the beam on the array. The entire setup was placed in a vacuum chamber to minimize beam interactions with air before entering the detector.

The recorded data set for the SCSF-78 scintillator contains seven runs: five with an incidence angle of 1.6° at momenta of 230 MeV/c, 240 MeV/c, 275 MeV/c, 300 MeV/c, and 335 MeV/c; and two further at 3.4° and 8.4°, both at 335 MeV/c. The recorded data set for the BC-408 scintillator contains six runs: four with an incidence angle of 1.6° at momenta of 240 MeV/c, 300 MeV/c, 335 MeV/c, and 350 MeV/c; and two further at 5.4° and 7.9°, both at 335 MeV/c.

4.3.3.1 Relative Light Yield Measurement

In each run, the beam contains both protons and pions. An event consists of one particle passing through a contiguous part of the fiber array (always including the first fiber, which was used as a trigger), producing scintillation light in each traversed fiber. The SiPMs convert this light into charge signals, which are digitized in the ADCs. We fit to the ADC output to determine the signal amplitude for each fiber. Figure 4.8 shows the signal-

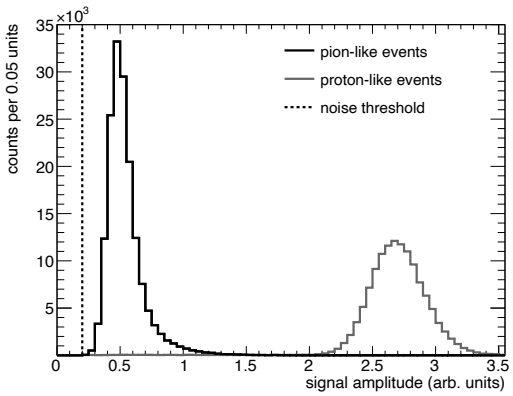

Figure 4.8: Pulse-height spectrum for the first fiber in the detector array for a beam momentum of 350 MeV/c and an incidence angle of 1.6°. The fiber type is SCSF-78. Figure taken from [253].

amplitude spectrum for a single fiber and a single run.

At our beam momenta, pions pass through all 16 fibers with a nearly constant energy-loss density; accordingly we define an event as pion-like if it passes through all fibers. The signal in each fiber must be above the noise threshold measured for that fiber. Pion-like events form the low-amplitude peak in figure 4.8. The arithmetic mean of the spectral distribution of pion-like events is the uncalibrated mean pion light yield.

Since the minimum energy-loss density for a proton is three times higher than that for a pion, we define a proton-like event as one with more than one fiber with a signal amplitude exceeding three times the mean pion light yield for that fiber. Proton-like events form the high-amplitude peak in figure 4.8. The arithmetic mean of the spectral distribution of proton-like events is the uncalibrated mean proton light yield. The ratio of the uncalibrated mean proton light yield to the uncalibrated mean pion light yield is the relative mean light yield, $\bar{\Lambda}_i$.

The signals from the SiPMs are smeared by noise, the resolutions of the ADCs, the pulse-shape fits, and the event-selection algorithm. We estimate the uncertainty on the relative mean light yield from these effects by fitting a Landau distribution folded with a normal distribution to the pion peak in the signal-amplitude spectrum. We take the standard deviation of the normal distribution, 5 % (relative), as a conservative estimate of the measurement uncertainty on the mean light yield and add it (in quadrature) to the statistical uncertainty from the above steps. The result is the σ_{ri} used in the likelihood for the model fit.

Figure 4.9 shows the relative mean light yield of five runs. For all four runs, we clearly see the Bragg curves for stopping particles, with the particle range increasing with increasing momentum. From the two runs at 335 MeV/c, we see that changing the incidence angle causes measurable changes in the $\bar{\Lambda}$ profile.

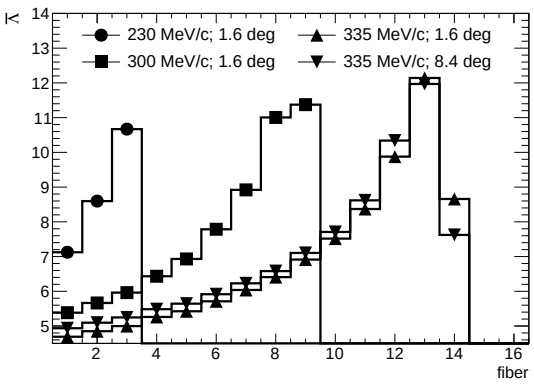

Figure 4.9: Relative mean light yield of proton-like events for four different runs measured with the SCSF-78 scintillator. The uncertainties are smaller than the symbols. Figure taken from [253].

model	par.	units	SCSF-78	corr.	BC-408	corr.
Birks	kB	mm/MeV	0.132 ± 0.004		0.155 ± 0.005	
Chou	kB	mm/MeV	$0.000 \leq 0.001^{\dagger}$	0.93	0.151 ± 0.040	0.75
	$\sqrt{C}$	mm/MeV	0.129 ± 0.005		$0.000 \leq 0.002^{\dagger}$	
Wright	W	mm/MeV	0.333 ± 0.009		0.406 ± 0.002	
Voltz	V	mm/MeV	0.091 ± 0.006	0.25	0.628 ± 0.108	0.89
	f		$0.000 \leq 0.057^{\dagger}$		0.427 ± 0.019	

Table 4.1: Parameter values at the best-fit points, 68 %-credibility-interval uncertainties, and the correlation factors (where applicable). †These best-fit values are at their boundaries, zero, so we give their 68 %-credibility upper limits. Table taken from [253].

4.3.4 Results[6]

To evaluate each model's posterior probability, we must choose prior probability distributions for the model's parameters. We choose each prior to be uniform within a reasonable range, imposing physical constraints, and to be zero outside this range. All model parameters are constrained by requiring

$$0 \leq \bar{Q}(\bar{\epsilon}; \vec{\lambda}) \leq 1 \qquad \forall\, \bar{\epsilon} \geq 0. \tag{4.24}$$

This is fulfilled for all our models when their parameters are greater than or equal to zero. Additionally, for Voltz' model, f is bounded above by one.
In table 4.1, for each of the four models and for each of the scintillating fiber types, we list the parameter points that maximize the posterior probability, which we refer to

[6]Section reprinted from [253]

$Q(\epsilon)$	998	996	962	922	856	629	419	405	309	113
ϵ	5	10	15	20	30	50	75	100	250	500
5	1.32	1.23	1.10	1.05	1.00	0.76	0.55	0.30	0.01	0.33
10		1.67	1.60	1.54	1.44	1.12	0.81	0.42	0.01	0.18
15			1.72	1.63	1.54	1.12	0.83	0.51	0.11	0.20
20				1.59	1.48	1.15	0.81	0.35	−0.16	0.04
30					1.44	0.99	0.81	0.41	−0.21	0.04
50						1.15	0.65	−0.40	−0.86	−0.65
75							1.94	−0.12	−1.51	−1.18
100								2.73	2.72	1.89
250									10.8	6.39
500										10.2

Table 4.2: Result of model-independent fit to SCSF-78: Q values (top) and covariances (bottom) in ‰ at fixed ϵ values (in MeV/cm). Table taken from [253].

as the best-fit point; the 68 %-credibility-interval uncertainties; and correlation factors (where applicable). The uncertainties and correlation factors include both statistical and systematic effects. We are able to measure Birks' coefficient to a relative precision of 3 %. Our value of Birks' kB for BC-408 agrees with that presented in [269].
We observe very different behavior of Chou's model for the two scintillators: For SCSF-78, the term linear in $\bar{\epsilon}$ is negligible and quenching is best described by the quadratic term alone, with $\sqrt{C}$ compatible with Birks' kB. For BC-408, the opposite is the case and quenching is best described by the linear term alone, with Chou's kB compatible with Birks'. Therefore Chou's model requires the shape of the quenching function strongly depend on the scintillator material.
We also observe very different behavior of Voltz' model for the two scintillators: For SCSF-78, f is small, with a best-fit value of zero; Table 4.1 lists the mode and 68 %-credibility upper limit. This means that all deposited energy is subject to quenching, as in Birks' model. Accordingly, for this fiber type, V is of a comparable scale to Birks' kB. For BC-408, f is closer to 50 %—only half the deposited energy is subject to quenching. Accordingly, V must be larger. This trend is confirmed by the positive correlation of the parameters in both fits with Voltz' model. Voltz' model also requires the shape of the quenching function strongly depend on the scintillator material.

4.3.4.1 Model-Independent Fit

The models we tested impose strong assumptions on the form of $Q(\epsilon)$: all but Chou's model have positive second derivatives for all ϵ; all but Voltz' model approach zero at large ϵ. Since a material's quenching function has never been directly measured before, these assumptions have gone untested. The data collected with our segmented detector allows us to directly fit for the shape of the quenching function free from model assumptions. For

$Q(\epsilon)$	989	847	768	709	652	517	444	412	263	115
ϵ	5	10	15	20	30	50	75	100	250	500
5	2.32	1.43	1.09	1.01	1.01	0.45	0.55	0.46	0.50	0.28
10		3.88	3.95	3.67	3.59	2.32	1.23	0.73	0.94	0.69
15			4.22	3.90	3.89	2.22	1.12	0.61	0.80	0.63
20				3.65	3.65	2.06	0.76	0.23	0.50	0.42
30					4.06	0.85	−0.41	−8.20	−0.35	−0.10
50						6.10	3.33	1.22	1.15	0.91
75							7.94	6.65	4.31	2.81
100								10.1	7.23	3.90
250									8.17	4.66
500										5.72

Table 4.3: Result of model-independent fit to BC-408: Q values (top) and covariances (bottom) in ‰ at fixed ϵ values (in MeV/cm). Table taken from [253].

this, we parametrized $Q(\epsilon)$ as a linear spline with eleven knots. We tried several different model-independent descriptions: using a cubic spline instead of a linear one; freeing the knot positions in the fit; and using fewer or more knots. The results were all consistent with each other. We show the results with fixed knot positions and a linear interpolation because it is the simplest to present the full results for, including parameter correlations. The knots positions were fixed at 0, 5, 10, 15, 20, 30, 50, 75, 100, 250, and 500 MeV/cm. We chose these values to cover the full range of ϵ of our experiment and have a higher knot density in regions our experiment is most sensitive to. The value of the quenching function at $\epsilon = 0\,\mathrm{MeV/cm}$ is fixed to unity. For our model-independent fits we used uniform prior probabilities on the value of Q at each knot. The resulting best-fit values and covariances are listed in tables 4.2 and 4.3.

Figure 4.10 shows the 68 %-credibility-interval bands for the model-dependent quenching functions and the best-fit values for the model-independent quenching functions for both scintillators. The bars on the model-independent results show the boundaries of the smallest 68 %-credibility intervals for the value at each knot. For many of the knots, the best-fit value is near the boundary of the interval—especially those near unity. The results of the model-independent fits yield quenching functions free from any theoretically-imposed constraints. Using these results, we qualitatively evaluate each model's ability to reproduce the data.

The model-independent quenching function for SCSF-78 has a negative second derivative at small ϵ and an inflection point at approximately 50 MeV/cm. It is inconclusive whether the quenching function approaches zero at large ϵ—the value of the quenching function at 500 MeV/cm is 1.5 standard deviations above zero (in the posterior probability). Only Chou's model, when C is nonzero, can accommodate a negative second derivative. Figure 4.10a includes the result of a fit using Chou's model with kB fixed to zero, which is identical to the fit result reported in table 4.1. We see that Chou's model is able to describe

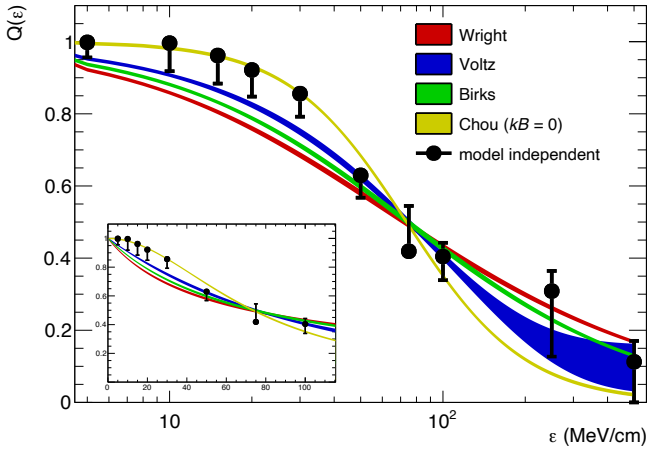

(a) SCSF-78.

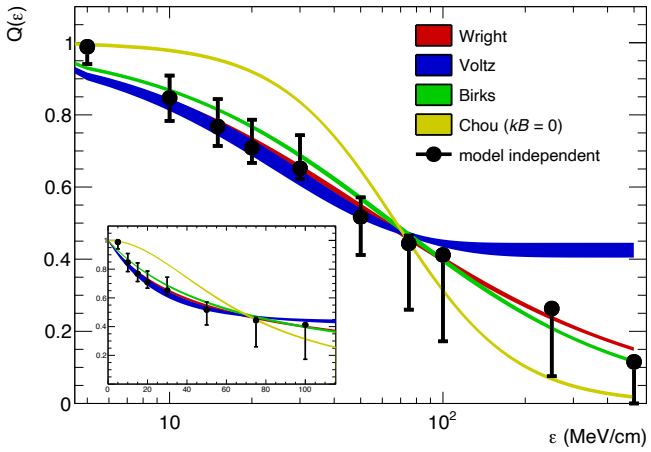

(b) BC-408.

Figure 4.10: 68 %-credibility-interval bands for the model-dependent quenching functions listed in table 4.1 and the best-fit values and the smallest 68 %-credibility intervals for the model-independent fits for both scintillator materials. The inset plots show the same results on a linear scale for the low-ϵ region; their axes have the same variables and units as the larger plots. Figures taken from [253].

the small-ϵ behavior better than all other models.

The model-independent quenching function for BC-408 has a positive second derivative everywhere. It again is inconclusive whether it tends to zero or to a finite quenching value at large ϵ—the value of the quenching function at 500 MeV/cm is 1.1 standard deviations above zero (in the posterior probability). These features are compatible with all the model-dependent fits. Figure 4.10b includes the result of a fit using Chou's model with kB fixed to zero—we do not show the result for a free kB since it is identical to the fit with Birks' model. We conclude that this model cannot describe the data well because it must have a negative second derivative at small ϵ, which is contradicted by the model-independent result.

	SCSF-78		BC-408	
model	$\log_{10} K$	$\Delta \log_{10} L$	$\log_{10} K$	$\Delta \log_{10} L$
Birks	—	—	—	—
Chou	5.1 ± 0.2	14.6	-3.6 ± 0.1	0.2
Chou ($kB = 0$)	7.9 ± 0.2	15.0	-14.7 ± 0.1	-21.3
Wright	-19.0 ± 0.2	-3.0	1.0 ± 0.1	0.1
Voltz	5.9 ± 0.2	5.6	1.0 ± 0.1	1.1

Table 4.4: The log of the Bayes factor and the difference of the log of the maximum likelihood, both with respect to the fit for Birks' model, for both scintillators. Table taken from [253].

The model-independent quenching functions indicate that it is likely that quenching does not asymptotically drop to zero and light is produced even at large energy-deposition density.

4.3.4.2 Model Comparisons

Table 4.4 compares our fits for each model for both scintillators: we list both Bayes factors and the difference in maximum likelihood.[7] We benchmark all models against Birks' model, which is the most commonly used quenching model. If a model fits to the data better than Birks' model, the value of $\log_{10} K$ is positive; if a model fits to the data worse than Birks' model, it is negative. Common interpretations of Bayes factors state that $|\log_{10} K| > 2$ means there is decisive evidence for a conclusion; and $|\log_{10} K| \approx 1$ means there is only substantial evidence [270, 271].

Our fits to the SCSF-78 data decisively prefer Chou's and Voltz' models to Birks', with no strong evidence for a preference of either one over the other. However, Chou's model with kB fixed to zero is decisively preferred to all other models—its preference over Chou's full model is a clear example of Occam's razor. Wright's model is strongly disfavored by our data.

These conclusions are borne out in visual comparison to the model-independent functions (figure 4.10a): Chou's model with $kB = 0$ is the only model that reproduces the model-independent function for SCSF-78 at small ϵ. Our fits are most sensitive to behavior at small ϵ, where a preponderance of our data is. So Chou's model with $kB = 0$ is still preferred to the other models, though it deviates the most from the model-independent behavior at medium and large ϵ. To better study the behavior at large ϵ, we need data using heavier and higher-charged particles, namely ions.

In fits to the BC-408 data, Birks' model is decisively preferred to Chou's model. This is expected: the fit with Chou's model prefers $\sqrt{C} = 0$, recreating Birks' model but with an extra degree of freedom. This unnecessary degree of freedom is a penalty when calculating

[7] Though there is no simple, true statistical interpretation of the difference in maximum likelihood as a basis for model comparison, we give this information since it is commonly used in the field.

the Bayes factor—again an example of Occam's razor. Wright's and Voltz' models are substantially preferred. The Bayes factor for comparing Wright's model (with its evidence in the numerator) to Voltz' (in the denominator) is 0.1 ± 0.1, barely favoring Wright's model, but inconclusively. That none of Birks', Voltz', or Wright's models is decisively preferred, is also borne out in visual comparison to the model-independent function (figure 4.10b): all three models reproduce the model-independent results within their 68 % credibility intervals.
Our studies above show that quenching in SCSF-78 and in BC-408 have different dependencies on energy-deposition density. The two scintillator types differ in base material, dopant material, and dopant density—all of which can contribute to differences in quenching. No model we tested is decisively favored in fits with both scintillators. Chou's model with $kB = 0$ is most favored in fits to SCSF-78 data, but most disfavored in fits to BC-408 data. The only model to perform better than Birks' in both fits is Voltz'.
A new model is needed to parametrize quenching in both materials. The most generic model that could fit all the features seen in the model-independent fits must allow for an asymptotic value at large ϵ; the possibility of a negative second derivative at small ϵ with an inflection point where the second derivative may change sign; and different curvatures below and above this inflection point. Such a model would require at least four parameters, with all or some of them being specific to the material composition used. To fully test such a model requires new measurements at small, medium, and large ϵ for multiple scintillating materials.

4.3.5 Conclusion

In the last sections, we have investigated the quenching function for two different scintillators as a function of the energy-loss density of traversing protons and determined by that the quenching parameters of the scintillators for different empirical quenching models. For the SCSF-78 that we use in MAPT, this was the first quantification of the ionization-quenching magnitude, which allows us to model the impact of ionization quenching on our reconstruction method based on Bragg curve spectroscopy. However, using the model-independent approach, we have found that none of the models well describes the true underlying shape of the quenching function over the whole range of probed energy-loss densities. For the SCSF-78 scintillator, the deviations of the empirical quenching functions from the result of the model-independent analysis is found to be on the order of 20 %.
Unfortunately, our experiment was only sensitive to energy-loss densities below approximately 50 MeV/mm as only protons were available in the beam. Higher charged nuclei reach much larger energy-loss densities when stopping, as the stopping power depends quadratically on the charge number of the nucleus. A stopping iron nucleus, for example, with a charge number $z = 26$, can reach energy-loss densities up to approximately 3×10^4 MeV/mm during the stopping process, which is much larger than the energy-loss probed by our experiment. If we extrapolate the quenching functions tested with their best-fit parameters to such high energy-loss densities, the different models yield very different quenching magnitudes. This can be seen in Figure 4.11, in which the quenching functions for the best-fit parameters of the different quenching models, together with the result of our model-independent analysis, for energy-loss densities up to 1×10^4 MeV/mm are shown. The extrapolations of the quenching functions deviate by orders of magnitude

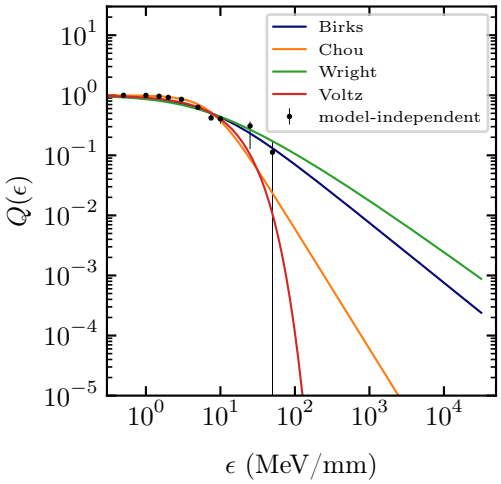

Figure 4.11: Quenching functions for different quenching models with their best-fit parameters extracted from our experiment using stopping protons. The experiment was only sensitive to energy-loss densities up to around 50 MeV/mm, which can be recognized by the increase of the uncertainties for the model-independent approach.

in the unprobed energy-loss-density region. As no experimental data for this region is available we cannot prefer one model over the other. An extension of our measurement to larger energy-loss densities is therefore inevitable to quantify the influence of ionization quenching for higher-charged particles that are stopped in MAPT.
The quenching-model dependence of the expected Bragg curves in MAPT for different charged nuclei is illustrated in Figure 4.12. The different figures show the Bragg curves obtained for the same particles as in Figure 4.4b, but including the effect of quenching. Instead of the total deposited energy by ionization, the figures show the so-called 'visible deposited energy', corresponding to the fraction of the deposited energy after quenching. The visible deposited energy, ΔE_{vis}, is defined as

$$\Delta E_{\text{vis}} = \int_{x_{\text{in}}}^{x_{\text{out}}} Q\left(\left\langle \frac{\mathrm{d}E}{\mathrm{d}x} \right\rangle\right) \left\langle \frac{\mathrm{d}E}{\mathrm{d}x} \right\rangle \mathrm{d}x. \tag{4.25}$$

The visible energy is defined similar as the deposited energy in Equation 4.2 but includes the effect of quenching. The different models yield vastly different shapes and magnitudes for the Bragg curves, especially for highly charged particles. While for Birks' model the visible energy in a fiber starts to saturate at around 15 MeV due to the increasing quenching effect for higher energy-loss densities, Chou's model and Voltz's model suppress the light creation for large energy-loss densities so strongly that the visible energy deposition of highly charged particles is even less than the visible energy deposition of stopping protons, or even minimum-ionizing particles, although the actual energy deposition is much larger. Without further experimental data we cannot decide which quenching model is more plau-

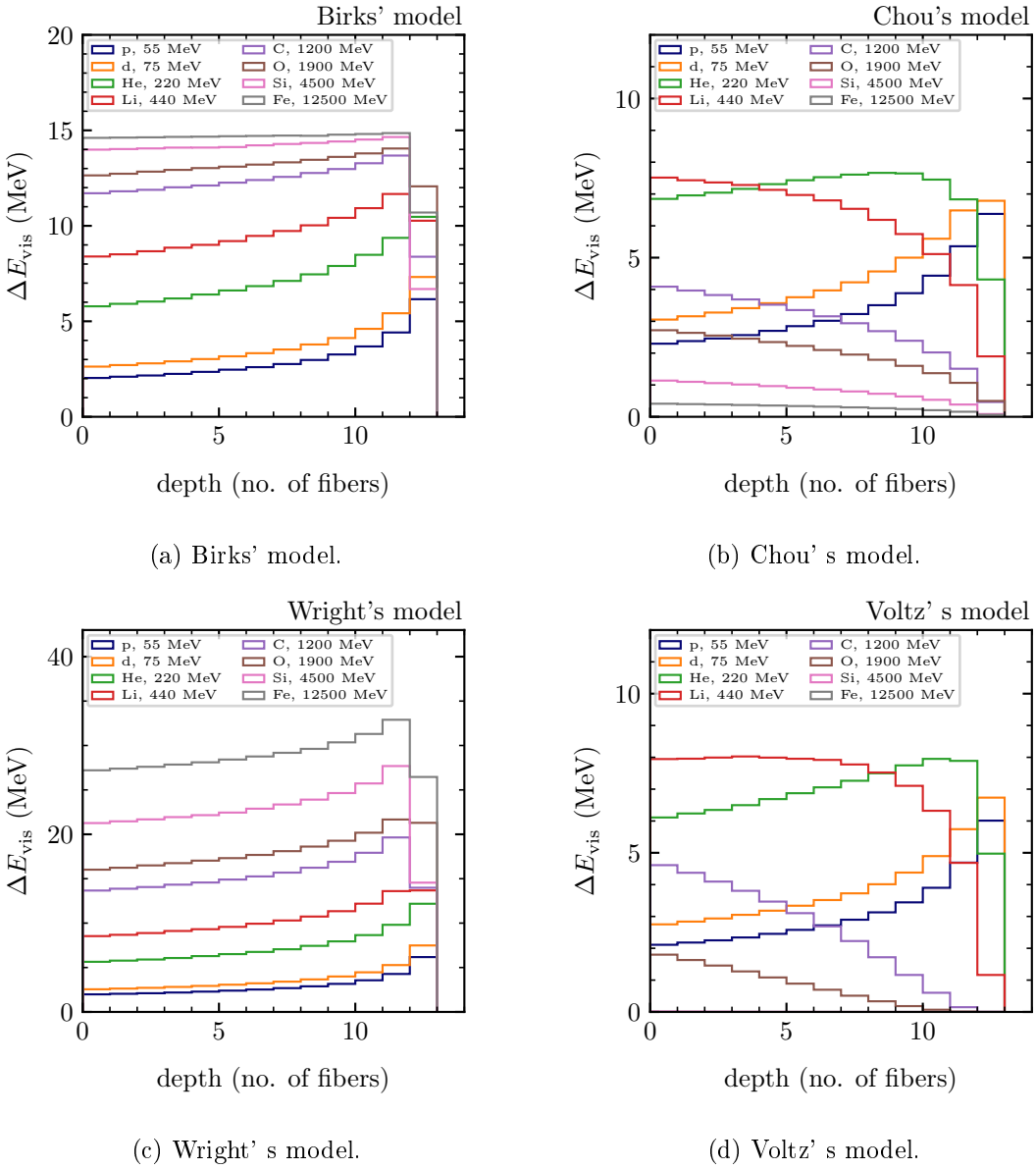

(a) Birks' model.

(b) Chou' s model.

(c) Wright' s model.

(d) Voltz' s model.

Figure 4.12: Bragg curves for different nuclei in MAPT for the of different models of ionization quenching and their best-fit parameters from our experiment.

sible and which shapes of the Bragg curves we should expect in MAPT. Unfortunately, the shapes of the Bragg curves are the main observables that we aim to use for our particle identification, and their shapes are an indispensable input required for further investigations of our particle reconstruction scheme. Therefore, a future experiment to investigate the response of the SCSF-78 fibers to stopping nuclei with higher charge is absolutely required.

To nevertheless investigate the feasibility of our developed particle identification method, we restrict our performance estimate for the time being to light ions like protons, deuterons,

and helium particles. For light ions, the effect of the quenching-model uncertainty is not as severe as for higher charged nuclei, and the performance is expected to be not significantly influenced by the selected model. For the following investigations I use Birks' model, which is the most commonly used quenching model.
Beside particle identification, I investigate in the following also the reconstruction of the particle's direction, which we do not expect to be influenced by the shape of the quenching function at all.

4.4 Reconstruction Algorithms

In the following, I present the planned reconstruction algorithms for MAPT and the current status of the development. The algorithms shall perform three main tasks on each individual event recorded by MAPT: To reconstruct the initial direction of the detected particle; to reconstruct the charge, mass, and initial energy of the particle; and to distinguish antiparticles from particles. In this thesis, I restrict myself to the description of the first two tasks. First studies on the antiparticle-particle separation can be found in the Bachelor's thesis of J. Müller [272].
For each of the two tasks we have pursued two different approaches for the developed algorithms: One analysis method to obtain the most accurate reconstruction possible given the detector signal, with no focus on the required computing resources, henceforth called offline reconstruction; and one algorithm that shall minimize the required computational effort and reconstruction time per event. While the first approach shall serve as a benchmark to analyze the recorded data with best possible accuracy, and to allow to assess the reachable performance of the MAPT detector concept for the different tasks; the latter shall allow a reconstruction of the data with limited computing resources on a spacecraft in near-real time, a so-called online reconstruction.
For both applications we have selected machine-learning algorithms: For the offline analysis we have chosen a Bayesian particle filter to extract the full posterior probability distributions of the particle's initial direction, energy, and charge and mass number given the the measurement of the detector in a Bayesian way. Despite the large computational effort of such an algorithm, this method allows to directly quantify the associated uncertainties of the extracted values and the credibility of the reconstruction for each event. I describe the algorithm in Section 4.4.2.
For the online reconstruction of the MAPT data, we aim to use an algorithm based on pre-trained artificial neural networks. The networks are trained before MAPT is deployed on a spacecraft using simulated detector data. The advantage of this procedure is that—although the training procedure is computationally expensive—the execution time of the trained neural network is orders of magnitude shorter compared to the Bayesian particle filter and requires only little computing resources. I describe the approach in Section 4.4.3. In Section 4.4.4 and Section 4.4.5 I evaluate the reconstruction capabilities of both methods using simulated MAPT data. I restrict the analysis of the particle identification capability of stopped particles to light nuclei, as we have seen that higher charged ions require a better constraint of the ionization-quenching effect in MAPT first. In Section 4.4.6, I give an overview about future required adaptions and improvements to reconstruct measured cosmic-ray data with the presented algorithms.

To reconstruct individual events, both algorithms must be able to cope with the statistical nature of the interactions of the particles with the detector material, which I briefly review in more details first.

4.4.1 Energy Loss Fluctuations and Multiple Scattering

The most important interactions of nuclei with the detector material are the electronic energy loss from interactions of the nuclei with the hull electrons of the material and directional changes of the nuclei due to elastic interactions with the nuclei of the material. So far, we only considered the mean effect of the former, meaning its expected influence on a large ensemble of identical particles. But as we aim to reconstruct individual events, we also must take into account the statistical nature of both processes when trying to reconstruct the event. Individual detector events for particles with equal initial states can create different hit pattern in the detector and the particles can have differences in the energy-deposition profile or in their penetration range.
The relative magnitude of the fluctuations and the distribution of the individual energy losses around their mean values depend strongly on the particle type, its energy, and the thickness and material of the traversed matter [235]. These fluctuations around the mean energy loss, $\langle \mathrm{d}E/\mathrm{d}x \rangle$, can be described in terms of energy-straggling functions. While for slow particles and large amount of traversed material the distributions follow a normal distribution, the distributions for fast particles and small amounts of traversed material exhibit a large tail towards larger energy losses with respect to the mean energy loss, being described by a so-called Landau distribution [240]. The tail towards high energy losses can be explained by infrequent, large energy transfers producing fast secondary electrons. With decreasing particle velocity and increasing thickness of the traversed material, the energy loss distributions become more symmetrical, and pass over from the Landau distribution to a normal distribution via the so-called Vavilov distribution [260]. The regions in which the energy-loss distribution should be described by the different functions can be separated in good approximation by the so-called κ parameter, defined as the ratio of the mean energy loss and the maximum energy that can be transferred within a single nucleon-electron interaction,

$$\kappa = \frac{\xi}{E_{\mathrm{max}}}, \tag{4.26}$$

where

$$\xi = \frac{2\pi z^2 e^4 N_{\mathrm{Av}} Z \rho \delta x}{m_0 \beta^2 A}, \tag{4.27}$$

with ρ being the density of the material, N_{Av} Avogadro's number and δx the traversed thickness of the material, and

$$E_{\mathrm{max}} = \frac{2 m_0 \beta^2 \gamma^2}{1 + 2\gamma m_0/m_{\mathrm{ion}} + (m_0/m_{\mathrm{ion}})^2}, \tag{4.28}$$

with m_{ion} being the mass of the traversing ion and $\gamma = E/m_{\mathrm{ion}}$ its Lorentz factor [258]. For $\kappa \lesssim 0.01$, the Landau distribution is commonly used; for $0.01 \lesssim \kappa \lesssim 10$, the Vavilov distribution is used; and for $\kappa \gtrsim 10$ a normal distribution can be used to describe the

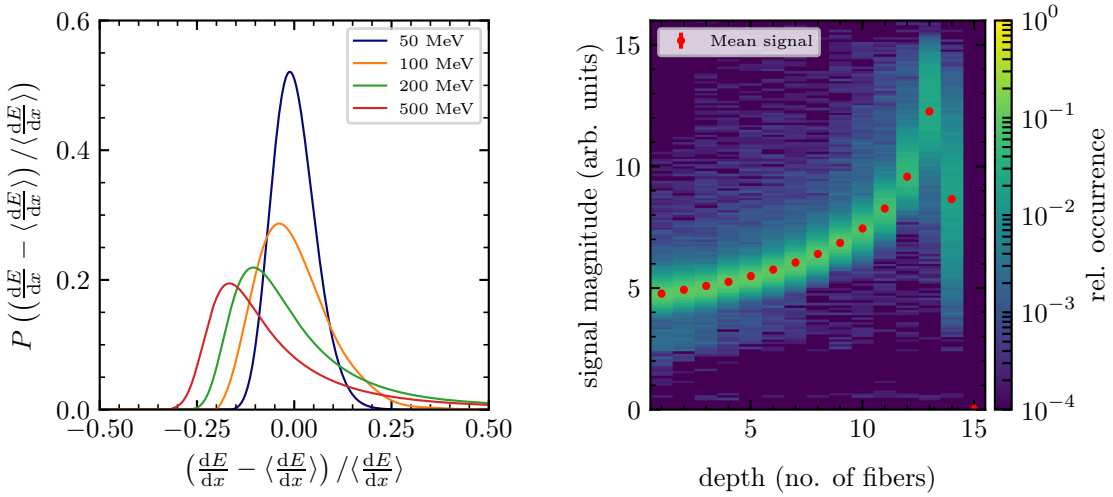

(a) Energy straggling distributions for protons.

(b) Measured Bragg curve.

Figure 4.13: Left: Variations of the energy-deposition and direction after traversing of 2 mm polystyrene for different particles. Right: Resulting energy-deposition distribution along the Bragg curve measured in a MAPT-like detector for a beam of 335 MeV/c protons.

energy-straggling distribution [273].
Figure 4.13a shows exemplarily the calculated energy straggling distributions—the probability distributions to find a certain energy deposition with respect to the mean energy deposition in the material—for protons with different energies traversing a single 2 mm fiber. Already for protons with a kinetic energy of around 100 MeV, the distribution is visibly asymmetric. This asymmetric energy-deposition distributions within our single channels prevents us from applying reconstruction algorithms that require statistically fluctuating signals to be distributed according to a normal distribution, such as the Kalman filter [274].
As a result, the Bragg curves in MAPT for individual particles deviate from the mean energy-loss profile due to the energy-straggling in the individual fibers, with increasing deviations along the track, as can be seen in Figure 4.13b. The figure shows the cumulative experimental data of many recorded Bragg curves from a mono-energetic beam of protons hitting a MAPT-like detector structure, together with the calculated mean signal for each fiber. Especially in the last two fibers before the particle is stopped, the accumulated energy straggling along the track leads to vastly different signal magnitudes for the different particles.
Stopping particles in MAPT have most often a $\kappa > 10$ in each fully traversed fiber along their trajectory and the straggling of the energy deposition can be described by normal distribution. But when the particle only partially traverses a fiber, or if the particle has an energy large enough that the particle is not stopped, the energy-distributions most often become visibly asymmetric. Such an asymmetric distribution measured by our detector can be seen exemplarily for pions in Figure 4.27.
Due to the importance of the effect of energy straggling, we must include the effect and

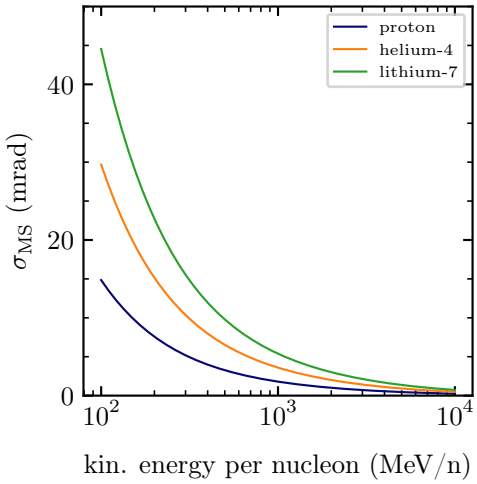

Figure 4.14: Energy-dependence of the magnitude of the standard deviation of the angular-scattering distribution for different ions. The values are calculated from the Highland formula (Equation 4.29) for 2 mm polystyrene.

the different energy straggling functions in both of our analysis approaches.

Besides the statistical nature of the energy loss, also the statistical nature of elastic scattering on the material's nuclei must be included in the event reconstruction, as it can change the direction of a particle along its track in the detector and alters the obtained hit pattern and signal magnitudes in the individual fibers, for example by increasing the track length within a certain fiber.

All particles that traverse matter experience many small-angle scatterings that for some particles add up to a macroscopic direction change. This effect is called multiple Coulomb scattering [235]. In addition, infrequently single large-angle scattering events occur, which are termed single Coulomb scattering.

Experimentally it was found that in most applications a Gaussian approximation of the distribution of the resulting scattering angle of a particle through a given material can be used to describe the central 98 % interval of the scattering-angle distribution accurately [275]. The obtained probability distribution for a directional change of a certain angle with respect to the incoming direction can be described by a normal distribution with a mean of zero and a standard deviation, σ_{MS}, which depends on the particle type, its energy, and the traversed material as

$$\sigma_{\mathrm{MS}} = \frac{13.6\,\mathrm{MeV}}{\beta cp} z \sqrt{\delta x / X_0}\,[1 + 0.038 \ln(\delta x / X_0)]\ \mathrm{rad}, \tag{4.29}$$

with X_0 being the radiation length of the traversed material [275]. The magnitude of the standard deviation for different particle types as a function of energy traversing 2 mm of polystyrene is shown in Figure 4.14.

About 2 % of particle experience large-angle scattering due to single Coloumb scattering, which is not included in Equation 4.29, which is also called the Highland formula [274]. Due to the rare occurrence of the process, we have not yet included it in our reconstruction using the Bayesian particle filter, which I describe in the next section. For the neural-network approach, the effect is indirectly included as the effect is included in the simulation used for the training of the network.

4.4.2 The Bayesian Particle Filter

The Bayesian particle filter is a generalization of the well-known Kalman filter [276]. Similarly, it applies a filtering technique in which information from different measurement points along the particle track is added successively in the track reconstruction to constrain the free parameters of the track and the associated particle. As the Kalman filter, however, is limited to Gaussian processes, it is not usable in our application due to the non-gaussian energy-loss distributions, and additionally due to the geometry of our fibers. The probability-distribution function (PDF) of the particle's location when traversing a fiber does not obtain a Gaussian shape but a constant non-zero probability within the active volume and zero outside, similar to a step function. Such a distribution cannot be used in a Kalman filter but only in a generalized particle filter, which can handle arbitrary PDFs, including non-analytical ones [276].
In our application, the Bayesian particle filter is used to obtain the posterior-probability density function (posterior PDF) of a particle's state when entering the detector, $\vec{x}_0$, given the measured signals of individual fibers, the data, D. The posterior PDF can be written as

$$P\left(\vec{x}_0 M|\vec{D}\right) = P\left(E_0, \theta_0, \phi_0, \theta_0^{\mathrm{p}}, \phi_0^{\mathrm{p}}, A, Z|z_1, ..., z_N\right), \tag{4.30}$$

with E_0 being the initial kinetic energy of the particle when entering the detector. θ_0 and ϕ_0 describe the direction of the particle in a fixed spherical coordinate system. θ_0^{p} and ϕ_0^{p} describe the spatial position of the intersection of the particle track with a sphere around the detector in spherical coordinates. A and Z are the particle's mass and charge number and z_1 to z_N the measured visible energy depositions of the hit fibers along the particle's track.[8] The spherical coordinate system of the angles for the description of the track direction and the starting point of the track on the spherical surface around the detector is defined such that the polar angles, θ and θ_0 are measured with respect to the z-axis defined in the coordinate system in Figure 4.1a, and the azimuth angles, ϕ and ϕ_0, are defined as the angle between the projection of the track onto the x-y plane and the x-axis.
During the propagation of the particle through the detector, the state of the particle and some of the associated parameters change. I label the particle's state after traversing k fibers as $\vec{x}_k$. As the physical processes happening during the penetration of the individual fibers are statistically independent, the probability to find the particle in a state $\vec{x}_{k+1}$ given the previous measurements $z_0, ..., z_k$ is only related to the previous state, $\vec{x}_k$. The relation

[8] We assume here that all detector effects beside ionization quenching can be unfolded from the measured signal by a calibration with a known energy deposition, e.g. by a beam of MIPs, and the obtained measurements represent the visible energy deposition of the particle in the fibers.

between both is given by the Chapman-Kolmogorov equation [277] as

$$P\left(\vec{x}_{k+1}|z_1,...,z_k\right) = \int P\left(\vec{x}_{k+1}|\vec{x}_k\right) P\left(\vec{x}_k|z_1,...,z_k\right) \mathrm{d}\vec{x}_k. \tag{4.31}$$

The term $P\left(\vec{x}_{k+1}|\vec{x}_k\right)$ is the transition probability between the two states of the particle during the transition of the $k+1$-th fiber and depends on the physical processes during the transition. The model of this transition is called system model and includes the statistical effects of the physical processes [277]. The integral over the system model takes into account all possible transitions to reach state $\vec{x}_{k+1}$.
If we take the information from the next measurement, z_{k+1}, into account, we can update our knowledge of the particle state $\vec{x}_{k+1}$ and write the probability distribution as

$$P\left(\vec{x}_{k+1}|z_1,...,z_{k+1}\right) = \frac{P\left(z_{k+1}|\vec{x}_{k+1}\right) P\left(\vec{x}_{k+1}|z_1,...,z_k\right)}{\int P\left(z_{k+1}|\vec{x}_{k+1}\right) P\left(\vec{x}_{k+1}|z_1,...,z_k\right) \mathrm{d}\vec{x}_{k+1}}, \tag{4.32}$$

with $P\left(z_{k+1}|\vec{x}_{k+1}\right)$ being the probability that a certain particle state creates a certain measurement, which is determined by our signal generation process, and is called measurement model [277]. $P\left(\vec{x}_{k+1}|z_1,...,z_k\right)$ is the result from Equation 4.31. The integral in the denominator is a normalization constant to normalize the obtained probability distribution. As we can calculate $P\left(z_{k+1}|\vec{x}_{k+1}\right)$ from $P\left(\vec{x}_{k+1}|z_1,...,z_k\right)$ using Equation 4.32, we can calculate successively all $\vec{x}_k$ recursively to obtain $P\left(\vec{x}_N|z_1,...,z_N\right)$ from a prior-probability distribution of the initial particle state, $P_0(\vec{x}_0)$. However, as we are interested in the posterior-probability distribution of $\vec{x}_0$, $P_0(\vec{x}_0|z_1,...,z_N)$, we require some further calculations compared to this standard procedure of the Bayesian filter. In addition to the forward recursion to obtain $P\left(\vec{x}_N|z_1,...,z_N\right)$, we need to use this result as a prior-probability distribution for a backward recursion to obtain the posterior-probability distribution $P(\vec{x}_0\,|z_N,...,z_1)$. The backward recursion is performed similar to the forward recursion, beside that the processes of the system model require to be modeled in a reversed time frame [277].
In order to represent the individual PDFs of the Bayesian-filtering process, the particle-filter uses a set of random samples, called particles, which approximate the corresponding PDFs [276]. The particle filter starts by drawing a predefined number of particles, $\left\{s_0^1,...,s_0^i,...,s_0^M\right\}$, from $P_0(\vec{x}_0)$ and performs the the first forward filtering step for each of the particles, s_0^i, starting with their corresponding particle-state parameters $\vec{x}_0^i$ as defined by the system model. After the step, the obtained probability $P(z_1\,|\vec{x}_1^i))$ is evaluated for each particle, and the particles get their obtained probability assigned as a weight, w_1^i. The weighted particles approximate $P(\vec{x}_1|z_1)$. By drawing new particles from this weighted distribution for the next filtering step, we can continue the filtering described above numerically until we obtain an approximation of $P\left(\vec{x}_0|z_1,...,z_N\right)$. An illustration of the method and the used terms is given in Figure 4.15.

Our current implementation of the measurement model includes the effect of ionization quenching using Birks' model as described by Equation 4.8 with our experimentally extracted best-fit value of Birks' coefficient, $kB = 0.132\,\mathrm{mm/MeV}$. Our system model includes the energy loss of the particles with energy-straggling and multiple scattering. A detailed description of the implementation of the processes in forward and reversed time

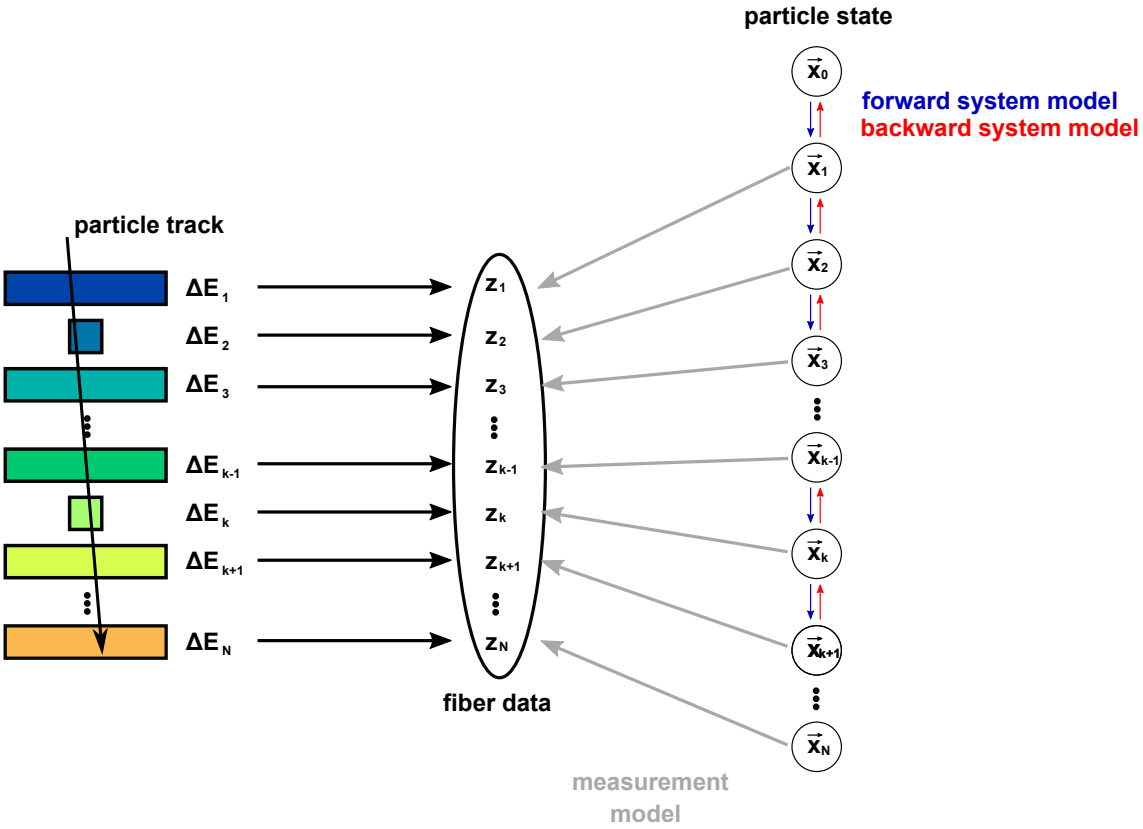

Figure 4.15: Sketch of the process of the Bayesian-filtering method.

direction are given in the Masters' theses of M. Milde and L. Hollender [278, 241]. The calculation of the average energy loss is based on the already discussed CSDA (see Section 4.3.2) and the influence of energy straggling is added by adapting the mean value according to a sampled value from the corresponding energy-straggling function as described in Section 4.4.1. The multiple-scattering process is described on basis of the Highland formula, Equation 4.29.

As input for the particle filter, we require a prior-probability distribution, $P_0(\vec{x}_0)$. In general, the prior could be non-informative, yielding a constant probability for all parameters within their allowed range of values. Practically, however, the coverage of such a large parameter space is not feasible as it would require an immense number of simulated particles for the filtering steps to not fail the filtering process. This happens if no particle obtains a non-zero weight during a filter step. The probability for this to happen depends strongly on the density of the sampled particles in the parameter space. The larger the parameter space to be sampled, the more particles are required to obtain a reasonable result and to not fail the filtering. Due to the large dimensionality of the parameter space, we need some additional constraints on the values of the parameters before employing the particle filter. This can be achieved either by using a preceding, simpler reconstruction algorithm or by reducing the dimensionality of the parameter space.

To constrain the prior ranges of the parameter we can use algorithms like the neural networks described in Section 4.4.3 or other classical pattern-recognition algorithms. To

constrain the directional and positional track parameters, for example, a pattern recognition that is based on a Hough transform has been developed for MAPT as an alternative fast online-reconstruction method to compare the results from the algorithm based on neural networks with [279, 280]. The Hough transform has already reached reconstruction accuracies for the track angles of approximately 5° (68 % CI), which has been shown by M. Milde to be sufficiently small as a prior distribution for the particle filter to reconstruct certain events with 1×10^4 particles per filter step [278].
To obtain a prior of the particle energy, a more complicated algorithm is required that can use the variations and magnitudes of the energy depositions in the fibers along the track to estimate the range of the particle. Such an algorithm is currently under development. As an intermediate step, an algorithm has been developed by L. Bierwirth that distinguishes stopping and non-stopping particles, also based on an Hough transformation. With this algorithm, the initial energy of a stopping particle can be constrained within a few tens of MeV per nucleon by using the number of hit fibers as a estimate for the particle range.
To decrease the dimensionality of the parameter space and to allow further parallelization of the particle reconstruction on our computers, we use a different approach for the mass and charge number of the nucleus that shall be reconstructed: Instead of handling these values as free parameters during the filtering steps, they are fixed prior to the filtering and an individual filter run is executed for each different possible particle type. Therefore, we treat the different types of nuclei as different model assumptions, and compare the obtained results of different assumptions afterwards by their corresponding evidence, $z = \int P\left(D|\vec{x}\right)$—similar to what we have done for the model comparison of the quenching functions in Section 4.3.2.2. The evidence for each particle-type assumption is calculated by sampling particles according to the obtained posterior-probability distribution from the particle filter and propagate them again through all fibers but without resampling after each step. The sum of the so-obtained particle weights, w_i for all fibers, j, is considered a good approximation of the evidence as

$$z \approx \frac{1}{N_{\text{fib}}} \sum_{i,j} \frac{w_j^i}{N_{\text{part}}}, \tag{4.33}$$

with N_{fib} being the number of fiber signals and N_{part} being the number of particles used by the filter [281]. Using the calculated evidences we can then compare the different assumptions of the charge and mass number of the nucleus by their Bayes factors to state which assumption is more likely to produce the measured event.

4.4.3 A Neural-Network-based Online Reconstruction

The relation between the hit pattern generated by a charged particle and the particle's initial state can be interpreted as a function, $f : D \rightarrow \vec{x}_0$. A representation of f would allow us to map for each event the hit topology to the initial particle state and thus reconstruct the event. Although the function is a-priori unknown, we can approximate it using neural networks and supervised learning, which I discuss in the following.
An artificial neural network consists of an interconnected number of individual processing elements, so-called neurons. Each neuron maps a given input to a certain output, called activation. Each of the neurons and the connections between them contain several adjustable

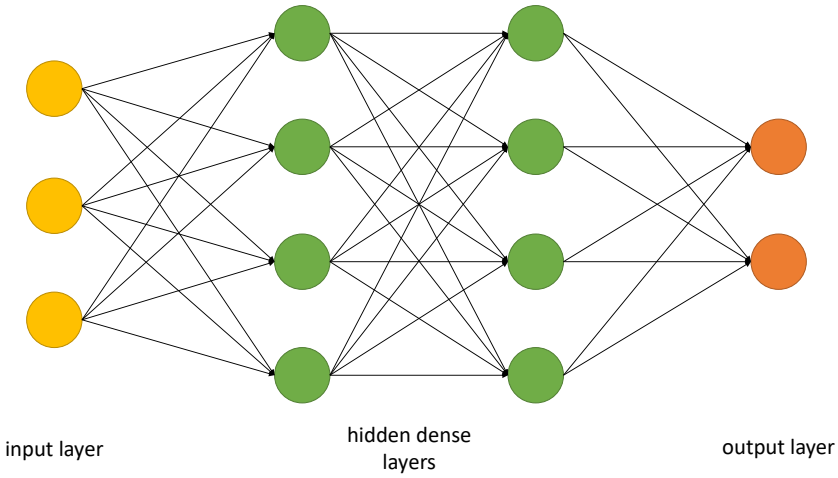

Figure 4.16: Sketch of a feed-forward neural network. Figure adapted from [285].

parameters that alter the activation for a given input, so-called hyperparameters [282]. It has been shown by Hornik, Stinchombe, and White in 1989 that certain classes of such networks are universal function approximators, meaning that they can approximate most functions to any level of accuracy if the network is large enough by adjusting the hyperparameters [283].
For a given network architecture, the search for the set of hyperparameters that approximates the function $f(D)$ as close as possible is the goal of the supervised-learning procedure. Using a set of labeled data—meaning pairs of $(D, \vec{x}_0)$, which can be generated for example by simulations or test measurements with known initial particle states—the hyperparameters are adjusted such that the differences between the predicted states by the neural network and the true states are minimized. The network with the obtained hyperparameters then yields the best approximation of f given the network architecture and training samples, and the network can be used to evaluate the state also for unlabeled data [284].
In the following, I describe the layout and components of feed-forward neural networks that we use for our application. After this, I explain our training procedure on simulated detector data, the analysis flow, and the network architectures used to obtain the initial particle states from MAPT data.

4.4.3.1 Feed-Forward Neural Networks

In our application, we use feed-forward neural networks, in which the neurons are organized in layers. Each layer obtains solely the output activation of the neurons of the preceding layer [282]. An exemplary layout of a feed-forward network is shown in Figure 4.16. The colored circles depict the neurons. The first layer is the input layer, representing in our case the hit pattern in the detector and the signal amplitude of each fiber. The last layer is the so-called output layer. The activation of the neurons in the output layer must be related to the parameters of the initial particle state, our parameters of interest. In between, several so-called hidden layers of neurons can be present, each with an individual

number of neurons. The number of hidden layers is often referred to as the depth of the network, and the number of neurons per layer as the width [282].
There are different types of layers that are defined by their connections to the preceding and succeeding layers. In our application, we use three different types of layers: fully connected layers, also called dense layers, convolutional layers, and pooling layers.
In a fully connected layer, each neuron of the layer is connected to all neurons of the preceding layer. Its input is the weighted sum of all output activations of the preceding layer, with individual weights for each connection, which serve as hyperparameters that we need to constrain during the network training. Therefore, the input of each neuron depends on the activations of all neurons in the preceding layer [284].
To be more sensitive to the geometrical distribution of features in the input layer, e.g. if the input layer represents a pixelized image in which the different neurons also contain spatial information, convolutional layers have been developed [286]. In such layers, the individual neurons are only connected to a subset of the neurons in the preceding layer which are spatially close to each other. The activations of the different neurons thus depend on local features only. By successively relocating the used subset on the preceding layer, the whole preceding layer is scanned and the obtained convoluted results are used as an input for the different neurons of the convolutional layer. The size of the used subset is referred to as the filter size and the shift of the filter for each neuron with respect to the previous as the stride. The size and strides of a convolutional layer are often fixed beforehand and are selected on the basis of the size of the features that the filter shall target in the preceding layer [282]. However, recently more sophisticated layers have been developed that can adjust the effective filter sizes during the training process and optimize the convolution for the desired task by learning the optimal filter size by itself. We use such layers in the form of so-called inception layers, as developed by Google LLC for their network GoogleNet [287]. It has been shown that in our and in similar applications the use of such layers improves the performance with respect to a pure fully connected network or simple convolutional networks with similar numbers of free hyperparameters [285, 288].
Most often after convolutional layers, pooling layers are deployed to reduce the dimensionality of the succeeding layers. The pooling layers either average the activations of several neurons or use the maximum of the activations of them for one neuron. By this the number of neurons is reduced, albeit at the cost of reducing the information contained in the network. On the other hand, the reduction of the complexity can improve the training process of the network. The use of pooling layers must be tested in the individual application to determine whether it improves or worsens the approximation of the underlying transformation [282].
Most networks employ a mixture of the different layers and a multitude of different network architectures is used. The optimal number of layers and neurons strongly depends on the complexity of the task the network is trained on and the available training data. The identification of a suitable network architecture therefore requires testing of different layouts and comparing the obtained performances.

The fundamental processing elements that are common to all layers of the neural network are the neurons. Each neuron calculates an activation from its input activations of the neurons of the preceding layer that are connected to it. The input value, z, is commonly

a weighted sum of all input activations and a bias parameter and can be expressed as

$$z = \left(\sum_i w_i a_i \right) + b, \tag{4.34}$$

with a_i being the activation of the i-th connected neuron from the preceding layer, w_i the corresponding weight, and b the so-called bias parameter [282]. The weight and the bias parameter are hyperparameters of the network that are tuned during the training process to approximate the underlying transformation as closely as possible. The output of the neuron is then calculated from z by applying an activation function, $\sigma(z)$. Many different activation functions are used in neural networks, starting from very simple functions like a rectifier linear function,

$$\sigma(z) = \max(0, z), \tag{4.35}$$

to more complex functions such as the sigmoid function,

$$\sigma(z) = \frac{1}{1 - e^{-z}}, \tag{4.36}$$

and others [282].
A shared feature of most of the commonly used activation functions is their non-linearity, which has been shown to be an important feature of the neurons to allow the learning of complex non-linear relations during the training [289]. Again, the selection of the best-performing activation function for the targeted task often must be found by testing.
The activation function used in the output layer must fulfill an additional requirement: As the activations of the neurons of the output layer are often interpreted in terms of physical values or probabilities related to the target feature, the value range of the activation function must match the domain of the physical values or probabilities. In case the activations of the different neurons correspond to different physical values—like for example our parameters of the initial particle state—the network is referred to as a regression model and the activation function of the neurons must allow all possible values that the parameters can assume. For unbound parameters most often a purely linear activation function is used. The second most common type of model is the classification model. Here, the goal of the network is to distinguish between different predefined choices and the different neurons of the output layer represent the disjoint classes—the allowed choices—and their corresponding activations the probability (or certainty) of the event to be of this class. In this case, the activations are interpreted as probabilities and must lie between 0 and 1, with their sum being 1. This can be achieved, for example, by the softmax-activation function. The activation for the j-th neuron of the output layer is defined as

$$\sigma(z_j) = \frac{e^{z_j}}{\sum_{k=1}^{N} e^{z_k}}, \tag{4.37}$$

with z_j being the input of the j-th neuron in the output layer, z_k being the input of the k-th neuron, and N being the total number of neurons in the output layer, which corresponds to the number of disjoint classes that can occur [282].

To approximate the transformation using the neural network, the hyperparameters of the network—the weights and biases of the individual neurons—must be tuned by a training procedure until the neural network obtains a good approximation of f. In order to maximize the agreement of the neural-network approximation with f, we require a metric that defines a measure of the disagreement, the so-called loss function [282]. The loss function for a sample gives a measure of how much the predicted output deviates from the true value. The goal of the training procedure is to minimize the cumulative loss—the sum of the loss function over the complete dataset used for training. Similar to the activation function of the output layer, the loss function must be selected based on the interpretation of the activation of the output layer neurons. For regression models, in which the activations represent different physical values, the most commonly used loss function is the mean-square loss,

$$l(y_i, \hat{y}_i) = \sum_{i=1}^{N} \frac{(\hat{y}_i - y_i)^2}{N}, \tag{4.38}$$

with y_i the predicted output of the i-th neuron—the activation—$\hat{y}_i$ the true value of the physical parameter corresponding to the output of the i-th neuron, and N the total number of output neurons [284]. Especially for applications in which different physical values are reconstructed simultaneously by the individual output neurons, the different domains of the physical values could complicate the training process. In such cases, the training process can be improved by using the relative deviation between the true and predicted values as

$$l(y_i, \hat{y}_i) = 100 \sum_{i=1}^{N} \frac{|\hat{y}_i - y_i|}{\hat{y}_i}. \tag{4.39}$$

For classification models often the cross-entropy loss function,

$$l(y_i, \hat{y}_i) = \sum_{i=1}^{N} \hat{y}_i \log(y_i), \tag{4.40}$$

is used, which is also based on the interpretation of the output activations as probabilities [284].
To minimize the loss by adjusting the networks hyperparameters, an optimization algorithm must be used. These algorithms numerically calculate the gradient of the loss function with respect to the hyperparameters and adjust them into the direction of decreasing loss. The most commonly used algorithms are based on stochastic gradient descent or more advanced algorithms such as the ADAM algorithm, specifically developed for training of neural networks[282, 290].
The algorithms iteratively calculate the gradient and adapt the hyperparameters using the samples of the training data. In order to reduce statistical fluctuations of the gradient evaluation, often more than one sample is used at a time for the calculation of the gradient. The loss is thereby averaged over a certain predefined number of samples, a so-called batch, and the calculation of the gradient is based on these averaged values [284]. Especially in applications like ours, in which the input signal is strongly influenced by statistical fluc-

tuations, the averaging over several events allows a faster convergence of the optimization algorithm towards the global minimum of the loss function.
Once the network is trained and the set of hyperparameters is found that corresponds to a good approximation of the transformation, the hyperparameters are fixed and the network can be used either to predict the parameters of interest for non-labeled data, or to evaluate the performance of the reconstruction using labeled test data.

In the following I describe in more detail the specific use of the neural networks in our reconstruction of the initial particle state from the signals of MAPT . I present the implementation method, the creation of the training data, and the deployed network architectures.

4.4.3.2 Neural Networks for MAPT

The aim of the neural networks is, similar to our approach using the particle filter, to reconstruct the initial state of a nucleus when entering the detector. More specifically, the parameters describing the direction, θ and ϕ, the type defined by the charge and mass number, Z and A, and the initial energy, E_0. In contrast to the particle filter, we do not need to reconstruct explicitly the track location, which is labeled by θ_p and ϕ_p in Section 4.4.2, as these parameters are not of explicit interest as physical parameters but are only required in the particle filter to calculate the energy deposition of the nucleus in the individual fibers. In the reconstruction based on neural networks, however, we do not explicitly model the individual energy depositions in the detector but let the network learn the corresponding particle state for a given energy deposition and hit pattern in the detector. Therefore, the hyperparameters θ_p and ϕ_p are not required in this approach.
We implement the neural networks using the machine-learning framework TensorFlow (version 2.4) [291, 292]. The development, training, and performance evaluation is implemented using the programming language Python [293]. The trained networks are then stored and can be loaded using a C++ library of TensorFlow with reduced computing demands to reconstruct data in near-real time.
To train the networks and evaluate their reconstruction performance we use simulated data. In order to not introduce systematic errors when using the trained networks to reconstruct real data, the simulation of the detector response to the particles must be as realistic as possible. For this task, we use the Geant4 simulation framework to model the interaction of the traversing particles with the detector material and the energy deposition of the particle in the scintillating fibers, including the statistical nature of the interactions [237]. In addition, the effects of the signal generation described in Section 4.2 are modeled, specifically the effect of ionization quenching. Similar to our implementation within the particle filter, we employ Birks' model of ionization quenching and our experimentally obtained best-fit value for Birks' coefficient of $kB = 0.132\,\mathrm{mm/MeV}$. From the simulation we obtain individual detector events together with the associated initial-state parameters of the simulated particle.
Although the reconstruction of the different parameters of the initial particle state could be obtained by using one large neural network, we developed distinct networks for the reconstruction of the particle's direction and for the reconstruction of the particle type and energy. The separation of the reconstruction is expected to require less training data

and to obtain better results for the individual tasks.
As input for both networks, the simulated signals of the MAPT detector are used. As discussed in Section 4.1, we can interpret the signals of the two fiber projections as two images of the event that encode the spatial distribution of the hits and the individual signal amplitudes. We represent the two images as two 16×32 matrices of scalar values and use them as individual input layers in our networks. Each fiber is represented by a neuron and the neuron's activation represents the visible energy deposition in the corresponding fiber. The output layers differ for the two different tasks and also depend on whether the task is interpreted as a regression problem or a classification problem. In principle, all of our tasks can be interpreted in both ways: Either, the physical parameters are directly represented by the activation of a certain output neuron, resulting in a regression problem, or the domain of possible values of the parameter is subdivided into bins and the activation of the different neurons represent the probability of the parameter value to be within the corresponding bin. Although the width of the individual bins limits the angular resolution for the individual events, we have found that the overall reconstruction performance of the initial direction can be improved by using a classification approach instead of a regression approach for similar-sized networks [294]. We use the classification approach for both, the reconstruction of the particle's direction and the combined reconstruction of its type and energy.
The output of the neural network to reconstruct the particle direction consists of two separate output layers, one representing the binned θ values, and one representing the binned ϕ values of the particle tracks. The θ parameter range is binned into 180 bins with a 1° bin width for each bin to cover the whole domain of θ from 0° to 180°. The ϕ parameter range is binned into 360 bins with a 1° bin width to cover the whole domain of ϕ from $-180°$ to 180°. Thus, the output layer representing the θ values consists of 180 neurons, and the output layer representing the ϕ values of 360 neurons.
The network for the reconstruction of the particle type and energy consists of one output layer, in which each neuron represents a certain particle type with an energy within a given range. The total probability of the particle to be of a certain type is the sum of the activations of all neurons that correspond to the particle type but different energies. The total number of neurons of the layer depends on the number of particle species that the network shall learn to distinguish and the energy range the reconstruction shall cover. This depends on the specific application of MAPT, and the networks are prior to deployment adapted to the specific range of particles and energies of interest for the mission of MAPT. In this study, we are mainly interested in reconstructing stopping light ions and we adapt the layout of the output layer accordingly. We cover the energy-per-nucleon range from 30 MeV/n to 100 MeV/n with bins with a width of 1 MeV/n each. The different particle-type classes included are protons, deuterons, helium-3, and helium-4. In total, the output layer thus consists of 280 neurons representing the different particles and energies.
The overall architecture of the neural network used for the reconstruction of the particle direction is shown in Figure 4.17a. In the Master's thesis of L. Meyer-Hetling [285] it has been shown that this architecture outperformed formerly used architectures, e.g. developed in [280]. The network consists of an inception module and several fully connected and convolution layers and has in total 2.905×10^6 trainable parameters. The network for the particle identification and energy reconstruction is shown in Figure 4.17b. The network consists of two inception modules and has in total 9.43×10^5 trainable parameters.

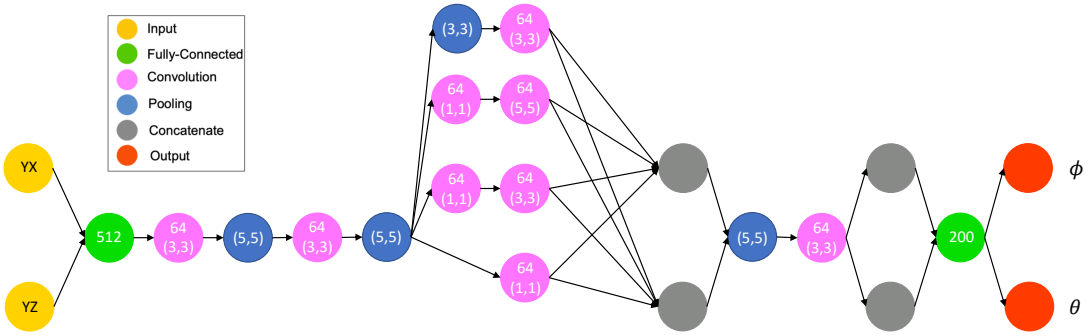

(a) Architecture of the neural network for the reconstruction of the track direction.

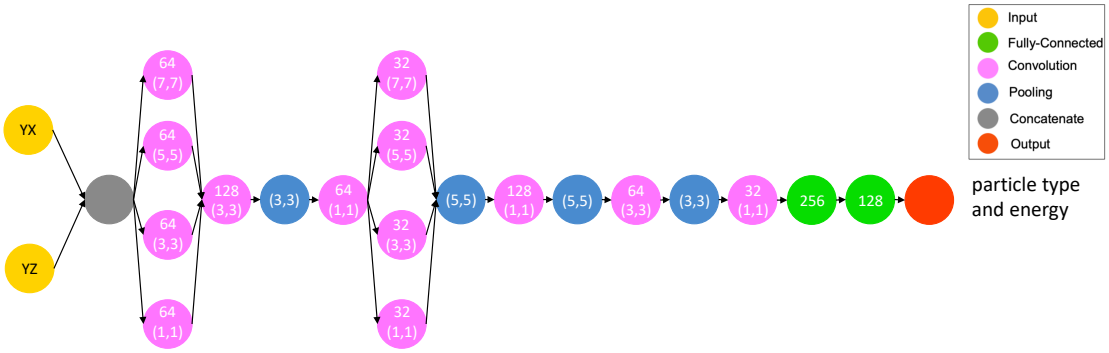

(b) Architecture of the neural network for the reconstruction of the particle type and kinetic energy.

Figure 4.17: Architectures of the neural networks used for the reconstruction of MAPT data. Figures adapted from [285].

In the following sections I evaluate the reconstruction capabilities of the described neural networks on exemplary datasets and compare the performance of the networks to the performance of the particle filter algorithm. First I compare the reconstruction of the particle-track direction, and afterwards the particle-type and energy reconstruction.

4.4.4 Performance of the Track Reconstruction

Although MAPT accepts particle tracks from all directions, we require at least a few fiber hits in both projections to be able to constrain both angles, ϕ and θ, to describe the direction of the track. We also expect the reconstruction performance to increase for particles that traverse more fibers of the detector. To simplistically estimate the expected angular resolution of MAPT, we can estimate geometrically the opening angle, $\Delta\alpha$, for which all tracks create the same hit pattern in one projection of the detector when traversing N fibers of consecutively layers as depicted in Figure 4.18. The allowed angular spread perpendicular to the projection as a function of the number of hit fibers can be approximated

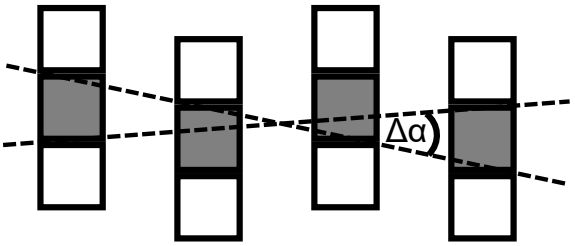

Figure 4.18: Sketch of the opening angle, $\Delta\alpha$.

as

$$\Delta\alpha = \arctan\left(\frac{1}{2N}\right), \tag{4.41}$$

as found by L. Bierwirth [280]. As the signals in the fibers can also give a more precise information on the track length within a certain fiber, the signal amplitude of the individual fibers is expected to increase the reconstruction performance. Detector effects like multiple scattering, on the other hand, are expected to decrease the performance.
To estimate the achievable resolution of the track direction from the reconstruction algorithms, we simulate detector signals for an isotropic flux of minimum-ionizing protons with a kinetic energy of 3 GeV. These particle have a large penetration power and traverse the full detector with a constant mean ionization loss, similar to the minimum-ionizing pions we used in our quenching measurement described in Section 4.3.2.
To ensure that in both projections enough fibers are hit to obtain a meaningful three-dimensional track, we select only events that produce a signal in at least three different fibers in each of the two projections. In addition, we select only events in which no secondary particles are created, which would give a second track in the detector. Such secondaries are created only in approximately 1 % of all simulated events. From the 1×10^7 proton tracks that we simulate, starting from a sphere with a radius of 7.5 cm around the detector, 2.4×10^6 events fulfill our selection criteria. The distribution of the number of fiber hits per event from these events is shown in Figure 4.19a together with the minimal required number of six fiber hits, represented by the gray dashed line. Most particles traverse the detector only partially and do not hit all 32 layers. In most events around 20 fibers are hit, but also events in which more fiber hits are present than detector layers. In these events, in some layers multiple fibers are hit.
The angular distribution of all accepted events is shown in Figure 4.19b. Although the initial simulated particle flux is isotropic, the acceptance of the detector and our event selection depends on the initial direction. Especially pronounced is the absence of accepted events with $\phi = -\pi, 0, \pi$, which corresponds to directions parallel to the fiber layers. These events traverse the detector within a layer and do not produce enough fiber hits in the other projection, and therefore would not allow to constrain both angular parameters simultaneously.

For the training and evaluation process of the neural network, we use 1×10^6 randomly selected events from the dataset. From those, 7×10^5 events are used for the training of the network, 2×10^5 events are used for the evaluation of the validation loss during the training procedure to monitor the performance of the network, and 1×10^5 events are used

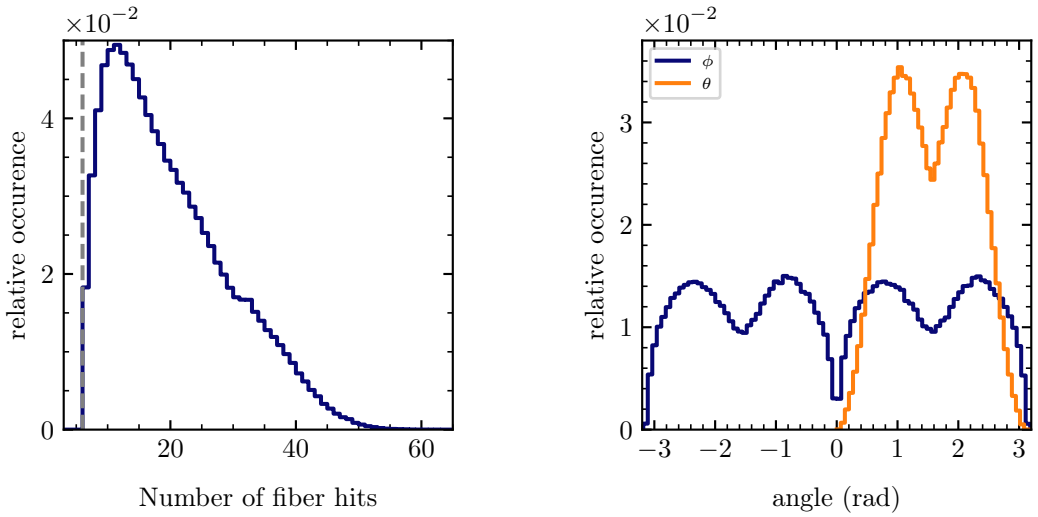

(a) Distribution of number of fiber hits.

(b) Angular distribution of the tracks.

Figure 4.19: Distribution of the selected particle tracks for an isotropic flux of minimum-ionizing protons in MAPT.

to determine the reconstruction performance after the network training and the hyper-parameters are fixed. For the training procedure we use the cross-entropy loss function from Equation 4.40 and a batch size of 512 events. To prevent overtraining, we include an early-stopping mechanism in the training and so-called dropout layers in the network, as described for example in [282].

Due to the large computational effort of the Particle Filter, we assess its performance as a function of the number of fiber hits per event by selecting randomly 100 events with 7, 10, 20, 30, and 40 fiber hits each and analyze them. For the prior-probability distributions used in the filter for ϕ, θ, ϕ_p, and θ_p, we use a conservative constant probability density within a range of $\pm 10°$ around the true value of the parameter from the simulation. For each filter step we employ 1×10^5 particles. With this large amount of particles per step, the execution time of the filter is around 1.5 h per event with 10 fiber hits and around 14 h for an event with 30 fiber hits on a single, modern CPU. An increase of the number of particles for the filter is thus hardly possible.

To quantify the reconstruction performance for both algorithms, we calculate the difference between the predicted angles, ϕ and θ, and the true angles for each tested event. For the neural network we assign the predicted values to be the output class of highest activation for the parameter. For the particle filter, we use the full posterior PDF of the parameter as the prediction for the event.
The accuracy and precision of the reconstruction as a function of number of fiber hits of the events is then calculated from the cumulative distributions of the deviations of all tested and reconstructed events. The accuracy is identified as the mean of the distribution and the precision as the central 68 % interval of the distribution.

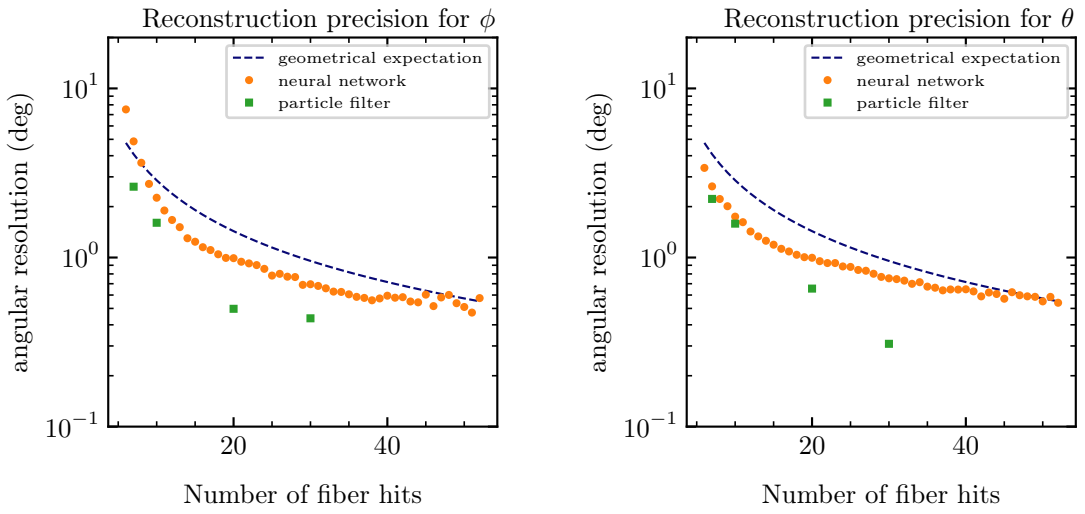

(a) Angle ϕ.

(b) Angle θ.

Figure 4.20: Reconstruction precision for simulated particle events in MAPT using the neural-network-based and particle-filter-based reconstruction method.

For both approaches, the found accuracies for both parameters, ϕ and θ, are on the level of 1×10^{-3}° and much smaller than the obtained precisions, showing no systematic shift. The precisions as a function of the number of fiber hits are shown in Figure 4.20, together with the simplistic geometrical estimate from Equation 4.41. Both reconstruction approaches reach better precisions as we expected from the purely geometrical estimate for most fiber-hit numbers. The particle filter and the neural network obtain a better precision with increasing number of fiber hits in the event. Both have a similar performance for low numbers of fiber hits, and the particle filter obtains a better precision than the neural network for larger number of fiber hits. However, the results from the particle filter are only of limited validity. While in the case of the neural network all tested events could be reconstructed and thus contribute to the shown precision, the particle filter failed for several events and only events contribute that did not fail during the filtering. While at low number of fiber hits the fail rate of the particle filter is low, only about 4 % for events with seven fiber hits, the fail rate increases with increasing number of fiber hits. For 10, 20, and 30 fiber hits, the fail rate already increases to 11 %, 59 %, 79 %, respectively. For events with 40 fiber hits, none of the 100 tested events was successfully reconstructed. This reveals the critical downside of the filtering method: Due to the large parameter space, even the use of 1×10^5 particles per step does not reach the required density that is necessary to obtain a valid particle path that is not filtered out during the successive filtering procedure. To solve this issue, the implementation of the particle filter must allow the use of even more particles per step. This requires an optimization of the code in terms of parallelization and computing speed, e.g. by porting the calculations on a graphical processor unit.
Nevertheless, both approaches reach a precision of the track reconstruction on the order of 1° for both, ϕ and θ, for most events, which is a sufficient resolution for most applications

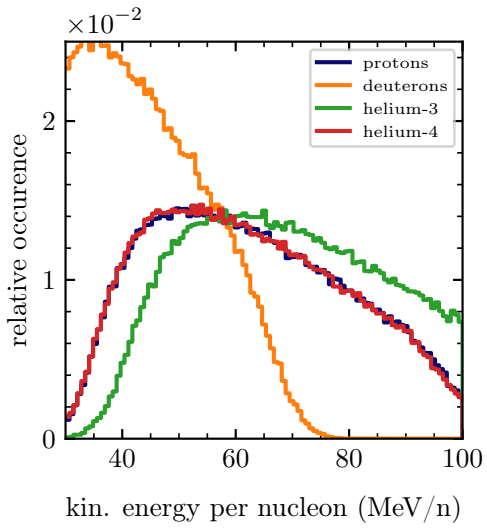

Figure 4.21: Energy distribution of the different particle types in the simulated dataset used for the particle-identification and energy-reconstruction investigation of MAPT.

and allows analyses of particle-flux anisotropies.
In the next section, I compare the reconstruction performance of MAPT for particle identification and energy reconstruction of light nuclei.

4.4.5 Performance of Particle-Characteristics Reconstruction

Similar to the analysis of the reconstruction of the track direction, I aim to investigate the capability of the detector and the reconstruction algorithms to determine the particle type and the initial energy of a light ion that hits the detector. In a first step, I analyze the reconstruction capability for particles that completely stop within the active volume of MAPT. In such events, the complete Bragg curve of the particles is visible, and the reconstruction performance should be best.
In this study, I try to distinguish stopping protons, deuterons, helium-3, and helium-4 nuclei—the lightest ions occurring in the cosmic-ray spectrum—in an energy regime of 30 MeV/n to 100 MeV/n. I simulate the detector response for an isotropic particle flux for all four nuclei species and select only events that hit at least three fibers per projection. Additionally, we require that the simulated nucleus is completely stopped within the detector. The created dataset obtained from 1×10^7 simulated events consists of 4×10^6 accepted events with an approximately equal amount of the different nuclei. The energy distributions for the different nuclei after the selection are depicted in Figure 4.21. The distributions are not completely uniform due to the event selection. The higher the energy, the lower the probability to stop completely within the detector. The lower the energy, the lower the probability that the nucleus hits enough fibers per layer to be accepted.

For the training of the neural network we use 70 % of the dataset for the hyperparameter training, 20 % for the validation during the training process, and 10 % for the performance

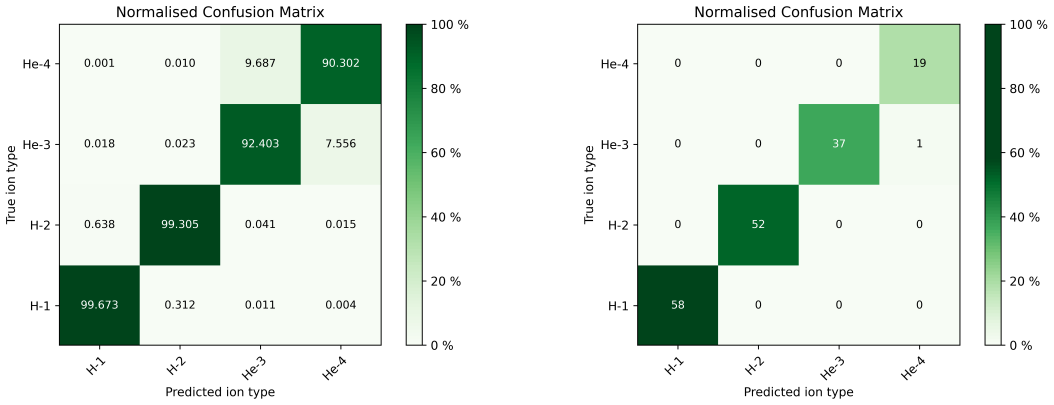

(a) Neural network.

(b) Particle filter.

Figure 4.22: Reconstruction performance of the nucleus type for simulated events stopping in MAPT using the reconstruction method based on a neural network and a particle filter. The missing percentage per row correspond to the number of events that could not be reconstructed at all.

evaluation of the reconstruction after the training. The training is conducted similarly as for the particle-direction reconstruction. The energy parameter is binned into equidistant bins of width 1 MeV/n, which is found to yield the best reconstruction performance for the energy reconstruction and the particle identification. A smaller bin width impedes the training of the particle-type reconstruction, and a larger bin width worsens the achievable resolution of the energy reconstruction.

For the particle filter, we select randomly 100 events for each type of nucleus and analyze each event using all four particle-type assumptions and calculate the evidence for each event for all types. We assign the reconstructed nucleus type for the event as the type that obtains the largest evidence of the reconstruction. The prior-probability distribution of the energy is a uniform probability-density distribution around the true value with a width of ± 20 MeV/n. As already discussed, the high dimensionality of the input-parameter space leads to many events in which the filter fails to find a possible parameter configuration for the event. To increase the probability to succeed the filtering, we use a normal-distributed prior-probability-density with a standard deviation of only 2° for the directional parameters of the event(ϕ,θ,ϕ_0,θ_0). Such a prior could, for example, be obtained by a preceding analysis of the event by the neural-network based track-direction reconstruction.

The obtained confusion matrices of the particle-type reconstruction of the two algorithms are shown in Figure 4.22. For the result of the particle filter, shown in Figure 4.22b, only events are included for which at least one type assumption yields a successful filter procedure. From the total 400 analyzed events by the particle filter, only 167 did not fail at least once. This again shows that the use of 1×10^5 particles per filter step is not sufficient to allow a reliable reconstruction. Even when only considering events that succeeded the filtering stage, the reconstruction based on a neural network outperforms the particle filter in terms of the reconstruction accuracy. The neural network reaches reconstruction

	particle filter	neural network
protons		
$\langle \Delta E \rangle$	0.16 MeV/n	0.04 MeV/n
$\sigma(\Delta E)$	5.25 MeV/n	0.85 MeV/n
deuterons		
$\langle \Delta E \rangle$	1.34 MeV/n	0.01 MeV/n
$\sigma(\Delta E)$	7.12 MeV/n	0.59 MeV/n
helium-3		
$\langle \Delta E \rangle$	0.368 MeV/n	−0.02 MeV/n
$\sigma(\Delta E)$	9.50 MeV/n	0.75 MeV/n
helium-4		
$\langle \Delta E \rangle$	−3.3 MeV/n	−0.04 MeV/n
$\sigma(\Delta E)$	9.81 MeV/n	0.66 MeV/n

Table 4.5: Accuracy ($\langle \Delta E \rangle$) and precision ($\sigma(\Delta E)$) of the energy reconstruction based on the particle filter and the neural network.

accuracies for all particle types above 90 %. The identification of protons and deuterons is even possible with accuracies above 99 %.
The performance of the energy reconstruction for the different particle types reached by the particle filter and the neural network is summarized in Table 4.5. The values are calculated from all tested events in which the particle type is correctly reconstructed. Again, the use of the neural network outperforms the obtained results from the particle filter and reaches an energy-reconstruction precision of around 0.8 MeV/n for all tested particle types.

As a large fraction of low-energy nuclei are not completely stopped, we would like to be able to include these events in the reconstruction as well to increase the acceptance of the detector. However, we expect the reconstruction performance to be reduced when including such events. In order to estimate the decrease of the reconstruction performance, we perform the same analysis using the neural network but on a dataset without the requirement that the particles have to be completely stopped. The obtained performance of the particle identification and energy reconstruction is shown in Figure 4.23. As expected, the overall performance is reduced but the network still reaches particle identification accuracies of above 80 % for all tested particle types. The energy resolution is only slightly affected and is still below 2.5 MeV/n for all tested particle types.

4.4.6 Required Improvements

Although the obtained reconstruction performances using simulated data promise good reconstruction capabilities and the employed reconstruction algorithms—especially for low-

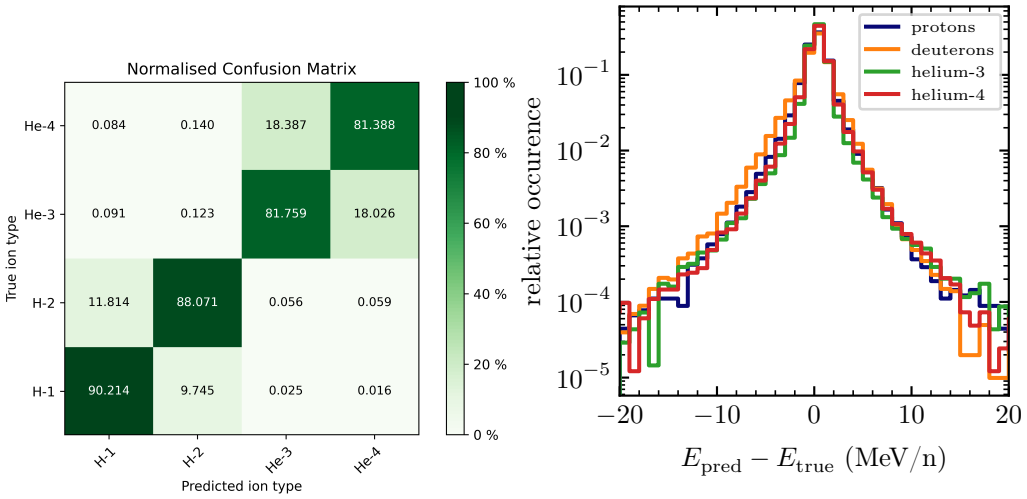

(a) Particle identification.

(b) Deviation of the reconstructed energy.

Figure 4.23: Reconstruction performance of the particle type and energy for simulated particle events in MAPT using the reconstruction method based on a neural network including non-stopped particles.

energy nuclei that stop within the detector—further studies and improvements of the reconstruction scheme are required to allow MAPT to measure energy-differential cosmic-ray particle fluxes for individual nuclei or antinuclei in the future. As the abundances of different nuclei in the cosmic-ray spectrum are differing over orders of magnitude, the separation power of the instrument has to be of similar magnitude. For many particle species, the required separation power has to be larger than what we reached so far: For example, the measured flux ratio of protons and deuterons is on the order of 1×10^2 and the expected flux ratio of antiprotons and antideuterons even on the order of 1×10^7 [295, 9]. To obtain a useful measurement, the separation power of the different species must be at least on the same order of magnitude, meaning that we must improve our particle identification capabilities to allow such measurements. Especially if one wishes to distinguish different antinuclei species, the sole usage of the Bragg curve to identify the charge and mass number of the particle seems not to be sufficient to reach the required separation power, and additional features must be used.

A promising approach is to additionally exploit the annihilation pattern of different antinuclei: As the number of produced secondary particles in the annihilation depends on the mass of the antinucleus that annihilates in the detector, the number of outgoing secondary tracks can be an additional feature in MAPT that helps to distinguish the particle types for antinuclei [247]. Whether this additional feature is sufficient to reach the desired separation power for antideuterons and antiprotons in MAPT is currently under investigation.

The reconstruction of higher-charged nuclei requires a better understanding of the effect of ionization quenching in MAPT. Although the so-far conducted experiment successfully probed the dependence of ionization quenching on the ionization density of the particle for stopping protons, the behavior of quenching for even higher ionization densities, as

they occur when higher charged nuclei stop within the detector, is not yet experimentally constrained.

When comparing the performance of the different approaches for the reconstruction algorithms, we found in the so-far conducted studies that both algorithms, the Bayesian particle filter and neural networks, can be used to extract the direction, energy, and type of a particle from MAPT's signals. However, both algorithms still need further investigation and improvements.
Despite of its mathematical correctness, the Bayesian filtering method has some disadvantages over the neural networks that must be addressed: The filtering method requires massive computational effort and is orders of magnitude slower than the neural-network approach. Without allowing for more parallelized computation, our current implementation requires several hours per event when using the filter with 1×10^5 particles per step. Even when using this large number of particles per step, the filter fails in a large fraction of reconstruction attempts—especially for events with a large number of fiber hits—because all particles are filtered out through the filtering stage with a non-zero weight. This issue is caused by the high dimensionality of the parameter space and a non-perfect implementation of the physical processes that occur during the passage of the particle through the detector. Currently, only multiple scattering and electronic energy losses are implemented in the filter. Only if all relevant processes are included, the filter can reproduce accurately all events that occur in the detector. For example, events that undergo large-angle scattering (single Coulomb scattering) or inelastic hadronic interactions cannot be described by the filter yet. One approach to extend the included physical processes is to use the Geant4 simulation framework, which is currently used for the simulation of the response of MAPT to particles, also for the modeling of the processes within the particle filter.
Although the neural networks already outperformed the particle filter in many regards, its performance has to be further investigated. Especially the transition from simulated data to real detector data potentially induces systematic effects in the reconstruction in case certain features of the signal generation are simulated incorrectly. To exclude such effects, tests of the reconstruction algorithm on real data with known particles and energies, like for example at a particle accelerator facility, must be conducted as soon as a fully functional detector is manufactured.

4.5 Technology Demonstration Missions

In order to further investigate MAPT's measurement capabilities and to verify its functionality in the complex environment of space, two technology demonstration experiments are being developed: In a first mission, a fully functional prototype of the MAPT detector shall be produced and used to measure the direction-dependent flux of charged nuclei inside the International Space Station and provide, together with other radiation-sensitive devices, a full characterization of the radiation environment the astronauts are exposed to during their stay on the ISS [251]. In a second mission, MAPT shall be deployed onto a small satellite to measure geomagnetically trapped antiprotons in the South Atlantic Anomaly (SAA) [180]. In the following sections, I shortly describe the motivation, planned implementation, and current status of both missions.

4.5.1 The RadMap Telescope on the International Space Station

The first in-space deployment of MAPT is planned within the framework of the RadMap-Telescope mission on the International Space Station (ISS). Beside the verification of the technology to be used in the environment of space, the scientific motivation is to measure the radiation environment inside the ISS. Although the spectrum and composition of cosmic rays is well known from measurements by many experiments, the particle flux inside of the ISS is altered due to the material of the hull [296]. On one hand, the material provides shielding, especially against low-energy radiation, but on the other hand, also secondary radiation is produced in high-energy interactions of cosmic rays with the hull, which increases the effective radiation inside the ISS. To properly estimate the radiation the astronauts are exposed to, and to investigate in more detail the effect of the surrounding material on the radiation environment, the particle fluxes, and especially the fluxes of low-energy ions, which are particularly harmful to the human body due to their large ionization losses, must be known precisely [297]. Due to its specialization to reconstruct such low-energy nuclei, MAPT could provide an important measurement that enhances the knowledge about the radiation environment inside the ISS.
As the RadMap Telescope shall primarily serve as a technology demonstrator for MAPT, its measurements are planned to be compared to existing measurements by locating the detector in areas where radiation measurements have been already conducted by other experiments. Additionally, RadMap is equipped with flight-proven dosimeters that can be used as a reference measurement but also extends the sensitivity of the system to radiation stemming from uncharged particles that cannot be detected by MAPT, like neutrons or photons [251].
For RadMap, the MAPT detector is housed in a $(13 \times 13 \times 15)\,\mathrm{cm}^3$ aluminum box together with the on-board computer and the DAQ system required for operation, both adding material around the detector that shields low-energy particles and alters the kinetic energy of the particles before entering the active volume of the detector. Most of the material is located beneath the detector (using the orientation shown in Figure 4.24), which allows particles to enter the detector from above or the sides with minimal additional material. The aluminum housing, however, is inevitable to shield the SiPMs of the detector from ambient light. The additional material that the particles must traverse before reaching the active volume of MAPT is around 0.9 cm of aluminum equivalent on average for an isotropic particle flux. For particles that enter the detector from the upper hemisphere, the average material is lower, only around 0.6 cm aluminum equivalent. Particles that enter MAPT from below, however, have to traverse the DAQ system, the on-board computer, and eventually the cooling channels made out of aluminum. These particles need to traverse on average 1.2 cm of aluminum equivalent and for certain incoming directions even up to 4.5 cm of aluminum equivalent. This material must be taken into account during data analysis, and the fraction of the energy lost before entering the active volume of MAPT must be modeled and added to the reconstructed energy of the nuclei. The additional material also changes the energy range for nuclei that stop within the active volume of MAPT. Compared to the bare MAPT detector that we modeled so far, the minimum energy that a particle must have, in order to create a long enough track in the detector that can be reconstructed, is therefore higher. To estimate the energy range in which nuclei are stopped within the active volume of the detector—and by this can be re-

Figure 4.24: Rendering of the RadMap Telescope. The size of the box is $(13 \times 13 \times 15)\,\mathrm{cm}^3$. Figure taken from [251].

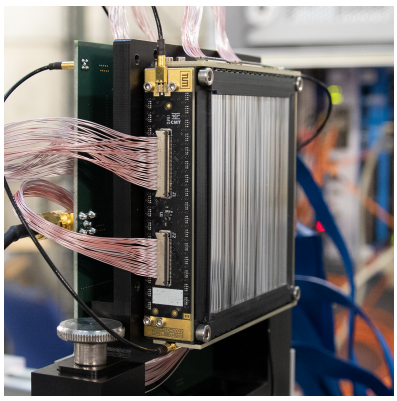

Figure 4.25: Picture of a single module of MAPT. Figure taken from [251].

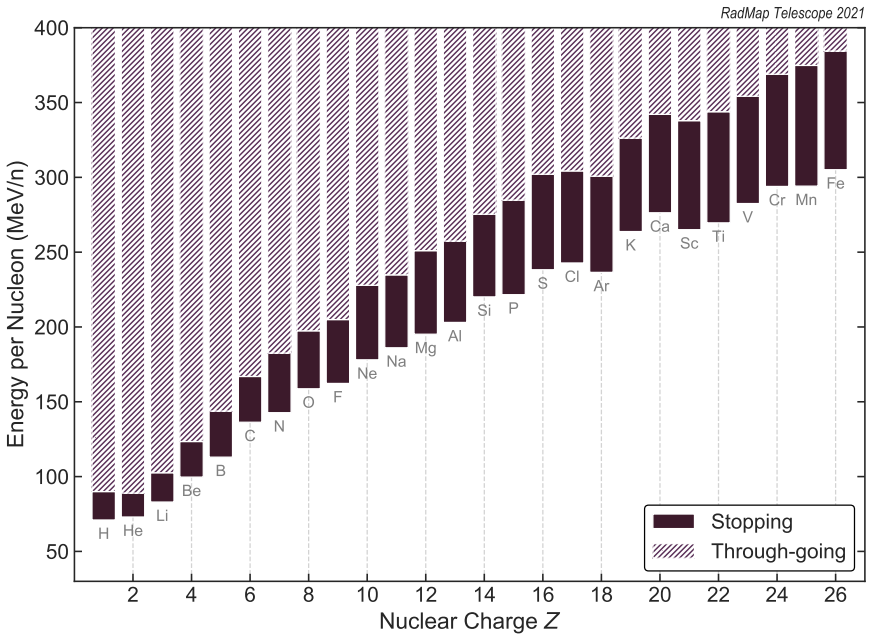

Figure 4.26: Sensitivity range of the RadMap Telescope for different nuclei. Figure taken from [251].

constructed with our Bragg-curve-spectroscopy method—we simulate nuclei with different energies impinging isotropically on a model of the detector and the surrounding material, and analyze which energy the nuclei require to reach the active volume of MAPT and to create at least three fiber hits. We estimate the energy range in which the particles stop in the active volume as the energy range for which at least 50 % of the particles are stopped completely in the active volume. The obtained sensitivity range for RadMap is depicted in Figure 4.26. For energies with stopping ranges larger than the detector, the reconstruction

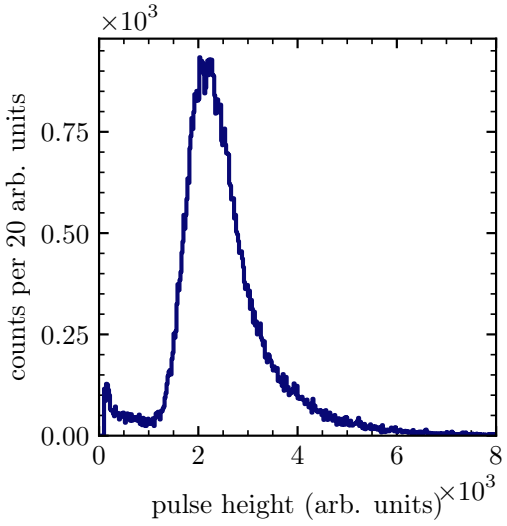

Figure 4.27: Exemplary pulse-height spectrum for one channel of the RadMap Telescope for a beam of minimum-ionizing pions with 450 MeV/c momentum.

precision is reduced, as we have seen in Section 4.4.5).

The detector hardware for the RadMap Telescope is currently in production and the active volume made out of the scintillating fibers coupled to the SiPMs is already manufactured. To ease the assembly, the active volume of MAPT has been subdivided into four modules with 32×8 fibers each, stacked to obtain the full active volume. A single module is shown in Figure 4.25, mounted onto a holding structure used during a functional test at a particle-accelerator facility.
To ensure a full functionality of all fiber-SiPM channels of MAPT, all modules were irradiated by a beam of minimum-ionizing pions with a momentum of 450 MeV/c and the signals of each channel were recorded. We investigated the signal quality of each individual channel in terms of functionality and relative signal amplitude to ensure that all channels yield a fairly similar signal amplitude for a given energy deposition. Figure 4.27 shows exemplarily a typical pulse-height spectrum of an individual channel within the pion beam. The mean signal magnitude of the distribution corresponds to the mean energy deposition of the pions when traversing 2 mm of the scintillating fibers, which is approximately 0.4 MeV of deposited energy. The relative signal variance of the individual channels was found to be on the order of 15 %, which is expected to be sufficiently constant to ensure a full functionality of the detector.
The finalization of the detector hardware, including the corresponding electronics and the deployment of the system to the ISS, is foreseen for 2022-2023. More details on the hardware design and the operational concept of RadMap can be found in the upcoming doctoral thesis of M. Losekamm [252].

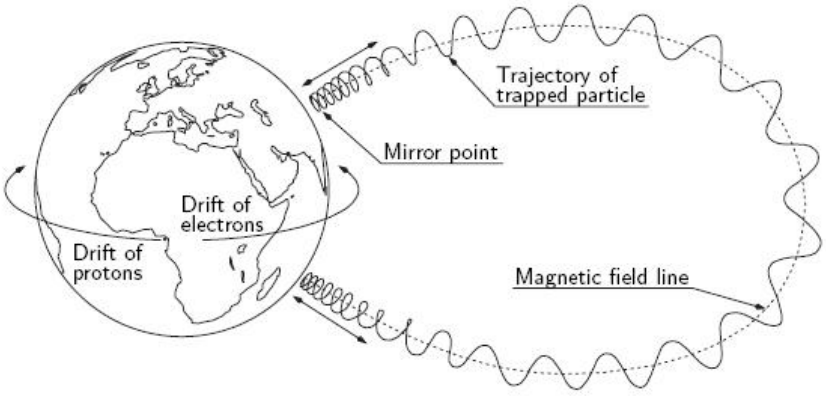

Figure 4.28: Schematic motion of a trapped charged particle in Earth's magnetic field. Adapted from [301].

4.5.2 The Antiproton Flux in Space Mission

In a second technology demonstration mission, MAPT's capability to measure antiparticles and distinguish them from ordinary particles shall be experimentally verified. As the RadMap Telescope is not expected to be exposed to a significant flux of low-energy antiprotons, a second MAPT detector shall be deployed on a dedicated small satellite to probe the sensitivity of MAPT to antiprotons by measuring the flux of low-energy antiprotons that are trapped within Earth's inner radiation belt.
Earth's radiation belts are torus-shaped regions around Earth with an increased density of charged particles. Measurements found two distinct belt-like structures with different particle content surrounding Earth: The inner and the outer radiation belt. The outer belt consists mainly of electrons with rigidities of several kV up to MV. The belt's location is approximately 18×10^3 km to 45×10^3 km above Earth's equator. The inner radiation belt consists mainly of protons, its location is approximately 1×10^3 km to 18×10^3 km above Earth's equator, and it approaches Earth nearest over the SAA, where it reaches down to altitudes below a few hundred kilometers [298, 299]. The protons have rigidities of several MV up to a few GV, which is below the local cut-off rigidity. Thus, the particles must be of secondary origin. They are mainly created in interactions of cosmic-ray particles with the atmosphere at lower altitudes. A small fraction of the created secondaries moves upwards and are called albedo particles [300]. These albedo particles are subsequently influenced by the magnetosphere and can be deflected such that they are trapped within Earth's magnetic field. Figure 4.28 depicts the motion of a trapped charged particle in the Earth's dipole field. The particle mainly gyrates around a field line with an additional movement along the field line, resulting in a helix-shaped motion. When it approaches one of the poles, the increasing local field-line density counteracts the movement along the field line until it reverses the direction of motion and the particle moves along the field line to the opposing pole, where it is again reflected [301]. This movement can repeat itself for several years depending on the depth of the mirror point: If the mirror point is relatively deep within the atmosphere, the probability for the particle to be absorbed or to lose a significant amount of energy—and thus being not energetic enough to maintain

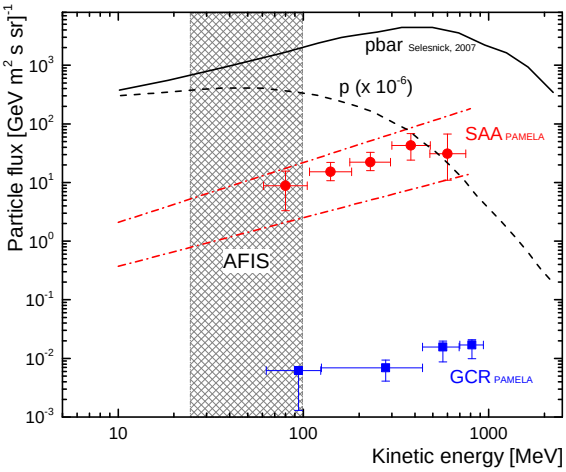

Figure 4.29: Energy spectrum of trapped antiprotons measured by PAMELA (red dots). Additionally, the galactic cosmic ray flux (blue squares) and the theoretical prediction by Selesnick et al. [300] are shown. As a reference, the interpolated proton flux (dashed line) is shown. The grey band is the expected range of energies the AFIS experiment is sensitive to. The dotted red line gives an estimated extrapolation of the trapped antiproton flux from the PAMELA measurement. Figure adapted from [304].

the stable trajectory—increases and the particle will leave the continual trajectory [302]. A second mechanism that can release a large fraction of the stably trapped particles is due to geomagnetic storms. During coronal mass ejections of the Sun, the ejected plasma can disturb the magnetosphere such that the particles are non-adiabatically displaced and do not move on a closed trajectory anymore [303]. Thus, the fluxes of geomagnetically trapped particles are highly varying with the solar cycle. A more detailed description of the trapping mechanism and the motion of the particles can be found in the Master's thesis of the author [180].

Most of the trapped protons above 10 MeV are expected to be created by the decay of albedo neutrons that are created in interactions of cosmic-rays with the atmosphere. Assuming the same mechanism also applies to antineutrons that are created in such interactions, it is expected to also find trapped antiprotons in the inner radiation belt [303]. Due to the resulting accumulation of antiprotons, the flux within the region of the inner radiation belt exceeds the galactic cosmic-ray antiproton flux. This was experimentally, for the first time, confirmed by a measurement of the PAMELA experiment in 2010 [304]. They found that the flux of antiprotons inside the SAA exceeds the galactic cosmic-ray flux by approximately two orders of magnitude in the measurement range of 60 MeV to 800 MeV, as visible in Figure 4.29. The found flux deviates largely from theoretical estimates of the antiproton flux stemming from the modeling of the antineutron-decay mechanism, which predicted an two-orders-of-magnitude larger antiproton flux for the PAMELA experiment. The reason for this deviation between the experimental result and the theoretical prediction is to date not understood. Therefore, further experimental data of the low-energy antiproton flux inside the SAA is required to confirm the measurement.

As MAPT is in particular sensitive to low-energy antiprotons, as they annihilate to a

large extend in the active detector volume, it can be used to provide such a measurement. However, the measurement of antiprotons inside of the radiation-belt environment is challenging: Due to the large flux of trapped protons, MAPT has to withstand proton rates of up to 1×10^2 kHz while the signal rate expected from the measurement by PAMELA is only in the range of a few events per minute. The large background rate and the small signal-to-background ratio of approximately 1×10^{-7} are especially challenging for the design of the readout electronics and data-acquisition system and set stringent requirements on the particle-identification power of the system. Detailed studies on the feasibility of the measurement using MAPT are currently ongoing and first particle-antiparticle separation studies using neural networks were performed [272]. Nevertheless, a successful measurement of antiprotons using MAPT would be an important step forward to prove MAPT's capability to identify cosmic-ray antinuclei.

4.6 Prospect of Measuring Antinuclei with MAPT

Besides the already discussed improvement of the separation power of the different species of antinuclei from each other—especially from the most abundant antiprotons—the very low absolute flux of antinuclei heavier than antiprotons makes it challenging to measure them with the current layout of MAPT. The expected number of events, N_i, for a given particle flux, $\psi_i(E, E + \Delta E)$, of a particle type, i, in the energy interval, $E + \Delta E$, can be calculated as

$$N_i(E, E + \Delta E) = \psi_i(E, E + \Delta E) A_i(E) \Delta t \Delta E, \tag{4.42}$$

with Δt being the measurement time and $A_i(E)$ the acceptance of the detector for particles of type i and energy E. In general, the acceptance of the detector is determined from the geometrical factor of the detector, G_{geom}, and the efficiency of the reconstruction, $\epsilon_i(E)$, as

$$A_i(E) = G_{\text{geom}} \epsilon_i(E). \tag{4.43}$$

Even in the case of a perfect detector—meaning that $\epsilon_i(E) = 1$ and all traversing particles can be measured and identified, the geometrical factor limits the event rate for a given flux and the minimum flux that can be probed by the system for a given mission duration.
The geometrical factor of MAPT for an isotropic particle flux cannot be calculated analytically but can be determined using a Monte-Carlo approach, as proposed by Sullivan et al. [305]. By generating random particle tracks starting from a sphere with radius r around the detector, the fraction of tracks that hit the detector and would create an measurable signal determine the geometrical factor of the detector as

$$G_{\text{geom}} = \frac{n_{\text{hit}}}{n_{\text{tot}}} G_{\text{sphere}}, \tag{4.44}$$

with n_{hit} the number of tracks that hit the detector, n_{tot} the total number of trials, and G_{sphere} the geometrical factor of the starting sphere, which can be analytically calculated as

$$G_{\text{sphere}} = 4\pi^2 r^2, \tag{4.45}$$

if all sampled tracks starting with a direction pointing inwards of the sphere's surface [305]. The obtained geometrical factor for MAPT using this method with 1×10^8 simulations is calculated to be $G_{\text{geom}} = (1013.16 \pm 0.24)\,\text{cm}^2\text{sr}$. Although this geometrical factor is large compared to the detector size—due to the near omnidirectional acceptance— the measurement time required to be sensitive to particle fluxes on the order of $1 \times 10^{-7}\,\text{m}^{-2}\text{sr}^{-1}\text{s}^{-1}(\text{GeV/n})^{-1}$ is several years for an energy range of approximately 1 GeV/n. As the geometrical factor increases quadratically with the edge length of the cubic detector layout, an increase of MAPT by a factor of three would already allow to probe such low fluxes within several months of measurement time, which is a realistic time domain for such missions. However, more detailed feasibility studies are needed and the efficiency of the reconstruction must be taken into account to determine whether such low particle fluxes can be realistically probed by the MAPT detector concept. Similar concepts that are based on the annihilation pattern of antinuclei in a particle detector are currently pursued by several groups and several experiments, for example, the GAPS experiment that aims to probe antideuterons with a similar detector concept on a stratospheric balloon flight over the antarctic in near future [247].

The concept of MAPT seems to be a promising approach for a next-generation particle detector to probe low-energy cosmic rays in space. Upcoming technology demonstration experiments will investigate whether the concept reaches sufficient particle identification power to obtain meaningful measurements of cosmic-ray particle fluxes.

Chapter 5

Summary and Conclusion

Measurements of charged galactic cosmic rays are a valuable tool to study the processes of fast-particle creation in our galaxy and their propagation to us in an indirect manner. By comparing models of the production and propagation of cosmic rays with measurements we can validate our understanding of the involved processes.

To interpret correctly the significance of a found deviation between the modeled flux and the measurements, we have to consider all uncertainties of the measurements and the models. In the last decades the measurement uncertainties have decreased strongly. Hence, a detailed analysis of the model uncertainties of our particle-flux predictions has become inevitable. In the case of antiprotons—the so-far only detected species of galactic antinuclei—the largest model uncertainties arise mainly from the propagation and the production cross section. Several different models exist for both processes that lead to vastly different predictions for the cosmic-ray antiproton flux at Earth.

In this work, the impact of the numerical solution of the propagation equation and the used production-cross-section models on the predicted antiproton cosmic-ray flux have been studied in a scenario of a purely secondary production of antiprotons. The found deviations of the modeled flux among the different models serves as an estimate of the modeling uncertainty of the antiproton-flux prediction. These uncertainties have to be taken into account when interpreting deviations of the models with experimental data.

In Chapter 2, I have investigated GALPROP, one of the most commonly used propagation frameworks, and estimated the uncertainties arising from its numerical-solution method on the steady-state particle flux at Earth. I have found that the numerical accuracy depends strongly on the applied settings of the solution-grid parameters and on the parameters of the numerical-solution algorithm. So far, most studies have used settings that result in a flux prediction that deviates from the underlying steady-state solution of the diffusion equation. The found deviations are in some cases even larger than the experimental uncertainties on the corresponding measured fluxes by AMS-02. However, in case of antiprotons, the found deviations are small compared to the experimental uncertainties and can be neglected in the current data situation.

To compare the antiproton-flux prediction for different models of the production cross section, a common propagation scheme has to be selected. I have reviewed different propagation schemes and have found that the propagation setup of Boschini et al. [163] is most suitable for this study as it is the numerically most accurate one and the propagation

parameters of the model are not tuned to antiproton measurements, which allows us to use the propagation setup to predict the antiproton flux for different production models in an unbiased way. However, deviations between different state-of-the-art propagation models yield antiproton fluxes for an identical production model of antiprotons of up to 50 %, much larger than the experimental uncertainties by AMS-02.

To date, the production cross section for antiprotons is not yet measured at all relevant collision energies and for all colliding systems that occur in cosmic-ray collisions. Therefore, models are required to inter and extrapolate the cross section from those kinematic regions where experimental data are available. Currently, two different methods are commonly used in the field: Either one of the multi-purpose Monte-Carlo event generators is used to model the antiproton production, or analytical parameterizations are employed, which are fitted to experimental antiproton-production data and approximate the phase-space distribution of antiprotons produced in the collisions.
In Chapter 3, I have compared both approaches to available experimental data of antiproton production from accelerator-based experiments. I have found that the most commonly used event generators, which are based on the PYTHIA or the EPOS model, cannot well reproduce the measured yields of antiprotons for most collision energies. Also, the tested parameterizations of the production cross section have been found to be unable to describe all used experimental datasets of antiproton production simultaneously with a single set of parameters. I identified this to be caused by a dependence of the x_r distribution of produced antiprotons on $\sqrt{s}$, which is not incorporated in the two tested parameterizations. By adapting one of the parameterizations to include this $\sqrt{s}$ dependence, we succeeded to obtain a much improved agreement with the experimental data for all collision energies. However, this ad-hoc approach is not theoretically founded and the functional form of the $\sqrt{s}$ dependence has to be studied further. Experimental data at non-central rapidity and large $\sqrt{s}$ could help to constrain the functional form of the antiproton distribution in phase space.
The obtained local interstellar antiproton fluxes using the different parameterizations of the antiproton production deviate from each other by approximately 25 % over the whole tested energy range. The obtained fluxes from the event generators exceed these fluxes by more than a factor of two. Also when comparing the solar-modulated fluxes obtained using the different production models to AMS-02 data, the fluxes from the event generators exceeded the measurement by far. The predictions of the antiproton flux for the different parameterizations agree with the experimental data on the 25 % level. The fluxes from the different parameterizations deviate from each other by approximately 25 %, yielding another model uncertainty larger than the experimental uncertainties by AMS-02. Due to the large model uncertainties of the propagation models (50 %) and the production models (25 %), a conclusive statement whether the measured flux is in accordance with an antiproton flux from pure secondary origin cannot be made.

Despite all the modeling uncertainties, the measured antiproton flux at Earth still provides one of the strongest limits on exotic antimatter sources in our galaxy to date. In the last decade, however, the search for heavier antinuclei, such as antideuterons and antihelium, has come into focus as they are believed to constrain exotic sources even stronger due to the much-reduced background from cosmic-ray collisions compared to antiprotons. So

far, such antinuclei have not yet been detected in cosmic rays experimentally due to their extremely low flux. New detector concepts and developments are needed that are focusing on low-energy antinuclei and very low particle fluxes. One way to improve the sensitivity to lower particle fluxes is to build detectors that can measure cosmic rays omnidirectionally, which increases the reachable geometric factor for a given detector size with respect to a typical telescope-like setup.
In Chapter 4, I have described the development and layout of a novel detector concept based on this approach. The detector measures and identifies nuclei and antinuclei by their characteristic interaction with the material of a segmented volume of plastic scintillators. While antinuclei can be identified by their characteristic annihilation pattern in the detector, the ion species can be distinguished from each other by their different energy-deposition profiles, their so-called Bragg curves. To reconstruct the Bragg curve for a traversing particle in the detector, the relation between the ionization loss of the particle and the produced scintillation-light yield in each fiber has to be known well. Especially for high ionization losses, this relation is, however, poorly understood due to saturation effects of the plastic scintillators, so-called ionization quenching. I have presented a dedicated experiment using a proton beam to investigate the ionization-density dependence of the quenching effect and to compare different phenomenological models that aim to quantify it. Using a model-independent approach, I have shown that currently none of the models is able to correctly reproduce the found relation and further measurements at even higher ionization densities are required to reliably model the expected Bragg curves for highly charged ions in the planned detector.
As a first realization of the detector concept, I have presented the MAPT detector, which consist of 1024 scintillating fibers coupled to silicon photomultipliers. To reconstruct direction, energy, and particle type of a measured particle from the detector signals, I have presented the development of two different reconstruction algorithms, one based on a Bayesian particle filter, and one on neural networks. I have tested the performance of both approaches using simulated detector data and obtained promising identification accuracies for light nuclei. In order to verify the capability of MAPT to measure cosmic-ray fluxes, two technology demonstration missions are currently planned for the next years. They shall demonstrate the sensitivity of MAPT to both, ions and antiprotons, and the operability of the detector in the space environment. A future usage of the detector concept to measure cosmic antideuterons requires an increased size of the detector with respect to MAPT by at least a factor of three and an improved particle-identification power.

Bibliography

[1] V. L. Ginzburg, "Cosmic ray astrophysics (history and general review)," *Physics-Uspekhi*, vol. 39, no. 2, pp. 155–168, 1996. Online available: http://dx.doi.org/10.1070/PU1996v039n02ABEH000132

[2] National Aeronautics and Space Administration, "NASA's Efforts to Manage Health and Human Performance Risks for Space Exploration," Report IG-16-003, 2015. Online available: https://humanresearchroadmap.nasa.gov/evidence/reports/EvidenceBook.pdf

[3] D. Maurin, R. Taillet, F. Donato *et al.*, "Galactic Cosmic Ray Nuclei as a Tool for Astroparticle Physics," *arXiv e-prints: astro-ph/0212111*. Online available: https://arxiv.org/abs/astro-ph/0212111

[4] A. W. Strong, I. V. Moskalenko, and V. S. Ptuskin, "Cosmic-Ray Propagation and Interactions in the Galaxy," *Annual Review of Nuclear and Particle Science*, vol. 57, no. 1, pp. 285–327, 2007. Online available: https://doi.org/10.1146/annurev.nucl.57.090506.123011

[5] E. Mocchiutti, "Direct detection of cosmic rays: through a new era of precision measurements of particle fluxes," *Nuclear Physics B - Proceedings Supplements*, vol. 256-257, pp. 161–172, 2014. Online available: http://www.sciencedirect.com/science/article/pii/S0920563214002138

[6] M. Kachelrieß and D. V. Semikoz, "Cosmic ray models," *Progress in Particle and Nuclear Physics*, vol. 109, p. 103710, 2019. Online available: http://www.sciencedirect.com/science/article/pii/S0146641019300456

[7] Y. Génolini, D. Maurin, I. V. Moskalenko *et al.*, "Current status and desired precision of the isotopic production cross sections relevant to astrophysics of cosmic rays: Li, Be, B, C, and N," *Physical Review C*, vol. 98, no. 3, p. 034611, 2018. Online available: https://link.aps.org/doi/10.1103/PhysRevC.98.034611

[8] N. Tomassetti, "Solar and nuclear physics uncertainties in cosmic-ray propagation," *Physical Review D*, vol. 96, no. 10, p. 103005, 2017. Online available: https://link.aps.org/doi/10.1103/PhysRevD.96.103005

[9] P. von Doetinchem, K. Perez, T. Aramaki *et al.*, "Cosmic-ray antinuclei as messengers of new physics: status and outlook for the new decade," *Journal of*

Cosmology and Astroparticle Physics, vol. 2020, no. 08, pp. 035–035, aug 2020. Online available: https://doi.org/10.1088/1475-7516/2020/08/035

[10] M. Walter and A. W. Wolfendale, "Early history of cosmic particle physics," *The European Physical Journal H*, vol. 37, no. 3, pp. 323–358, 2012. Online available: https://doi.org/10.1140/epjh/e2012-30020-1

[11] V. Hess, "Über Beobachtungen der durchdringenden Strahlung bei sieben Freiballonfahrten," *Physik. Zeitschr.*, vol. XIII, pp. 1084–1091, 1912.

[12] V. F. Hess, *Nobel Lecture Physics 1936*. Elsevier, 2013, pp. 351–377. Online available: http://www.sciencedirect.com/science/article/pii/B9781483197456500192

[13] W. Kolhörster, "Messungen der durchdringenden Strahlungen bis in Höhen von 9300 m," *Verhandlungen der Deutschen Physikalischen Gesellschaft*, vol. 16, pp. 719–721, 1914.

[14] R. A. Millikan and I. S. Bowen, "High Frequency Rays of Cosmic Origin I. Sounding Balloon Observations at Extreme Altitudes," *Physical Review*, vol. 27, no. 4, pp. 353–361, 1926. Online available: https://link.aps.org/doi/10.1103/PhysRev.27.353

[15] A. H. Compton, "Variation of the Cosmic Rays with Latitude," *Physical Review*, vol. 41, no. 1, pp. 111–113, 1932. Online available: https://link.aps.org/doi/10.1103/PhysRev.41.111.2

[16] L. Alvarez and A. H. Compton, "A Positively Charged Component of Cosmic Rays," *Physical Review*, vol. 43, no. 10, pp. 835–836, 1933. Online available: https://link.aps.org/doi/10.1103/PhysRev.43.835

[17] P. A. M. Dirac and R. H. Fowler, "The quantum theory of the electron," *Proceedings of the Royal Society of London. Series A, Containing Papers of a Mathematical and Physical Character*, vol. 117, no. 778, pp. 610–624, 1928. Online available: https://doi.org/10.1098/rspa.1928.0023

[18] C. D. Anderson, "The Positive Electron," *Physical Review*, vol. 43, no. 6, pp. 491–494, 1933. Online available: https://link.aps.org/doi/10.1103/PhysRev.43.491

[19] D. H. Perkins, "FROM PIONS TO PROTON DECAY: Tales of the Unexpected," *Annual Review of Nuclear and Particle Science*, vol. 55, no. 1, pp. 1–26, 2005. Online available: https://www.annualreviews.org/doi/abs/10.1146/annurev.nucl.55.102703.130016

[20] J. W. Cronin, "The 1953 Cosmic Ray Conference at Bagnères de Bigorre: the Birth of Sub Atomic Physics," *European Physical Journal H*, vol. 36, pp. 183–201, 2011. Online available: https://doi.org/10.1140/epjh/e2011-20014-4

[21] P. D. Group, P. A. Zyla, R. M. Barnett *et al.*, "Review of Particle Physics," *Progress of Theoretical and Experimental Physics*, vol. 2020, no. 8, 2020. Online available: https://doi.org/10.1093/ptep/ptaa104

[22] J. R. Winckler and L. Peterson, "Cosmic Rays and the Sunspot Cycle: A Large Cosmic-Ray Decrease accompanying the Solar Maximum of 1957," *Nature*, vol. 181, no. 4619, pp. 1317–1319, 1958. Online available: https://doi.org/10.1038/1811317a0

[23] P. Meyer and J. A. Simpson, "Changes in the Low-Energy Particle Cutoff and Primary Spectrum of Cosmic Rays," *Physical Review*, vol. 106, no. 3, pp. 568–571, 1957. Online available: https://link.aps.org/doi/10.1103/PhysRev.106.568

[24] M. S. Potgieter, "Solar Modulation of Cosmic Rays," *Living Reviews in Solar Physics*, vol. 10, no. 1, p. 3, 2013. Online available: https://doi.org/10.12942/lrsp-2013-3

[25] Y. Shikaze, S. Haino, K. Abe *et al.*, "Measurements of 0.2–20GeV/n cosmic-ray proton and helium spectra from 1997 through 2002 with the BESS spectrometer," *Astroparticle Physics*, vol. 28, no. 1, pp. 154–167, 2007. Online available: http://www.sciencedirect.com/science/article/pii/S0927650507000710

[26] W. R. Webber, N. Lal, and B. Heikkila, "Measurements in Interstellar Space of Galactic Cosmic Ray Isotopes of Li, Be, B and N, Ne Nuclei Between 40-160 MeV/nuc by the CRS Instrument on Voyager 1," October 01, 2018. Online available: https://arxiv.org/abs/1810.08589

[27] E. C. Stone, A. C. Cummings, B. C. Heikkila *et al.*, "Cosmic ray measurements from Voyager 2 as it crossed into interstellar space," *Nature Astronomy*, vol. 3, no. 11, pp. 1013–1018, 2019. Online available: https://doi.org/10.1038/s41550-019-0928-3

[28] M. J. Boschini, S. Della Torre, M. Gervasi *et al.*, "The HelMod model in the works for inner and outer heliosphere: From AMS to Voyager probes observations," *Advances in Space Research*, vol. 64, no. 12, pp. 2459–2476, 2019. Online available: http://www.sciencedirect.com/science/article/pii/S0273117719302509

[29] N. Hilberry, "Extensive Cosmic-Ray Showers and the Energy Distribution of Primary Cosmic Rays," *Physical Review*, vol. 60, no. 1, pp. 1–9, 1941. Online available: https://link.aps.org/doi/10.1103/PhysRev.60.1

[30] E. Fermi, "On the Origin of the Cosmic Radiation," *Physical Review*, vol. 75, no. 8, pp. 1169–1174, 1949. Online available: https://link.aps.org/doi/10.1103/PhysRev.75.1169

[31] A. R. Bell, "The acceleration of cosmic rays in shock fronts – I," *Monthly Notices of the Royal Astronomical Society*, vol. 182, no. 2, pp. 147–156, 1978. Online available: https://doi.org/10.1093/mnras/182.2.147

[32] P. Freier, E. J. Lofgren, E. P. Ney *et al.*, "Evidence for Heavy Nuclei in the Primary Cosmic Radiation," *Physical Review*, vol. 74, no. 2, pp. 213–217, 1948. Online available: https://link.aps.org/doi/10.1103/PhysRev.74.213

[33] H. L. Bradt and B. Peters, "Investigation of the Primary Cosmic Radiation with Nuclear Photographic Emulsions," *Physical Review*, vol. 74, no. 12, pp. 1828–1837, 1948. Online available: https://link.aps.org/doi/10.1103/PhysRev.74.1828

[34] V. L. Ginzburg, "On the origin of cosmic rays," *Il Nuovo Cimento (1955-1965)*, vol. 8, no. 2, pp. 430–439, 1958. Online available: https://doi.org/10.1007/BF02962551

[35] D. Maurin, F. Melot, and R. Taillet, "A database of charged cosmic rays," *Astronomy and Astrophysics*, vol. 569, p. A32, 2014. Online available: https://doi.org/10.1051/0004-6361/201321344

[36] V. Grebenyuk, D. Karmanov, I. Kovalev *et al.*, "Energy spectra of abundant cosmic-ray nuclei in the NUCLEON experiment," *Advances in Space Research*, vol. 64, no. 12, pp. 2546–2558, 2019. Online available: http://www.sciencedirect.com/science/article/pii/S0273117719307379

[37] G. T. Zatsepin and V. A. Kuz'min, "Upper Limit of the Spectrum of Cosmic Rays," *Soviet Journal of Experimental and Theoretical Physics Letters*, vol. 4, p. 78.

[38] K. Greisen, "End to the Cosmic-Ray Spectrum?" *Physical Review Letters*, vol. 16, no. 17, pp. 748–750, 1966. Online available: https://link.aps.org/doi/10.1103/PhysRevLett.16.748

[39] A. M. Hillas, "The Origin of Ultra-High-Energy Cosmic Rays," *Annual Review of Astronomy and Astrophysics*, vol. 22, p. 425, 1984. Online available: https://doi.org/10.1146/annurev.aa.22.090184.002233

[40] P. L. Biermann and P. A. Strittmatter, "Synchrotron Emission from Shock Waves in Active Galactic Nuclei," *The Astrophysical Journal*, vol. 322, p. 643, 1987. Online available: https://ui.adsabs.harvard.edu/abs/1987ApJ...322..643B

[41] J. Abraham, P. Abreu, M. Aglietta *et al.*, "Correlation of the Highest-Energy Cosmic Rays with Nearby Extragalactic Objects," *Science*, vol. 318, p. 938, 2007. Online available: https://science.org/doi/10.1126/science.1151124

[42] J. R. Hörandel, "Models of the knee in the energy spectrum of cosmic rays," *Astroparticle Physics*, vol. 21, no. 3, pp. 241–265, 2004. Online available: http://www.sciencedirect.com/science/article/pii/S0927650504000209

[43] A. D. Panov, J. H. Adams, H. S. Ahn *et al.*, "Energy spectra of abundant nuclei of primary cosmic rays from the data of ATIC-2 experiment: Final results," *Bulletin of the Russian Academy of Sciences: Physics*, vol. 73, no. 5, pp. 564–567, 2009. Online available: https://doi.org/10.3103/S1062873809050098

[44] Y. S. Yoon, T. Anderson, A. Barrau *et al.*, "Proton and Helium Spectra from the CREAM-III Flight," *The Astrophysical Journal*, vol. 839, no. 1, p. 5, 2017. Online available: http://dx.doi.org/10.3847/1538-4357/aa68e4

[45] Q. An, R. Asfandiyarov, P. Azzarello *et al.*, "Measurement of the cosmic ray proton spectrum from 40 GeV to 100 TeV with the DAMPE satellite," *Science Advances*, vol. 5, no. 9, p. eaax3793, 2019. Online available: http://advances.sciencemag.org/content/5/9/eaax3793.abstract

[46] W. D. Apel, J. C. Arteaga-Velázquez, K. Bekk *et al.*, "Kneelike Structure in the Spectrum of the Heavy Component of Cosmic Rays Observed with KASCADE-Grande," *Physical Review Letters*, vol. 107, no. 17, p. 171104, 2011. Online available: https://link.aps.org/doi/10.1103/PhysRevLett.107.171104

[47] M. Aguilar, L. Ali Cavasonza, B. Alpat *et al.*, "Observation of the Identical Rigidity Dependence of He, C, and O Cosmic Rays at High Rigidities by the Alpha Magnetic Spectrometer on the International Space Station," *Physical Review Letters*, vol. 119, no. 25, p. 251101, 2017. Online available: https://link.aps.org/doi/10.1103/PhysRevLett.119.251101

[48] H. S. Ahn, P. Allison, M. G. Bagliesi *et al.*, "ENERGY SPECTRA OF COSMIC-RAY NUCLEI AT HIGH ENERGIES," *The Astrophysical Journal*, vol. 707, no. 1, pp. 593–603, 2009. Online available: http://dx.doi.org/10.1088/0004-637X/707/1/593

[49] M. Aguilar, L. Ali Cavasonza, G. Ambrosi *et al.*, "Observation of New Properties of Secondary Cosmic Rays Lithium, Beryllium, and Boron by the Alpha Magnetic Spectrometer on the International Space Station," *Physical Review Letters*, vol. 120, no. 2, p. 021101, 2018. Online available: https://link.aps.org/doi/10.1103/PhysRevLett.120.021101

[50] H. S. Ahn, P. S. Allison, M. G. Bagliesi *et al.*, "Measurements of cosmic-ray secondary nuclei at high energies with the first flight of the CREAM balloon-borne experiment," *Astroparticle Physics*, vol. 30, no. 3, pp. 133–141, 2008. Online available: http://www.sciencedirect.com/science/article/pii/S092765050800114X

[51] M.-Y. Cui, X. Pan, Q. Yuan *et al.*, "Revisit of cosmic ray antiprotons from dark matter annihilation with updated constraints on the background model from AMS-02 and collider data," *Journal of Cosmology and Astroparticle Physics*, vol. 2018, no. 06, pp. 024–024, 2018. Online available: http://dx.doi.org/10.1088/1475-7516/2018/06/024

[52] P. Blasi, "On the origin of high energy cosmic rays," *Journal of Physics: Conference Series*, vol. 203, p. 012017, 2010. Online available: http://dx.doi.org/10.1088/1742-6596/203/1/012017

[53] W. Baade and F. Zwicky, "On Super-Novae," *Proceedings of the National Academy of Sciences*, vol. 20, no. 5, pp. 254–259, 1934. Online available: https://www.pnas.org/content/pnas/20/5/254.full.pdf

[54] W. Baade and F. Zwicky, "Cosmic Rays from Super-Novae," *Proceedings of the National Academy of Sciences*, vol. 20, no. 5, pp. 259–263, 1934. Online available: https://www.pnas.org/content/pnas/20/5/259.full.pdf

[55] W. Baade and F. Zwicky, "Remarks on Super-Novae and Cosmic Rays," *Physical Review*, vol. 46, no. 1, pp. 76–77, 1934. Online available: https://link.aps.org/doi/10.1103/PhysRev.46.76.2

[56] W. I. Axford, E. Leer, and G. Skadron, "The Acceleration of Cosmic Rays by Shock Waves."

[57] R. D. Blandford and J. P. Ostriker, "Particle acceleration by astrophysical shocks," *The Astrophysical Journal*, vol. 221, p. L29, 1978. Online available: https://ui.adsabs.harvard.edu/abs/1978ApJ...221L..29B

[58] G. F. Krymskii, "A regular mechanism for the acceleration of charged particles on the front of a shock wave," *Akademiia Nauk SSSR Doklady*, vol. 234, p. 1306.

[59] J. Skilling, "Cosmic Ray Streaming—I Effect of Alfvén Waves on Particles," *Monthly Notices of the Royal Astronomical Society*, vol. 172, no. 3, pp. 557–566, 1975. Online available: https://doi.org/10.1093/mnras/172.3.557

[60] J. Skilling, "Cosmic ray streaming - III. Self-consistent solutions," *Monthly Notices of the Royal Astronomical Society*, vol. 173, p. 255, 1975. Online available: https://doi.org/10.1093/mnras/173.2.255

[61] J. R. Jokipii, "a Model of Fermi Acceleration at Shock Fronts with an Application to the Earth's Bow Shock," *The Astrophysical Journal*, vol. 143, p. 961, 1966. Online available: https://ui.adsabs.harvard.edu/abs/1966ApJ...143..961J

[62] L. A. Frank and J. A. Van Allen, "Measurements of energetic electrons in the vicinity of the sunward magnetospheric boundary with Explorer 14," *Journal of Geophysical Research (1896-1977)*, vol. 69, no. 23, pp. 4923–4932, 1964. Online available: https://agupubs.onlinelibrary.wiley.com/doi/abs/10.1029/JZ069i023p04923

[63] Z. Kopal, "On the nature of physical processes underlying the nova phenomenon," *Vistas in Astronomy*, vol. 2, pp. 1491–1505, 1956. Online available: http://www.sciencedirect.com/science/article/pii/0083665656900782

[64] G. Morlino, *High-Energy Cosmic Rays from Supernovae.* Cham: Springer International Publishing, 2017, pp. 1711–1736. Online available: https://doi.org/10.1007/978-3-319-21846-5_11

[65] P. Blasi, "The origin of galactic cosmic rays," *The Astronomy and Astrophysics Review*, vol. 21, no. 1, p. 70, 2013. Online available: https://doi.org/10.1007/s00159-013-0070-7

[66] T. C. Licquia and J. A. Newman, "IMPROVED ESTIMATES OF THE MILKY WAY'S STELLAR MASS AND STAR FORMATION RATE FROM HIAB," *The Astrophysical Journal*, vol. 806, no. 1, p. 96, 2015. Online available: http://dx.doi.org/10.1088/0004-637X/806/1/96

[67] T. K. Gaisser, R. Engel, and E. Resconi, *Cosmic Rays and Particle Physics*, 2nd ed. Cambridge: Cambridge University Press, 2016. Online available: https://www.cambridge.org/core/books/cosmic-rays-and-particle-physics/C81BA71195ADFC89EFCC2C565B617702

[68] L. L. Watkins, R. P. van der Marel, S. T. Sohn *et al.*, "Evidence for an Intermediate-mass Milky Way from Gaia DR2 Halo Globular Cluster Motions," *The Astrophysical Journal*, vol. 873, p. 118, 2019. Online available: https://ui.adsabs.harvard.edu/abs/2019ApJ...873..118W

[69] S. Profumo, L. Giani, and O. F. Piattella, "An Introduction to Particle Dark Matter," *Universe*, vol. 5, p. 213, 2019. Online available: https://www.mdpi.com/2218-1997/5/10/213

[70] F. Donato, "Indirect searches for dark matter," *Physics of the Dark Universe*, vol. 4, pp. 41–43, 2014. Online available: https://www.sciencedirect.com/science/article/pii/S221268641400020X

[71] A. Eckart and R. Genzel, "First Conclusive Evidence for a Massive Black Hole in the Center of the Milky Way," ser. Black Holes: Theory and Observation. Springer Berlin Heidelberg, Conference Proceedings, pp. 60–68. Online available: https://doi.org/10.1007/978-3-540-49535-2_3

[72] F. Eisenhauer, R. Schödel, R. Genzel *et al.*, "A Geometric Determination of the Distance to the Galactic Center," *The Astrophysical Journal*, vol. 597, no. 2, pp. L121–L124, 2003. Online available: http://dx.doi.org/10.1086/380188

[73] R. Abuter, A. Amorim, M. Bauböck *et al.*, "A geometric distance measurement to the Galactic center black hole with 0.3*Astronomy and Astrophysics*, vol. 625, p. L10, 2019. Online available: https://ui.adsabs.harvard.edu/abs/2019A&A...625L..10G

[74] R. A. Chevalier, "Supernova Remnants in Molecular Clouds," *The Astrophysical Journal*, vol. 511, pp. 798–811, 1999. Online available: https://ui.adsabs.harvard.edu/abs/1999ApJ...511..798C

[75] G. Case and D. Bhattacharya, "Revisiting the galactic supernova remnant distribution," *Astronomy and Astrophysics Supplement Series*, vol. 120, p. 437, 1996. Online available: https://ui.adsabs.harvard.edu/abs/1996A&AS..120C.437C

[76] D. R. Lorimer, "The Galactic Population and Birth Rate of Radio Pulsars," in *Young Neutron Stars and Their Environments, IAU Symposium*, vol. 218, Conference Proceedings, p. 105. Online available: https://ui.adsabs.harvard.edu/abs/2004IAUS..218..105L

[77] J. S. Urquhart, C. C. Figura, T. J. T. Moore *et al.*, "The RMS survey: galactic distribution of massive star formation," *Monthly Notices of the Royal Astronomical Society*, vol. 437, no. 2, pp. 1791–1807, 2013. Online available: https://doi.org/10.1093/mnras/stt2006

[78] F. W. Stecker and F. C. Jones, "The galactic halo question: new size constraints from galactic gamma -ray data," *The Astrophysical Journal*, vol. 217, p. 843, 1977. Online available: https://ui.adsabs.harvard.edu/abs/1977ApJ...217..843S

[79] D. A. Green, "Constraints on the distribution of supernova remnants with Galactocentric radius," *Monthly Notices of the Royal Astronomical Society*, vol. 454, no. 2, pp. 1517–1524, 2015. Online available: https://doi.org/10.1093/mnras/stv1885

[80] B. Arbutina and D. Urošević, "Σ-D relation for supernova remnants and its dependence on the density of the interstellar medium," *Monthly Notices of the Royal Astronomical Society*, vol. 360, p. 76, 2005. Online available: https://doi.org/10.1111/j.1365-2966.2005.09033.x

[81] D. A. Green, "Galactic supernova remnants: an updated catalogue and some statistics," *Bulletin of the Astronomical Society of India*, vol. 32, p. 335, 2004. Online available: https://ui.adsabs.harvard.edu/abs/2004BASI...32..335G

[82] F. Aharonian, *Gamma-Ray Emission of Supernova Remnants and the Origin of Galactic Cosmic Rays.* Dordrecht: Springer Netherlands, 2013, pp. 789–827. Online available: https://doi.org/10.1007/978-94-007-5612-0_15

[83] A. W. Strong, J. B. G. M. Bloemen, T. M. Dame *et al.*, "The radial distribution of galactic gamma rays. IV. The whole galaxy," *Astronomy and Astrophysics*, vol. 207, p. 1, 1988. Online available: https://ui.adsabs.harvard.edu/abs/1988A&A...207....1S

[84] A. W. Strong, I. V. Moskalenko, O. Reimer *et al.*, "The distribution of cosmic-ray sources in the Galaxy, γ-rays and the gradient in the CO-to-H_2 relation," *Astronomy and Astrophysics*, vol. 422, p. L47, 2004. Online available: https://ui.adsabs.harvard.edu/abs/2004A&A...422L..47S

[85] C. J. Cesarsky, "Cosmic-Ray Confinement in the Galaxy," *Annual Review of Astronomy and Astrophysics*, vol. 18, no. 1, pp. 289–319, 1980. Online available: https://www.annualreviews.org/doi/abs/10.1146/annurev.aa.18.090180.001445

[86] V. Ptuskin, "Propagation of galactic cosmic rays," *Astroparticle Physics*, vol. 39-40, pp. 44–51, 2012. Online available: http://www.sciencedirect.com/science/article/pii/S0927650511002039

[87] R. Schlickeiser, *Cosmic Ray Astrophysics.* Springer Berlin, Heidelberg.

[88] M. Korsmeier, "Unveiling dark matter with cosmic messengers," Thesis, 2020. Online available: https://publications.rwth-aachen.de/record/795949

[89] C. Evoli, D. Gaggero, A. Vittino *et al.*, "Cosmic-ray propagation with DRAGON2: II. Nuclear interactions with the interstellar gas," *Journal of Cosmology and Astroparticle Physics*, vol. 2018, p. 006, 2018. Online available: https://doi.org/10.1088/1475-7516/2018/07/006

[90] K. M. Ferrière, "The interstellar environment of our galaxy," *Reviews of Modern Physics*, vol. 73, no. 4, pp. 1031–1066, 2001. Online available: https://link.aps.org/doi/10.1103/RevModPhys.73.1031

[91] I. V. Moskalenko, A. W. Strong, J. F. Ormes *et al.*, "Secondary Antiprotons and Propagation of Cosmic Rays in the Galaxy and Heliosphere," *The Astrophysical Journal*, vol. 565, no. 1, pp. 280–296, 2002. Online available: http://dx.doi.org/10.1086/324402

[92] H. I. Ewen and E. M. Purcell, "Observation of a Line in the Galactic Radio Spectrum: Radiation from Galactic Hydrogen at 1,420 Mc./sec," *Nature*, vol. 168, no. 4270, pp. 356–356, 1951. Online available: https://doi.org/10.1038/168356a0

[93] A. Diplas and B. D. Savage, "Neutral Hydrogen in the Outer Galaxy," *The Astrophysical Journal*, vol. 377, p. 126, 1991. Online available: https://ui.adsabs.harvard.edu/abs/1991ApJ...377..126D

[94] A. D. Bolatto, M. Wolfire, and A. K. Leroy, "The CO-to-H2 Conversion Factor," *Annual Review of Astronomy and Astrophysics*, vol. 51, no. 1, pp. 207–268, 2013. Online available: https://www.annualreviews.org/doi/abs/10.1146/annurev-astro-082812-140944

[95] T. J. Sodroski, N. Odegard, E. Dwek *et al.*, "The Ratio of H2 Column Density to 12CO Intensity in the Vicinity of the Galactic Center," *The Astrophysical Journal*, vol. 452, p. 262, 1995. Online available: https://ui.adsabs.harvard.edu/abs/1995ApJ...452..262S

[96] W. Maciel, *Astrophysics of the Interstellar Medium*. New York: Springer, 2013.

[97] J. P. Vallee, "The Milky Way's Spiral Arms Traced by Magnetic Fields, Dust, Gas, and Stars," *The Astrophysical Journal*, vol. 454, p. 119, 1995. Online available: https://doi.org/10.1086/176470

[98] L. D. Anderson, T. V. Wenger, W. P. Armentrout *et al.*, "A Galactic Plane Defined by the Milky Way H ii Region Distribution," *The Astrophysical Journal*, vol. 871, no. 2, p. 145, 2019. Online available: http://dx.doi.org/10.3847/1538-4357/aaf571

[99] F. Boulanger, P. Cox, and A. P. Jones, "Course 7: Dust in the Interstellar Medium," in *Les Houches - Ecole d'Ete de Physique Theorique*, vol. 70, Conference Proceedings, p. 251. Online available: https://doi.org/10.1007/3-540-45573-6

[100] A. W. Strong and I. V. Moskalenko, "Propagation of Cosmic-Ray Nucleons in the Galaxy," *The Astrophysical Journal*, vol. 509, no. 1, pp. 212–228, 1998. Online available: http://dx.doi.org/10.1086/306470

[101] V. S. Ptuskin, S. I. Rogovaya, V. N. Zirakashvili *et al.*, "Diffusion and drift of very high energy cosmic rays in galactic magnetic fields," *Astronomy and Astrophysics*, vol. 268, p. 726, 1993. Online available: https://ui.adsabs.harvard.edu/abs/1993A&A...268..726P

[102] A. Castellina and F. Donato, *Astrophysics of Galactic Charged Cosmic Rays*. Dordrecht: Springer Netherlands, 2013, pp. 725–788. Online available: https://doi.org/10.1007/978-94-007-5612-0_14

[103] V. S. Berezinskii, S. V. Bulanov, V. A. Dogiel *et al.*, *Astrophysics of cosmic rays*. Amsterdam: North-Holland, 1990. Online available: https://ui.adsabs.harvard.edu/abs/1990acr..book.....B

[104] M. E. Wiedenbeck and D. E. Greiner, "A cosmic-ray age based on the abundance of Be-10," *The Astrophysical Journal*, vol. 239, p. L139, 1980. Online available: https://doi.org/10.1086/183310

[105] A. J. Owens, "The Age Distribution of Galactic Cosmic Rays. II: Interacting Decaying and Secondary Particles," *Astrophysics and Space Science*, vol. 44, p. 35, 1976. Online available: https://doi.org/10.1007/bf00650471

[106] D. P. Cox, "The Three-Phase Interstellar Medium Revisited," *Annual Review of Astronomy and Astrophysics*, vol. 43, no. 1, pp. 337–385, 2005. Online available: https://www.annualreviews.org/doi/abs/10.1146/annurev.astro.43.072103.150615

[107] S. Veilleux, G. Cecil, and J. Bland-Hawthorn, "Galactic Winds," *Annual Review of Astronomy and Astrophysics*, vol. 43, no. 1, pp. 769–826, 2005. Online available: https://www.annualreviews.org/doi/abs/10.1146/annurev.astro.43.072103.150610

[108] F. M. Ipavich, "Galactic winds driven by cosmic rays," *The Astrophysical Journal*, vol. 196, p. 107, 1975. Online available: https://doi.org/10.1086/153397

[109] C.-A. Faucher-Giguère and E. Quataert, "The physics of galactic winds driven by active galactic nuclei," *Monthly Notices of the Royal Astronomical Society*, vol. 425, p. 605, 2012. Online available: https://doi.org/10.1111/j.1365-2966.2012.21512.x

[110] C. Evoli, D. Gaggero, A. Vittino *et al.*, "Cosmic-ray propagation with DRAGON2: I. numerical solver and astrophysical ingredients," *Journal of Cosmology and Astroparticle Physics*, vol. 2017, no. 02, pp. 015–015, 2017. Online available: http://dx.doi.org/10.1088/1475-7516/2017/02/015

[111] L. O. C. Drury and A. W. Strong, "Power requirements for cosmic ray propagation models involving diffusive reacceleration; estimates and implications for the damping of interstellar turbulence," *Astronomy and Astrophysics*, vol. 597, p. A117, 2017. Online available: https://doi.org/10.1051/0004-6361/201629526

[112] P. M. W. Kalberla and J. Kerp, "Hydrostatic equilibrium conditions in the galactic halo," *Astronomy and Astrophysics*, vol. 339, p. 745, 1998. Online available: https://ui.adsabs.harvard.edu/abs/1998A&A...339..745K

[113] R. J. Gould, "Energy loss of relativistic electrons and positrons traversing cosmic matter," *The Astrophysical Journal*, vol. 196, p. 689, 1975. Online available: https://doi.org/10.1086/153457

[114] E. Orlando and A. Strong, "Galactic synchrotron emission with cosmic ray propagation models," *Monthly Notices of the Royal Astronomical Society*, vol. 436, no. 3, pp. 2127–2142, 2013. Online available: https://doi.org/10.1093/mnras/stt1718

[115] K. Mannheim and R. Schlickeiser, "Interactions of cosmic ray nuclei," *Astronomy and Astrophysics*, vol. 286, p. 983, 1994. Online available: https://ui.adsabs.harvard.edu/abs/1994A&A...286..983M

[116] M. J. Berger, "ESTAR, PSTAR, and ASTAR: Computer programs for calculating stopping-power and range tables for electrons, protons, and helium ions," Report, December 01, 1992 1992. Online available: https://dx.doi.org/10.18434/T4NC7P

[117] P. L. Biermann, N. Langer, E.-S. Seo *et al.*, "Cosmic rays IX. Interactions and transport of cosmic rays in the Galaxy," *Astronomy and Astrophysics*, vol. 369, p. 269, 2001. Online available: https://doi.org/10.1051/0004-6361:20010083

[118] X. Campi and J. Hüfner, "Nuclear spallation-fragmentation reactions induced by high-energy projectiles," *Physical Review C*, vol. 24, no. 5, pp. 2199–2209, 1981. Online available: https://link.aps.org/doi/10.1103/PhysRevC.24.2199

[119] G. Bendiscioli and D. Kharzeev, "Antinucleon-nucleon and antinucleon-nucleus interaction. A review of experimental data," *La Rivista del Nuovo Cimento (1978-1999)*, vol. 17, no. 6, p. 1, 2007. Online available: https://doi.org/10.1007/BF02724447

[120] R. Cowsik, Y. Pal, S. N. Tandon *et al.*, "Steady State of Cosmic-Ray Nuclei—Their Spectral Shape and Path Length at Low Energies," *Physical Review*, vol. 158, no. 5, pp. 1238–1242, 1967. Online available: https://link.aps.org/doi/10.1103/PhysRev.158.1238

[121] R. Cowsik and L. W. Wilson, "The Nested Leaky-Box Model for Galactic Cosmic Rays," in *Proceedings from the 14th International Cosmic Ray Conference*, vol. 2, Conference Proceedings, p. 659. Online available: https://ui.adsabs.harvard.edu/abs/1975ICRC....2..659C

[122] S. K. Solanki, B. Inhester, and M. Schüssler, "The solar magnetic field," *Reports on Progress in Physics*, vol. 69, no. 3, pp. 563–668, 2006. Online available: http://dx.doi.org/10.1088/0034-4885/69/3/R02

[123] P. Charbonneau, "Dynamo models of the solar cycle," *Living Reviews in Solar Physics*, vol. 17, no. 1, p. 4, 2020. Online available: https://doi.org/10.1007/s41116-020-00025-6

[124] T. G. Cowling, "The Magnetic Field of Sunspots," *Monthly Notices of the Royal Astronomical Society*, vol. 94, no. 1, pp. 39–48, 1933. Online available: https://doi.org/10.1093/mnras/94.1.39

[125] H. Antia, A. Bhatnagar, and P. Ulmschneider, Eds., *Lectures on Solar Physics*, ser. Lecture Notes in Physics. Springer Berlin Heidelberg, 2003. Online available: http://dx.doi.org/10.1007/3-540-36963-5

[126] E. N. Parker, "The Generation of Magnetic Fields in Astrophysical Bodies. I. The Dynamo Equations," *The Astrophysical Journal*, vol. 162, p. 665, 1970. Online available: https://doi.org/10.1086/150697

[127] E. N. Parker, "The Formation of Sunspots from the Solar Toroidal Field," *The Astrophysical Journal*, vol. 121, p. 491, 1955. Online available: https://doi.org/10.1086/146010

[128] H. W. Babcock, "The Topology of the Sun's Magnetic Field and the 22-YEAR Cycle," *The Astrophysical Journal*, vol. 133, p. 572, 1961. Online available: https://doi.org/10.1086/147060

[129] E. N. Parker, "Dynamics of the Interplanetary Gas and Magnetic Fields," *The Astrophysical Journal*, vol. 128, p. 664, 1958. Online available: https://doi.org/10.1086/146579

[130] J. D. Richardson, C. Wang, and K. I. Paularena, "The solar wind: from solar minimum to solar maximum," *Advances in Space Research*, vol. 27, no. 3, pp. 471–479, 2001. Online available: https://www.sciencedirect.com/science/article/pii/S0273117701000746

[131] J. T. Gosling, *CHAPTER 5 - The Solar Wind*. San Diego: Academic Press, 2007, pp. 99–116. Online available: https://www.sciencedirect.com/science/article/pii/B9780120885893500098

[132] E. J. Smith, "The heliospheric current sheet," *Journal of Geophysical Research: Space Physics*, vol. 106, no. A8, pp. 15 819–15 831, 2001. Online available: https://agupubs.onlinelibrary.wiley.com/doi/abs/10.1029/2000JA000120

[133] M. J. Owens and R. J. Forsyth, "The Heliospheric Magnetic Field," *Living Reviews in Solar Physics*, vol. 10, no. 1, p. 5, 2013. Online available: https://doi.org/10.12942/lrsp-2013-5

[134] M. Orcinha, N. Tomassetti, F. Barão *et al.*, "Observation of a time lag in solar modulation of cosmic rays in the heliosphere," *Journal of Physics: Conference Series*, vol. 1181, p. 012013, 2019. Online available: http://dx.doi.org/10.1088/1742-6596/1181/1/012013

[135] S. E. S. Ferreira and M. S. Potgieter, "Modulation over a 22-year cosmic ray cycle: On the tilt angles of the heliospheric current sheet," *Advances in Space Research*, vol. 32, no. 4, pp. 657–662, 2003. Online available: https://www.sciencedirect.com/science/article/pii/S0273117703003600

[136] N. V. Pogorelov, J. Heerikhuisen, V. Roytershteyn *et al.*, "Three-dimensional Features of the Outer Heliosphere Due to Coupling between the Interstellar and Heliospheric Magnetic Field. V. The Bow Wave, Heliospheric Boundary Layer, Instabilities, and Magnetic Reconnection," *The Astrophysical Journal*, vol. 845, no. 1, p. 9, 2017. Online available: http://dx.doi.org/10.3847/1538-4357/aa7d4f

[137] D. J. McComas, J. S. Rankin, N. A. Schwadron *et al.*, "Termination Shock Measured by Voyagers and IBEX," *The Astrophysical Journal*, vol. 884, no. 2, p. 145, 2019. Online available: http://dx.doi.org/10.3847/1538-4357/ab441a

[138] J. D. Richardson and R. B. Decker, "Plasma and Flows in the Heliosheath," *Journal of Physics: Conference Series*, vol. 577, p. 012021, 2015. Online available: http://dx.doi.org/10.1088/1742-6596/577/1/012021

[139] N. V. Pogorelov, S. N. Borovikov, J. Heerikhuisen *et al.*, "The Heliotail," *The Astrophysical Journal*, vol. 812, p. L6, 2015. Online available: https://ui.adsabs.harvard.edu/abs/2015ApJ...812L...6P

[140] D. J. McComas, M. A. Dayeh, H. O. Funsten *et al.*, "The Heliotail Revealed by the Interstellar Boundary Explorer," *The Astrophysical Journal*, vol. 771, p. 77, 2013. Online available: https://ui.adsabs.harvard.edu/abs/2013ApJ...771...77M

[141] D. J. McComas, D. Alexashov, M. Bzowski *et al.*, "The Heliosphere's Interstellar Interaction: No Bow Shock," *Science*, vol. 336, p. 1291, 2012. Online available: https://ui.adsabs.harvard.edu/abs/2012Sci...336.1291M

[142] K. Yoshida, S. Matsukiyo, K. Shimokawa *et al.*, "Trajectory Analysis of Galactic Cosmic Rays Invading into the Heliosphere," *The Astrophysical Journal*, vol. 916, no. 1, p. 29, 2021. Online available: http://dx.doi.org/10.3847/1538-4357/ac02c2

[143] A. C. Cummings and E. C. Stone, "Anomalous Cosmic Rays and Solar Modulation," *Space Science Reviews*, vol. 83, no. 1, pp. 51–62, 1998. Online available: https://doi.org/10.1023/A:1005057010311

[144] E. N. Parker, "The passage of energetic charged particles through interplanetary space," *Planetary and Space Science*, vol. 13, no. 1, pp. 9–49, 1965. Online available: https://www.sciencedirect.com/science/article/pii/0032063365901315

[145] M. S. Potgieter, J. A. Le Roux, L. F. Burlaga *et al.*, "The Role of Merged Interaction Regions and Drifts in the Heliospheric Modulation of Cosmic Rays beyond 20 AU: A Computer Simulation," *The Astrophysical Journal*, vol. 403, p. 760, 1993. Online available: https://doi.org/10.1086/172247

[146] E. Ross and W. J. Chaplin, "The Behaviour of Galactic Cosmic-Ray Intensity During Solar Activity Cycle 24," *Solar Physics*, vol. 294, no. 1, p. 8, 2019. Online available: https://doi.org/10.1007/s11207-019-1397-7

[147] M. S. Potgieter, "The charge-sign dependent effect in the solar modulation of cosmic rays," *Advances in Space Research*, vol. 53, no. 10, pp. 1415–1425, 2014. Online available: https://www.sciencedirect.com/science/article/pii/S0273117713002275

[148] M. S. Potgieter, E. E. Vos, M. Boezio *et al.*, "Modulation of Galactic Protons in the Heliosphere During the Unusual Solar Minimum of 2006 to 2009," *Solar Physics*, vol. 289, no. 1, pp. 391–406, 2014. Online available: https://doi.org/10.1007/s11207-013-0324-6

[149] P. Dunzlaff, B. Heber, A. Kopp *et al.*, "Observations of recurrent cosmic ray decreases during solar cycles 22 and 23," *Ann. Geophys.*, vol. 26, no. 10, pp. 3127–3138, 2008. Online available: https://angeo.copernicus.org/articles/26/3127/2008/

[150] J. R. Jokipii and D. A. Kopriva, "Effects of particle drift on the transport of cosmic rays III Numerical models of galactic cosmic-ray modulation," *Astrophysical Journal*, vol. 233, no. 4, pp. 384–392, 1979. Online available: http://inis.iaea.org/search/search.aspx?orig_q=RN:11529845

[151] L. J. Gleeson and W. I. Axford, "Solar Modulation of Galactic Cosmic Rays," *The Astrophysical Journal*, vol. 154, p. 1011, 1968. Online available: https://doi.org/10.1086/149822

[152] J. R. Jokipii, "Cosmic-Ray Propagation. II. Diffusion in the Interplanetary Magnetic Field," *The Astrophysical Journal*, vol. 149, p. 405, 1967. Online available: https://doi.org/10.1086/149265

[153] C. Corti, "Validity of the Force-Field Approximation with AMS-02 and PAMELA Monthly Fluxes," in *36th International Cosmic Ray Conference (ICRC2019)*.

[154] M. J. Boschini, S. Della Torre, M. Gervasi *et al.*, "Propagation of cosmic rays in heliosphere: The HelMod model," *Advances in Space Research*, vol. 62, no. 10, pp. 2859–2879, 2018. Online available: https://www.sciencedirect.com/science/article/pii/S0273117717302971

[155] P. Bobik, G. Boella, M. J. Boschini *et al.*, "SYSTEMATIC INVESTIGATION OF SOLAR MODULATION OF GALACTIC PROTONS FOR SOLAR CYCLE 23 USING A MONTE CARLO APPROACH WITH PARTICLE DRIFT EFFECTS AND LATITUDINAL DEPENDENCE," *The Astrophysical Journal*, vol. 745, no. 2, p. 132, 2012. Online available: http://dx.doi.org/10.1088/0004-637X/745/2/132

[156] M. J. Boschini, S. Della Torre, M. Gervasi *et al.*, "Forecasting of cosmic rays intensities with HelMod Model," *Advances in Space Research*, 2022. Online available: https://www.sciencedirect.com/science/article/pii/S0273117722000667

[157] M. J. Boschini, S. D. Torre, M. Gervasi *et al.*, "Solution of Heliospheric Propagation: Unveiling the Local Interstellar Spectra of Cosmic-ray Species," *The Astrophysical Journal*, vol. 840, no. 2. Online available: https://doi.org/10.3847/1538-4357/aa6e4f

[158] M. Korsmeier and A. Cuoco, "Implications of lithium to oxygen AMS-02 spectra on our understanding of cosmic-ray diffusion," *Physical Review D*, vol. 103, no. 10, p. 103016, 2021. Online available: https://link.aps.org/doi/10.1103/PhysRevD.103.103016

[159] P. Lipari, "Beryllium isotopic composition and Galactic cosmic ray propagation," *arXiv e-prints: arXiv:2204.13085*, Apr. 2022. Online available: https://doi.org/10.48550/arXiv.2204.13085

[160] M. J. Boschini, S. D. Torre, M. Gervasi *et al.*, "Deciphering the Local Interstellar Spectra of Primary Cosmic-Ray Species with HelMod," *The Astrophysical Journal*, vol. 858, no. 1, p. 61, 2018. Online available: http://dx.doi.org/10.3847/1538-4357/aabc54

[161] M. J. Boschini, S. D. Torre, M. Gervasi *et al.*, "HelMod in the Works: From Direct Observations to the Local Interstellar Spectrum of Cosmic-Ray Electrons," *The Astrophysical Journal*, vol. 854, no. 2, p. 94, 2018. Online available: http://dx.doi.org/10.3847/1538-4357/aaa75e

[162] M. J. Boschini, S. D. Torre, M. Gervasi *et al.*, "Deciphering the Local Interstellar Spectra of Secondary Nuclei with the Galprop/Helmod Framework and a Hint for Primary Lithium in Cosmic Rays," *The Astrophysical Journal*, vol. 889, no. 2, p. 167, 2020. Online available: http://dx.doi.org/10.3847/1538-4357/ab64f1

[163] M. J. Boschini, S. D. Torre, M. Gervasi *et al.*, "Inference of the Local Interstellar Spectra of Cosmic-Ray Nuclei $Z \leq 28$ with the GalProp–HelMod Framework," *The Astrophysical Journal Supplement Series*, vol. 250, no. 2, p. 27, 2020. Online available: http://dx.doi.org/10.3847/1538-4365/aba901

[164] M. Korsmeier and A. Cuoco, "Galactic cosmic-ray propagation in the light of AMS-02: Analysis of protons, helium, and antiprotons," *Physical Review D*, vol. 94, no. 12, p. 123019, 2016. Online available: https://link.aps.org/doi/10.1103/PhysRevD.94.123019

[165] M. Korsmeier and A. Cuoco, "Testing the universality of cosmic-ray nuclei from protons to oxygen with AMS-02," *arXiv e-prints: arXiv:2112.08381*, December 01, 2021 2021. Online available: https://doi.org/10.48550/arXiv.2112.08381

[166] M. J. Boschini, S. Della Torre, M. Gervasi *et al.*, "Propagation of cosmic rays in heliosphere: The HelMod model," *Advances in Space Research*, vol. 62, no. 10, pp. 2859–2879, 2018. Online available: https://www.sciencedirect.com/science/article/pii/S0273117717302971

[167] A. W. Strong, I. V. Moskalenko, T. A. Porter *et al.*, "GALPROP Version 54: Explanatory Supplement," 2010. Online available: https://galprop.stanford.edu/download/manuals/galprop_v54.pdf

[168] H. P. Langtangen, *Computational Partial Differential Equations: Numerical Methods and Diffpack Programming*. Springer-Verlag, 1999.

[169] G. Strang, *Linear Algebra and Its Applications*. Kent, United States: Elsevier Science and Technology.

[170] C. Grossmann, H. Roos, and M. Stynes, *Finite Difference Methods*. Berlin, Heidelberg: Springer Berlin Heidelberg, 2007, pp. 23–124. Online available: https://doi.org/10.1007/978-3-540-71584-9_2

[171] J. Crank and P. Nicolson, "A practical method for numerical evaluation of solutions of partial differential equations of the heat-conduction type," *Advances in Computational Mathematics*, vol. 6, no. 1, pp. 207–226, 1996. Online available: https://doi.org/10.1007/BF02127704

[172] M. Aguilar, L. Ali Cavasonza, G. Ambrosi *et al.*, "The Alpha Magnetic Spectrometer (AMS) on the international space station: Part II — Results from the first seven years," *Physics Reports*, vol. 894, pp. 1–116, 2021. Online available: https://www.sciencedirect.com/science/article/pii/S0370157320303434

[173] L. C. Tan and L. K. Ng, "Parametrisation of hadron inclusive cross sections in p-p collisions extended to very low energies," *Journal of Physics G: Nuclear Physics*, vol. 9, no. 10, pp. 1289–1308, 1983. Online available: http://dx.doi.org/10.1088/0305-4616/9/10/015

[174] D. Gomez Coral, "Deuteron and antideuteron production in galactic cosmic-rays," Thesis, Universidad Nacional Autonoma De Mexico, 2019.

[175] A. E. Vladimirov, S. W. Digel, G. Jóhannesson *et al.*, "GALPROP WebRun: An internet-based service for calculating galactic cosmic ray propagation and associated photon emissions," *Computer Physics Communications*, vol. 182, no. 5, pp. 1156–1161, 2011. Online available: https://www.sciencedirect.com/science/article/pii/S0010465511000373

[176] J. Buchner, "UltraNest - a robust, general purpose Bayesian inference engine," *The Journal of Open Source Software*, vol. 6, p. 3001, 2021. Online available: https://doi.org/10.21105/joss.03001

[177] J. Buchner, "A statistical test for Nested Sampling algorithms," *Statistics and Computing*, vol. 26, no. 1, pp. 383–392, 2016. Online available: https://doi.org/10.1007/s11222-014-9512-y

[178] J. Buchner, "Collaborative Nested Sampling: Big Data vs. complex physical models," *arXiv e-prints: arXiv:1707.04476*, July 01, 2017 2017. Online available: https://doi.org/10.48550/arXiv.1707.04476

[179] T.-G. Lee and C.-Y. Wong, "Extended Glauber model of antiproton-nucleus annihilation for all energies and mass numbers," *Physical Review C*, vol. 89, no. 5. Online available: https://doi.org/10.1103/PhysRevC.89.054601

[180] T. Poeschl, "Modeling and Prototyping of a Novel Active-Target Particle Detector for Balloon and Space Applications," Master's Thesis, Technical University of Munich, 2015.

[181] M. Korsmeier, F. Donato, and M. Di Mauro, "Production cross sections of cosmic antiprotons in the light of new data from the NA61 and LHCb experiments," *Physical Review D*, vol. 97, no. 10, p. 103019, 2018. Online available: https://link.aps.org/doi/10.1103/PhysRevD.97.103019

[182] B. Povh, K. Rith, C. Scholz *et al.*, *Teilchen und Kerne*. Springer Berlin Heidelberg, 2009. Online available: https://doi.org/10.1007/978-3-642-37822-5

[183] B. Martin and G. Shaw, *Particle Physics*, ser. Manchester Physics Series. Wiley, 2008. Online available: https://wiley.com/en-gb/Particle+Physics%2C+4th+Edition-p-9781118911907

[184] J. M. Richard, "Exotic Hadrons: Review and Perspectives," *Few-Body Systems*, vol. 57, no. 12, pp. 1185–1212, 2016. Online available: https://doi.org/10.1007/s00601-016-1159-0

[185] P. Collins and A. D. Martin, "Hadron reaction mechanisms," *Reports on Progress in Physics*, vol. 45, no. 4, pp. 335–426, apr 1982. Online available: https://doi.org/10.1088/0034-4885/45/4/001

[186] M. Tanabashi, K. Hagiwara, K. Hikasa *et al.*, "Review of Particle Physics," *Physical Review D*, vol. 98, no. 3, p. 030001, 2018. Online available: https://link.aps.org/doi/10.1103/PhysRevD.98.030001

[187] S. Syritsyn, "Review of Hadron Structure Calculations on a Lattice," *arXiv e-prints: arXiv:1403.4686*, 2014. Online available: https://doi.org/10.48550/arXiv.1403.4686

[188] R. K. Ellis, W. J. Stirling, and B. R. Webber, *Deep inelastic scattering*, ser. Cambridge Monographs on Particle Physics, Nuclear Physics and Cosmology. Cambridge University Press, 1996, p. 86–156. Online available: https://doi-org.ezproxy.cern.ch/10.1017/CBO9780511628788

[189] B. Andersson, G. Gustafson, G. Ingelman *et al.*, "Parton fragmentation and string dynamics," *Physics Reports*, vol. 97, no. 2, pp. 31–145, 1983. Online available: https://www.sciencedirect.com/science/article/pii/0370157383900807

[190] P. Collins and A. D. Martin, *Hadron Interactions*, ser. Graduate student series in physics. United Kingdom: Adam Hilger Ltd (in association with the University of Sussex Press), 1984.

[191] R. Cutler and D. Sivers, "Quantum-chromodynamic gluon contributions to large-p_T reactions," *Physical Review D*, vol. 17, no. 1, pp. 196–211, 1978. Online available: https://link.aps.org/doi/10.1103/PhysRevD.17.196

[192] O. Chamberlain, E. Segrè, C. Wiegand *et al.*, "Observation of Antiprotons," *Physical Review*, vol. 100, no. 3, pp. 947–950, 1955. Online available: https://doi.org/10.1103/PhysRev.100.947

[193] M. Adamczyk, L. Antvorskov, K. Ashktorab *et al.*, "The BRAHMS experiment at RHIC," *Nuclear Instruments and Methods in Physics Research Section A: Accelerators, Spectrometers, Detectors and Associated Equipment*, vol. 499, no. 2, pp. 437–468, 2003. Online available: https://doi.org/10.1016/S0168-9002(02)01949-6

[194] A. A. Alves, L. M. A. Filho, A. F. Barbosa *et al.*, "The LHCb Detector at the LHC," *Journal of Instrumentation*, vol. 3, no. 08, pp. S08 005–S08 005, aug 2008. Online available: https://doi.org/10.1088/1748-0221/3/08/s08005

[195] M. W. Winkler, "Cosmic ray antiprotons at high energies," *Journal of Cosmology and Astroparticle Physics*, vol. 2017, no. 02, pp. 048–048, 2017. Online available: http://dx.doi.org/10.1088/1475-7516/2017/02/048

[196] P. Skands, S. Carrazza, and J. Rojo, "Tuning PYTHIA 8.1: the Monash 2013 tune," *The European Physical Journal C*, vol. 74, no. 8, p. 3024, 2014. Online available: https://doi.org/10.1140/epjc/s10052-014-3024-y

[197] O. Buss, T. Gaitanos, K. Gallmeister *et al.*, "Transport-theoretical description of nuclear reactions," *Physics Reports*, vol. 512, no. 1, pp. 1–124, 2012. Online available: https://www.sciencedirect.com/science/article/pii/S0370157311003619

[198] K. Werner, B. Guiot, I. Karpenko *et al.*, "Analyzing radial flow features in p-Pb and p-p collisions at several TeV by studying identified-particle production with the event generator EPOS3," *Physical Review C*, vol. 89, no. 6, p. 064903, 2014. Online available: https://link.aps.org/doi/10.1103/PhysRevC.89.064903

[199] T. Pierog, I. Karpenko, J. M. Katzy *et al.*, "EPOS LHC: Test of collective hadronization with data measured at the CERN Large Hadron Collider," *Physical Review C*, vol. 92, no. 3, p. 034906, 2015. Online available: https://link.aps.org/doi/10.1103/PhysRevC.92.034906

[200] R. Ulrich, T. Pierog, and C. Baus, "Cosmic Ray Monte Carlo Package, CRMC," 2021. Online available: https://doi.org/10.5281/zenodo.5270381

[201] M. di Mauro, F. Donato, A. Goudelis *et al.*, "New evaluation of the antiproton production cross section for cosmic ray studies," *Physical Review D*, vol. 90, no. 8, p. 085017, 2014. Online available: https://link.aps.org/doi/10.1103/PhysRevD.90.085017

[202] D. Dekkers, J. A. Geibel, R. Mermod *et al.*, "Experimental Study of Particle Production at Small Angles in Nucleon-Nucleon Collisions at 19 and 23 GeV/c," *Physical Review*, vol. 137, no. 4B, pp. B962–B978, 1965. Online available: https://link.aps.org/doi/10.1103/PhysRev.137.B962

[203] A. Aduszkiewicz, Y. Ali, E. Andronov *et al.*, "Measurements of $\pi^{\pm}$, $K^{\pm}$, p and $\bar{p}$ spectra in proton-proton interactions at 20, 31, 40, 80 and 158 GeV /cwith the NA61/SHINE spectrometer at the CERN SPS," *The European Physical Journal C*, vol. 77, no. 10, p. 671, 2017. Online available: https://doi.org/10.1140/epjc/s10052-017-5260-4

[204] T. Anticic, B. Baatar, J. Bartke *et al.*, "Inclusive production of protons, anti-protons and neutrons in p+p collisions at 158 GeV/c beam momentum," *The European Physical Journal C*, vol. 65, no. 1, p. 9, 2009. Online available: https://doi.org/10.1140/epjc/s10052-009-1172-2

[205] A. Adare, S. Afanasiev, C. Aidala *et al.*, "Identified charged hadron production in p+p collisions at $\sqrt{s} = 200$ and 62.4 GeV," *Physical Review C*, vol. 83, no. 6, p. 064903, 2011. Online available: https://link.aps.org/doi/10.1103/PhysRevC.83.064903

[206] I. Arsene, I. G. Bearden, D. Beavis *et al.*, "Production of Mesons and Baryons at High Rapidity and High p_T in Proton-Proton Collisions at $\sqrt{s} = 200$ GeV," *Physical Review Letters*, vol. 98, no. 25, p. 252001, 2007. Online available: https://link.aps.org/doi/10.1103/PhysRevLett.98.252001

[207] K. Aamodt, N. Abel, U. Abeysekara *et al.*, "Production of pions, kaons and protons in pp collisions at $\sqrt{s} = 900$ GeVwith ALICE at the LHC," *The European Physical Journal C*, vol. 71, no. 6, p. 1655, 2011. Online available: https://doi.org/10.1140/epjc/s10052-011-1655-9

[208] F. E. Taylor, D. C. Carey, J. R. Johnson *et al.*, "Analysis of radial scaling in single-particle inclusive reactions," *Physical Review D*, vol. 14, no. 5, pp. 1217–1242, 1976. Online available: https://link.aps.org/doi/10.1103/PhysRevD.14.1217

[209] K. K. n. H. Noda, "Limiting Behaviour of Inclusive Baryon Spectra: Inclusive Reactions and Urbaryon Rearrangement Diagrams. VI," *Progress of Theoretical Physics*, vol. 50, no. 3, pp. 915–925, 1973. Online available: https://doi.org/10.1143/PTP.50.915

[210] L. C. Tan and L. K. Ng, "Calculation of the equilibrium antiproton spectrum," *Journal of Physics G: Nuclear Physics*, vol. 9, no. 2, pp. 227–242, 1983. Online available: http://dx.doi.org/10.1088/0305-4616/9/2/015

[211] M. D. Azmi and J. Cleymans, "Transverse momentum distributions in proton–proton collisions at LHC energies and Tsallis thermodynamics," *Journal of Physics G:*

Nuclear and Particle Physics, vol. 41, no. 6, p. 065001, 2014. Online available: http://dx.doi.org/10.1088/0954-3899/41/6/065001

[212] S. Ostapchenko, M. Bleicher, T. Pierog *et al.*, "Constraining high energy interaction mechanisms by studying forward hadron production at the LHC," *Physical Review D*, vol. 94, no. 11, p. 114026, 2016. Online available: https://link.aps.org/doi/10.1103/PhysRevD.94.114026

[213] A. Caldwell, D. Kollár, and K. Kröninger, "BAT – The Bayesian analysis toolkit," *Computer Physics Communications*, vol. 180, no. 11, pp. 2197–2209, 2009. Online available: https://www.sciencedirect.com/science/article/pii/S0010465509002045

[214] F. Beaujean, A. Caldwell, D. Greenwald *et al.*, "Bayesian Analysis Toolkit: 1.0 and beyond," *Journal of Physics: Conference Series*, vol. 664, no. 7, p. 072003, 2015. Online available: http://dx.doi.org/10.1088/1742-6596/664/7/072003

[215] F. Beaujean, A. Caldwell, D. Greenwald *et al.*, "BAT release, version 1.0.0," 2018. Online available: https://doi.org/10.5281/zenodo.1322675

[216] D. G. Ireland, M. Döring, D. I. Glazier *et al.*, "Kaon Photoproduction and the Λ Decay Parameter α_-," *Physical Review Letters*, vol. 123, no. 18, p. 182301, 2019. Online available: https://link.aps.org/doi/10.1103/PhysRevLett.123.182301

[217] R. Kappl and M. W. Winkler, "The cosmic ray antiproton background for AMS-02," *Journal of Cosmology and Astroparticle Physics*, vol. 2014, no. 09, pp. 051–051, 2014. Online available: http://dx.doi.org/10.1088/1475-7516/2014/09/051

[218] NA 49 Collaboration, "Inclusive production of charged pions in p+p collisions at 158 GeV/c beam momentum," *The European Physical Journal C - Particles and Fields*, vol. 45, no. 2, pp. 343–381, 2006. Online available: https://doi.org/10.1140/epjc/s2005-02391-9

[219] B. I. Abelev, J. Adams, M. M. Aggarwal *et al.*, "Strange particle production in $p+p$ collisions at $\sqrt{s} = 200$ GeV," *Physical Review C*, vol. 75, no. 6, p. 064901, 2007. Online available: https://link.aps.org/doi/10.1103/PhysRevC.75.064901

[220] F. James, "Monte Carlo phase space," 1968. Online available: https://cds.cern.ch/record/275743

[221] R. Brun and F. Rademakers, "ROOT — An object oriented data analysis framework," *Nuclear Instruments and Methods in Physics Research Section A: Accelerators, Spectrometers, Detectors and Associated Equipment*, vol. 389, no. 1, pp. 81–86, 1997. Online available: https://www.sciencedirect.com/science/article/pii/S016890029700048X

[222] K. Aamodt, A. Abrahantes Quintana, D. Adamová *et al.*, "Strange particle production in proton-proton collisions at 0.9 TeV with ALICE at the LHC. The ALICE Collaboration," *European Physical Journal C*, vol. 71, p. 1594, Mar. 2011. Online available: https://doi.org/10.1140/epjc/s10052-011-1594-5

[223] D. Griffiths, *Introduction to elementary particles*, ser. Physics textbook. New York: Wiley, 1987.

[224] H. G. Fischer for the NA49 Collaboration, "Baryon yields, isospin effects and strangeness production in elementary hadronic interactions," *Acta Physica Hungarica Series A, Heavy Ion Physics*, vol. 17, no. 2, pp. 369–386, 2003. Online available: https://doi.org/10.1556/APH.17.2003.2-4.20

[225] K. Aamodt, N. Abel, U. Abeysekara *et al.*, "Midrapidity Antiproton-to-Proton Ratio in *pp* Collisons at $\sqrt{s} = 0.9$ and 7 TeV Measured by the ALICE Experiment," *Physical Review Letters*, vol. 105, no. 7, p. 072002, 2010. Online available: https://link.aps.org/doi/10.1103/PhysRevLett.105.072002

[226] P. Braun-Munzinger, K. Redlich, and J. Stachel, *Particle Production in Heavy Ion Collisions*, 2004, pp. 491–599. Online available: https://doi.org/10.1142/9789812795533_0008

[227] B. Baatar, G. Barr, J. Bartke *et al.*, "Inclusive production of protons, anti-protons, neutrons, deuterons and tritons in p+C collisions at 158 GeV/c beam momentum," *arXiv e-prints: arXiv:1207.6520*, July 01, 2012 2012. Online available: https://doi.org/10.48550/arXiv.1207.6520

[228] R. Aaij, C. Abellán Beteta, B. Adeva *et al.*, "Measurement of Antiproton Production in $p-$He Collisions at $\sqrt{s_{\mathrm{NN}}} = 110$ GeV," *Physical Review Letters*, vol. 121, no. 22, p. 222001, 2018. Online available: https://link.aps.org/doi/10.1103/PhysRevLett.121.222001

[229] L. Loennblad, "Modelling pp, pA and AA in Pythia8," *EPJ Web Conf.*, vol. 208, p. 11003, 2019. Online available: https://doi.org/10.1051/epjconf/201920811003

[230] F. Donato, "Antimatter from Supersymmetric Dark Matter," in *Sources and Detection of Dark Matter and Dark Energy in the Universe*, D. B. Cline, Ed., Conference Proceedings, p. 236. Online available: https://ui.adsabs.harvard.edu/abs/2001sddm.symp..236D

[231] A. Ibarra and S. Wild, "Determination of the cosmic antideuteron flux in a Monte Carlo approach," *Physical Review D*, vol. 88, no. 2, p. 023014, 2013. Online available: https://link.aps.org/doi/10.1103/PhysRevD.88.023014

[232] L. Šerkšnytė, S. Königstorfer, P. von Doetinchem *et al.*, "Reevaluation of the cosmic antideuteron flux from cosmic-ray interactions and from exotic sources," *Physical Review D*, vol. 105, no. 8, p. 083021, 2022. Online available: https://link.aps.org/doi/10.1103/PhysRevD.105.083021

[233] D.-M. Gomez-Coral, A. Menchaca Rocha, V. Grabski *et al.*, "Deuteron and antideuteron production simulation in cosmic-ray interactions," *Physical Review D*, vol. 98, no. 2, p. 023012, 2018. Online available: https://link.aps.org/doi/10.1103/PhysRevD.98.023012

[234] M. M. Kachelrieß, S. Ostapchenko, and J. Tjemsland, "Revisiting cosmic ray antinuclei fluxes with a new coalescence model," *Journal of Cosmology and Astroparticle Physics*, vol. 2020, no. 08, pp. 048–048, 2020. Online available: http://dx.doi.org/10.1088/1475-7516/2020/08/048

[235] G. F. Knoll, *Radiation detection and measurement*, 3rd ed. New York, John Wiley and Sons, Inc., 2000.

[236] D. Renker, "Geiger-mode avalanche photodiodes, history, properties and problems," *Nuclear Instruments and Methods in Physics Research Section A: Accelerators, Spectrometers, Detectors and Associated Equipment*, vol. 567, no. 1, pp. 48–56, 2006. Online available: https://www.sciencedirect.com/science/article/pii/S0168900206008680

[237] S. Agostinelli, J. Allison, K. Amako *et al.*, "Geant4—a simulation toolkit," *Nuclear Instruments and Methods in Physics Research Section A: Accelerators, Spectrometers, Detectors and Associated Equipment*, vol. 506, no. 3, pp. 250–303, 2003. Online available: https://www.sciencedirect.com/science/article/pii/S0168900203013688

[238] S. M. Seltzer and M. J. Berger, "Evaluation of the collision stopping power of elements and compounds for electrons and positrons," *The International Journal of Applied Radiation and Isotopes*, vol. 33, no. 11, pp. 1189–1218, 1982. Online available: https://www.sciencedirect.com/science/article/pii/0020708X82902447

[239] W. H. Bragg and R. Kleeman, "LXXIV. On the ionization curves of radium," *The London, Edinburgh, and Dublin Philosophical Magazine and Journal of Science*, vol. 8, no. 48, pp. 726–738, 1904. Online available: https://doi.org/10.1080/14786440409463246

[240] M. J. Berger, M. Inokuti, H. H. Andersen *et al.*, "ICRU Report 49: Stopping Powers and Ranges for Protons and Alpha Particles," *Reports of the International Commission on Radiation Units and Measurements*, vol. os-25, no. 2, 1993. Online available: https://journals.sagepub.com/toc/crub/os-25/2

[241] L. Hollender, "A Bayesian Particle Filter for Particle Identification," Master's Thesis, Technical University of Munich, 2019.

[242] Brookhaven Science Associates, "Bragg Curves and Peaks." Online available: https://www.bnl.gov/nsrl/userguide/bragg-curves-and-peaks.php

[243] C. R. Gruhn, M. Binimi, R. Legrain *et al.*, "Bragg curve spectroscopy," *Nucl Instrum Methods Phys Res*, vol. 196, no. 1, pp. 33–40, 1982. Online available: http://inis.iaea.org/search/search.aspx?orig_q=RN:13700439

[244] C. Terasa, J. Labrenz, P. Kühl *et al.*, "Extension of measurement capabilities of the Electron Proton Helium Instrument aboard SOHO," in *33rd International Cosmic Ray Conference*, vol. 33, Conference Proceedings, p. 3627. Online available: https://ui.adsabs.harvard.edu/abs/2013ICRC...33.3627T

[245] W. H. Barkas, J. N. Dyer, and H. H. Heckman, "Resolution of the Σ^--Mass Anomaly," *Physical Review Letters*, vol. 11, no. 1, pp. 26–28, 1963. Online available: https://link.aps.org/doi/10.1103/PhysRevLett.11.26

[246] G. Steigman, "Observational Tests of Antimatter Cosmologies," *Annual Review of Astronomy and Astrophysics*, vol. 14, no. 1, pp. 339–372, 1976. Online available: https://doi.org/10.1146/annurev.aa.14.090176.002011

[247] T. Aramaki, C. J. Hailey, S. E. Boggs *et al.*, "Antideuteron sensitivity for the GAPS experiment," *Astroparticle Physics*, vol. 74, pp. 6–13, 2016. Online available: https://www.sciencedirect.com/science/article/pii/S0927650515001292

[248] "Kuraray Co. Ltd." Online available: http://kuraraypsf.jp

[249] J. B. Birks, "Scintillations from Organic Crystals: Specific Fluorescence and Relative Response to Different Radiations," *Proceedings of the Physical Society. Section A*, vol. 64, no. 10, pp. 874–877, 1951. Online available: http://dx.doi.org/10.1088/0370-1298/64/10/303

[250] Ketek GmbH, "Product Data Sheet SiPM - Silicon Photomultiplier," 2022. Online available: https://www.ketek.net/wp-content/uploads/2018/12/KETEK-PM3325-WB-D0-Datasheet.pdf

[251] M. J. Losekamm, S. Paul, T. Pöschl *et al.*, "The RadMap Telescope on the International Space Station," in *2021 IEEE Aerospace Conference (50100)*, Conference Proceedings, pp. 1–10.

[252] M. J. Losekamm, "TBD," Dissertation, Technical University of Munich, 2022.

[253] T. Pöschl, D. Greenwald, M. J. Losekamm *et al.*, "Measurement of ionization quenching in plastic scintillators," *Nuclear Instruments and Methods in Physics Research Section A: Accelerators, Spectrometers, Detectors and Associated Equipment*, vol. 988, p. 164865, 2021. Online available: https://www.sciencedirect.com/science/article/pii/S0168900220312626

[254] C. N. Chou, "The Nature of the Saturation Effect of Fluorescent Scintillators," *Physical Review*, vol. 87, no. 5, pp. 904–905, 1952. Online available: https://link.aps.org/doi/10.1103/PhysRev.87.904

[255] R. L. Craun and D. L. Smith, "Analysis of response data for several organic scintillators," *Nuclear Instruments and Methods*, vol. 80, no. 2, pp. 239–244, 1970. Online available: https://www.sciencedirect.com/science/article/pii/0029554X70907688

[256] G. T. Wright, "Scintillation Response of Organic Phosphors," *Physical Review*, vol. 91, no. 5, pp. 1282–1283, 1953. Online available: https://link.aps.org/doi/10.1103/PhysRev.91.1282.2

[257] R. Voltz, J. L. d. Silva, G. Laustriat *et al.*, "Influence of the Nature of Ionizing Particles on the Specific Luminescence of Organic Scintillators," *The Journal*

of Chemical Physics, vol. 45, no. 9, pp. 3306–3311, 1966. Online available: https://aip.scitation.org/doi/abs/10.1063/1.1728106

[258] B. B. Rossi, *High-energy particles*, ser. Prentice-Hall physics series. New York, NY: Prentice-Hall, 1952. Online available: https://cds.cern.ch/record/99081

[259] L. D. Landau, in *Collected Papers of L.D. Landau.*

[260] P. V. Vavilov, "IONIZATION LOSSES OF HIGH-ENERGY HEAVY PARTICLES," *Soviet Phys. JETP*, vol. Vol: 5, pp. 749–51, 1957. Online available: https://www.osti.gov/biblio/4311507

[261] R. E. Kass and A. E. Raftery, "Bayes Factors," *Journal of the American Statistical Association*, vol. 90, no. 430, pp. 773–795, 1995. Online available: https://www.tandfonline.com/doi/abs/10.1080/01621459.1995.10476572

[262] M. A. Newton and A. E. Raftery, "Approximate Bayesian Inference with the Weighted Likelihood Bootstrap," *Journal of the Royal Statistical Society. Series B (Methodological)*, vol. 56, no. 1, pp. 3–48, 1994. Online available: http://www.jstor.org/stable/2346025

[263] A. Caldwell, P. Eller, V. Hafych *et al.*, "Integration with an Adaptive Harmonic Mean Algorithm," *arXiv e-prints: arXiv:1808.08051*, August 01, 2018 2018. Online available: https://doi.org/10.48550/arXiv.1808.08051

[264] "Saint-Gobain Ceramics & Plastics, Inc." Online available: https://www.crystals.saint-gobain.com

[265] "Hamamatsu Photonics K. K." Online available: http://www.hamamatsu.com

[266] A. B. Mann, I. Konorov, H. Angerer *et al.*, "The universal sampling ADC readout system of the COMPASS experiment," in *2009 IEEE Nuclear Science Symposium Conference Record (NSS/MIC)*, pp. 2225–2228. Online available: https://doi.org/10.1109/NSSMIC.2009.5402077

[267] "Paul Scherrer Institute, Switzerland." Online available: https://www.psi.ch

[268] D. Reggiani *et al.*, "Characterization of the PiM1 Beam Line at the PSI-HIPA Facility," in *5th Beam Telescopes and Test Beams Workshop*, Conference Proceedings. Online available: https://indico.desy.de/indico/event/16161/session/12/contribution/34/material/slides/0.pdf

[269] M. Almurayshid, Y. Helo, A. Kacperek *et al.*, "Quality assurance in proton beam therapy using a plastic scintillator and a commercially available digital camera," *Journal of Applied Clinical Medical Physics*, vol. 18, no. 5, pp. 210–219, 2017. Online available: https://aapm.onlinelibrary.wiley.com/doi/abs/10.1002/acm2.12143

[270] R. E. Kass and A. E. Raftery, "Bayes Factors," *Journal of the American Statistical Association*, vol. 90, no. 430, pp. 773–795, 1995. Online available: https://www.tandfonline.com/doi/abs/10.1080/01621459.1995.10476572

[271] H. Jeffreys, *The Theory of Probability, 3rd Edition, in: Oxford Classic Texts in the Physical Sciences*. Oxford University Press, 2003.

[272] J. Mueller, "Particle-Antiparticle Discrimination using Neural-Networks," Bachelor's Thesis, Technical University of Munich, 2018.

[273] B. Schorr, "Programs for the Landau and the Vavilov distributions and the corresponding random numbers," *Computer Physics Communications*, vol. 7, no. 4, pp. 215–224, 1974. Online available: https://www.sciencedirect.com/science/article/pii/0010465574900915

[274] R. Fruewirth, M. Regler, R. Bock *et al.*, *Data Analysis Techniques for High-Energy Physics*. Cambridge University Press, 2000.

[275] G. R. Lynch and O. I. Dahl, "Approximations to multiple Coulomb scattering," *Nuclear Instruments and Methods in Physics Research Section B: Beam Interactions with Materials and Atoms*, vol. 58, no. 1, pp. 6–10, 1991. Online available: https://www.sciencedirect.com/science/article/pii/0168583X9195671Y

[276] B. Ristic and A. Sanjeev, *Beyond the Kalman filter : particle filters for tracking applications*. Boston, MA: Artech House, 2004.

[277] M. S. Arulampalam, S. Maskell, N. Gordon *et al.*, "A tutorial on particle filters for online nonlinear/non-Gaussian Bayesian tracking," *IEEE Transactions on Signal Processing*, vol. 50, no. 2, pp. 174–188. Online available: https://doi.org/10.1109/78.978374

[278] M. Milde, "Development of a Data-Analysis Framework for the Multi-purpose Active-target Particle Telescope," Master's Thesis, Technical University of Munich, 2016.

[279] M. Kronmueller, "Pattern Recognition for the Multi-purpose Active-target Particle Telescope with Hough Transforms," Bachelor's Thesis, Technical University of Munich, 2016.

[280] L. Bierwirth, "Development of a Neural Network for Online Event Reconstruction for a Radiation Monitor," Master's Thesis, Technical University of Munich, 2019.

[281] S. Saerkkae, *Bayesian Filtering and Smoothing*, ser. IMS Textbooks. Cambrige University Press, 2013, vol. 3.

[282] P. Galeone, *Hands.On Neural Networks with TensorFlow 2.0*. Brimingham: Packt, 2019.

[283] K. Hornik, M. Stinchcombe, and H. White, "Multilayer feedforward networks are universal approximators," *Neural Networks*, vol. 2, no. 5, pp. 359–366, 1989. Online available: https://www.sciencedirect.com/science/article/pii/0893608089900208

[284] I. Goodfellow, Y. Bengio, and A. Courville, *Deep learning*. MIT Press, 2016. Online available: http://www.deeplearningbook.org

[285] L. Meyer-Hetling, "A Neural-Network-Based Event Reconstruction for the RadMap Telescope," Master's Thesis, Technical University of Munich, 2021.

[286] A. Geron, *Hands-on Machine Learning with Scikit-Learn, Keras, and TensorFlow: Concepts, Tools, and Techniques to Build Intelligent Systems.* O'REILLY Media Inc., 2017.

[287] C. Szegedy, W. Liu, Y. Jia *et al.*, "Going Deeper with Convolutions," *arXiv e-prints: arXiv:1409.4842*, September 01, 2014 2014. Online available: https://doi.org/10.48550/arXiv.1409.4842

[288] J. Mueller, "Particle-Antiparticle Discrimination using Neural Networks," Master's Thesis, Technical University of Munich, 2021.

[289] C. M. Bishop, *Pattern Recognition and Machine Learning.* Springer New York, NY, 2011.

[290] D. P. Kingma and J. Ba, "Adam: A Method for Stochastic Optimization," p. arXiv:1412.6980, December 01, 2014.

[291] Google LLC., "TensorFlow," 2022. Online available: https://www.tensorflow.org/

[292] M. Abadi, A. Agarwal, P. Barham *et al.*, "TensorFlow: Large-Scale Machine Learning on Heterogeneous Distributed Systems," *arXiv e-prints: arXiv:1603.04467*, March 01, 2016 2016. Online available: https://doi.org/10.48550/arXiv.1603.04467

[293] "Python programming language,"2022. Online available: https://www.python.org/

[294] L. Meyer-Hetling, "Particle Tracking with Neural Networks," Bachelor's Thesis, Technical University of Munich, 2018.

[295] F. Dimiccoli, R. Battiston, K. Kanishchev *et al.*, "Measurement of Cosmic Deuteron Flux with the AMS-02 Detector," *Journal of Physics: Conference Series*, vol. 1548, no. 1, p. 012034, 2020. Online available: http://dx.doi.org/10.1088/1742-6596/1548/1/012034

[296] O. Larsson, "Analysis of the Radiation Environment on Board the International Space Station Using Data from the SilEye-3/Alteino Experiment," Doctoral Thesis, KTH, 2014. Online available: http://www.diva-portal.se/smash/get/diva2:717764/FULLTEXT01.pdf

[297] J. Saha, P. Wilson, P. Thieberger *et al.*, "Biological Characterization of Low-Energy Ions with High-Energy Deposition on Human Cells," *Radiation Research*, vol. 182, no. 3, pp. 282–291, 10, 2014. Online available: https://doi.org/10.1667/RR13747.1

[298] N. Ganushkina, I. Dandouras, and H. Rème, "Locations of boundaries of outer and inner radiation belts as observed by Cluster and Double Star," *EGU General Assembly 2010*, p. 9622, May 01, 2010 2010. Online available: https://ui.adsabs.harvard.edu/abs/2010EGUGA..12.9622G

[299] W. Li and M. K. Hudson, "Earth's Van Allen Radiation Belts: From Discovery to the Van Allen Probes Era," *Journal of Geophysical Research (Space Physics)*, vol. 124, p. 8319, 2019. Online available: https://doi.org/10.1029/2018ja025940

[300] R. S. Selesnick, D. N. Baker, A. N. Jaynes *et al.*, "Observations of the inner radiation belt: CRAND and trapped solar protons," *Journal of Geophysical Research: Space Physics*, vol. 119, no. 8, pp. 6541–6552, 2014. Online available: https://agupubs.onlinelibrary.wiley.com/doi/abs/10.1002/2014JA020188

[301] A. S. Jursa, "Handbook of Geophysics and the Space Environment. 4th edition (Final)," Report, 1985. Online available: https://www.osti.gov/biblio/5572212

[302] W. N. Hess, "Energetic particles in the inner Van Allen belt," *Space Science Reviews*, vol. 1, no. 2, pp. 278–312, 1962. Online available: https://doi.org/10.1007/BF00240580

[303] R. S. Selesnick, M. K. Hudson, and B. T. Kress, "Injection and loss of inner radiation belt protons during solar proton events and magnetic storms," *Journal of Geophysical Research: Space Physics*, vol. 115, no. A8, 2010. Online available: https://agupubs.onlinelibrary.wiley.com/doi/abs/10.1029/2010JA015247

[304] O. Adriani, G. C. Barbarino, G. A. Bazilevskaya *et al.*, "THE DISCOVERY OF GEOMAGNETICALLY TRAPPED COSMIC-RAY ANTIPROTONS," *The Astrophysical Journal*, vol. 737, no. 2, p. L29, 2011. Online available: http://dx.doi.org/10.1088/2041-8205/737/2/L29

[305] J. D. Sullivan, "Geometric factor and directional response of single and multi-element particle telescopes," *Nuclear Instruments and Methods*, vol. 95, no. 1, pp. 5–11, 1971. Online available: http://www.sciencedirect.com/science/article/pii/0029554X71900334

Appendix A

Galdef Files

In the following, the parameters used in our GALPROP simulation are shown. The parameters are from the Galdef file, which configures all required variables of the galactic setup and the injection and propagation parameters in GALPROP. The used Galdef file is as used in Boschini et al. [163].The variables are explained by comments, which start with a hash. I present only settings which are used in our simulation. For all parameters that are not shown, the default settings of GALPROP are used. The parameters used in the Galdef file are:

```
n_spatial_dimensions =  2    # 2-D propagation in the galaxy

z_min                = -4  # negative halo size  (kpc)
z_max                = +4  # positive halo size  (kpc)
dz                   = 0.1 # distance of grid points along z (kpc)

r_min                = 0    # position of galactic center (kpc)
r_max                = 20   # size of the galactic disc (kpc)
dr                   = 1.0  # distance of grid points along r (kpc)

p_Ekin_grid          = Ekin  # use kinetic-energy grid
Ekin_min             = 1.0e0 # minimal Ekin (MeV/n)
Ekin_max             = 1.0e9 # maximal Ekin (MeV/n)
Ekin_factor          = 1.07  # energy-grid-density factor

D0_xx        = 4.26e28 # diffusion coefficient at D_rigid_ref (cm^2/s)
D_rigid_ref  = 4.0e3   # normalizing- rigidity of the diff. coeff. (MV)
D_rigid_br   = 4.3e3   # break rigidity of the diffusion power law (MV)
D_g_1        = 0.415   # power-law coefficient below the diffusion break
D_g_2        = 0.416   # power-law coefficient above the diffusion break
D_eta        = 0.70    # exponent on beta in D0_xx calc.

diff_reacc       = 1      #include diffusive reacceleration
v_Alfven         = 30.049 #Alfven velocity (km/s)
```

```
convection       = 1    #include convection
v0_conv          = 0    # constant galactic wind velocity (km/s)
dvdz_conv        = 9.75 #velocity increase of gal. wind along z (km/s)

fragmentation         = 1    #include fragmentation
momentum_losses       = 1    #include momentum losses
radioactive_decay     = 1    #include radioactive decay
K_capture             = 1    #include K-capture
ionization_losses     = 1    #include ionization losses
coulomb_losses        = 1    #include coulomb losses
bremss_losses         = 1    #include bremsstrahlung losses
IC_losses             = 1    #include inverse Compton losses
sync_losses           = 1    #include synchrotron losses

tertiary_antiprotons = 1    #compute tertiary antiprotons
secondary_protons    = 1    #compute secondary protons

proton_norm_Ekin = 1.00e+5 # Ekin of protons used
                             for flux normalization (MeV)
proton_norm_flux = 4.32e-9 # flux normalization at proton_norm_Ekin
                             (cm^-2 sr^-1 s^-1 MeV^-1)

source_model          = 1    # parameterized source distribution,
                               constant for r > source_parameters_4
source_parameters_0   = 0.2  # z distr. of sources:
                               exp(z/source_parameters_0) (kpc)
source_parameters_1   = 1.5  # alpha parameter from Eq(1.5)
source_parameters_2   = 3.5  # B parameter from Eq(1.5)
source_parameters_4   = 15.0 # for r > source_parameters_4
                               use constant source density


network_iterations    = 1 # how often the ion-network
                            is evaluated
total_cross_section   = 2 # model of total cs
cross_section_option = 012 # option of total cs model
t_half_limit          = 1.0e4 # lower limit for rad. decay (yr)

solution_method       = 1 #solution method (1 = CN, 2 = explicit)

start_timestep        = 1.0e8 # start timestep of CN method
end_timestep          = 1.0e2 # end timestep of CN method
timestep_factor       = 0.75  # timestep-reduction factor
timestep_repeat       = 30    #repetitions per timestep
timestep_repeat2      = 1e4 # repetion of timestep
```

```
                                in explicit method
                                (uses start_timestep steps)

He_H_ratio              = 0.11 # He-to-H ratio in ISM

inj_spectrum_type       = rigidity # injection spectra in rigidity
max_Z                   = 14 # max. Z of ions that are included
use_Z_1                 = 1  # use Z = 1 particles
use_Z_2                 = 1  # use Z = 2 particles
use_Z_3                 = 1  # use Z = 3 particles
use_Z_4                 = 1  # use Z = 4 particles
use_Z_5                 = 1  # use Z = 5 particles
use_Z_6                 = 1  # use Z = 6 particles
use_Z_7                 = 1  # use Z = 7 particles
use_Z_8                 = 1  # use Z = 8 particles
use_Z_9                 = 1  # use Z = 9 particles
use_Z_10                = 1  # use Z = 10 particles
use_Z_11                = 1  # use Z = 11 particles
use_Z_12                = 1  # use Z = 12 particles
use_Z_13                = 1  # use Z = 13 particles
use_Z_14                = 1  # use Z = 14 particles

#the iso_abundence parameters sets the abundance of a
  certain particle in the sources. The values are used
  to calculate a relative abundance w.r.t. to the proton
  abundance iso_abundance_01_001.

iso_abundance_01_001 = 0.8765e+06 # protons
iso_abundance_01_002 = 0          # deuterons
iso_abundance_02_003 = 1e-04      # helium-3
iso_abundance_02_004 = 0.7528e+05 # helium-4
iso_abundance_03_006 = 1e-06      # lithium-6
iso_abundance_03_007 = 52         # lithium-7
iso_abundance_04_007 = 0          # beryllium-7
iso_abundance_04_009 = 2.65e-05   # beryllium-9
iso_abundance_04_010 = 5.30e-06   # beryllium-10
iso_abundance_05_010 = 1.80e-04   # boron-10
iso_abundance_05_011 = 7.42e-04   # boron-11
iso_abundance_06_012 = 2720       # carbon-12
iso_abundance_06_013 = 5.268e-07  # carbon-13
iso_abundance_07_014 = 207        # nitrogen-14
iso_abundance_07_015 = 5.961e-05  # nitrogen-15
iso_abundance_08_016 = 3510       # oxygen-16
iso_abundance_08_017 = 6.713e-07  # oxygen-17
iso_abundance_08_018 = 1.286      # oxygen-18
iso_abundance_09_019 = 0.95       # oxygen-19
```

```
iso_abundance_10_020 = 338          # neon-20
iso_abundance_10_021 = 0.003556     # neon-21
iso_abundance_10_022 = 107          # neon-22
iso_abundance_11_023 = 24.1         # sodium-23
iso_abundance_12_024 = 490          # sodium-24
iso_abundance_12_025 = 70           # magnesium-25
iso_abundance_12_026 = 90           # magnesium-26
iso_abundance_13_027 = 51.12        # aluminum-27
iso_abundance_14_028 = 580          # silicon-28
iso_abundance_14_029 = 35.02        # silicon-29
iso_abundance_14_030 = 24.68        # silicon-30

#the injection spectra are modeled as
 broken power laws. The source_pars for each ion
 species consists of three values per constant spectral
 index: The spectral index, the upper break rigidity, and
 a smoothing parameter to smooth the break.

spectral_pars_01_001 = 2.24  0.95e3 0.29 1.696 6.97e3 0.22 2.443
                       415e3  0.0877  2.188  16.0e6 0.09  2.37
spectral_pars_01_002 = 2.24 0.95e3 0.29 1.696 6.97e3  0.22 2.443
                       415e3  0.0877  2.188  16.0e6 0.09  2.37
spectral_pars_02_003 = 2.05  1.0e3 0.26  1.76   7.487e3 0.33 2.41
                       340e3 0.13  2.117   30.0e6 0.10  2.37
spectral_pars_02_004 = 2.05  1.0e3 0.26  1.76   7.487e3 0.33 2.41
                       340e3 0.13  2.117   30.0e6 0.10  2.37
spectral_pars_03_006 = 1.1   12e3 0.16 2.72  355e3 0.13  1.90
spectral_pars_03_007 = 1.1   12e3 0.16 2.72  355e3 0.13  1.90
spectral_pars_06_012 = 1.00  1.1e3 0.19 1.978 6.54e3 0.31  2.43
                       348e3 0.17 2.12
spectral_pars_06_013 = 1.00  1.1e3 0.19 1.978 6.54e3 0.31  2.43
                       348e3 0.17 2.12
spectral_pars_07_014 = 1.00  1.30e3 0.17 1.96 7.0e3 0.20  2.460
                       300e3 0.17 1.90
spectral_pars_08_016 = 0.95  0.9e3 0.18 1.989  7.5e3 0.30  2.458
                       368e3 0.17 2.128
spectral_pars_08_017 = 0.95  0.9e3 0.18 1.989  7.5e3 0.30  2.458
                       368e3 0.17 2.128
spectral_pars_08_018 = 0.95  0.9e3 0.18 1.989  7.5e3 0.30  2.458
                       368e3 0.17 2.128
spectral_pars_09_019 = 0.20   1.5e3 0.19 1.97 7e3 0.20 2.48
                       355e3 0.17 2.14
spectral_pars_10_020 = 0.60  1.15e3 0.17 1.92 9.42e3 0.26 2.44
                       355e3 0.15 1.965
spectral_pars_10_021 = 0.60  1.15e3 0.17 1.92 9.42e3 0.26 2.44
                       355e3 0.15 1.965
```

```
spectral_pars_10_022 = 0.60  1.15e3 0.17 1.92 9.42e3 0.26 2.44
                       355e3 0.15 1.965
spectral_pars_11_023 = 0.5  0.75e3 0.17 1.98  7e3 0.21 2.485
                       350e3 0.16 2.14
spectral_pars_12_024 = 0.20 0.85e3 0.12 1.985 7e3 0.23 2.48
                       350e3 0.15 2.15
spectral_pars_12_025 = 0.20 0.85e3 0.12 1.985 7e3 0.23 2.48
                       350e3 0.15 2.15
spectral_pars_12_026 = 0.20 0.85e3 0.12 1.985 7e3 0.23 2.48
                       350e3 0.15 2.15
spectral_pars_13_027 = 0.20 0.6e3 0.17 2.04 7e3 0.20 2.48
                       355e3 0.17 2.14
spectral_pars_14_028 = 0.20 0.85e3 0.17 1.967 7e3 0.26 2.47
                       355e3 0.15 2.19
spectral_pars_14_029 = 0.20 0.85e3 0.17 1.967 7e3 0.26 2.47
                       355e3 0.15 2.19
spectral_pars_14_030 = 0.20 0.85e3 0.17 1.967 7e3 0.26 2.47
                       355e3 0.15 2.19
```

Appendix B

Additional Details on the Model Comparison For Prompt-Antiproton Production

B.1 Experimental Data

The datasets with lowest center-of-momentum energy we consider are from Dekkers et al., published in 1965 [202]. They measured the momentum-differential antiproton-production cross section in proton-proton collisions for two different collision energies and two different scattering angles. The experimental uncertainties are on the order of 10 % to 30 % due to a low count rate. As the experiment was only able to measure particles at a fixed scattering angle at a time, the covered phase space by the experiment is small compared to more recent fixed-target experiments. Due to the experimental setup, antiprotons from weak decays are not distinguished and are included in the experimental data. Also, no correction for this effect has been conducted afterwards. The published data are shown in Figure B.1.

The NA61 collaboration has conducted measurements at several center-of-momentum energies between 7.7 GeV and 17.3 GeV at CERN's Super Proton Synchrotron (SPS) in the last years and provides antiproton-multiplicity measurements in several bins of transverse momentum and rapidity, covering nearly the complete phase space [203]. Their experimental setup allows to distinguish and reject antiprotons from weak decays in order to obtain spectra that consist only of promptly produced antiprotons. The data are shown in Figure B.2.

The predecessor experiment of NA61, the NA49 experiment, conducted a similar measurement at a single center-of-momentum energy of 17.3 GeV [204]. They published the invariant antiproton-production cross section in bins of p_{t} and x_{F}. The data are shown in Figure B.3.

At even larger collision energies, only data from collider experiments are available, which often do not cover the whole phase space of the produced antiprotons. The PHENIX experiment, located at the Relativistic Heavy Ion Collider (RHIC) at the Brookhaven

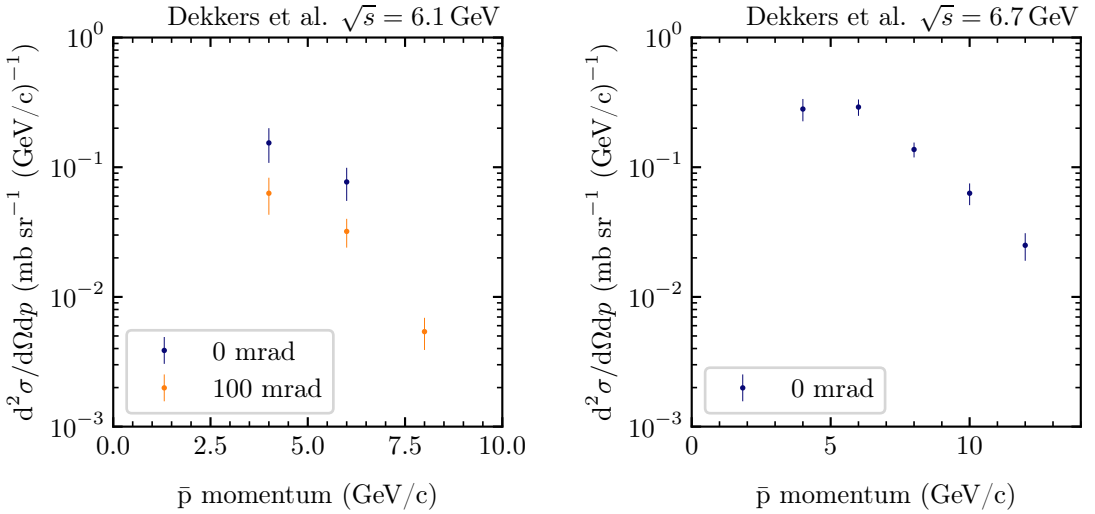

(a) Beam momentum of 18.8 GeV/c.

(b) Beam momentum of 23.1 GeV/c.

Figure B.1: Experimental data of antiproton production in p-p collisions from [202].

National Laboratory, provides data at $\sqrt{s} = 62.4\,\mathrm{GeV}$ and $\sqrt{s} = 200.0\,\mathrm{GeV}$ for central rapidity [205]. The collaboration provides the data with and without correction for antiprotons from decayed antihyperons. As can be deduced from Figure B.4, the magnitude of the correction is not identical for different values of p_t and increases with decreasing p_t. Additionally at $\sqrt{s} = 200.0\,\mathrm{GeV}$, the BRAHMS experiment at RHIC provides antiproton production measurements at forward rapidity [206]. The experiment measured the invariant antiproton-production cross section in two rapidity regions, for $2.9 < y < 3.0$ and $3.25 < y < 3.35$. Antiprotons produced in this kinematic region have particular large kinetic energy in the lab frame and are of special interest when investigating the production of high-energy antiprotons in the galaxy. The data for both rapidity bins are shown in Figure B.5.

At even larger energies, data from LHC experiments are available. We will use the data from the ALICE experiment at $\sqrt{s} = 900.0\,\mathrm{GeV}$, as the even higher collision energies are not of interest for galactic cosmic rays since such high-energy collisions are rare in the galaxy and do not contribute significantly to the production of antiprotons that are in the energy range measurable by AMS-02 [207]. They measured the invariant antiproton multiplicity at central rapidity, as shown in Figure B.6.

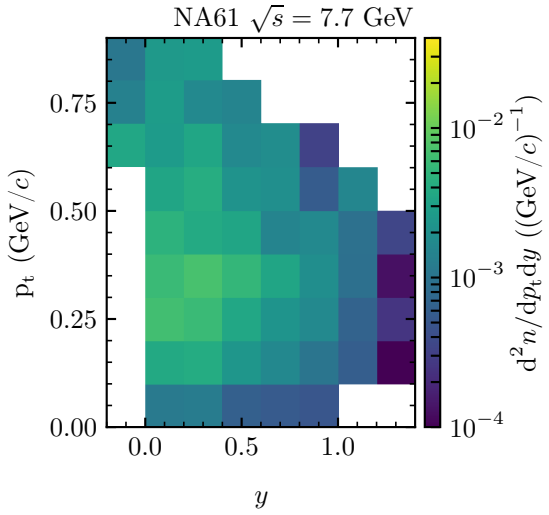

(a) Beam momentum of 31 GeV/c.

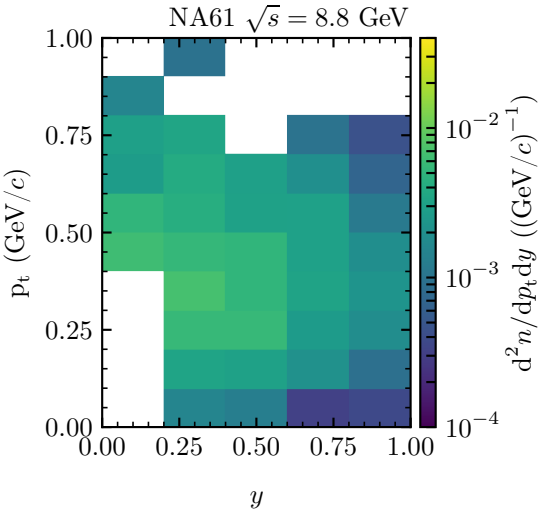

(b) Beam momentum of 40 GeV/c.

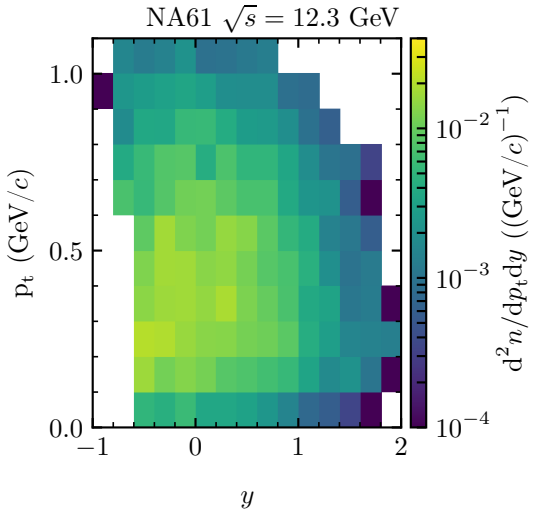

(c) Beam momentum of 80 GeV/c.

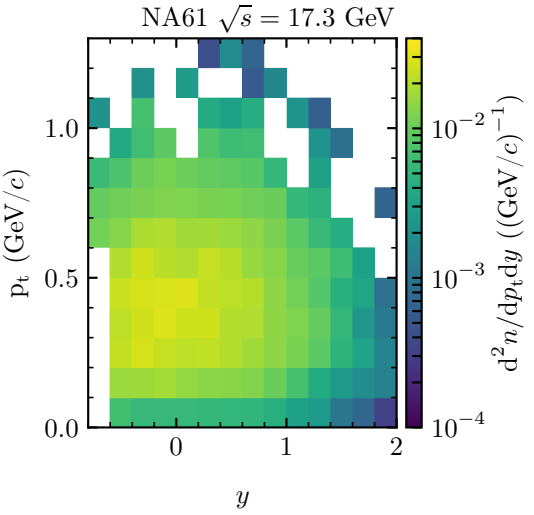

(d) Beam momentum of 158 GeV/c.

Figure B.2: Experimental data of antiproton production in p-p collisions from NA61 [203].

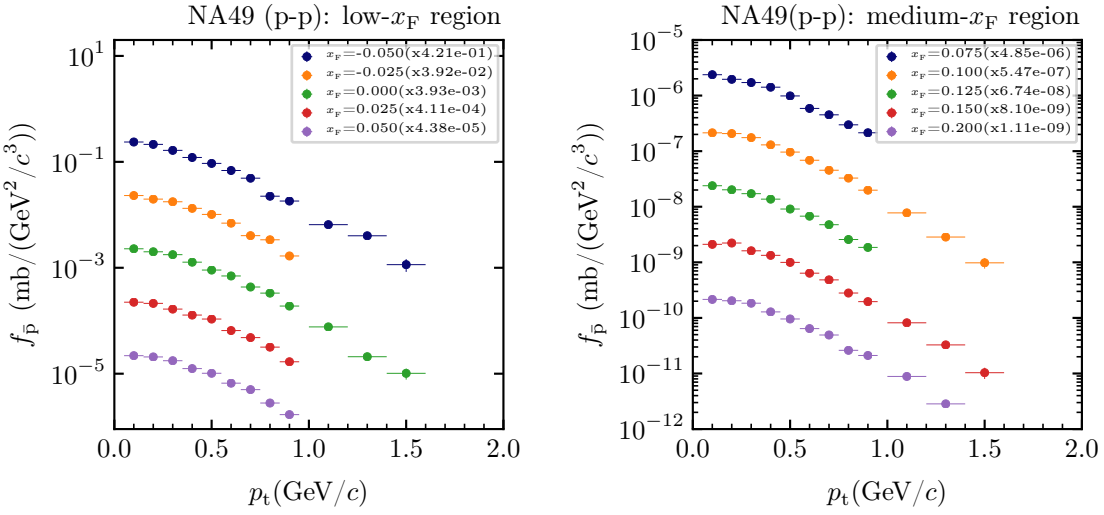

(a) $-0.050 \leq x_F \leq 0.050$.

(b) $0.075 \leq x_F \leq 0.200$.

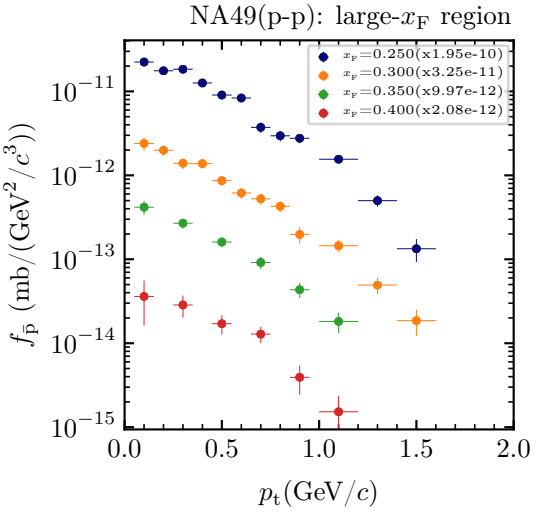

(c) $0.250 \leq x_F \leq 0.400$.

Figure B.3: Experimental data of antiproton production in p-p collisions from NA49 [204].

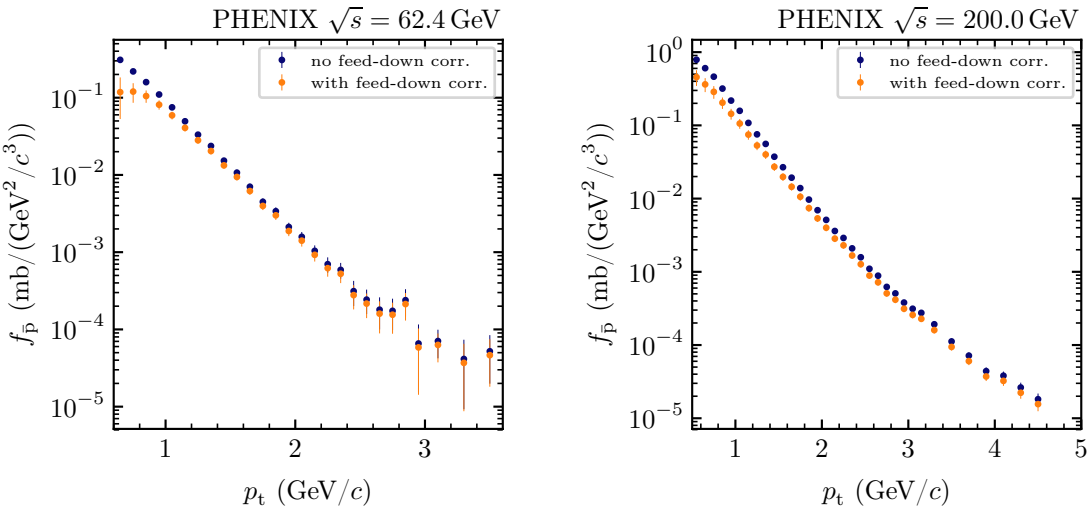

(a) Collision energy of $\sqrt{s} = 62.4\,\mathrm{GeV}$. (b) Collision energy of $\sqrt{s} = 200\,\mathrm{GeV}$.

Figure B.4: Experimental data of antiproton production in p-p collisions from PHENIX [205].

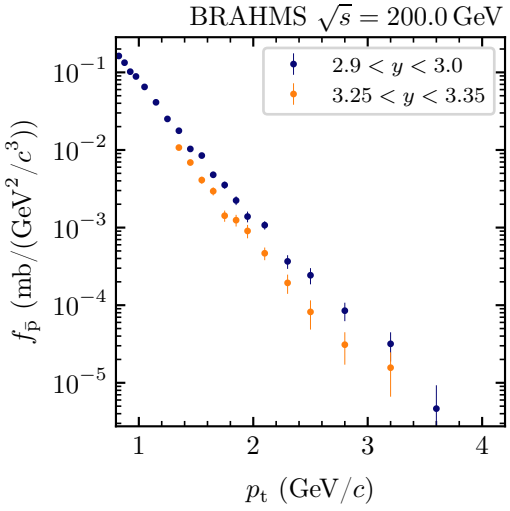

Figure B.5: Experimental data of antiproton production in p-p collisions from BRAHMS [206].

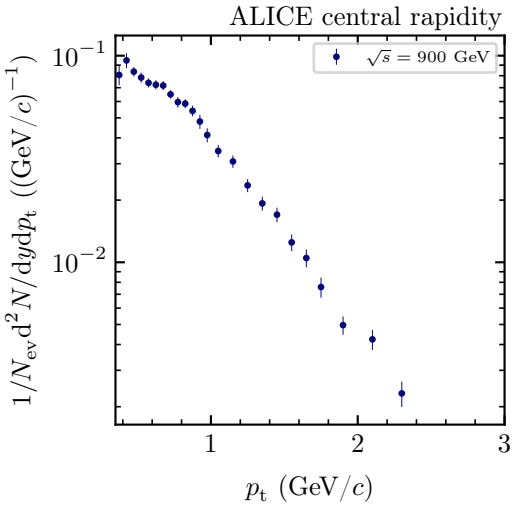

Figure B.6: Experimental data of antiproton production in p-p collisions from ALICE [207].

B.2 Event Generators

In this section, I give additional information on the found deviations of the antiproton production by the different event generators and the experimental data.
The experimental data with the lowest collision energies we compare to, is from Dekkers et al. at $\sqrt{s} = 6.1\,\mathrm{GeV}$ and $\sqrt{s} = 6.7\,\mathrm{GeV}$ [202]. As their experimental setup did not allow to differentiate prompt antiprotons from antiprotons from antihyperon decay and no further correction has been applied, we include the decay of antihyperons in the event generators for this dataset. The experimental data together with the results obtained with the different event generators are shown in Figure B.7. The antiproton yield is best reproduced by the EPOS-LHC event generator. The two PYTHIA-model based generators, PYTHIA-8 and GiBUU, both overestimate the antiproton yield by more than a factor three.
More precise information on the phase-space distribution of the found deviations is obtained by the help of the measurements of the double-differential antiproton multiplicity in bins of p_{t} and y by the NA61 collaboration [203]. The deviations of the antiproton yields from the different event generators compared to the experimental data for each of the collision energies are shown in Figure B.8. The lowest collision energy for which the antiproton-production data is published is $\sqrt{s} = 7.7\,\mathrm{GeV}$, only slightly above the Dekkers et al. measurements. The found deviations of the different event generators from the NA61 data are comparable to the deviations found to the Dekkers et al. data. Due to the more precise measurement and larger phase-space coverage, changes of the deviations within the phase space are visible. Especially for PYTHIA-8 and GiBUU the deviations increase with increasing p_{t} and y. With increasing collision energy, the deviation of the antiproton production by the PYTHIA-8 generator from the NA61 data decreases, but PYTHIA-8 still overproduces antiprotons by around a factor two at $\sqrt{s} = 17.3\,\mathrm{GeV}$. For the EPOS models, the deviations increase with increasing collision energy. EPOS-LHC overproduces antiprotons by approximately 40 % and EPOS-3 by approximately 90 % at $\sqrt{s} = 17.3\,\mathrm{GeV}$.

At the same collision energy, also data from the predecessor experiment NA49 is available and I show the comparison of the event generators to the data in Figure B.9. Again, the overproduction of the event generators generally increases with increasing transverse and longitudinal momentum of the produced antiprotons and is in agreement with the findings from the comparison to the NA61 data.
At larger collision energies, the experiments cover only a smaller fraction of the phase space of produced antiprotons. The production of antiprotons from the event generators at central rapidity is investigated by comparing their production to the experimental data of the PHENIX experiment at $\sqrt{s} = 62.4\,\mathrm{GeV}$ and $\sqrt{s} = 200\,\mathrm{GeV}$. As can be seen in Figure B.10, the shape of the p_t spectrum is reproduced well by almost all event generators. However, the total yields deviate. At low p_t, none of the tested event generators reproduces the flattening of the experimental data and all generators overproduce significantly antiprotons with low p_t. However, as the feed-down correction by PHENIX is unnaturally large compared to the assumptions e.g. by Winkler [195], the deviation might stem from the feed-down correction.
In addition to the PHENIX data, the BRAHMS experiment published a measurement of antiproton production at $\sqrt{s} = 200\,\mathrm{GeV}$ in a very forward rapidity region of $2.9 \leq y \leq 3.35$. The combination of both data sets allows to investigate the rapidity-dependence of the antiproton production at collision energies only accessible with collider experiments. The comparison of the antiproton production by the event generators with the experimental data from BRAHMS is shown in Figure B.11. Similar to the comparison with the PHENIX data, most event generators are able to reproduce the shape of the p_t spectrum but fail to reproduce the total yield.
The data with the highest collision energies considered in this study are from ALICE at $\sqrt{s} = 900\,\mathrm{GeV}$. The obtained antiproton spectra from the event generators and the comparison to the experimental data are given in Figure B.12. None of the event generators can reproduce the shape of the measured p_t distribution well.

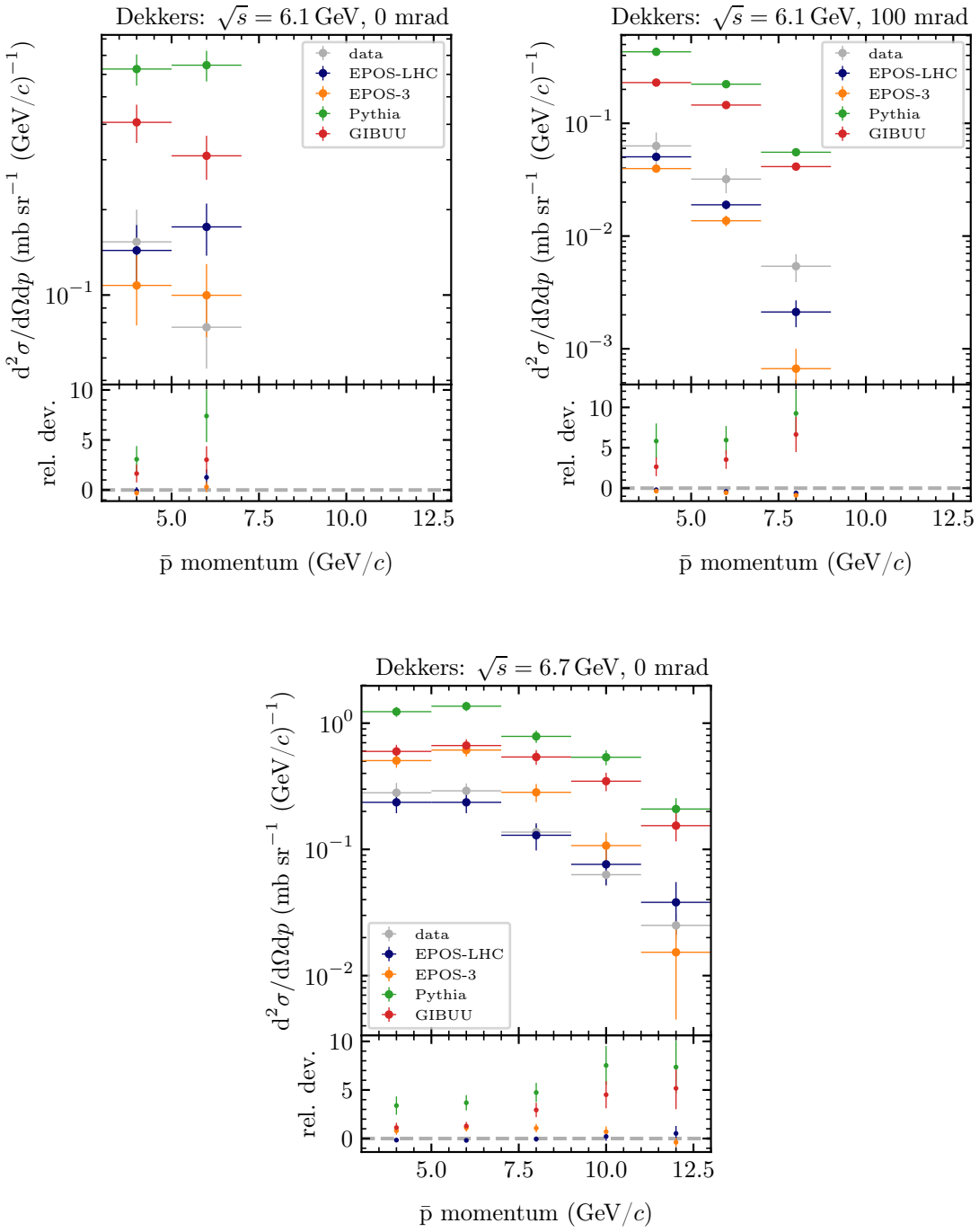

Figure B.7: Comparison of antiproton production of different event generators at $\sqrt{s} = 6.1\,\mathrm{GeV}$ and $\sqrt{s} = 6.7\,\mathrm{GeV}$ compared to the experimental data from Dekkers et al. [202].

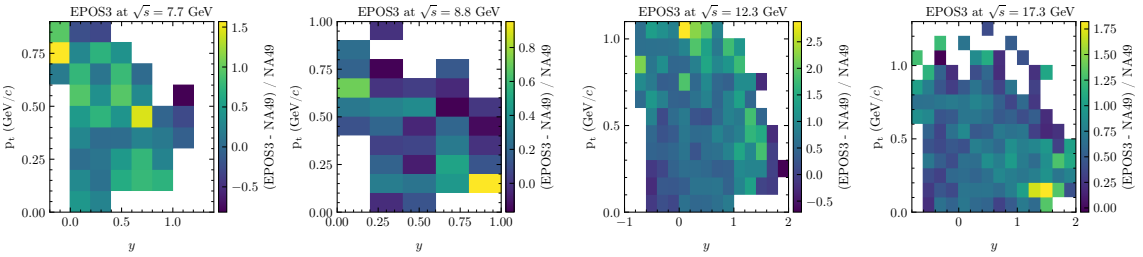

(a) Relative deviations of the antiproton spectra simulated by EPOS-3 and NA61 data.

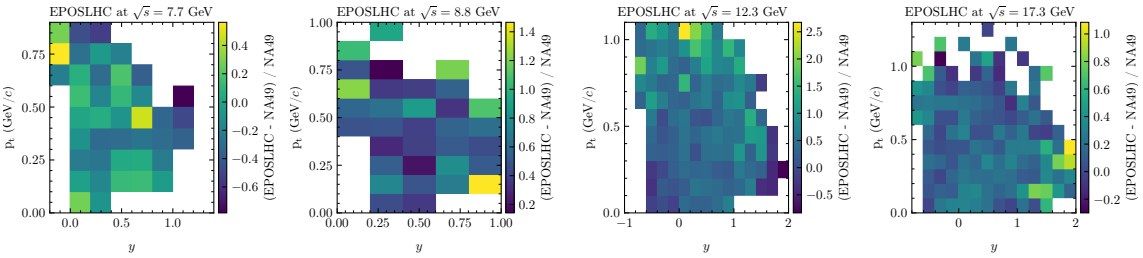

(b) Relative deviations of the antiproton spectra simulated by EPOS-LHC and NA61 data.

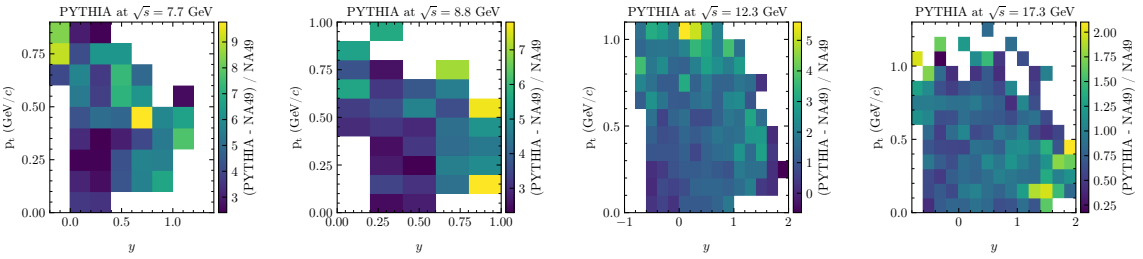

(c) Relative deviations of the antiproton spectra simulated by PYTHIA-8 and NA61 data.

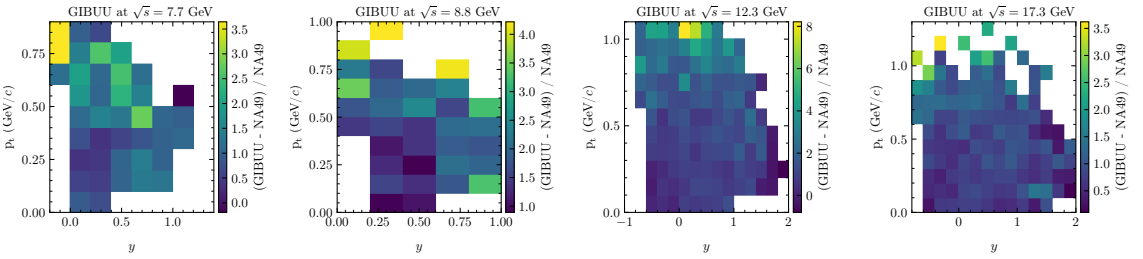

(d) Relative deviations of the antiproton spectra simulated by GiBUU and NA61 data.

Figure B.8: Comparison of antiproton production of different event generators with experimental data from NA61 [203].

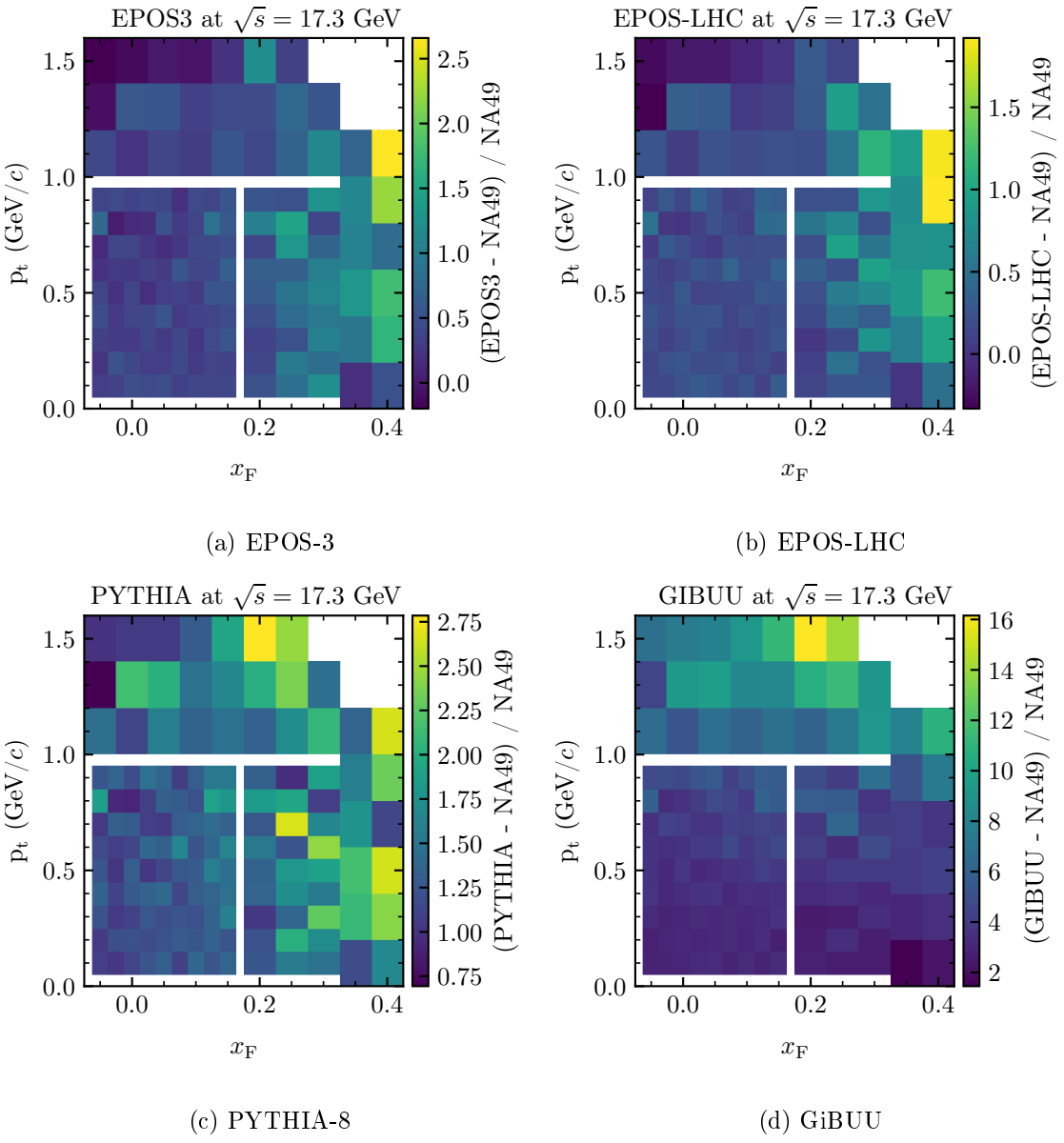

(a) EPOS-3

(b) EPOS-LHC

(c) PYTHIA-8

(d) GiBUU

Figure B.9: Comparison of antiproton production of different event generators at $\sqrt{s} = 17.3\,\text{GeV}$ with the experimental data from NA49 [204].

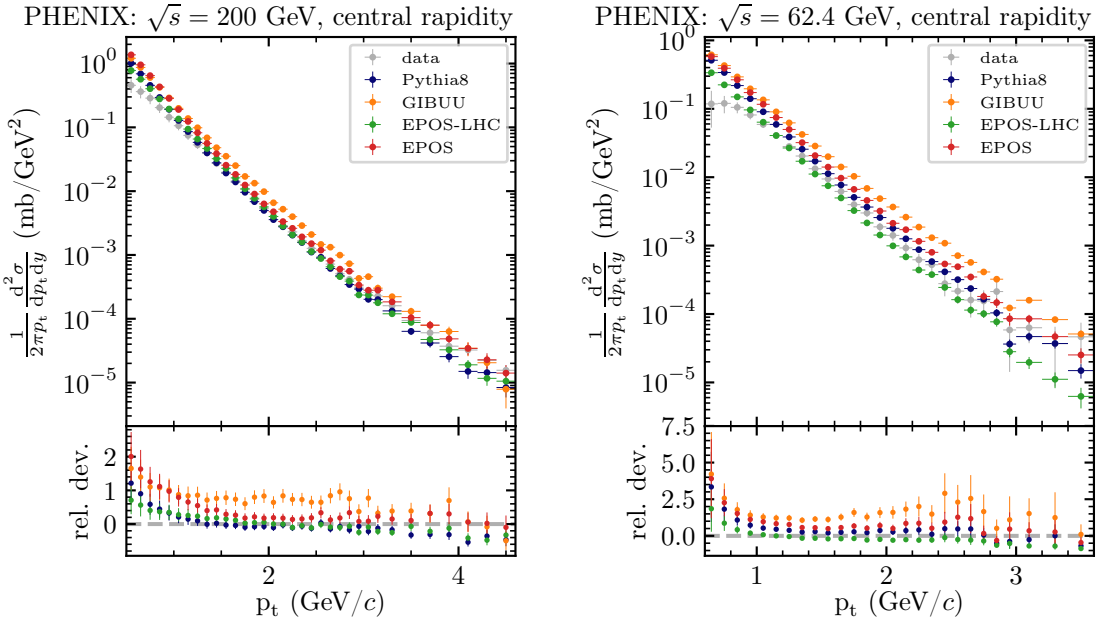

Figure B.10: Comparison of antiproton production of different event generators at $\sqrt{s} = 62.4\,\text{GeV}$ and $\sqrt{s} = 200.0\,\text{GeV}$ compared to the experimental data from PHENIX [205].

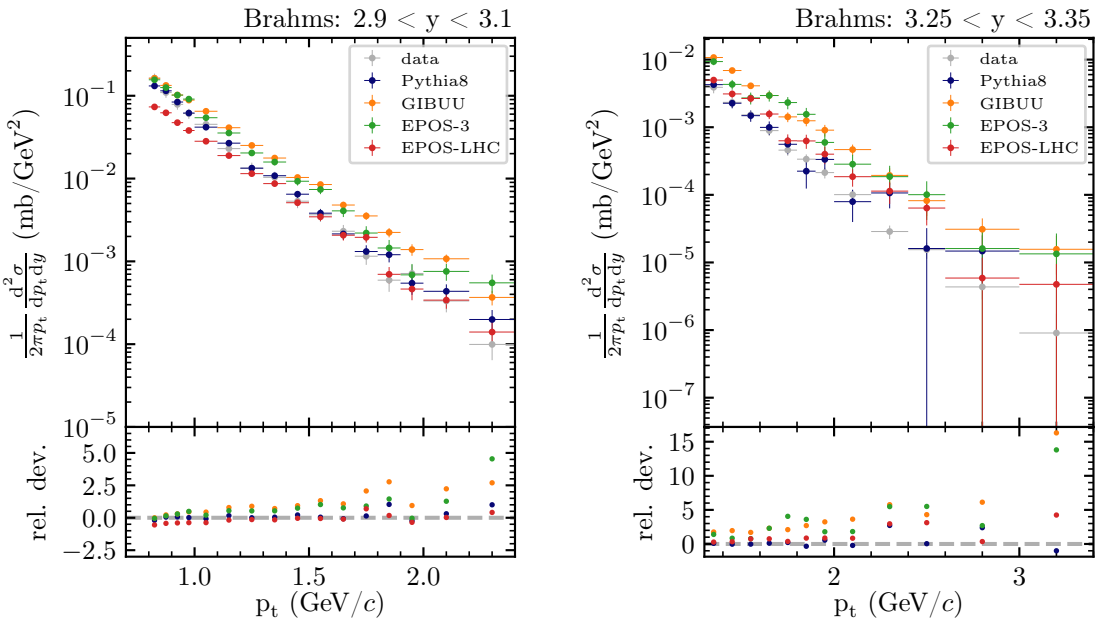

Figure B.11: Comparison of antiproton production of different event generators at $\sqrt{s} = 200.0\,\text{GeV}$ compared to the experimental data from BRAHMS [206].

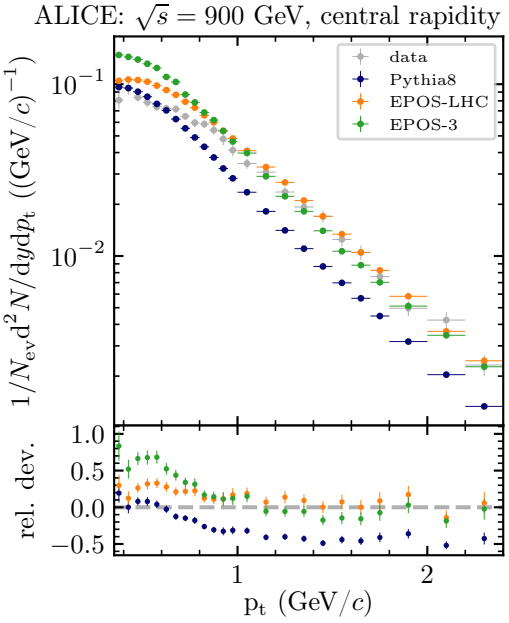

Figure B.12: Comparison of antiproton production of different event generators at $\sqrt{s} = 900.0\,\text{GeV}$ compared to the experimental data from ALICE [207].

B.3 Analytical Parameterizations

In the following, I present the fit results of the different parameterizations and the deviations of them to the individual experimental data. In Table B.1, Table B.2, and Table B.3 I give the correlation matrices of the fit parameters obtained by the MCMC-based fitting procedure for the different analytical parameterizations by Di Mauro et al., M. Winkler, and for the adapted Winkler parameterization, as described in Section 3.3.1.2.
To visually compare the agreement of the fits with the experimental data they are fitted to, the samples of the MCMC are used to calculate the prediction of the antiproton production distributed according to the posterior-probability distribution in each bin of the experimental data. In addition to our fit results, I also show the prediction for the original models and parameters by M. Winkler and Di Mauro et al. as obtained in their works [195, 181].
I again start the comparison with the experimental data from Dekkers et al., which corresponds to the lowest collision energy considered in this study. Figure B.13 shows the obtained antiproton yields for the different fitted models and the deviation to the experimental data. All models obtain systematically smaller antiproton yields as measured by Dekkers et al., with increasing deviations for increasing antiproton momentum.
For the NA61 data between $\sqrt{s} = 7.7\,\text{GeV}$ and $\sqrt{s} = 17.3\,\text{GeV}$ and the NA49 data at $\sqrt{s} = 17.3\,\text{GeV}$, the refitted parameterizations from Winkler and Di Mauro et al. show larger deviations with respect to the original parameters obtained by them and to the fitted adapted Winkler parameterization, as can be seen in Figure B.14 and Figure B.15. This is caused by the inability of the models to simultaneously explain the phase-space distribution of the data from low collision energies, below $\sqrt{s}$ 20 GeV, and the phase-space distribution for the data for higher collision energies. As a result, the refitted parameterization from Di Mauro et al. underproduces antiprotons over the whole phase space for all collision energies of NA61 and NA49. As the original parameters from Winkler and Di Mauro et al. were both extracted from fits employing mainly the NA49 data, their agreement with NA49 and NA61 data is expected. The fitted adapted Winkler parameterization, however, describes these datasets similarly well.
The comparison with the experiment data from the PHENIX experiment at $\sqrt{s} = 62.4\,\text{GeV}$ and $\sqrt{s} = 200\,\text{GeV}$ are shown in Figure B.16. While the overall shape of the spectrum and the total yield can be described within 20 % at $\sqrt{s} = 62.4\,\text{GeV}$ and 50 % at $\sqrt{s} = 200\,\text{GeV}$ by all refitted models, the results obtained by the parameterizations with the original parameters from the studies by Winkler and Di Mauro et al.—in which the data from PHENIX was not included—show even larger deviations.
The results for the complementary dataset by BRAHMS at $\sqrt{s} = 200\,\text{GeV}$, which in addition to the central rapidity region covered by PHENIX covers the forward rapidity region, are shown in Figure B.17. Especially the parameterization by Winkler with the original parameters yields a too large production of antiprotons for the forward-rapidity region covered by BRAHMS. The best agreement with the data is achieved by the model by Di Mauro et al. with the original parameters and the adapted Winkler model. Both are fitted to the BRAHMS data but in the study of Di Mauro et al. no additional central-rapidity data at this collision energy was used. Therefore, the good agreement of this parameterization with BRAHMS data comes at the cost of large deviations for the PHENIX data. Only the adapted Winkler model simultaneously describes both datasets equally well.

For the highest probed collision energy, $\sqrt{s} = 900\,\text{GeV}$, the parameterizations are compared with the dataset from the ALICE experiment. The obtained results for the parameterizations are shown in Figure B.18. All but the parameterization by Di Mauro et al. with the original parameters reproduce the spectrum well within 20 %.

	C_1	C_2	C_3	C_4	C_5	C_6	C_7	C_8
C_1	+1	-0.99	-0.26	+0.26	+0.17	-0.30	-0.10	+0.15
C_2		+1	+0.28	-0.28	-0.19	+0.34	+0.10	-0.16
C_3			+1	-0.93	+0.22	+0.23	+0.05	0.09
C_4				+1	+0.07	-0.32	-0.07	-0.11
C_5					+1	-0.50	-0.03	+0.04
C_6						+1	-0.15	-0.02
C_7							+1	-0.02
C_8								+1

Table B.1: Correlation matrix of the fit parameters of the parameterization by Di Mauro et al., as obtained by BAT.

	C_1	C_2	C_3	C_4	C_5	C_6
C_1	+1	+0.25	-0.26	+0.07	-0.02	-0.15
C_2		+1	+0.36	-0.22	+0.40	+0.20
C_3			+1	-0.78	+0.22	+0.12
C_4				+1	-0.11	-0.17
C_5					+1	-0.11
C_6						+1

Table B.2: Correlation matrix of the fit parameters of the parameterization by Winkler, as obtained by BAT.

	C_1	C_2	C_3	C_4	C_5	C_6	C_7
C_1	+1	+0.10	-0.10	+0.04	-0.14	+0.05	+0.25
C_2		+1	+0.25	-0.23	+0.23	+0.40	-0.56
C_3			+1	-0.82	-0.02	+0.18	+0.05
C_4				+1	+0.04	-0.16	+0.07
C_5					+1	-0.12	-0.21
C_6						+1	-0.21
C_7							+1

Table B.3: Correlation matrix of the fit parameters of the adapted Winkler parameterization, as obtained by BAT.

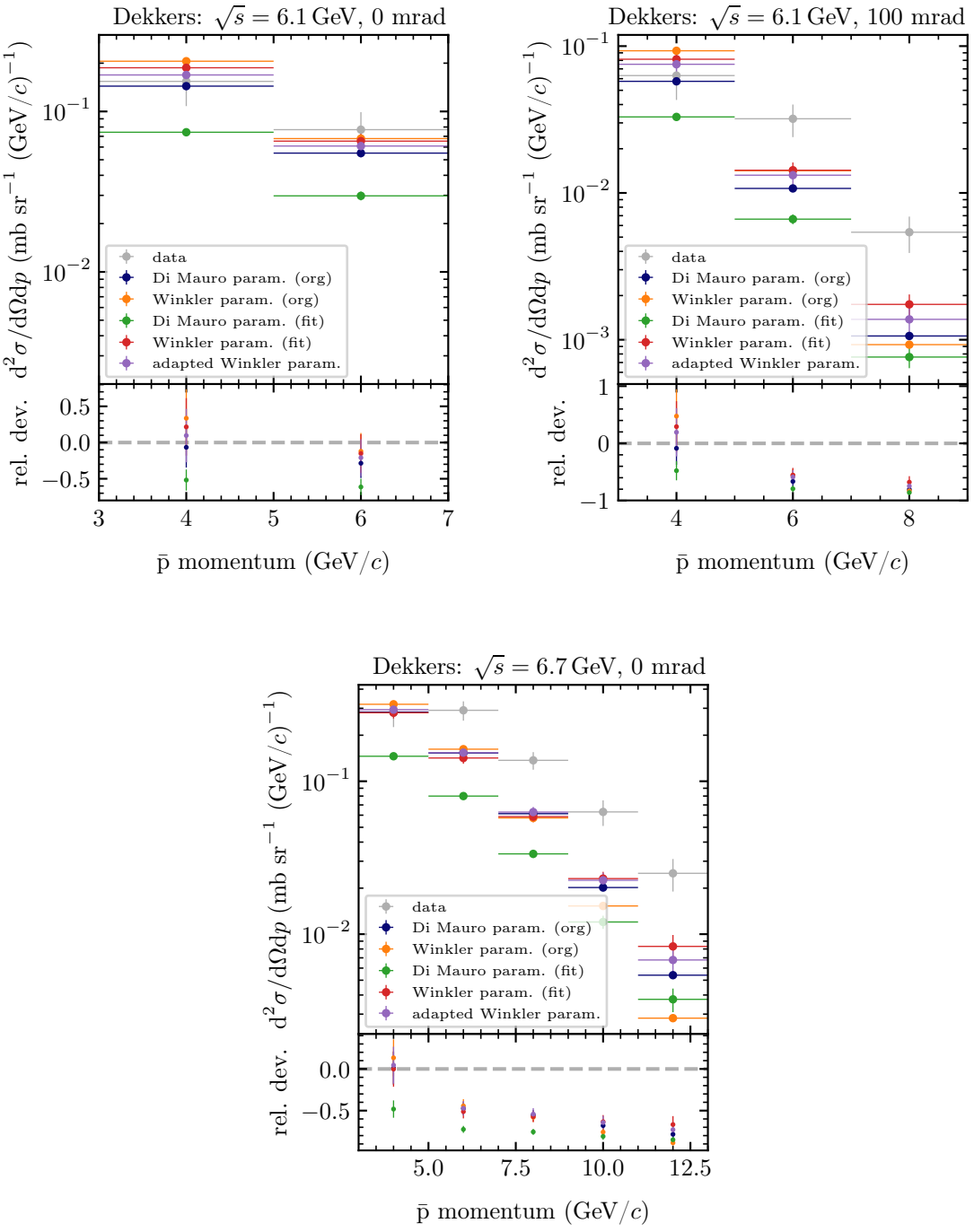

Figure B.13: Comparison of the antiproton production by the tested parameterizations with the experimental data from Dekkers et al. [202].

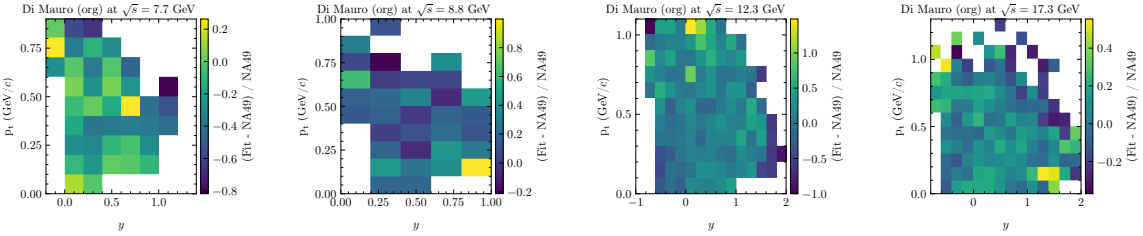

(a) Comparison of the parameterization by Di Mauro et al. with the original parameters and NA61 data.

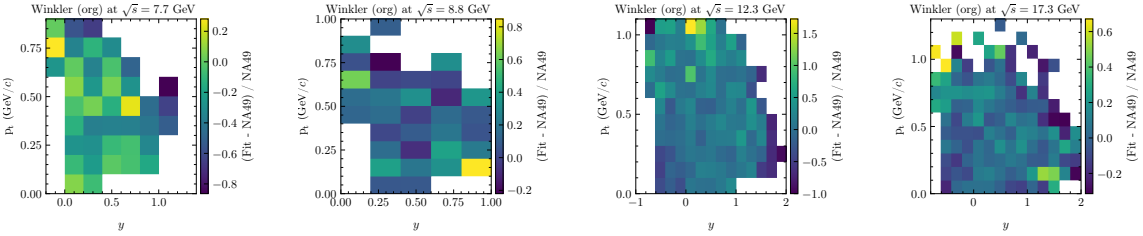

(b) Comparison of the Winkler parameterization with the original parameters and NA61 data.

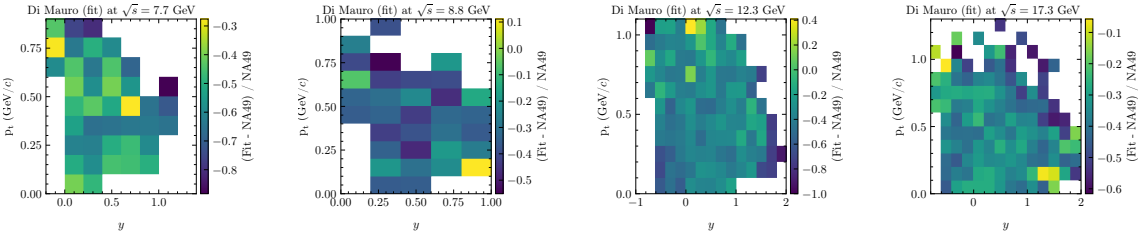

(c) Comparison of the refitted parameterization by Di Mauro et al. and NA61 data.

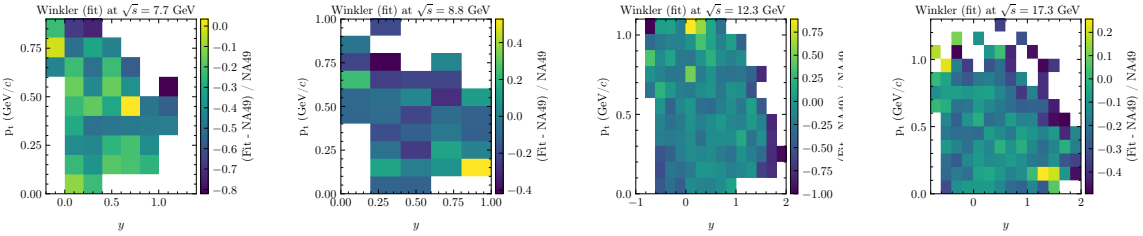

(d) Comparison of the refitted Winkler parameterization and NA61 data.

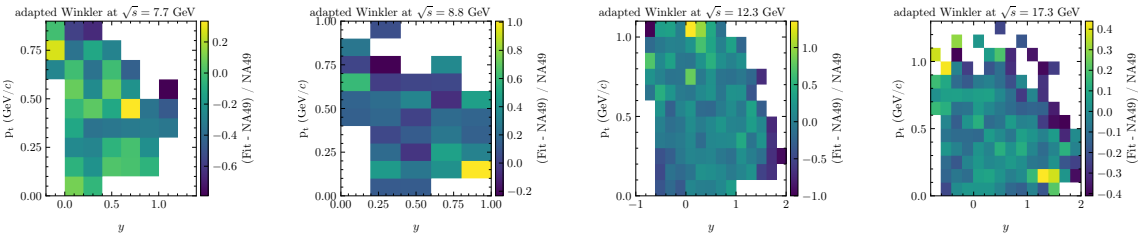

(e) Comparison of the adapted Winkler parameterization and NA61 data.

Figure B.14: Comparison of the antiproton production by the tested parameterizations with the experimental data from NA61 [203].

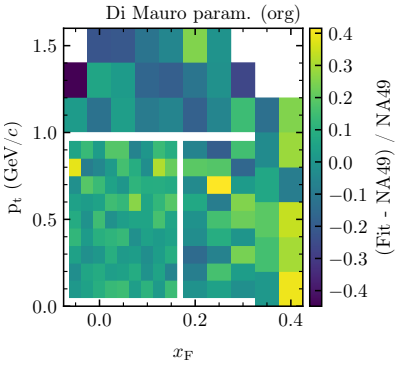

(a) Di Mauro et al. parameterization with the original parameter values.

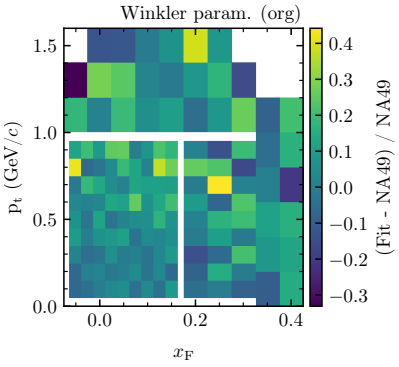

(b) Winkler parameterization with the original parameter values.

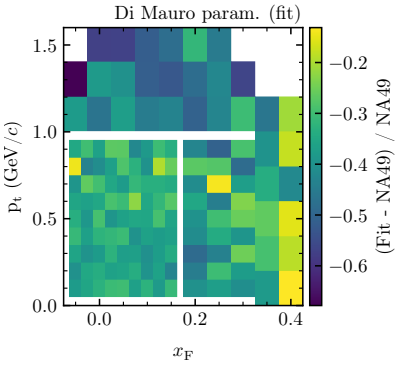

(c) Refitted Di Mauro et al. parameterization.

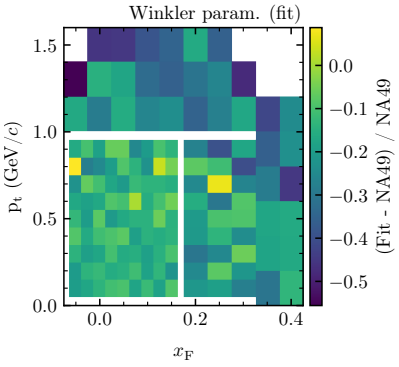

(d) Refitted Winkler parameterization.

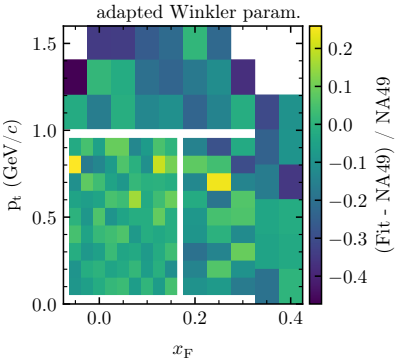

(e) Adapted Winkler parameterization.

Figure B.15: Comparison of the antiproton production by the tested parameterizations with the experimental data from NA49 [204].

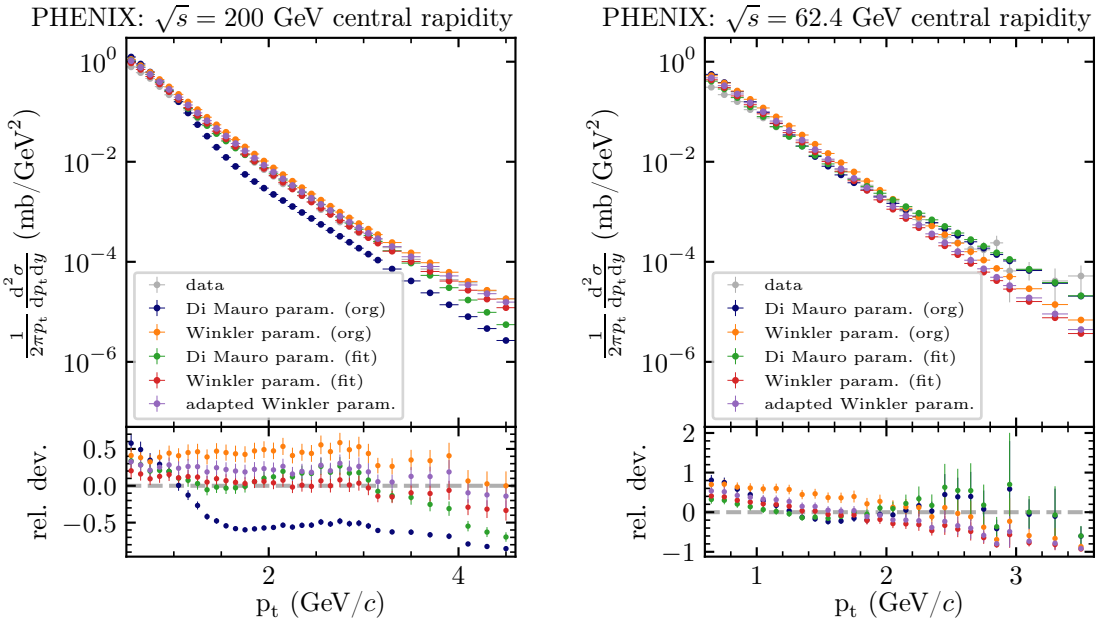

Figure B.16: Comparison of the antiproton production by the tested parameterizations with the experimental data from PHENIX [205].

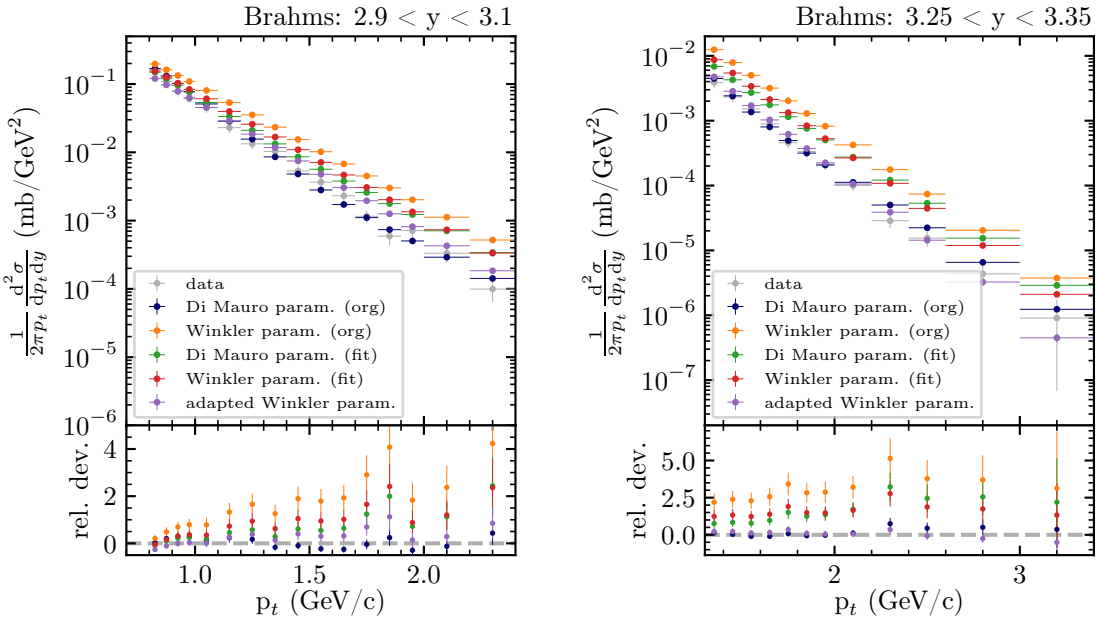

Figure B.17: Comparison of the antiproton production by the tested parameterizations with the experimental data from BRAHMS [206].

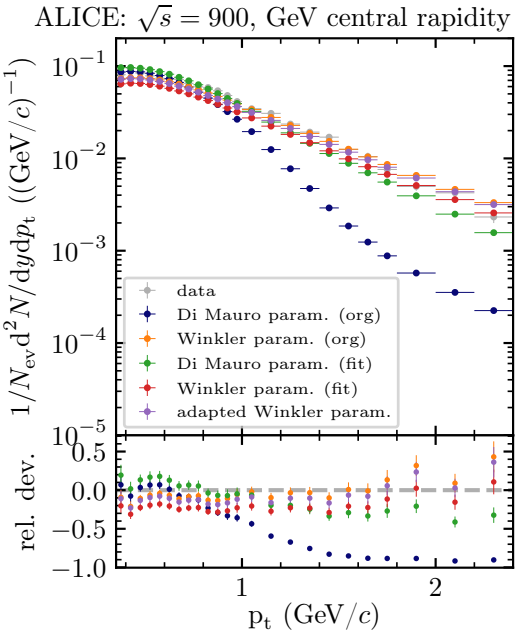

Figure B.18: Comparison of the antiproton production by the tested parameterizations with the experimental data from ALICE [207].

Appendix C

Own Contributions

As a starting member of the AFIS experiment in 2014 for my Master's thesis, I have contributed to the development of MAPT since then. Together with my fellow doctoral student Martin Losekamm, I have worked on the conception, science-case development, funding acquisition, project management, and technical development of the novel detector system under the supervision of Prof. Dr. Stephan Paul. The main focus of my development activity has been to design, implement, and improve the simulation and analysis framework of MAPT and to contrive the particle-identification scheme. During my work, I have supervised six Master-thesis projects and nine Bachelor-thesis projects on the development of analysis tools for MAPT and simulations of cosmic-ray phenomena, which are listed in Appendix D. To experimentally verify the principles of the detector concept and to validate design choices, I have applied for, planned, conducted, and analyzed several test-beam campaigns at Paul-Scherrer Institute together with my colleague and students. I have investigated the effect of ionization quenching from experimental data taken at one of the test-beam campaigns and published the results as corresponding author.
The study on the accuracy of the numerical-solution in GALPROP has been performed under the advice of Dr. Andrew Strong; The comparison of the different antiproton-production cross sections has been conducted under the advice of Prof. Dr. Laura Fabbietti in collaboration with Maximilian Horst—who has conducted the EPOS-3 simulations presented in this work—and Laura Serksnyte—who has implemented the interface for the different antiproton-production cross sections in GALPROP.
I have contributed to several publications, which are listed chronologically in Chapter E, and I have presented parts of this work at several national and international conferences.
In addition to the here-presented work, I have worked on further research projects during that time. I have been founding member of the LUVMI-X consortium, in which I have developed—together with Martin Losekamm—a neutron spectrometer and a charged cosmic-ray spectrometer as part of a suite of instruments for a Moon rover to search for water ice on the Moon. In 2016-2017 I have led a team of students of TUM within the REXUS/BEXUS program. Within the project, we have developed parts of a data-handling and communication system for CubeSats and validated them during a stratospheric-balloon flight. I am founding member of the AMBER collaboration at CERN and participated actively in the proposal process of the experiment.
Since 2015 I act as radiation-safety officer at the Department of Physics of the Technical

University of Munich in the group of Prof. Dr. Stephan Paul and since 2018 additionally in the group of Prof. Dr. Bastian Märkisch. I have actively contributed to teachings at the Technical University of Munich and founded and organized the seminar 'Satellite-Based Particle Physics'.

Appendix D

List of Supervised MAPT-related Theses

As the development of MAPT shall also serve educational and training purposes, many sub-tasks have been performed by students within the scope of Bachelors' and Masters' theses at the Technical University of Munich. In the following list, theses which have been co-supervised by the author are listed chronologically.

- L. Prüfer: *Detection of Cosmic Rays—from the Satellite to the Classroom* (Master's thesis) 2016.
- M. Kronmüller: *Pattern Recognition for the Multi-purpose Active-target Particle Telescope with Hough Transforms* (Bachelor's thesis) 2016.
- A. Meraner: *Simulation of Particle Fluxes in the Stratosphere* (Bachelor's Thesis) 2016.
- M. Milde: *Development of a Data-Analysis Framework for the Multi-purpose Active-target Particle Telescope* (Master's thesis) 2016.
- J. Kholdkov: *Development of Neural Networks for Online Track Reconstruction* (Bachelor's thesis) 2017.
- L. Ekemar: *Simulation of the Antiproton Flux in the Atmosphere* (Bachelor's thesis) 2017.
- M. Hanke: *Energy Reconstruction of Low-Energy Protons using Multi-Layer Perceptrons* (Bachelor's thesis) 2018.
- J. Müller: *Particle-Antiparticle Discrimination using Neural Networks* (Bachelor's thesis) 2018.
- M. Agarwal: *Particle Identification with Neural Networks for a Radiation Monitor* (Bachelor's thesis) 2018.
- L. Meyer-Hetling: *Particle Tracking with Neural Networks* (Bachelor's thesis) 2018.

- L. Bierwirth: *Development of a Neural Network for Online Event Reconstruction for a Radiation Monitor* (Master's thesis) 2019.
- L. Hollender: *A Bayesian Particle Filter for Particle Identification* (Master's thesis) 2019.
- M. Höschler: *Particle Identification for a Radiation Monitor based on Neural Networks* (Master's thesis) 2020.
- M. Hoch: *Simulation of the Cosmic Ray Albedo Neutron Decay* (Master's thesis) 2020.
- L. Eckert: *Integration and Calibration of the RadMap Telescope Detector Modules* (Bachelor's thesis) 2020.
- L. Meyer-Hetling: *A Neural-Network-Based Event Reconstruction for the RadMap Telescope* (Master's thesis) 2021.

Appendix E

List of Publications

During the research for this thesis, the author contributed to several publications, which are listed chronologically:

- A Novel CubeSat-Sized Antiproton Detector for Space Applications *Proceedings of the 34th International Cosmic Ray Conference* (2015)
- AFIS: A New Instrument for Cosmic Radiation Studies on BEXUS 18 and Future Nanosatellite Missions. *Proceedings of the 22nd ESA Symposium on European Rocket and Balloon Programmes and Related Research* (2015)
- MOVE-II – der zweite Kleinsatellit der Technischen Universität München. *Deutscher Luft-und Raumfahrtkongress 2015* (2015)
- Real-Time Omnidirectional Radiation Monitoring on Spacecraft. *AIAA SPACE 2016*(2016)
- A new analysis method using Bragg curve spectroscopy for a Multi-purpose Active-target Particle Telescope for radiation monitoring. *Nuclear Instruments and Methods in Physics Research Section A, Vol. 845* (2017)
- TDP-3 Vanguard: Verification of a New Communication System for CubeSats on BEXUS 22. *Proceedings of the 23nd ESA Symposium on European Rocket and Balloon Programmes and Related Research* (2017)
- Letter of Intent: A New QCD facility at the M2 beam line of the CERN SPS (COMPASS++/AMBER) *arXiv:1808.00848*(2018)
- LUVMI and LUVMI-X: Lunar Volatiles Mobile Instrumentation Concept and Extension. *15th Symposium on Advanced Space Technologies in Robotics and Automation* (2019)
- Cosmic-ray antinuclei as messengers of new physics: Status and outlook for the new decade. *Journal of Cosmology and Astroparticle Physics (JCAP08(2020)035)*(2020)
- Searching for Water Ice with the LUVMI-X Lunar Rover. *Proceedings of the International Symposium on Artificial Intelligence, Robotics and Automation in Space* (2020)

- Measurement of ionization quenching in plastic scintillators. *Nuclear Instruments and Methods in Physics Research Section A, Vol. 988* (2021)
- A Compact Cosmic-Ray and Neutron Spectrometer to Search for Water Ice on the Moon. *Proceedings of the 52nd Lunar and Planetary Science Conference* (2021)
- The RadMap Telescope on the International Space Station. *2021 IEEE Aerospace Conference (50100)* (2021)
- LUVMI-X: A Versatile Platform for Resource Prospecting on the Moon. *Proceedings of the 17th Biennial International Conference on Engineering, Science, Construction, and Operations in Challenging Environments* (2021)
- LUVMI-X: An Innovative Instrument Suit and Versatile Mobility Solution for Lunar Exploration. *Proceedings of the 72nd International Astronautical Congress* (2021)
- Reevaluation of the cosmic antideuteron flux from cosmic-ray interactions and from exotic sources. *Physical Review D (105,083021)* (2022)
- The Lunar Cosmic-Ray and Neutron Spectrometer: Phase-A Design and Technology Studies. *2022 IEEE Aerospace Conference* (2022)

Appendix F

Acknowledgments

Foremost, I would like to thank Prof. Dr. Stephan Paul for the possibility to conduct this research, the longstanding support, and the scientific freedom that I have experienced during my thesis. In addition, I would like to thank my colleague Martin Losekamm. The detector development would not have been possible without his endless enthusiasm and positive work ethic. Further, I want to give thanks to all colleagues, and experts with whom I had the pleasure to work with during my thesis. In particular Prof. Dr. Laura Fabbietti, Prof. Dr. Bastian Märkisch, Dr. Andrew Strong, Dr. Boris Grube, Dr. Daniel Greenwald, Laura Serksnyte, Maximilian Horst, Christian Dreisbach, Dominik Ecker, Dr. Dominic Gaissbauer, Dr. Stephan Huber, Karina Bernert, Florian Kasper, Karl Eichhorn, Lukas Bierwirth, Karin Frank, and all encouraged and curious students.
I also would like to thank all of my friends and former fellow students that have supported me during the—sometimes stressful—time and provided pleasant distraction from the work. In particular Dr. Philip Schmidt, Dr. Steffen Maurus, and Dr. Joana Wirth.
I want to express my special gratitude to my family, without their support none of my academic work would have been possible. Concluding, I would like to thank my girlfriend Martina Weigl for her never-ending patience and thoughtfulness over all the years of this work.